Doctoral Dissertation 2023

Biomimetic platforms for modeling *in vitro* the functional unit of the exocrine pancreas

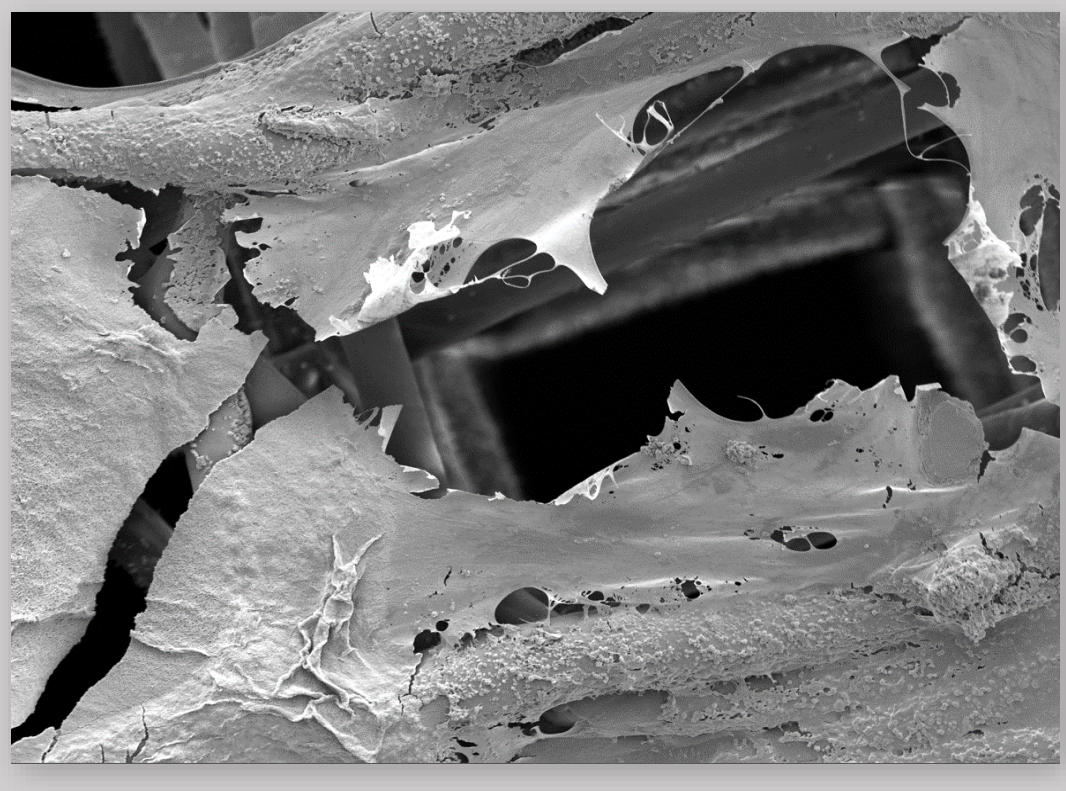

Viola Sgarminato

Politecnico di Torino

UNIVERSITÀ DI TORINO

Doctoral Program in Bioengineering
and Medical-Surgical Sciences
(35th Cycle)

Biomimetic platforms for modeling *in vitro* the functional unit of the exocrine pancreas

By

Viola Sgarminato

******

Supervisors:
Prof. Gianluca Ciardelli, Supervisor
Prof. Chiara Tonda-Turo, Co-Supervisor

Politecnico di Torino
2023

Declaration

I hereby declare that the contents of this dissertation constitute my own original work and do not compromise in any way the rights of third parties, including those relating to the security of personal data.

Viola Sgarminato
2023

I would like to dedicate this thesis to all the people who encouraged my thirst for knowledge and my love for science.

Table of Contents

Acknowledgements

I would like to express my deepest gratitude to all the people who made this PhD course an amazing experience, starting from my supervisors. Prof. Ciardelli (Gianluca), who is the first person who believed in me as researcher and passed down to me the passion for this project, and Prof. Tonda-Turo (Chiara), a brilliant scientist and an exceptional woman. She knew how to be a mentor, a confidant and a friend at the same time.

Special thanks to all the researchers and PhD students of the big group of Prof. Ciardelli and Prof. Chiono, who have been always available to help and support me.

I could not have undertaken this journey without Michela, Giulia, Camilla and Cecilia, whom I have shared it from the very beginning. Thank you for standing by me in the happiest moments, as well as in the hardest ones.

Thanks should also go to the Master students who worked on this project, especially Beatrice, Antonella and Matteo.

Words cannot express my gratitude to Prof. Moser for welcoming me in his research group at EPFL. There, I have had the honor of interfacing with other scientific realities and meeting colleagues who became great friends to me.
This endeavor would not have been possible without the magic team, Jorge and Antoine, who allowed the achievement of important results in a very short time.

I am also grateful to all my friends who, despite external to this world, are always ready to celebrate my successes and comfort me for failures.

Lastly, I would like to thank my main supporters. My parents and my family who have supported me every step of my life and Stefano (with Lucio) who more than anyone else has lived with me all the moments of these four years, making them even more beautiful.

Curriculum Vitae

- **EDUCATION**

2016 – 2018 Master's Degree in Biomedical Engineering, Politecnico di Torino, Torino (Italy)

Final grade: 110/110 *summa cum laude*

2012 – 2016 Bachelor's Degree in Biomedical Engineering, Politecnico di Torino, Torino (Italy)

2007 – 2012 High School Diploma in Scientific Studies, Liceo Scientifico G. Parodi, Acqui Terme (Italy)

- **TRAINING**

2019 Internship at University of Westminster, London (UK) and CIC nanoGUNE, San Sebastian (Spain)

2015 ; 2017 Internships (3+3 months), A.O. CITTÁ SALUTE E SCIENZA, Turin (Italy)

- **ACADEMIC POSITIONS**

2019 – PhD - Bioengineering and Medical-Surgical Sciences, Politecnico di Torino, Turin (Italy)

2022 Visiting PhD student, EPFL, Lausanne (Switzerland) for 4 months

2018 – 2019 Postgraduate Scholarship, Politecnico di Torino – Turin (Italy)

2018 Visiting Master student, Italian Institute of Technology, Pontedera (Italy) for 1 month

2017 Visiting Master student, Loughborough University, Loughborough (UK) for 4 months

- **SUPERVISION OF GRADUATE STUDENTS**

2022 Co-supervisor of a Master student in Biomedical Engineering at Politecnico di Torino (Italy)

2019 – 2022 Tutor of several students in Biomedical Engineering at Politecnico di Torino (Italy)

- **TEACHING ACTIVITIES**

2021 – Tutor: "Bio- and nano-technologies in medicine" Bachelor's Degree in Engineering, Politecnico di Torino (Italy)

2020 – Teaching Assistant: "Frontiers in Bioengineering Enabling Nanotechnologies, Master's Degree in Biomedical Engineering, Politecnico di Torino (Italy)

2019 – Teaching Assistant: "Biomimetic Systems", Master's Degree in Biomedical Engineering, Politecnico di Torino (Italy)

2019 – 2021 Tutor: "Bionanotechnology", Master's Degree in Biomedical Engineering, Politecnico di Torino (Italy)

- **MEMBERSHIPS OF SCIENTIFIC SOCIETIES**

2019 – Centro 3R, Interuniversity Center for the promotion of the 3Rs principles in teaching and research, Italy

2020 European Organ-on-Chip Society, International Independent Organization

- **CONFERENCES AND WORKSHOPS**

2023 TERMIS 2023 - Oral Presentation

2021 TERMIS 2021 - Poster Presentation

2021 Centro 3R Annual Meeting - Poster Presentation

(1st best poster award)

2021 ESB 2021 - Poster Presentation

2020 WBC 2020 - Poster Presentation

2020 I-RIM 2020 - Oral Presentation

2020 5th Int Health and Science Workshop, Pisa (Italy)

2020 EUROoCS 2020 - Poster Presentation

2019 MIPOL 2019 - Poster Presentation

2019 8th Workshop on 3D advanced in vitro models, Pavia (Italy)

- **PUBLICATIONS**

2023 V. Sgarminato, …, G. Ciardelli, C. Tonda-Turo, C. Moser, *under submission*

2023 V. Sgarminato, …, G. Ciardelli, C. Tonda-Turo, **Biomater. Sci.**, p. 208-224, doi: 10.1039/d2bm00881e

2021 V. Sgarminato, C. Tonda-Turo, G. Ciardelli, **J. Biomed. Sci. Eng.**, *Conference Proceeding*, doi: 10.4081/bse.2021.194

2019 V. Sgarminato, C. Tonda-Turo, G. Ciardelli, **J. Biomed. Mater. Res. - B Appl. Biomater.**, p. 1-10, doi: 10.1002/jbm.b.34467

2017 A. Bistolfi, …, V. Sgarminato, … , A. Massè, **JCRR**, p. 1-7, doi: 10.15761/CSRR.1000101

Executive Summary

The functional unit of exocrine pancreas is responsible for the secretion of digestive enzymes and it is the region where the first lesions of the most lethal pancreatic cancers (*i.e.*, pancreatic ductal adenocarcinoma, PDAC) develop. PDAC is a type of exocrine pancreas tumor which currently represents one of the leading causes of cancer-related death worldwide (5-year survival rate below 9%). Current research is focusing on better understanding of this pathology through creating effective *in vitro* models that can be used to recapitulate the key mechanisms involved in pancreatic cancer. However, although recent studies have shown the possibility of modeling the PDAC microenvironment *in vitro*, the microanatomy (in terms of 3D architecture and cellular composition) of the human pancreatic gland remains extremely challenging to be reproduced and monitored in functionally reliable models.

The main purpose of my PhD research is to reproduce the functional unit of the exocrine pancreas, constituted by epithelial and stromal cells. Specifically, this work aims at developing human *in vitro* models that allow to analyze the PDAC-stroma interplay and the mechanisms implicated during the initial stage of PDAC progression.

To achieve this goal, different biofabrication strategies were explored to obtain models which can be classified as two-dimensional (2D), two-and-a-half-dimensional (2.5D) and three-dimensional (3D). Each one, although being a simplified model showing both advantages and limitations, represented an important step in the process toward the development of a valuable and effective *in vitro* platform for the study of pancreatic cancer.
Moreover, all the here designed and fabricated models constitute, for different reasons, innovative engineering strategies that go beyond the state-of-the-art in cancer research.

The 2D model, composed by transwell inserts including a polycaprolactone/gelatin (PCL/Gel) electrospun membrane, allowed to preliminary study the reciprocal influence of different cell types (*i.e.*, stromal and epithelial cells) and it was able to reassemble the highest cytokines release and changes in cell morphology by fibroblasts co-cultured with epithelial cells overexpressing the KRAS oncogene which are also reported *in vivo*.
The information acquired using this simplified model were then transferred to a more complex 2.5D model, represented by a multilayer PDAC-on-chip system. This microfluidic device was designed to incorporate PDAC cells and a stromal cell-laden type I collagen hydrogel in the top and bottom layers, respectively. The use of a nanofibrous and biomimetic electrospun membrane, the same that has been integrated in the 2D model, allowed to compartmentalize the microfluidic device and thus separate the cancer component from the stromal tissue. In this way, the effect of the inflammation stimuli on stromal cells was studied in a controlled and specific way. This 2.5D model permitted to perform tests (*e.g.*, evaluation of cell resistance to chemotherapy) and analyses in a fast, medium-throughput and accessible manner.
Finally, the 3D models were obtained by two different approaches, *i.e.* layer-by-layer approaches (FDM and MEW models) and tomographic volumetric bioprinting (VBP model).
The layer-by-layer techniques used in this thesis project allowed to obtain macro- and microscale models replicating the half-structure of the complex gland morphology.
Specifically, the FDM model was used to preliminary assess the feasibility of reproducing the glandular structure by using a layer-by-layer approach and to monitor the fibroblasts viability on PCL printed structures over several weeks. Nevertheless, melt electrowriting (MEW) permitted to achieve better resolutions of the printed structures, that have dimensions about four times smaller than those of FDM constructs. These studies led us to proceed with the implementation of co-culture conditions only in

MEW scaffolds. The biomimicry of this model was demonstrated in terms of (i) capability to recreate the compartmentalization of stroma and epithelium found in PDAC microenvironment and (ii) ability to mirror the fibroblasts inflammation process occurring during pathology development.
Finally, the innovative technique of volumetric bioprinting was here adopted to develop a 3D *in vitro* model at the microscale, resembling the physiological "closed" structure typical of the pancreatic gland. In particular, a gelatin metacrylate (GelMA) hydrogel was *ad hoc* prepared and loaded with human fibroblasts to mimic the stromal compartment. Healthy or KRAS-mutated human pancreatic ductal epithelial cells were then introduced inside the construct's cavity to reproduce the exocrine tissue that evolves to neoplastic lesions during pancreatic carcinogenesis. The ability of VBP model in recapitulating the tumor-stroma interplay occurring in pancreatic cancer while also accurately reproducing the microanatomy of the exocrine gland was proved.

In conclusion, the *in vitro* models developed in this PhD work represent attractive and powerful tools for the establishment of new diagnostic approaches and for the screening and testing of drugs. Therefore, they can be fundamental to improve the knowledge of the complex mechanisms implicated in PDAC and find innovative therapeutical strategies to fight pancreatic cancer.

List of abbreviations

B
BSA: bovine serum albumin

C
CAD: computer-aided design
CAFs: cancer-associated fibroblasts
CRISPR: Clustered Regularly Interspaced Short Palindromic Repeats
CSF1: colony-stimulating factor 1
CTGF: connective tissue growth factor

D
DAPI: 4′,6-diamidino-2-phenylindole
DDR-1: discoidin receptor 1
DMEM: dulbecco's modified eagle's medium
DMSO: dimethyl sulfoxide
DNA: deoxyribonucleic acid

E
E-cadherin: epithelial cadherin
ECM: extracellular matrix
ELISA: enzyme-linked immunoassay
EMMPRIN: extracellular matrix metalloproteinase inducer
EMT: epithelial-mesenchymal transition

F
FAK: focal adhesion kinase
FBS: fetal bovine serum
FDM: fused deposition modeling
FESEM: field emission scanning electron microscopy
FITC: fluorescein isothiocyanate

G
Gel: gelatin
GelMA: gelatin methacrylate
GPTMS: 3-glycidoxypropyltrimethoxysilane

H
HA: hyaluronic acid
HFF1: human foreskin fibroblasts
HPDE: human pancreatic ductal epithelial
HUVECs: human umbilical vascular endothelial cells

I
IL-: interleukin-
IFN- γ: interferon-γ
IFP: interstitial fluid pressure

INVADE: integrated vasculature for assessing dynamic events
IPMNs: intraductal papillary mucinous neoplasms

L
LAP: lithium phenyl-2,4,6 trimethylbenzoylphosphinate
LOX: lysyl oxidase

M
MDSCs: myeloid-derived suppressor cells
MEW: melt elctrowriting
MMP2: matrix metalloproteinase 2
MMPs: matrix metalloproteinases
MRC-5: human lung fibroblasts

N
N-cadherin: neural cadherin
NK: natural killer
P
PANC-1: human pancreatic cancer cell line
PanIN: pancreatic intraepithelial neoplasia
PBS: phosphate buffer saline
PC: polycarbonate
PCL: poly(ε-caprolactone)
PCL-Gel: poly(Ɛ-caprolactone) - gelatin
PDAC: pancreatic ductal adenocarcinoma
PDMS: polydimethylsiloxane
PDOs: patient-derived organoids
PDX: patient-derived xenograft
PEGPH20: pegvorhyaluronidase alfa
PSCs: pancreatic stellate cells
PDGF: platelet-derived growth factor
PDGF-BB: platelet-derived growth factor BB
PEG: poly (ethylene glycol)
PET: poly (ethylene terephthalate)
PFA: paraformaldeide
PLGA: poly(lactic-co-glycolide)
PMMA: polymethylmethacrylate
PVA: polyvinyl alcohol

R
RPMI: Roswell Park Memorial Institute
RT: room temperature

S
SDF-1: stromal cell-derived factor-1
SEM: scanning electron microscopy

T
TAMs: tumor-associated macrophages
TG2: tissue transglutaminase 2
TGF-β1: transforming growth factor-β1
TNF-α: tumor necrosis factor α
TME: tumor microenvironment
TE: tissue engineering
Tregs: regulatory T cells

U
UFAW: universities federation for animal welfares

V
VBP: volumetric bioprinting
VEGF: vascular endothelial growth factor

W
WCA: water contact angle

2D: two-dimensional
2.5D: two-and-a-half-dimensional
3D: three-dimensional
α-SMA: alpha-smooth muscle actin

Introduction to the thesis format

The contents of this thesis are grouped into **four chapters**, whose brief description is reported below. Each experimental chapter (Chapter II and Chapter III) contains an abstract summarizing the chapter's contents, an introduction describing the premises of the experimental process and a "Conclusion" section, where the most important outcomes of the work are stated.

Chapter I is a general introduction focusing on the state-of-the-art related to tissue engineering strategies for modeling *in vitro* the exocrine pancreatic tissue. An overview of the healthy pancreatic tissue is provided, as well as the description of the pathological mechanisms involved in PDAC evolution. Moreover, this chapter descant on the current tissue models used for the study of pancreatic cancer, by reporting the advantages and limitations of each approach. Finally, the purpose of this dissertation is defined in the last section of Chapter I.

Chapter II aims at describing the development process of 2D and 2.5D models used to evaluate the PDAC-stromal cells relationship. Two sections "2.2 Transwell-based model" and "2.3 PDAC-on-chip" distinctly report the methodologies and the results (with discussion) of the work performed to develop the 2D and the 2.5D model, respectively. The work was performed in the framework of POLITOBIOMed LAB, an interdepartmental laboratory financed by Politecnico di Torino, and in collaboration with Chilab (Materials and Microsystems Laboratory) in Chivasso (TO).

Chapter III describes the exploitation of two different technical approaches (*i.e.*, layer-by-layer techniques and tomographic volumetric bioprinting) to reproduce the typical gland morphology of the functional unit of exocrine pancreas. In particular, the section "3.2 Layer-by-layer approaches" focuses on the models developed by fused deposition modeling (FDM) and melt electrowriting (MEW), while the model obtained through tomographic volumetric bioprinting is illustrated in "3.3 VBP model" section. The experimental work described in "3.2 Layer-by-layer approaches" has been mainly performed in the framework of POLITOBIOMed LAB, an interdepartmental laboratory financed by Politecnico di Torino. The research activities relative to the development of the VBP model were carried out at the Laboratory of Applied Photonics Devices (LAPD), EPFL in Lausanne (Switzerland).

Chapter IV contains the general discussion of the results presented in this dissertation as well as the most important achievements and the future steps of this PhD work.

Chapter I

Tissue engineering of exocrine pancreas

1.1 Overview of the pancreatic tissue

Pancreas is a glandular and parenchymatous organ of the digestive and endocrine systems with both exocrine and endocrine functions. Macroscopically, it appears as an elongated, flattened, S-shaped gland with three main portions identified as head, body and tail[1]. It is located in the retroperitoneal space, behind the peritoneum and the stomach, anterior to the first and second lumbar vertebrae (Fig. 1.1). The pancreas is the only organ in the body composed of exocrine and endocrine units intermixed within the parenchyma[2]. The exocrine part represents the 90% of the total mass and is constituted by pancreatic adenomeres while the endocrine component comprises about 1 to 2% and is composed by the islets of Langerhans. The interstitium with the blood vessels, lymphatics, nerves, and fibrous connective tissue constitutes the remainder[3].

1.1.1 Endocrine pancreas

The endocrine pancreas regulates glucose homeostasis by releasing hormones (*i.e.*, insulin and glucagon) into the blood stream. It is composed by different endocrine cell types, like Alpha cells (responsible for the production of glucagon), Beta cells (responsible for the insulin secretion), Delta cells (responsible for the synthesis of somatostatin) and finally the F cells (responsible for the production of pancreatic polypeptide). More specifically glucagon and insulin respectively increase and decrease the level of glucose, somatostatin inhibits the release of numerous hormones in the blood while the pancreatic polypeptide is an important feedback inhibitor of pancreatic secretion after a meal. The endocrine cells reside in small cell clusters, called islets of Langerhans, that are surrounded by the exocrine pancreas units and pancreatic capillaries[4] (Fig. 1.1).

1.1.2 Exocrine pancreas

The exocrine pancreas is the gland responsible for the production and secretion of a digestive juice rich in proteolytic (*e.g.*, trypsin and chymotrypsin), glycolytic (*e.g.*, amylase), and lipolytic (*e.g.*, lipase) enzymes, that is released into the duodenum, the first part of the small intestine, to favor the decomposition of macronutrients such as proteins, carbohydrates, and lipids[5]. This particular function is granted by the anatomical hierarchical structure of the exocrine pancreas, which consists of lobes, constituted themselves by lobules, each of them composed of acini[6]. The acini, called pancreatic acino-ductal units or pancreatic adenomeres, represent the fundamental units of the exocrine pancreas (Fig. 1.1). Each adenomere is composed of adjacent and highly oriented, pyramidal-shaped acinar cells arranged as a monolayer, with their apical membranes that coat a central lumen (*i.e.*, intercellular canaliculus or duct) and their basolateral membranes that form the acinar periphery[7]. Acinar cells have a developed Golgi apparatus and an abundant rough endoplasmic reticulum that are the anatomical areas responsible for enzymatic production[8]. The acinar cell secretions flow into the intercellular ducts composed of ductal epithelial cells and gradually converge into larger ducts. Finally, they reach the main pancreatic duct which combines, before the pancreatic juice enters the duodenum, with the common bile duct[9,10]. Each pancreatic acinus is surrounded by a thin basal lamina, scant reticular stroma, and pancreatic stellate cells (PSCs). The quiescent pancreatic stellate cells, whose protuberances may encompass a portion of an acinus, multiple acini, or portions of the ducts, are characterized by a contractile nature and stain positive for vimentin, desmin, glial fibrillary acidic

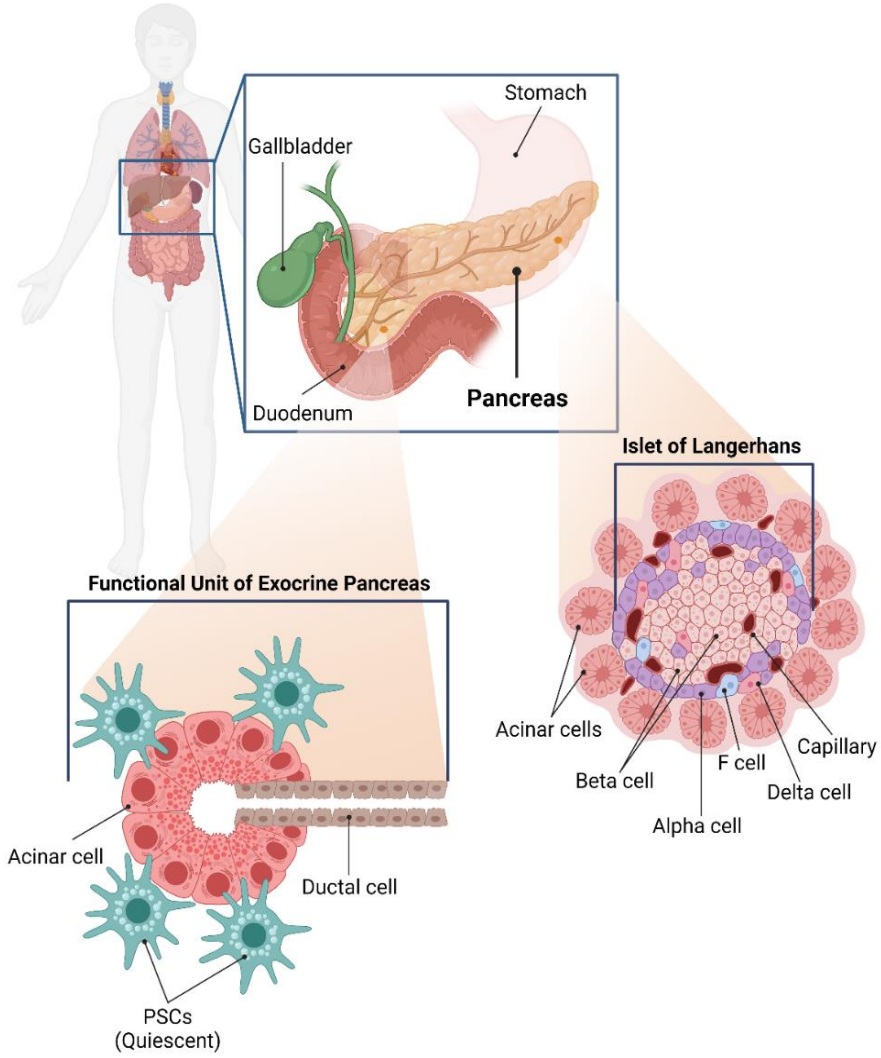

Fig. 1.1 Overview of the pancreatic tissue. Schematic representation of the anatomy of pancreas, constituted by exocrine and endocrine units. (Figure drawn using Biorender.com).

protein, neural cell adhesion molecule and nestin[2]. When activated, these stellate cells express α-smooth muscle actin[11], as described in the following paragraphs.

1.2 Pancreatic cancer

Pancreatic cancer represents one of the leading causes of cancer-related death worldwide, with a five-year survival rate below 9%[12,13]. Among all types of known pancreatic cancer subtypes, pancreatic ductal adenocarcinoma (PDAC) is the most frequent, accounting for 93% of cancers arising from the pancreas[14]. The absence of clear symptoms in the first stages of PDAC evolution reduces the chances to make an early diagnosis, resulting in a poor clinical prognosis. Indeed, only approximately 10% of the patients are eligible for surgical resection in combination with adjuvant and/or pre-operative therapy, since the majority of cases present spread metastases and extended lesions at diagnosis[15,16]. Moreover, the unique bioarchitecture of the pancreatic tumor microenvironment (TME) weakens the

effectiveness of the current treatments that, despite the advances in the discovery of new therapeutic strategies, result insufficient to treat this particularly aggressive pathology[15,17].

1.2.1 Pathogenesis

According to genetic studies, PDAC mainly develops within the acino-ductal unit from pancreatic ductal epithelial cells and progresses through distinct stages of precursor lesions, called pancreatic intraepithelial neoplasias (PanINs)[18]. Typically, 60–70% of tumors occur in the head of the pancreas, 5–10% in the body, and 10–15% in the tail[19]. Although the alterations that give rise to PanIN are still to be clarified[20,21], hallmarks associated to pathology onset have been identified[22,23]. Indeed, among the genetic mutations associated with PDAC currently known, the more frequent are represented by the activation of proto-oncogene KRAS and by the inactivation of tumor-suppressor genes CDKN2A, TP53 and SMAD4, related to the progression and the increasing aggressiveness of the disease[24,25]. Other less common alterations involve BRCA2, PALP2, and p16 germline mutations and are correlated with familial pancreatic cancer (Table 1.1). Moreover, important risk factors, like smoking, obesity, type 2 diabetes, chronic pancreatitis, and alcoholism, can contribute to PDAC progression[26].
The development of pancreatic cancer is a complex multi-step process resulting from the sequential accumulation of genetic mutations that lead to the PanIN evolution through different stages classified as PanIN-1 (papillary lesions), PanIN-2 (atypical papillary lesions), PanIN-3 (carcinoma *in situ* lesions)[27] and finally invasive PDAC. Furthermore, based on histopathological studies, pancreatic cancer may also arise from larger precursor lesions such as intraductal papillary mucinous neoplasms (IPMNs) and mucinous cystic neoplasms (MCNs)[28,29]. A common issue observed during PanIN evolution is the accumulation of inflammatory cues causing the recruitment *in situ* of cells from the immune system[30] and the PSCs activation which leads to an intense desmoplastic reaction consisting in an abnormal extracellular matrix (ECM) deposition within the tissue surrounding the cancer site (Fig. 1.2).

Table 1.1 - Principal signaling pathways and processes genetically altered in PDAC.

Signaling pathways and biological processes	Genetically altered genes	Genetic alteration
KRAS signaling	KRAS	Activation
TGF-β signaling	SMAD 4	Inactivation
Cell cycle regulation	CDKN2A, p16	Inactivation
DNA damage control	TP53, BRCA2, PALP2	Inactivation

1.2.2 PDAC-stroma crosstalk

The PDAC microenvironment is composed of approximately 90% desmoplastic stroma which creates a hypoxic environment and plays a key role in disease progression and drug resistance, constituting a barrier which impedes therapeutics (chemotherapy and radiotherapy) access[31,32]. The fibrotic stroma arises from the excessive ECM deposition by pancreatic stellate cells that are indeed responsible for the intense desmoplastic reaction occurring within the tissue surrounding the cancer cells[33,34]. During the pancreatic carcinogenesis, the PSCs, that are in a quiescent state and exhibit a star-shaped morphology, activate in response to inflammatory cues and cancer cells-derived factors, acquiring a myofibroblasts-like phenotype which is characterized by spindle-shaped morphology[35] (Fig. 1.2).

PDAC stroma is highly heterogeneous and consists of key fundamental building blocks and core effectors including: (i) stromal cells (PSCs and cancer-associated fibroblasts), (ii) endothelial cells, (iii) immune system cells, in addition to the basement membrane and extracellular matrix (ECM) components like collagen (with type I and III fibrillar collagens accounting for > 90% of all collagen mass), fibronectin, fibrillar collagen and hyaluronic acid (HA)[36,37].
The stromal components actively interact with pancreatic tumor cells through different ways that significantly affect gene expression patterns, metabolic activities, invasion/metastasis phenomena and resistance mechanisms[38] (Fig. 1.3). Furthermore, pancreatic cancer affects surrounding lymphatic and autonomic nervous system elements, by direct and indirect means of communication through soluble or insoluble biomolecular mediators (*e.g.*, growth factors, cytokines, extracellular vesicles)[39].

1.2.2.1 Interaction between stromal and cancer cells

In healthy tissue, PSCs are characterized by high expression of both ectodermal and mesenchymal markers and significative amount of retinoids such as vitamin A-rich in lipid droplets[40]. As a result of inflammatory cues and cancer cells-derived factors, these cells become active and switch to a myofibroblasts-like phenotype capable of deregulating ECM homeostasis, while actively interfering with immune cells response[41]. Activated PSCs increase the expression of cytoskeletal protein α-SMA, andthey loss cytoplasmic vitamin-A, resulting in a cell morphology changing to a spindle-shaped. Typically, activated PSCs assemble in a core-shell like structure surrounding the cancer cells and start to interact with them by generating a complex autocrine and paracrine signaling interplay[30,42,43] (Fig. 1.3).
The bidirectional paracrine interaction between PSCs and cancer cells has been largely studied under co-cultured conditions. Pancreatic stellate cells in activated form express different proteins that are important drivers of the PDAC-stroma crosstalk. For instance, galectin-1 causes the anti-tumor immunity suppression[44], while Galectin-3, thrombospondin-2, stromal cell-derived factor-1 (SDF-1) and nerve growth factor (NGF) expressed by PSCs are shown to drive the invasion of pancreatic cancer[43]. PDAC cells, on the other hand, stimulate the PSCs activation and transformation to cancer associated fibroblasts (CAFs). Indeed, PSCs can also transform to CAFs through the cancer cells-mediated secretion of transforming growth factor-β1 (TGF-β1), tumor necrosis factor α (TNF-α), platelet-derived growth factor (PDGF), and several interleukins (*e.g.*, IL-1, IL-6)[43].
CAFs exhibit an important role on cancer cells metabolic reprogramming by providing necessary biomolecular cues that support cancer survival under nutrient-deprived conditions[45]. So far, four main subtypes of pancreatic CAFs have been identified and classified according to their bio-markers/phenotypes: (i) inflammatory CAFs (iCAFs), which show low and high expressions of α-SMA and inflammatory mediators (*e.g.*, IL-6, IL-11) respectively and are located in the peripheral regions of the tumor, (ii) juxtatumoral myofibroblasts (myCAFs), that exhibit high levels of α-SMA and low levels of inflammatory mediators, (iii) antigen-presenting CAFs (apCAFs) which express a combination of iCAF and myCAF biomarkers with low levels of α-SMA and IL-6, and (iv) complement-secreting CAFs (csCAFs) characterized by high expression levels of α-SMA and complement associated factors (*e.g.*, C3, C7, CFB, CFD, CFH, CFI).
Interestingly, the direct interplay of csCAFs with pancreatic cancer cells has only been observed in early tumor development[46].
In addition to the paracrine signaling, an autocrine loop maintain the PSCs activated phenotype *via* different cytokines (*i.e.*, IL-6 and IL- 1β) and TGF-β[43].

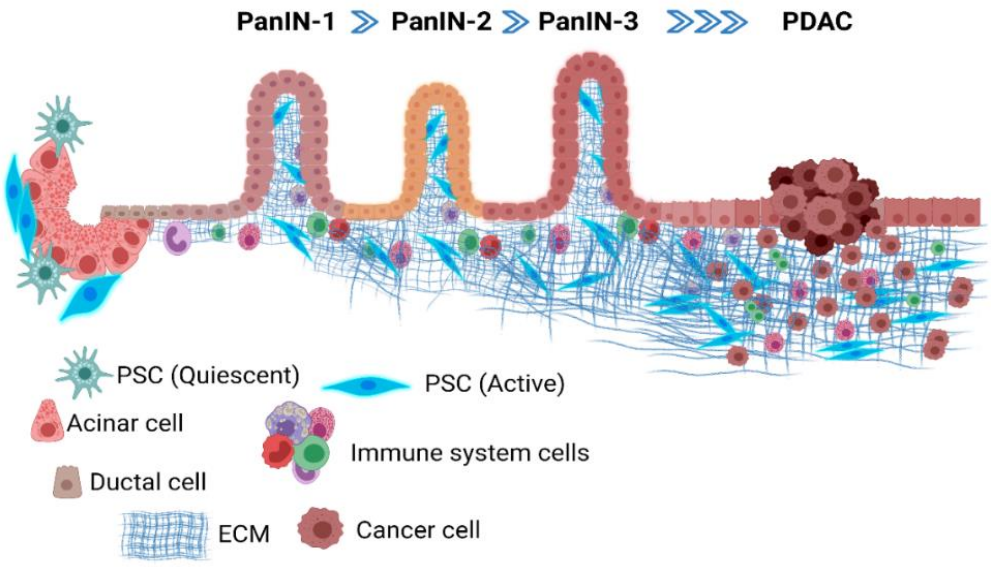

Fig. 1.2 Evolution of pancreatic cancer. The PDAC development is a complex multi-step process that involves the PSCs activation, the recruitment of immune system cells and the gradual deposition of extracellular matrix (ECM) within the tissue surrounded the cancer site. (Figure drawn using Biorender.com).

1.2.2.2 The influence of ECM in cancer progression

During the tumorigenesis, stromal cells are triggered by cancer cell-derived mediators such as IL-6, IL-1, colony-stimulating factor 1 (CSF1), TNF-α, TGF-β1 and platelet-derived growth factor BB (PDGF-BB)[42], leading to a desmoplastic response which consists in increased matrix deposition and remodeling[47] (Fig.1.3). As a consequence, the tissue surrounding the cancer site is subjected to a process called *stiffening* which involves the increment of stroma's mechanical properties (*e.g.*, Young's modulus and stiffness)[48,49]. The modulation of ECM mechanical properties significantly affects the tumor progression.

Indeed, the stroma is stiffened for the crosslinking of collagen fibers induced by extracellular amine oxidases (*i.e.*, lysyl oxidase - LOX)[50] and TGF-β inducible proteins (*i.e.*, tissue transglutaminase 2 - TG2)[51] causing enhanced cancer cell proliferation, migration, epithelial-mesenchymal transition (EMT) and chemoresistance. In particular, the stiffness associated with desmoplasia can favor tumor malignancy across multiple organs, since the rigid stroma causes, as a reaction, a tensional homeostasis with high levels of cell contractility, inducing intracellular signaling and malignant transformation (EMT)[52]. Indeed, PDAC cells downregulate epithelial markers, such as E-cadherin, and overexpress mesenchymal markers as vimentin and fibronectin[44]. EMT is also present in PanINs, suggesting that it could have a role in the early progression of the tumor[47]. Several studies have also demonstrated a link between the epithelial-mesenchymal transition and the origin of cancer stem cells, a population of malignant cells with expression of mesenchymal markers (vimentin)[47]. The link seems to lie in YAP and TAZ, transcription factors known to be associated with EMT, that have emerged recently as key players that control induction of fundamental cell processes in response to ECM stiffness. In particular, as a result of aberrant mechanical cues (stiffening) they cause the formation of cancer stem cells and are associated to malignant properties, including metastatic capacity and chemoresistance[53,54].

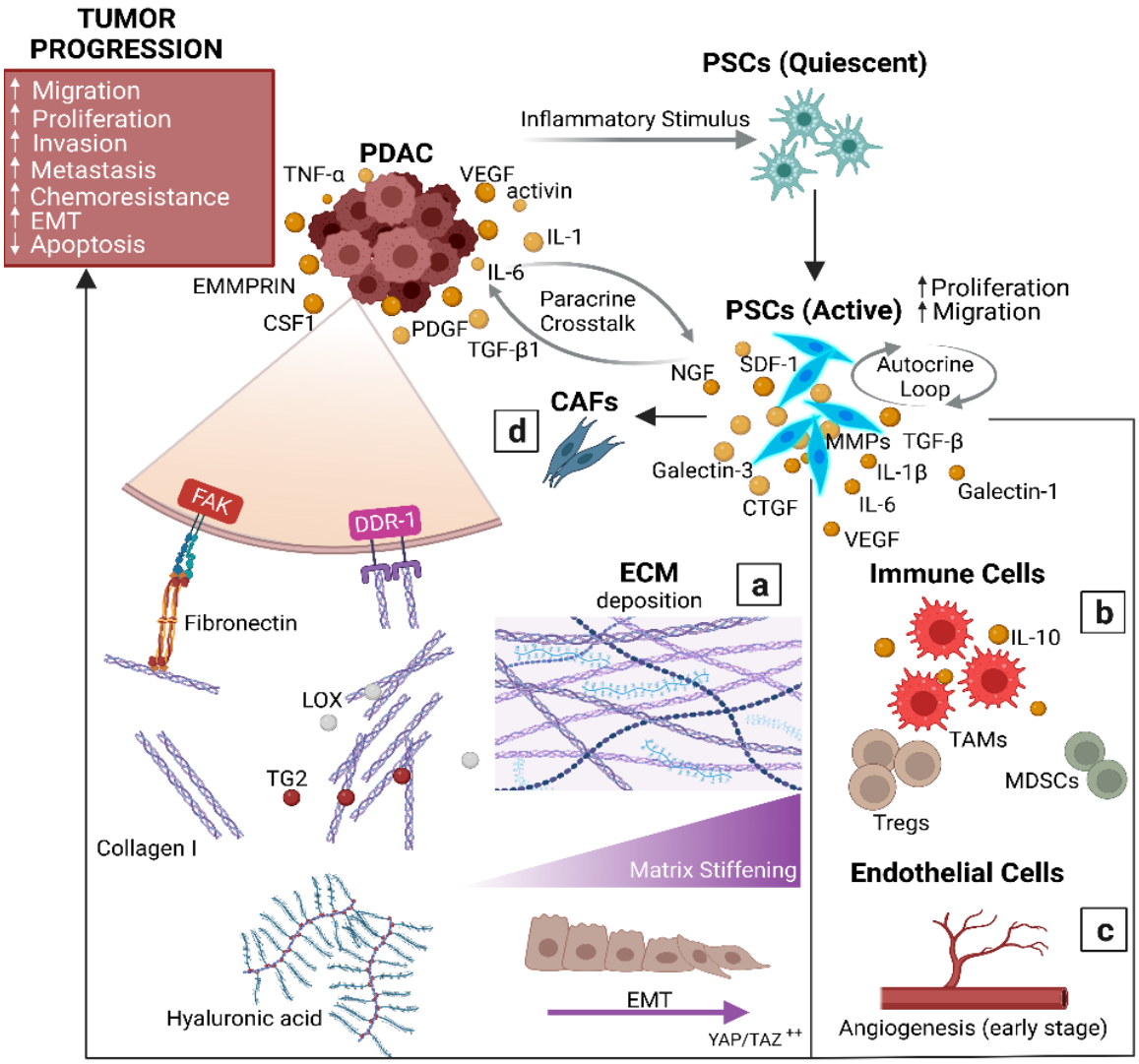

Fig. 1.3 PDAC-stroma crosstalk. The stroma components promote the tumor progression through complex paracrine and autocrine signaling pathways. The quiescent PSCs become active as a result of an inflammatory stimulus and start to express/release different proteins that lead to: (a) an intense desmoplastic response; (b) immunosuppression and (c) angiogenesis during the initial stage of PDAC evolution. (a) The excessive deposition of extracellular matrix (ECM) causes the increment of stroma's mechanical properties (stiffening). In particular, stiffening is a consequence of collagen fibers crosslinking induced by LOX and TG2. The rigid stroma induces, as a reaction, the epithelial-mesenchymal transition (EMT) which is associated to an increment of YAP/TAZ expression. Collagen I and fibronectin interact with integrin receptors on the surface of PDAC cells thus triggering intracellular pathways (*i.e.*, FAK and DDR-1 signaling) which lead to tumor progression. The hyaluronic acid contributes to the high interstitial fluid pressure that reduces tumor's perfusion and hinders the delivery of cytotoxic therapy. (b) The secretion of interleukins (*e.g.*, IL-6) by PSCs, lead to the macrophages polarization towards TAMs, that are supported by MDSCs and Tregs. (d) PSCs can also transform to CAFs through the cancer cells-mediators secretion. (Figure drawn using Biorender.com).

In addition, cancer cells express the extracellular matrix metalloproteinase inducer (EMMPRIN), which stimulates the adjacent PSCs to secrete matrix metalloproteinase 2 (MMP2). MMP2 is a protein of matrix metalloproteinases (MMPs) family and has a central role in the degradation of normal basement membrane and consequently in cancer progression[55]. Thus, the direct cell contact between PSCs and cancer cells facilitates both the tumor growth *in loco* and the formation of distant metastasis[48,56].
Collagen represents the most abundant ECM proteins produced by PSCs and play a fundamental role in the stroma-pancreatic cancer complex relationship. Among the different types of collagens expressed in PDAC, collagen I, located in interstitial space, has the major influence in tumor progression, promoting PDAC cells proliferation and migration through integrin and discoidin receptor 1 (DDR-1) signaling[57]. Specifically, collagen I interact with signaling α2β1 integrins expressed on the surface of PDAC cells (Fig. 1.3).
Moreover, the activation of focal adhesion kinase (FAK) pathway with integrin receptors is mediated by fibronectin and partly regulates the EMT, leading to the loss of E-cadherin and cell-cell adhesion, and to the expression of N-cadherin[48].
One of the main consequences of the large deposition of dense and crosslinked ECM, besides the tissue stiffening, is the high interstitial fluid pressure (IFP) that reduces tumor's perfusion and hinders the delivery of cytotoxic therapy. This effect is determined by the abundance of hyaluronic acid (HA) in PDAC stroma and in PanIN lesions, in accordance with some studies demonstrating that the use of PEGPH20, a hyaluronan-degrading enzyme, reduces IFP and improves drug delivery[58].

1.2.2.3 Role of immune cells in PDAC development

As already mentioned, tumor stroma is populated by different types of immune cells that normally have an anti-tumorigenic effect. However, in pathological conditions, these cells interact with other cellular components of PDAC stroma resulting in the formation of an immunosuppressed microenvironment. Indeed, the presence of tumor-associated macrophages (TAMs), regulatory T cells (Tregs) and myeloid-derived suppressor cells (MDSCs), stimulates tumor progression and immune evasion when bioinstructed by activated PSCs, CAFs and cancer cells[35,59] (Fig.1.3). Specifically, macrophages can be classified into two categories, according to their interaction with tumor cells. The M1 macrophages are antitumor cells and produce pro-inflammatory cytokines, while the M2 macrophages (or TAMs) are pro-tumorigenic and exert an immunosuppressive role by secreting several growth factors, including IL-10, which prevent dendritic cell-mediated anti-tumor immune responses[60]. In PDAC, the synergistic interplay between stromal (PSCs and CAFs) and cancer cells, which is associated with the secretion of interleukins (*e.g.*, IL-6) by PSCs, lead to the macrophages polarization towards a M2 phenotype (*i.e.*, expression of $CD136^+$ and $CD204^+$). Thus, the immunosuppression promoted by TAMs is mediated and supported by MDSCs and Tregs.
This complex immune cell niche in pancreatic tumor microenvironment is also rich in effector T cells and natural killer (NK) cells that counteract TAMs, MDSCs and Tregs.
T cells are a large population of cells including CD8+ T cells and CD4+ T cells. CD8+ T cells, for example, normally have a significant role in preventing tumor growth, eliminating cancer cell through the secretion of interferon-γ (IFN-γ). However, the proliferation and the cytotoxic activity of these cells are limited in PDAC microenvironment, due to the signaling mediated by inhibitors which transform CD8+ T cells in a dysfunctional state[59]. As concern the CD4+ T cells, recent studies have demonstrated that a CAFs subtype present antigens to these immune cells and thus contribute to the modulation of the immune response in pancreatic cancer[61].

Finally, the density of tumor stroma and the lack of an efficient vascularity in the mature PDAC tissue represent a physical barrier for immune cells infiltration and contribute to the modulation of immune response, creating an immunosuppressive microenvironment.

1.2.2.4 Poor vascularity in PDAC microenvironment

PDAC is characterized by a significant hypoxia caused by the low vascularity, especially in tumor stroma, and a consequent poor perfusion. Hypoxic conditions are demonstrated by the overexpression of pro-angiogenic factors, such as vascular endothelial growth factor (VEGF) and other hypoxia-inducible factors in PDAC cells and PSCs[47]. The alteration in vascularity, despite pro-angiogenic stimuli, is mainly generated by the intense deposition of ECM and by the high solid pressure, that lead to the collapse of blood vessels and hinder the delivery of oxygen and nutrients. Studies have demonstrated that the excessive ECM deposition is in turn promoted by the hypoxic conditions that induce the expression of connective tissue growth factor (CTGF) in PSCs[44]. In other words, the desmoplastic response represents both a cause and a consequence of hypoxia. However, due to genetic and metabolic changes, pancreatic cancer cells are able to survive and proliferate under hypoxic conditions, as the majority of cancer tissues. In particular, PDAC cells use micropinocytosis to uptake nutrients and employ collagen as source of energy. Moreover, the poor blood perfusion impedes the delivery of cytotoxic drugs inside the tumor, thus contributing to the inefficiency of chemotherapy treatments. While hypovascularity and the paucity of capillary vessels within the mature tumor are well recognized and documented, the reasons why pancreatic cancer cells can escape the tumor and enter the circulation at the very earliest stages of tumor progression are still unclear. Recently, the *vascular ablation* theory has been proposed to explain this paradox. PDAC cells are able to invade into the vessel lumen, and ablate the endothelial cells, leaving behind tumor-filled luminal structures. Endothelial ablation was observed both *in vitro* and *in vivo* PDAC models and the activin-ALK7 pathway as a mediator of endothelial ablation by PDAC has also been identified[62].

1.3 Tissue models for pancreatic cancer

The understanding of pancreatic cancer raises interests among the scientific community, currently developing efficient exocrine pancreatic models in order to improve the knowledge of the disease with the ultimate goal of performing early diagnoses and design effective therapies, thus enhancing patients' prognosis[62–67]. Specifically, the research is focusing on the fine-tuning of both *in vivo* and *in vitro* strategies to mimic pancreatic cancer and particularly the PDAC-stroma crosstalk, widely recognized to play a crucial role in the progression of the disease as shown above.
The use of *in vivo* and *in vitro* models to study the pancreatic cancer will be discussed in the following paragraphs.

1.3.1 *In vivo* models

In vivo models rely on animals to recapitulate the complexity of living systems that are characterized by biological interactions in a dynamic environment. PDAC *in vivo* models can arise from spontaneous generation of tumors by chemical induction, implantation of tumor cells or tissue as well as the manipulation of animal's genetic material by inducing mutagenesis[68]. For instance, animals can be

genetically modified to generate specific inflammatory pathways typical of PDAC[69,70] or they can be employed to recapitulate the desmoplastic response occurring in pancreatic cancer[71].
In particular, among the existing PDAC *in vivo* models, four main categories can be distinguished: chemically induced models, genetic mouse models, patient-derived xenograft (PDX) models and cell-line derived models. The latter include the syngeneic and the xenogeneic models[28].
An ideal animal model of pancreatic adenocarcinoma should have the tumor development process and malignant phenotype (*e.g*., anti-apoptotic effect, immune escape, invasion and metastasis) similar to those of human pancreatic cancer. Moreover, pancreatic cancer *in vivo* models used in clinical studies must have a high success rate and be suitable for large-scale preparation to ensure that they provide evidence regarding individualized treatment options for patients with a short survival time[72].
However, until now there is no effective and reliable animal models that can completely recapitulate the pathological process and hallmarks of pancreatic cancer. Recent efforts have moved to "humanize" the tumor microenvironment into mice models[73]. Briefly, immune-deficient mice (*i.e*., that lack part of their immune system) were used to introduce human cells minimizing the rejection. Alternatively, mouse embryos can be modified with human DNA using CRISPR technology to obtain human-like cells inside mice. Nonetheless, this recent strategy still fails to fully represent the human PDAC microenvironment, which normally surround cancer cells in patients, as reported in the previous sections. In addition, the existing PDAC *in vivo* models are poorly predictive of the drug response in humans[74]. Besides the scientific difficulties in obtaining PDAC models that can be considered representative of the human physiology, the high-costs, low-throughput and the ethical issues are important limitations associated with *in vivo* studies[75].

1.3.1.1 Three Rs: reduction, refinement and replacement

Alternatives to animal testing were proposed to overcome some of the drawbacks associated with animal experiments and avoid unethical procedures. The idea of replacement of animals was first introduced in 1957 by Charles Hume and William Russell at the Universities Federation for Animal Welfares (UFAW). In the European Union the concept has been translated into legislation through the Directive 2010/63/EU revising Directive 86/609/ECC which aims at regulating the use of animals for scientific purposes. The 3Rs approach motivates the use of minimum number of animals used in an experiment (*i.e*., reduction) and promotes scientific strategies that limit the pain and distress (*i.e*., refinement). In addition, animals should be replaced with alternative methodologies (*i.e*., replacement). The replacement can be defined as 'relative' or 'absolute' if animals are used but not exposed to any distress during experiment or they are not employed at any stage of the experiment[76].

1.3.2 *In vitro* models

In vitro models represent an important alternative for animal experiments and powerful tools for biomedical research, drug discovery, diagnostics, and regenerative medicine. Indeed, they are typically cheaper and faster than studies performed on animal models and they can be used at a preclinical stage to filter out drugs that will not work in mice or humans, considering that only 1 in 10 drugs that were effective in mice are then successful in human clinical trials[77,78]. Pancreatic cancer has been modeled *in vitro* using several systems that can be distinguished as 2D cultures, microfluidic devices and 3D models (Fig.1.4). These categories as well as their advantages and limitations will be illustrated in the following sections.

1.3.2.1 2D models

In a 2D model cells grow in adherent conditions on a substrate, arranging themselves as a monolayer[79]. In general, 2D cultures are widely used to study the biology of PDAC as well as to investigate the efficacy of novel drug candidates *in vitro*, as they are characterized by easy manipulation and low-cost feasibility that make the functional tests extremely accessible[68]. Among the substrates employed to implement 2D culture conditions, transwell inserts are particularly suitable to analyze the mechanisms involved in pancreatic cancer. Indeed, they consist of an apical and a basolateral chambers divided by a microporous polyester membrane (*e.g.*, poly (ethylene terephthalate) - PET) or polycarbonate - PC), thus allowing to culture two different cell types on the same platform and therefore investigate their paracrine crosstalk or evaluate cell migration[68]. For instance, PDAC cell lines can be co-cultured together with stromal cells on transwell inserts to observe the effect of tumor-stroma interplay on cancer cells behavior[80,81].

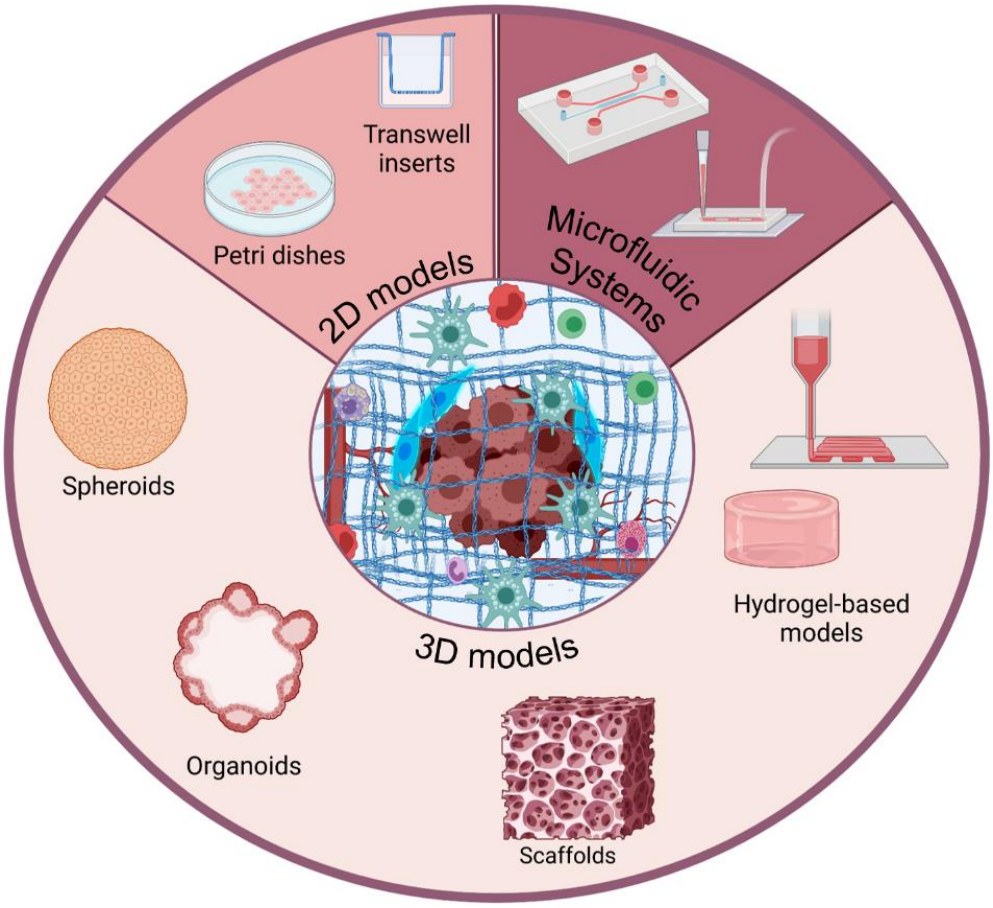

Fig. 1.4 Overview of the available PDAC *in vitro* models. The pancreatic cancer microenvironment has been reproduced by implementing different bioengineering strategies that lead to the development of 2D models, microfluidic systems and 3D models.
(Figure drawn using Biorender.com).

However, as all 2D cultures, they have several limitations that make these models insufficient to reproduce the complex biological features observed *in vivo*.
Despite the high-throughput and cost-efficacy, 2D models do not mimic the three-dimensional natural structure of the tissue, leading to the modification of cell morphology and the loss of specific phenotype and polarity. The lack of cell-matrix interactions, typical of solid tumors, affects cellular functions such as cell differentiation, proliferation, vitality, gene expression and response to stimuli[82]. Furthermore, cells have unlimited access to oxygen, nutrients and other molecules contained in the culture medium, in contrast to cells growing in tumor microenvironment[79]. For these reasons, the research is currently oriented toward the development of other engineered models to replicate the human tissues, especially the pancreatic cancer where the three-dimensional microenvironment plays a key role in the disease progression.

1.3.2.2 Microfluidic systems

Organ-on-chips or microfluidic systems are cutting-edge devices with one or multiple micro-sized hollow channels, preferably fabricated on transparent surfaces such as glass or transparent polymers (*e.g.*, polydimethylsiloxane) and therefore suitable for microscopic imaging[65,83]. These automatized devices allow to mimic the dynamic conditions typical of many anatomical districts found *in vivo*, by processing fluids that simulates the physiological vascular perfusion within the microchannels.
Microfluidic models may also include microsensors to constantly monitor system parameters and, at the same time, they enable real-time imaging as well as *in vitro* analysis of cellular activity in response to dynamic culture conditions[80].
Moreover, these platforms obtained at a miniaturized length scale by microfabrication techniques as the common soft litography[84], permit to achieve similar resolutions to those found in the physiological anatomical structures and therefore study the biological phenomena at a single cell level[85]. Thus, the organ-on-chips serve as very effective systems to study the relationship between pancreatic cancer and its microenvironment in controllable conditions and under real-time monitoring[39,65,86,87]. In addition, the presence of the micrometer-sized channels allow a controlled patterning of stromal and cancer cells, making drug tests and cell analysis accessible and immediate[83].
During the last few years, several studies have showed the potential of microfluidic systems in reproducing some important features of PDAC[36,87–91]. Specifically, many efforts have been spent to include the stromal component on chips to better replicate the TME, by integrating hallmarks of the pancreatic cancer desmoplastic tissue[66,91–95]. For instance, Lee and coworkers co-cultured tumor spheroids† with PSCs in different compartments of a microfluidic platform to analyze the reciprocal influence of stromal and cancer cells. They observed morphological changes in PSCs and increased migration of spheroids in co-culture conditions[96].
Other research groups explored the possibility to increase the models complexity by introducing multiple stroma components in the devices[49,66,95]. Lai *et al*., for example, developed a synergistic platform in which human umbilical vein endothelial cells (HUVEC), human dermal fibroblasts and PDAC organoids† were cultured together. They used a commercial system called Integrated Vasculature for Assessing Dynamic Events (INVADE), based on a 96-well plate with inlet and outlet wells connected to a tissue chamber containing a microfabricated tubular scaffold. Endothelial cells were cultured within the lumen of the scaffold while the parenchymal cells were seeded outside in a Matrigel matrix. The capacity of the model in recapitulating the desmoplastic reaction was confirmed by the

† Spheroids and organoids are described in the following section '*3D models*'

results showing a higher collagen deposition by fibroblasts co-cultured with PDAC organoids in comparison to monocultures controls. In addition, they also tested molecule transfer in monoculture and co-culture and concluded that the transfer from endothelial cell vessels is inhibited under co-culture conditions, which supports the thesis on the role of the tumor stroma as barrier against the chemotherapeutic treatments[49].

The interaction between immune system cells and PDAC, on the other hand, was evaluated by Mollica and co-authors who implemented a microfluidic-based PDAC-TME model to assess the infiltration of T cells across the vasculature. In particular, they monitored T cell migration toward PDAC cells embedded into a collagen type I matrix, providing a quantitative assessment of T cell efficiency in transmigrating into the TME in relation to the presence of PDAC cells, PSCs and endothelial cells linings.

Thus, organ-on-a-chip platforms are improving the knowledge of the pathology upon enabling pancreatic cancer studies in a high-throughput setting. However, the complete understanding of the disease and of the mechanisms involved in the PDAC-stroma relationship remains a challenge. Further improvements are therefore needed to overcome the limitations associated with these models. Indeed, functional microfluidic systems are very complex to implement, they frequently represent only a specific tissue or organ function[97] and the non-physiological geometry can lead to alterations in cellular behavior compared to *in vivo* cell activity. Another limitation is that cultures cannot be maintained for a protracted time period which would be necessary to perform long follow-up in the evaluation of treatments effects.

In addition, although the scalability and automation are fundamental characteristics for effective drug screenings, most organ-on-a-chip platforms are still far to achieve a real high-throughput[36].

1.3.2.3 3D models

So far, animal models and 2D cell cultures represent the most popular systems at the preclinical stage, due to the possibility of testing drugs in a complete living system (*i.e.*, animal models) and the reproducibility/low-costs (*i.e.*, 2D models)[98]. However, as already mentioned, these approaches fail to truly recapitulate the biological and biophysical complexity of human tumor microenvironment[79]. Indeed, several evidences demonstrate that cells in 3D bioengineered cancer models respond to drugs differently than cells in 2D and show a chemoresistance similar to the natural resistance observed in patient tumors[99,100]. Specifically, 3D cell cultures allow to mimic the heterogeneity and the fibrotic nature of pancreatic stroma, as well as the physiological biochemical gradients (*e.g.*, nutrients, metabolites, gas exchange, pH, etc.), the tumor-stroma cytoarchitecture, the ECM composition, the mechanical properties and the cell-cell, cell-ECM interactions along the three space axis[101,102].

Therefore, 3D cancer models can realistically be considered as a bridge between the animal experimentation and the human trials, leading to a reduction in the use of animals for scientific tests[103]. Researchers are currently involved in improving and standardizing the protocols to develop high-throughput effective 3D models. In particular, 3D cancer models should be suitable for a screening approach and for analyses by mean of the most advanced –omics techniques (genomics, transcriptomics, proteomics). Moreover, the use of patient-derived cells offers a huge potential to these *in vitro* models towards a personalized medicine approach.

Heterotypic 3D spheroids, patient-derived organoids, scaffold-based systems and hydrogel-based models are the currently available bioengineered 3D models mimicking the pancreatic tumor[104] (Fig. 1.4).

Spheroids are three-dimensional cell aggregates obtained from one or multiple cell types under specific culture conditions that allow cells to self-assemble into anchorage-independent spherical constructs[105]. These models exhibit some characteristics found in *in vivo* solid tumors, such as cell morphology and polarity[106], expression of specific genes and chemoresistance[107,108]. Moreover, the 3D conformation of cells in clusters partially reproduces the three-dimensional structure of the tissue, allowing the formation of pH, oxygen and gradients of nutrients. In addition, these random agglomerates favorite the formation of cell-cell interactions, even between different cell types within the same contruct[109]. Typically, spheroids are obtained by hanging drop cell culture technique which consists in suspending cells in a drop of medium deposited on a common coverslips or plastic wells.

Alternatively, non-adhesive plastic plates, stirring bioreactors or magnetic levitation can be used to force cell to aggregate[39,110,111].
In 2020, spheroids resulted the most popular method to model pancreatic cancer *in vitro*, probably due to the relatively simple set-up and the low numbers of other biofabricated 3D platforms for this cancer compared to other tumor types[39]. Among the existing PDAC spheroids models[109,110,112–115], the 3D platforms aiming at reproducing the tumor-stroma interplay can be distinguished. For instance, Lazzari *et al*. developed a multicellular spheroid model by co-culturing pancreatic cancer cells (PANC-1), fibroblasts (MRC-5) and vascular endothelial cells (HUVECs). The authors then characterized the construct and demonstrated that the presence of a complex microenvironment reduces the sensitivity of PDAC cells to chemotherapy and therefore mirrors the chemoresistance observed *in vivo*[109]. Thus, these results further support the importance of mimicking the PDAC-stroma relationship in preclinical bioengineered models. Besides the stromal cells, immune system component of pancreatic TME has been recently introduced in spheroids by Kuen *et al*., who replicated the immunosuppressive environment typical of PDAC. In particular, the differentiation of 3D cultured monocytes in TAMS exhibiting an M2-like phenotype was observed. The possibility to obtain such multi-cellular population dynamics is certainly promising to find new valid immunotherapies.
However, 3D spheroids platforms still have important limitations such as the lack of a pre-existing ECM in early culture time points which leads to unproper ECM-associated biomolecular cues. Unphysiological mechanotransduction pathways consequently generate, causing a modification in cellular phenotypes[116].
This makes spheroids inadequate in accurately modelling the pancreatic cancer microenvironment and all the hallmarks observed *in vivo.*

Organoids are self-organizing organotypic structures originated from adult stem cells, developed in three-dimensional culture conditions[117]. They are characterized by self-renewal and self-organization capacities and by the ability to recapitulate the structural and functional features of the native tissue[86].
Organoid models are generated from the enzymatic and/or mechanical dissociation and digestion of normal or cancer tissue into small fragments, that are then embedded in specific matrix, typically Matrigel (a solubilized basement membrane preparation extracted from mouse sarcoma, rich of ECM proteins as laminin and collagen IV) to produce an organ-like structure[118].

Comparing to cellular spheroids, organoids are easier to maintain in long term culture preserving the genetic stability of cells, as they receive more physiological stimuli from the surrounding environment. The unique ability of these organ-like structures in reflecting the key cellular features of the native tissue allow to use them as 3D tumor models and make them valuable preclinical screening platforms. Indeed, organoids resemble the tumor-specific cellular heterogeneity, gene and protein expression patterns, morphological features and highly reflect the *in vivo* response to treatments[117,119]. In particular, the patient-derived organoids (PDOs) represent powerful tools for drug screening in a personalized medicine approach, as they arise from biopsied human specimens and thus mimic the patient-specific pathophysiological hallmarks[112,120]. Moreover, their application in xenograft models, in which they generate precursor lesions and progress to invasive cancer and metastasis, can contribute to better understand the tumor evolution[121,122]. This is why organoids are considered promising 3D *in vitro* models for pancreatic cancer[64,123–127]. Another important advantage in the use of organoids is the possibility to combine them with microfluidic systems, to develop high-throughput analysis systems like the platform by Lai *et al.* already cited[94] and the device recently developed by Geyer and colleagues[125].

However, PDAC organoid models are not able to "naturally" reproduce the microanatomical compartmentalization of pancreatic TME and consequently mimic the tumor-stoma crosstalk[128]. To overcome this limitation, the research is focusing on the introduction, within the organoid cultures, of stromal components that make these model more complex and consequently more biomimetic[129]. Tsai *et al.*, for instance, co-cultured PDAC organoids with stromal (CAFs) and immune ($CD3^+$ T-lymphocytes) cells to evaluate the T-cells migration toward the juxta-tumoral stroma constituting a barrier which protects the cancer cells[130]. In another study, PDAC organoids were cultured with CAFs isolated from different TME regions to analyze the influence of stroma spatial organization on tumor progression and sensitivity to chemotherapy. Interestingly, different stroma states (reactive or deserted) lead to distinct tumor behaviors, causing increased PDAC organoids proliferation and response to therapeutics (*i.e.*, reactive stroma) or higher differentiation and resistance to chemotherapy (*i.e.*, deserted) stroma[131].

Although the tumor-stroma relationship appears to be now replicable in 3D organoids, several technical difficulties undermine the establishment of robust protocols for their standardization. Indeed, a fully differentiation into pancreatic ductal and acinar organoids that recapitulate properties of the neonatal exocrine pancreas remains still challenging to achieve[132]. Moreover, controlled conditions and well-defined culture media containing growth factors (*e.g.*, EGF, FGF), morphogens (*e.g.*, WNT modulators, Noggin), inhibitors (*e.g.*, the TGF-β inhibitor A8301), and supplements (*e.g.*, B27, Nicotinamide, N-Acetyl Cysteine) are required to obtain functional organoids. These culture components may have significant effects on the gene expression and signaling pathways in pancreatic organoids and they can affect the drugs sensitivity[133].

Finally, these models are not able to reproduce the acino-ductal geometry typical of the physiological exocrine pancreas unit, thus lacking in recapitulating the morphological cues.

This specific issue can be addressed using scaffolds as 3D *in vitro* models.

Scaffolds are three-dimensional engineered constructs made up of biocompatible materials that aim at reproducing the architecture and the properties of the native ECM to support cell attachment, migration and growth. Several fabrication techniques (*e.g.*, additive manufacturing) allow to process biomaterials and obtain constructs with defined mechanical and biochemical properties as well as geometrical features[86,134]. Thus, scaffolds represent tools to directly modulate cell functionality through their composition, morphology and surface topography, by providing the right cues to guide cells in the

generation of the newly developed tissue. Specifically, pore size plays a fundamental role in defining topological features which contribute to obtain a functional interface between cells and material[135,136]. Indeed, cellular response can be mediated by tuning scaffold pore size thus consequently tailoring the cell cytoskeleton arrangement. Indeed, cell membrane receptors interact with the multiscale topographical features of the scaffold inducing cytoskeleton deformation and assembly with a direct effect on cell functionalities (adhesion, proliferation, gene expression) and morphologies[137]. Several techniques have been adopted to optimize the manufacturing of scaffolds with controlled, engineered pore size across a variety of length scales. They include conventional fabrication techniques such as salt leaching, gas foaming, phase separation, freeze-drying, freeze-casting, solid-state porogen thermal decomposition, cell encapsulation, electrospinning[138,139]. Nonetheless, these traditional methods do not allow to obtain a precise control of scaffold architecture and to achieve reproducible size and shape of pores[140,141]. On the contrary, additive manufacturing layer-by-layer techniques (*e.g.*, fused deposition modeling[142]; melt electrowriting[143]) using computer-aided design (CAD) modeling introduced remarkable improvements in terms of repeatability and accuracy on scaffold micro- and macrotopography. Although different materials can be used to obtain effective 3D scaffolds for pancreatic tissue, biodegradable polymers, both natural and synthetic, are the most popular since they exhibit several benefits such as low toxicity, biocompatibility, tunable physico-chemical properties and processability[134,144–147].

Among the polymeric-based scaffolds used as 3D *in vitro* models to recapitulate the pancreatic cancer[148–151], the one developed by Gupta and colleagues represent the first highly porous polyurethane 3D scaffold used as a model of PDAC. Specifically, scaffolds were fabricated through thermally induced phase separation[152], obtaining 100–150 μm pore size and 85–90 % porosity. The tumor-stroma compartmentalization was reproduced in this model by cutting the scaffold into two parts that were distinctly functionalized with collagen to promote the growth of stromal and endothelial cells seeded in the outer compartment, and fibronectin to favor the growth of PDAC cells in the inner section.

The co-cultured constructs were characterized, after 4 weeks from seeding, in terms of cell proliferation, collagen production and expression of phenotype markers. Results showed the homogeneous merging of the two compartments, significant ECM deposition by pancreatic stellate cells and a good distribution of cells within the porous scaffold[151]. The model was successively used to perform treatment screening by administering chemotherapy, radiotherapy and a combination of the two[152].

Despite polymeric scaffolds allow long-term cultures, tunable cellular assembly, controlled biophysical cues and geometries, several challenges obstruct the applicability of such models at the preclinical stage. Indeed, the development of complex and biomimetic scaffold-based models is often a low-throughput process, thus making the manufacturing scalability and reproducibility difficult to achieve[75].

In addition to the polymeric constructs obtained by conventional or rapid prototyping techniques, scaffolds can be generated by tissue decellularization[153].

Specifically, cells and genetic component are removed from the tissue to originate a scaffold constituted by native ECM which ideally preserves its biochemical and biomechanical properties[154]. Decellularized human tissues as scaffolds for pancreatic cancer cells were used, for instance, by Al-Akkad *et al.* who cultured both primary and metastatic PDAC cells and evaluated the chemoresistance *in vitro*[155]. However, as previously discussed, the physiological PDAC ECM is characterized by, for example, increased collagen deposition and stiffness, resulting in a structurally and chemically different ECM to that of healthy tissues. For these reasons, scientists have recently started to decellularize patient-derived tumor tissues, giving rise to matrices that resemble the pathological characteristics. As concerns pancreatic cancer, an innovative tissue engineering approach has been proposed by Sensi and co-authors in their work, where human biopsies were decellularized to generate an organotypic 3D *in vitro* model.

The study provided important insights by identifying a total of 110 non-redundant differently expressed proteins between decellularized healthy pancreas and PDAC[156]. However, the disadvantages of using patient-specific decellularized matrices are, for instance, the difficulty in obtaining the ethical approval and patient consent, the tissue availability and patient variability, which leads to a low reproducibility[157,158].

Hydrogel-based models comprise gelatinous 3D constructs that can be produced by conventional processes such as simple casting[159] or by using other advanced techniques like 3D bioprinting[160,161]. Cells are directly loaded in the initial solution or seeded on the top of gel surfaces in a second step of biofabrication, once the crosslinking has been achieved[162–164]. Hydrogels can be crosslinked *via* physical (*e.g.*, crystallite formation, ionic interaction, and hydrogen bonding) or chemical (*e.g.*, chemical grafting) processes depending on the polymers used[165]. Typically, synthetic or naturally derived materials can be employed to develop 3D engineered hydrogel-based models. Among the synthetic polymers, polycaprolactone (PCL), poly (ethylene glycol) (PEG), poly(lactic-co-glycolide) (PLGA) and polyvinyl alcohol (PVA) are widely used for biomedical applications. Natural polymers include, for example, collagen, hyaluronic acid, gelatin, fibronectin, alginate, chitosan, agarose, cellulose and decellularized extracellular matrix (dECM)[160]. Hybrid hydrogels represent a further category comprising the constructs developed by blending between natural and synthetic materials[164]. Thus, the advantages of both natural polymers (*i.e.*, cell-adhesion ligands, hydrophilicity) and synthetic polymers (*i.e.*, tunable mechanical properties and controlled biodegradation) are combined in a unique material[166]. Hydrogels are considered excellent platforms to model the pancreatic cancer microenvironment, mainly due to their ECM-like features as viscoelasticity, high water content, tunable mechanical properties and cell adhesive motifs[167]. Although synthetic hydrogels have been explored as PDAC *in vitro* models[168], they fail to fully recapitulate the physiologic pancreatic TME and were thus overcome by more biomimetic system based on natural or hybrid hydrogels[162,169–173]. In particular, these constructs have been recently used in combination with spheroids to better recapitulate the dynamics involved in tumor-stroma crosstalk[159,163,174,175]. For instance, Pednekar *et al*., developed PDAC microtissue models to mimic the pancreatic cancer compartmentalization found *in vivo*, which consists in a tumor site surrounded by a dense fibrotic stroma as already shown. Specifically, spheroids constituted by PDAC cells (PANC-1) were assembled in a collagen-based hydrogel loaded with human PSCs representing the stromal component. The tests (immunostaining analyses) confirmed the successfully embedding of PDAC spheroids within the PSCs-laden collagen hydrogels. In addition, the tumor-stroma crosstalk has been evaluated by quantifying specific tumor markers including POSTN, FN1, COL1, IL-6 and VIM that resulted highly expressed by these microtissue models[175].

Another example of hydrogel incorporating spheroids is provided by Hakobian and coworkers, who used the 3D laser-assisted bioprinted process to fabricate high-throughput spheroid arrays[176]. In particular, authors developed an early-stage PDAC *in vitro* model by depositing 3D microdoplets containing acinar and ductal cells on a methacrylated gelatin (GelMA) biopaper (*i.e,.* an external biomaterial used as a support for the printed cells). GelMA-based hydrogels are widely used in tissue engineering due to the inherent biological properties and the capacity to mimic the extracellular matrix. Indeed, GelMA is a hybrid polymer containing specific integrin motifs and metalloproteinase degradable sequences, which favor cell attachment, proliferation, and migration[177]. Moreover, GelMA can be crosslinked by ultraviolet or visible light in presence of a photoinitiator (*i.e.*, lithium phenyl-2,4,6 trimethylbenzoylphosphinate, LAP). Thus, the mechanical properties of GelMA hydrogels are tunable in relation with the crosslinking procedure[178]. All these features make this material really suitable for biofabrication procedures like 3D bioprinting, which is becoming an emerging technique

for the *in vitro* modelling of exocrine pancreas tissue[179,180]. Indeed, it allows to fabricate cellularized constructs with controlled spatial cellular distribution, accurate complex geometries and well-defined mechanical/biochemical properties[181,182].
However, research is still far from recapitulating all the pancreatic cancer hallmarks in 3D bioprinted systems and requires efforts in reproducing the gland morphology of the functional unit as well as in developing bioinks that better resemble the composition of PDAC microenvironment.

1.4 Thesis Goal

As widely discussed, the understanding of the complex and dynamic phenomena involved in PDAC-stroma crosstalk might truly expands the knowledge of the pathology and consequently facilitates the discovery of innovative biological targets, that could improve diagnosis and treatments of pancreatic cancer. Although recent studies showed the possibility of modeling the pancreatic cancer microenvironment *in vitro*[49,63,64,109,112,183,184], the tumor-stroma interplay remains arduous to replicate and monitor in functionally effective models[77,185–187].
The main purpose of this doctoral thesis is to reproduce the functional unit of the exocrine pancreas, constituted by epithelial and stromal cells. Specifically, this work aims at developing human *in vitro* models that allow to analyze the PDAC-stroma relationship and the mechanisms implicated during the initial stage of tumor progression.
In detail, different approaches are explored to fabricate devices that can be classified as two-dimensional (2D), two-and-a-half-dimensional (2.5D) and three-dimensional (3D) models (Fig.1.5). All the proposed approaches are simplified models of the *in vivo* conditions, however each model is able to mimic several key biological features providing a step forward to unravel the mechanism of pancreatic cancer development and consequently to design more efficient therapies.
The PDAC-stroma relationship is firstly evaluated under co-culture conditions in a 2D model, constituted by transwell inserts including a polycaprolactone/gelatin (PCL/Gel) electrospun membrane. The information acquired using this simplified model are then transferred to develop a more biomimetic 2.5D model, represented by a multilayer PDAC-on-chip system. This microfluidic device is designed to incorporate PDAC cells and PSCs-laden type I collagen hydrogel in the top and bottom layers, respectively. The use of a nanofibrous and biomimetic membrane to compartmentalize the microfluidic device and thus separate the cancer component from the stromal tissue allows to study the effect of the inflammation stimuli on stromal cells in a controlled and specific way. Moreover, this 2.5D approach consisting in encapsulating human fibroblasts in a collagen matrix within the microfluidic chip provides biomimetic cues that are fundamental to replicate the initial steps of PDAC evolution.
However, PDAC-on-chip lacks to mimic the 3D complex gland morphology of the functional unit of exocrine pancreas.
The 3D models are obtained at different length scales by using distinct additive manufacturing approaches: fused deposition modeling (FDM), melt electrowriting (MEW) and volumetric bioprinting (VBP). These techniques allow to design and develop innovative biomimetic 3D constructs that fully replicates the complex microanatomy of the human pancreatic gland, which has not yet been accurately reproduced in the currently available *in vitro* models[104]. Specifically, these engineered platforms intrinsically provide the morphological cues that cells experience *in vivo* and can reproduce the inflammatory cascade typical of pancreatic cancer from the very early stages.

- The layer-by-layer approaches (*i.e.*, FDM and MEW) are employed to obtain the half structure of the pancreatic adenomere at the macro- and microscale. In particular, the FDM model is used to preliminary assess the feasibility of reproducing the glandular structure by using a layer-by-layer approach and to monitor the fibroblasts viability on PCL printed structures over several weeks. Melt electrowriting is employed to enhance the model resolution as an electric potential difference between needle and collector reduces the filament size of the extruded polymer[188]. Moreover, the layer-by-layer techniques allow to produce PCL scaffolds with controlled pore-size and high-defined geometry; however, the precise spatial distribution of stromal and PDAC cells is difficult to control.

- The cutting-edge technique of volumetric bioprinting is here adopted to develop a 3D *in vitro* model at the microscale resembling the physiological "closed" structure typical of the pancreatic gland. Indeed, VBP represents an emerging light-based technology capable of fast fabricating 3D constructs with high-resolution and complex geometries[189–194]. In particular, a gelatin metacrylate (GelMA) hydrogel is *ad hoc* prepared and loaded with human fibroblasts to mimic the stromal compartment. Healthy or KRAS-mutated human pancreatic ductal epithelial cells are introduced inside the construct's cavity to reproduce the exocrine tissue that evolves to neoplastic lesions during the pancreatic carcinogenesis.
  Finally, the stromal cells activation in response to the inflammatory stimulus given by the cancer cells is analyzed.

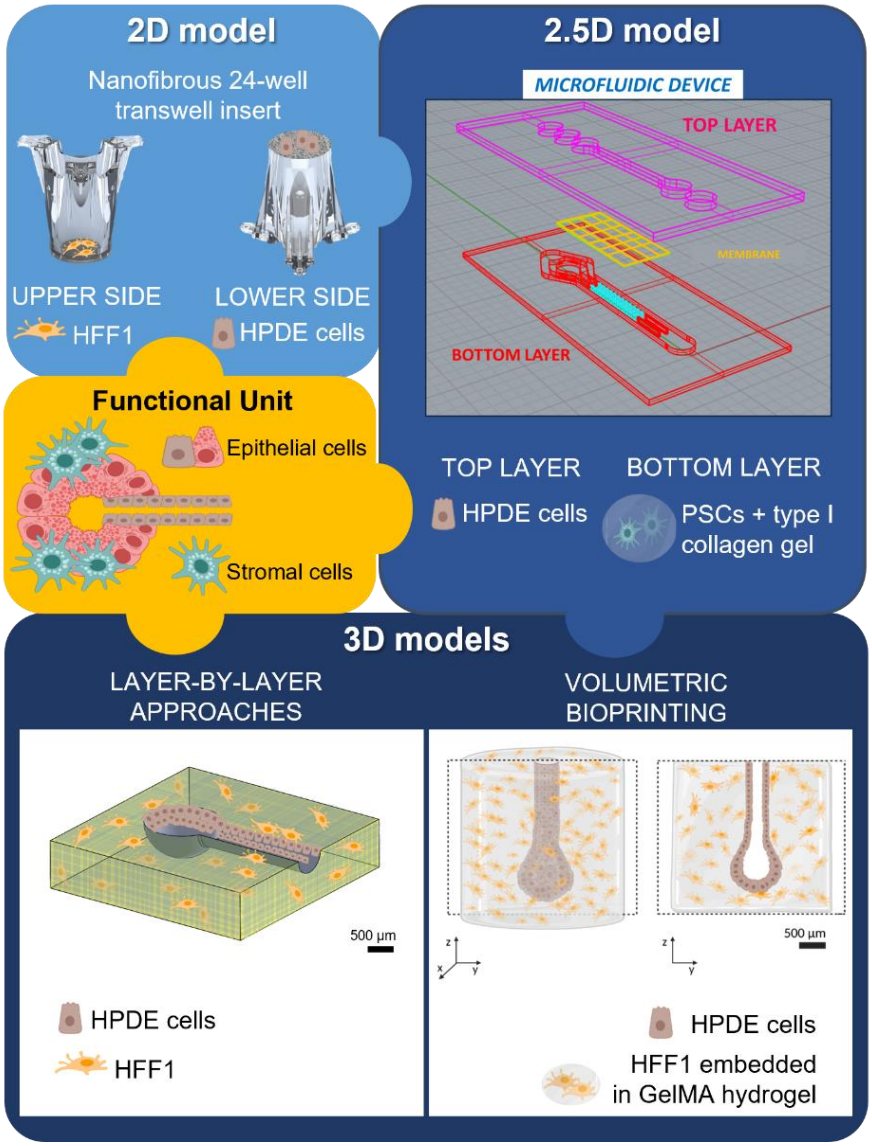

Fig. 1.5 Thesis goal. The purpose of this work is to reproduce the functional unit of the exocrine pancreas by using different approaches. 2D and 2.5D models, consisting of *ad hoc* prepared transwell inserts and a microfluidic device respectively, are here developed to analyze the interactions between stromal and pancreatic ductal cells (healthy or cancerous). 3D models are also designed and fabricated by additive manufacturing (*i.e.*, FDM, MEW and VBP) to better mimic the gland morphology and therefore provide the morphological stimuli of pancreatic TME at the early stages. HFF1: Human foreskin fibroblasts; HPDE: Human Pancreatic Ductal Epithelial; PSCs: Pancreatic Stellate Cells; GelMA: Gelatin-methacryloyl.

References

1. Karpińska M, Czauderna M. Pancreas—Its Functions, Disorders, and Physiological Impact on the Mammals' Organism. *Front Physiol* 2022; 13: 317.
2. Pandiri AR. Overview of exocrine pancreatic pathobiology. *Toxicol Pathol* 2014; 42: 207–216.
3. Longnecker DS. Anatomy and Histology of the Pancreas. *Pancreapedia* 2021; 1: 1–24.
4. Shih HP, Wang A, Sander M. Pancreas organogenesis: From lineage determination to morphogenesis. *Annual Review of Cell and Developmental Biology* 2013; 29: 81–105.
5. Hu JX, Lin YY, Zhao CF, et al. Pancreatic cancer: A review of epidemiology, trend, and risk factors. *World J Gastroenterol* 2021; 27: 4298–4321.
6. Dolenšek J, Rupnik MS, Stožer A. Structural similarities and differences between the human and the mouse pancreas. *Islets* 2015; 7: 2–9.
7. Motta PM, Macchiarelli G, Nottola SA, et al. Histology of the exocrine pancreas. *Microsc Res Tech* 1997; 37: 384–398.
8. Haschek WM, Rousseaux CG, Wallig MA. Pancreas. In: *Fundamentals of Toxicologic Pathology*. Elsevier, 2010, pp. 237–260.
9. Hegyi P, Petersen OH. The Exocrine Pancreas: The Acinar-Ductal Tango in Physiology and Pathophysiology. 2013, pp. 1–30.
10. Shih HP, Wang A, Sander M. Pancreas Organogenesis: From Lineage Determination to Morphogenesis. *Annu Rev Cell Dev Biol* 2013; 29: 81–105.
11. Omary MB, Lugea A, Lowe AW, et al. The pancreatic stellate cell: A star on the rise in pancreatic diseases. *Journal of Clinical Investigation* 2007; 117: 50–59.
12. Khomiak A, Brunner M, Kordes M, et al. Recent Discoveries of Diagnostic, Prognostic and Predictive Biomarkers for Pancreatic Cancer. *Cancers (Basel)* 2020; 12: 3234.
13. Siegel RL, Miller KD, Jemal A. Cancer statistics, 2020. *CA Cancer J Clin* 2020; 70: 7–30.
14. Siegel RL, Miller KD, Fuchs HE, et al. Cancer statistics, 2022. *CA Cancer J Clin* 2022; 72: 7–33.
15. Orth M, Metzger P, Gerum S, et al. Pancreatic ductal adenocarcinoma: Biological hallmarks, current status, and future perspectives of combined modality treatment approaches. *Radiation Oncology* 2019; 14: 1–20.
16. Porciuncula A, Hajdu C, David G. The Dual Role of Senescence in Pancreatic Ductal Adenocarcinoma. *Adv Cancer Res* 2016; 131: 1–20.
17. Brunet LR, Hagemann T, Andrew G, et al. Have lessons from past failures brought us closer to the success of immunotherapy in metastatic pancreatic cancer? *Oncoimmunology*; 5. Epub ahead of print 2 April 2016. DOI: 10.1080/2162402X.2015.1112942.
18. Hidalgo M, Cascinu S, Kleeff J, et al. Addressing the challenges of pancreatic cancer: Future directions for improving outcomes. *Pancreatology* 2015; 15: 8–18.
19. Scialpi M, Reginelli A, D'Andrea A, et al. Pancreatic tumors imaging: An update. *Int J Surg* 2016; 28: S142–S155.
20. Cui SJ, Tang TY, Zou XW, et al. Role of imaging biomarkers for prognostic prediction in patients with pancreatic ductal adenocarcinoma. *Clin Radiol*. Epub ahead of print 2020. DOI: 10.1016/j.crad.2019.12.023.
21. Backx E, Coolens K, Van den Bossche J-L, et al. On the Origin of Pancreatic Cancer: Molecular Tumor Subtypes in Perspective of Exocrine Cell Plasticity. *Cell Mol Gastroenterol Hepatol* 2022; 13: 1243–1253.
22. Hruban RH, Adsay NV, Albores-Saavedra J, et al. Pathology of genetically engineered mouse models of pancreatic exocrine cancer: Consensus report and recommendations. *Cancer Res* 2006; 66: 95–106.
23. Chari ST. Detecting Early Pancreatic Cancer: Problems and Prospects. *Semin Oncol* 2007; 34: 284–294.
24. Liot S, Balas J, Aubert A, et al. Stroma Involvement in Pancreatic Ductal Adenocarcinoma: An Overview Focusing on Extracellular Matrix Proteins. *Frontiers in Immunology* 2021; 12: 709.
25. Ji Z, Mei FC, Xie J, et al. Oncogenic KRAS activates hedgehog signaling pathway in pancreatic cancer cells. *J Biol Chem* 2007; 282: 14048–14055.

26. Nielsen MFB, Mortensen MB, Detlefsen S. Key players in pancreatic cancer-stroma interaction: Cancer-associated fibroblasts, endothelial and inflammatory cells. *World Journal of Gastroenterology* 2016; 22: 2678–2700.
27. Sikdar N, Saha G, Dutta A, et al. Genetic Alterations of Periampullary and Pancreatic Ductal Adenocarcinoma: An Overview. *Curr Genomics* 2018; 19: 444–463.
28. Heinrich MA, Mostafa AMRH, Morton JP, et al. Translating complexity and heterogeneity of pancreatic tumor: 3D in vitro to in vivo models. *Adv Drug Deliv Rev* 2021; 174: 265–293.
29. Rhim AD, Stanger BZ. Molecular biology of pancreatic ductal adenocarcinoma progression: Aberrant activation of developmental pathways. In: *Progress in Molecular Biology and Translational Science*. Elsevier B.V., 2010, pp. 41–78.
30. Apte M V., Wilson JS, Lugea A, et al. A starring role for stellate cells in the pancreatic cancer microenvironment. *Gastroenterology* 2013; 144: 1210–1219.
31. Pandol S, Edderkaoui M, Gukovsky I, et al. Desmoplasia of Pancreatic Ductal Adenocarcinoma. *Clin Gastroenterol Hepatol* 2009; 7: S44–S47.
32. Gaviraghi M, Tunici P, Valensin S, et al. Pancreatic cancer spheres are more than just aggregates of stem marker-positive cells. *Biosci Rep* 2011; 31: 45–55.
33. Weniger M, Honselmann KC, Liss AS. The extracellular matrix and pancreatic cancer: A complex relationship. *Cancers*; 10. Epub ahead of print 6 September 2018. DOI: 10.3390/cancers10090316.
34. Fu Y, Liu S, Zeng S, et al. The critical roles of activated stellate cells-mediated paracrine signaling, metabolism and onco-immunology in pancreatic ductal adenocarcinoma. *Molecular Cancer*; 17. Epub ahead of print 19 February 2018. DOI: 10.1186/s12943-018-0815-z.
35. Wang S, Li Y, Xing C, et al. Tumor microenvironment in chemoresistance, metastasis and immunotherapy of pancreatic cancer. *Am J Cancer Res* 2020; 10: 1937.
36. Geyer M, Queiroz K. Microfluidic Platforms for High-Throughput Pancreatic Ductal Adenocarcinoma Organoid Culture and Drug Screening. *Front Cell Dev Biol* 2021; 9: 1–9.
37. Stopa KB, Kusiak AA, Szopa MD, et al. Pancreatic Cancer and Its Microenvironment—Recent Advances and Current Controversies. *Int J Mol Sci* 2020; 21: 3218.
38. Zhan H-X, Zhou B, Cheng Y-G, et al. Crosstalk between stromal cells and cancer cells in pancreatic cancer: New insights into stromal biology. *Cancer Lett* 2017; 392: 83–93.
39. Tomás-Bort E, Kieler M, Sharma S, et al. 3D approaches to model the tumor microenvironment of pancreatic cancer. *Theranostics* 2020; 10: 5074–5089.
40. Pothula SP, Pirola RC, Wilson JS, et al. Pancreatic stellate cells: Aiding and abetting pancreatic cancer progression. *Pancreatology* 2020; 20: 409–418.
41. Wang S, Li Y, Xing C, et al. Tumor microenvironment in chemoresistance, metastasis and immunotherapy of pancreatic cancer. *Am J Cancer Res* 2020; 10: 1937–1953.
42. Wu Y, Zhang C, Jiang K, et al. The Role of Stellate Cells in Pancreatic Ductal Adenocarcinoma: Targeting Perspectives. DOI: 10.3389/fonc.2020.621937.
43. Bynigeri RR, Jakkampudi A, Jangala R, et al. Pancreatic stellate cell: Pandora's box for pancreatic disease biology. *World J Gastroenterol* 2017; 23: 382.
44. Manuscript A. A Starring Role for Stellate Cells in the Pancreatic Cancer. 2014; 144: 1210–1219.
45. Schnittert J, Bansal R, Prakash J. Targeting Pancreatic Stellate Cells in Cancer. *Trends in Cancer* 2019; 5: 128–142.
46. Chen K, Wang Q, Li M, et al. Single-cell RNA-seq reveals dynamic change in tumor microenvironment during pancreatic ductal adenocarcinoma malignant progression. *EBioMedicine* 2021; 66: 103315.
47. Nielsen MFB, Mortensen MB, Detlefsen S. Key players in pancreatic cancer-stroma interaction: Cancer-associated fibroblasts, endothelial and inflammatory cells. *World Journal of Gastroenterology* 2016; 22: 2678–2700.
48. Weniger M, Honselmann KC, Liss AS. The Extracellular Matrix and Pancreatic Cancer: A Complex Relationship. *Cancers (Basel)*; 10. Epub ahead of print 6 September 2018. DOI: 10.3390/CANCERS10090316.
49. Lai BFL, Lu RXZ, Hu Y, et al. Recapitulating Pancreatic Tumor Microenvironment through Synergistic Use of Patient Organoids and Organ-on-a-Chip Vasculature. *Adv Funct Mater* 2020; 2000545: 1–16.

50. Cox TR, Bird D, Baker AM, et al. LOX-mediated collagen crosslinking is responsible for fibrosis-enhanced metastasis. *Cancer Res* 2013; 73: 1721.
51. Lee J, Condello S, Yakubov B, et al. Tissue Transglutaminase Mediated Tumor–Stroma Interaction Promotes Pancreatic Cancer Progression. *Clin Cancer Res* 2015; 21: 4482–4493.
52. Rice AJ, Cortes E, Lachowski D, et al. Matrix stiffness induces epithelial-mesenchymal transition and promotes chemoresistance in pancreatic cancer cells. *Oncogenesis* 2017; 6: e352.
53. Brusatin G, Panciera T, Gandin A, et al. Biomaterials and engineered microenvironments to control YAP/TAZ-dependent cell behaviour. *Nat Mater* 2018; 17: 1063–1075.
54. Dupont S, Morsut L, Aragona M, et al. Role of YAP/TAZ in mechanotransduction. *Nature* 2011; 474: 179–183.
55. Li Y, Song T, Chen Z, et al. Pancreatic Stellate Cells Activation and Matrix Metallopeptidase 2 Expression Correlate With Lymph Node Metastasis in Pancreatic Carcinoma. *Am J Med Sci* 2019; 357: 16–22.
56. Xu Z, Vonlaufen A, Phillips PA, et al. Role of pancreatic stellate cells in pancreatic cancer metastasis. *Am J Pathol* 2010; 177: 2585–2596.
57. Perez VM, Kearney JF, Yeh JJ. The PDAC Extracellular Matrix: A Review of the ECM Protein Composition, Tumor Cell Interaction, and Therapeutic Strategies. *Front Oncol* 2021; 11: 1–10.
58. Provenzano PP, Hingorani SR. Hyaluronan, fluid pressure, and stromal resistance in pancreas cancer. *Br J Cancer* 2013; 108: 1–8.
59. Liu X, Xu J, Zhang B, et al. The reciprocal regulation between host tissue and immune cells in pancreatic ductal adenocarcinoma: new insights and therapeutic implications. *Mol Cancer* 2019; 18: 184.
60. Murakami T, Hiroshima Y, Matsuyama R, et al. Role of the tumor microenvironment in pancreatic cancer. *Ann Gastroenterol Surg* 2019; 3: 130–137.
61. Elyada E, Bolisetty M, Laise P, et al. Cross-Species Single-Cell Analysis of Pancreatic Ductal Adenocarcinoma Reveals Antigen-Presenting Cancer-Associated Fibroblasts. *Cancer Discov* 2019; 9: 1102–1123.
62. Nguyen DHT, Lee E, Alimperti S, et al. A biomimetic pancreatic cancer on-chip reveals endothelial ablation via ALK7 signaling. *Sci Adv* 2019; 5: 1–10.
63. Cave DD, Rizzo R, Sainz B, et al. The revolutionary roads to study cell–cell interactions in 3d in vitro pancreatic cancer models. *Cancers (Basel)* 2021; 13: 1–19.
64. Osuna de la Peña D, Trabulo SMD, Collin E, et al. Bioengineered 3D models of human pancreatic cancer recapitulate in vivo tumour biology. *Nat Commun 2021 121* 2021; 12: 1–15.
65. Haque MR, Rempert TH, Al-Hilal TA, et al. Organ-Chip Models: Opportunities for Precision Medicine in Pancreatic Cancer. *Cancers (Basel)* 2021; 13: 4487.
66. Mollica H, Teo YJ, Tan ASM, et al. A 3D pancreatic tumor model to study T cell infiltration. *Biomater Sci* 2021; 9: 7420–7431.
67. Schuster B, Junkin M, Kashaf SS, et al. Automated microfluidic platform for dynamic and combinatorial drug screening of tumor organoids. *Nat Commun* 2020; 11: 1–12.
68. Heinrich MA, Mostafa AMRH, Morton JP, et al. Translating complexity and heterogeneity of pancreatic tumor: 3D in vitro to in vivo models. *Advanced Drug Delivery Reviews* 2021; 174: 265–293.
69. Hingorani SR, Petricoin EF, Maitra A, et al. Erratum: Preinvasive and invasive ductal pancreatic cancer and its early detection in the mouse (Cancer Cell (4) (437-450)). *Cancer Cell* 2004; 5: 103.
70. Ijichi H, Chytil A, Gorska AE, et al. Aggressive pancreatic ductal adenocarcinoma in mice caused by pancreas-specific blockade of transforming growth factor-β signaling in cooperation with active Kras expression. *Genes Dev* 2006; 20: 3147–3160.
71. Suklabaidya S, Dash P, Das B, et al. Experimental models of pancreatic cancer desmoplasia. *Lab Investig* 2018; 98: 27–40.
72. Kong K, Guo M, Liu Y, et al. Progress in Animal Models of Pancreatic Ductal Adenocarcinoma. *J Cancer* 2020; 11: 1555–1567.
73. De La Rochere P, Guil-Luna S, Decaudin D, et al. Humanized Mice for the Study of Immuno-Oncology. *Trends Immunol* 2018; 39: 748–763.
74. Boussommier-Calleja A. *In vitro models of cancer*. Elsevier Ltd., 2020. Epub ahead of print 2020.

DOI: 10.1016/b978-0-12-813886-1.00013-9.
75. Pieri A De, Korman BD, Jüngel A, et al. Engineering Advanced In Vitro Models of Systemic Sclerosis for Drug Discovery and Development. Epub ahead of print 2021. DOI: 10.1002/adbi.202000168.
76. Doke SK, Dhawale SC. Alternatives to animal testing: A review. *Saudi Pharm J* 2015; 23: 223–229.
77. Yu Y, Yang G, Huang H, et al. Preclinical models of pancreatic ductal adenocarcinoma: challenges and opportunities in the era of precision medicine. *Journal of Experimental and Clinical Cancer Research* 2021; 40: 1–13.
78. Hackam DG, Redelmeier DA. Translation of Research Evidence From Animals to Humans. *JAMA* 2006; 296: 1727.
79. Kapałczyńska M, Kolenda T, Przybyła W, et al. 2D and 3D cell cultures - a comparison of different types of cancer cell cultures. *Arch Med Sci* 2018; 14: 910–919.
80. Chen ST, Kuo TC, Liao YY, et al. Silencing of MUC20 suppresses the malignant character of pancreatic ductal adenocarcinoma cells through inhibition of the HGF/MET pathway. *Oncogene* 2018; 37: 6041–6053.
81. Yan Z, Ohuchida K, Fei S, et al. Inhibition of ERK1 / 2 in cancer-associated pancreatic stellate cells suppresses cancer – stromal interaction and metastasis. 2019; 8: 1–16.
82. Shichi Y, Sasaki N, Michishita M, et al. Enhanced morphological and functional differences of pancreatic cancer with epithelial or mesenchymal characteristics in 3D culture. *Sci Rep* 2019; 9: 10871.
83. Bhatia SN, Ingber DE. Microfluidic organs-on-chips. *Nat Biotechnol 2014 328* 2014; 32: 760–772.
84. Qin D, Xia Y, Whitesides GM. Soft lithography for micro- and nanoscale patterning. *Nat Protoc* 2010; 5: 491–502.
85. Leung CM, de Haan P, Ronaldson-Bouchard K, et al. A guide to the organ-on-a-chip. *Nat Rev Methods Prim*; 2. Epub ahead of print 2022. DOI: 10.1038/s43586-022-00118-6.
86. Swayden M, Soubeyran P, Iovanna J. Upcoming Revolutionary Paths in Preclinical Modeling of Pancreatic Adenocarcinoma. *Front Oncol* 2020; 9: 1443.
87. Low LA, Mummery C, Berridge BR, et al. Organs-on-chips: into the next decade. *Nature Reviews Drug Discovery* 2021; 20: 345–361.
88. Nguyen DHT, Lee E, Alimperti S, et al. A biomimetic pancreatic cancer on-chip reveals endothelial ablation via ALK7 signaling. *Sci Adv* 2019; 5: 1–10.
89. Venis SM, Moon HR, Yang Y, et al. Engineering of a functional pancreatic acinus with reprogrammed cancer cells by induced: PTF1a expression. *Lab Chip* 2021; 21: 3675–3685.
90. Moon HR, Ozcelikkale A, Yang Y, et al. An engineered pancreatic cancer model with intra-tumoral heterogeneity of driver mutations. *Lab Chip* 2020; 20: 3720–3732.
91. Bradney MJ, Venis SM, Yang Y, et al. A Biomimetic Tumor Model of Heterogeneous Invasion in Pancreatic Ductal Adenocarcinoma. *Small* 2020; 1905500: 1–10.
92. Gioeli D, Snow CJ, Simmers MB, et al. Development of a multicellular pancreatic tumor microenvironment system using patient-derived tumor cells. *Lab Chip* 2019; 19: 1193–1204.
93. Lee JH, Kim SK, Khawar IA, et al. Microfluidic co-culture of pancreatic tumor spheroids with stellate cells as a novel 3D model for investigation of stroma-mediated cell motility and drug resistance. *J Exp Clin Cancer Res* 2018; 37: 1–12.
94. Lai BFL, Lu RXZ, Hu Y, et al. Recapitulating Pancreatic Tumor Microenvironment through Synergistic Use of Patient Organoids and Organ-on-a-Chip Vasculature. *Adv Funct Mater* 2020; 2000545.
95. Bi Y, Shirure VS, Liu R, et al. Tumor-on-a-chip platform to interrogate the role of macrophages in tumor progression. *Integr Biol* 2020; 12: 221–232.
96. Lee JH, Kim SK, Khawar IA, et al. Microfluidic co-culture of pancreatic tumor spheroids with stellate cells as a novel 3D model for investigation of stroma-mediated cell motility and drug resistance. *J Exp Clin Cancer Res* 2018; 37: 1–12.
97. Lai BFL, Huyer LD, Lu RXZ, et al. InVADE: Integrated Vasculature for Assessing Dynamic Events. *Adv Funct Mater* 2017; 27: 1703524.
98. Weeber F, Ooft SN, Dijkstra KK, et al. Tumor Organoids as a Pre-clinical Cancer Model for

Drug Discovery. *Cell Chem Biol* 2017; 24: 1092–1100.
99. Desoize B. Multicellular resistance: a paradigm for clinical resistance? *Crit Rev Oncol Hematol* 2000; 36: 193–207.
100. Brancato V, Oliveira JM, Correlo VM, et al. Could 3D models of cancer enhance drug screening? *Biomaterials*; 232. Epub ahead of print 2020. DOI: 10.1016/j.biomaterials.2019.119744.
101. Fang Y, Eglen RM. Three-Dimensional Cell Cultures in Drug Discovery and Development. *SLAS Discov* 2017; 22: 456–472.
102. Laschke MW, Menger MD. Life is 3D: Boosting Spheroid Function for Tissue Engineering. *Trends Biotechnol* 2017; 35: 133–144.
103. Jensen C, Teng Y. Is It Time to Start Transitioning From 2D to 3D Cell Culture? *Front Mol Biosci*; 7. Epub ahead of print 6 March 2020. DOI: 10.3389/fmolb.2020.00033.
104. Monteiro M V, Ferreira LP, Rocha M, et al. Journal Pre-proof Advances in bioengineering pancreatic tumor-stroma physiomimetic Biomodels. *Biomaterials*. Epub ahead of print 2022. DOI: 10.1016/j.biomaterials.2022.121653.
105. Shahin-Shamsabadi A, Selvaganapathy PR. A rapid biofabrication technique for self-assembled collagen-based multicellular and heterogeneous 3D tissue constructs. *Acta Biomater* 2019; 92: 172–183.
106. Matsuda Y, Ishiwata T, Kawamoto Y, et al. Morphological and cytoskeletal changes of pancreatic cancer cells in three-dimensional spheroidal culture. *Med Mol Morphol* 2010; 43: 211–217.
107. Longati P, Jia X, Eimer J, et al. 3D pancreatic carcinoma spheroids induce a matrix-rich, chemoresistant phenotype offering a better model for drug testing. *BMC Cancer* 2013; 13: 95.
108. Barros AS, Costa EC, Nunes AS, et al. Comparative study of the therapeutic effect of Doxorubicin and Resveratrol combination on 2D and 3D (spheroids) cell culture models. *Int J Pharm* 2018; 551: 76–83.
109. Lazzari G, Nicolas V, Matsusaki M, et al. Multicellular spheroid based on a triple co-culture: A novel 3D model to mimic pancreatic tumor complexity. *Acta Biomater* 2018; 78: 296–307.
110. Brancato V, Comunanza V, Imparato G, et al. Bioengineered tumoral microtissues recapitulate desmoplastic reaction of pancreatic cancer. *Acta Biomater* 2017; 49: 152–166.
111. Ferreira LP, Gaspar VM, Mano JF. Design of spherically structured 3D in vitro tumor models - Advances and prospects. *Acta Biomater* 2018; 75: 11–34.
112. Monteiro M V., Ferreira LP, Rocha M, et al. Advances in bioengineering pancreatic tumor-stroma physiomimetic Biomodels. *Biomaterials* 2022; 287: 121653.
113. Ware, Matthew J. Keshishian V, Law JJ, Ho JC, et al. Generation of an in vitro 3D PDAC stroma rich spheroid model. *Biomaterials* 2016; 55: 9557–9561.
114. Kuen J, Darowski D, Kluge T, et al. Pancreatic cancer cell/fibroblast co-culture induces M2 like macrophages that influence therapeutic response in a 3D model. *PLoS One* 2017; 12: e0182039.
115. Norberg KJ, Liu X, Fernández Moro C, et al. A novel pancreatic tumour and stellate cell 3D co-culture spheroid model. *BMC Cancer* 2020; 20: 475.
116. Pradhan S, Clary JM, Seliktar D, et al. A three-dimensional spheroidal cancer model based on PEG-fibrinogen hydrogel microspheres. *Biomaterials* 2017; 115: 141–154.
117. Drost J, Clevers H. Organoids in cancer research. *Nat Rev Cancer*. Epub ahead of print 2018. DOI: 10.1038/s41568-018-0007-6.
118. Xu H, Lyu X, Yi M, et al. Organoid technology and applications in cancer research 11 Medical and Health Sciences 1112 Oncology and Carcinogenesis. *Journal of Hematology and Oncology* 2018; 11: 1–15.
119. Shukla HD, Dukic T, Roy S, et al. Pancreatic cancer derived 3D organoids as a clinical tool to evaluate the treatment response. 2023; 1–12.
120. Nagle PW, Plukker JTM, Muijs CT, et al. Patient-derived tumor organoids for prediction of cancer treatment response. *Semin Cancer Biol* 2018; 53: 258–264.
121. Moreira L, Bakir B, Chatterji P, et al. Pancreas 3D Organoids: Current and Future Aspects as a Research Platform for Personalized Medicine in Pancreatic Cancer. *CMGH* 2018; 5: 289–298.
122. Boj SF, Hwang C Il, Baker LA, et al. Organoid models of human and mouse ductal pancreatic cancer. *Cell* 2015; 160: 324–338.
123. Baker LA, Tiriac H, Clevers H, et al. Modeling Pancreatic Cancer with Organoids. *Trends in*

Cancer 2016; 2: 176–190.
124. Hou S, Tiriac H, Sridharan BP, et al. Advanced Development of Primary Pancreatic Organoid Tumor Models for High-Throughput Phenotypic Drug Screening. *SLAS Discov* 2018; 23: 574–584.
125. Geyer M. A micro fl uidic-based PDAC organoid system reveals the impact of hypoxia in response to treatment. Epub ahead of print 2023. DOI: 10.1038/s41420-023-01334-z.
126. Huang W, Navarro-Serer B, Jeong YJ, et al. Pattern of Invasion in Human Pancreatic Cancer Organoids Is Associated with Loss of SMAD4 and Clinical Outcome. *Cancer Res* 2020; 80: 2804–2817.
127. Below CR, Kelly J, Brown A, et al. A microenvironment-inspired synthetic three-dimensional model for pancreatic ductal adenocarcinoma organoids. *Nat Mater* 2022; 21: 110–119.
128. Xu H, Lyu X, Yi M, et al. Organoid technology and applications in cancer research 11 Medical and Health Sciences 1112 Oncology and Carcinogenesis. *Journal of Hematology and Oncology*; 11. Epub ahead of print 15 September 2018. DOI: 10.1186/s13045-018-0662-9.
129. Fiorini E, Veghini L, Corbo V. Modeling Cell Communication in Cancer With Organoids: Making the Complex Simple. *Front Cell Dev Biol*; 8. Epub ahead of print 18 March 2020. DOI: 10.3389/fcell.2020.00166.
130. Tsai S, McOlash L, Palen K, et al. Development of primary human pancreatic cancer organoids, matched stromal and immune cells and 3D tumor microenvironment models. *BMC Cancer* 2018; 18: 335.
131. Grünwald BT, Devisme A, Andrieux G, et al. Spatially confined sub-tumor microenvironments in pancreatic cancer. *Cell* 2021; 184: 5577-5592.e18.
132. Huang L, Desai R, Conrad DN, et al. Commitment and oncogene-induced plasticity of human stem cell-derived pancreatic acinar and ductal organoids. *Cell Stem Cell* 2021; 28: 1090-1104.e6.
133. Miralles F, Czernichow P, Ozaki K, et al. Signaling through fibroblast growth factor receptor 2b plays a key role in the development of the exocrine pancreas. *Proc Natl Acad Sci U S A* 1999; 96: 6267.
134. Caddeo S, Boffito M, Sartori S. Tissue engineering approaches in the design of healthy and pathological in vitro tissue models. *Frontiers in Bioengineering and Biotechnology* 2017; 5: 40.
135. Loh QL, Choong C. Three-Dimensional Scaffolds for Tissue Engineering Applications: Role of Porosity and Pore Size. *Tissue Eng Part B Rev* 2013; 19: 485–502.
136. Guadarrama Bello D, Fouillen A, Badia A, et al. A nanoporous titanium surface promotes the maturation of focal adhesions and formation of filopodia with distinctive nanoscale protrusions by osteogenic cells. *Acta Biomater* 2017; 60: 339–349.
137. Garoli D, Lovato L, Della Giustina G, et al. Directly nanopatternable nanoporous titania – Application to cell growth engineering. *Microelectron Eng* 2016; 155: 102–106.
138. Kundu B, Rajkhowa R, Kundu SC, et al. Silk fibroin biomaterials for tissue regenerations. *Adv Drug Deliv Rev* 2013; 65: 457–470.
139. Jakus AE, Geisendorfer NR, Lewis PL, et al. 3D-printing porosity: A new approach to creating elevated porosity materials and structures. *Acta Biomater* 2018; 72: 94–109.
140. Salerno A, Di Maio E, Iannace S, et al. Tailoring the pore structure of PCL scaffolds for tissue engineering prepared via gas foaming of multi-phase blends. *J Porous Mater* 2012; 19: 181–188.
141. Danilevicius P, Georgiadi L, Pateman CJ, et al. The effect of porosity on cell ingrowth into accurately defined, laser-made, polylactide-based 3D scaffolds. *Appl Surf Sci* 2015; 336: 2–10.
142. Rajan K, Samykano M, Kadirgama K, et al. Fused deposition modeling: process, materials, parameters, properties, and applications. *Int J Adv Manuf Technol* 2022; 120: 1531–1570.
143. Cao K, Zhang F, Zaeri A, et al. Advances in design and quality of melt electrowritten scaffolds. *Mater Des*; 226. Epub ahead of print 1 February 2023. DOI: 10.1016/J.MATDES.2023.111618.
144. Kumar N, Joisher H, Ganguly A. Polymeric scaffolds for pancreatic tissue engineering: A review. *Review of Diabetic Studies* 2017; 14: 334–353.
145. Licciardello M, Ciardelli G, Tonda-Turo C. Biocompatible Electrospun Polycaprolactone-Polyaniline Scaffold Treated with Atmospheric Plasma to Improve Hydrophilicity. *Bioengineering* 2021; 8: 1–18.
146. Chiono V, Sartori S, Calzone S, et al. Synthetic biodegradable medical polyurethanes. In: *Science and Principles of Biodegradable and Bioresorbable Medical Polymers: Materials and*

Properties. 2017, pp. 189–216.
147. Tonda-Turo C, Boffito M, Cassino C, et al. Biomimetic polyurethane – Based fibrous scaffolds. *Mater Lett* 2016; 167: 9–12.
148. Chiellini F, Puppi D, Piras AM, et al. Modelling of pancreatic ductal adenocarcinoma: In vitro with three-dimensional microstructured hydrogels. *RSC Adv* 2016; 6: 54226–54235.
149. Ricci C, Danti S. 3D Models of Pancreatic Ductal Adenocarcinoma via Tissue Engineering. 2019, pp. 81–95.
150. Totti S, Allenby MC, Dos Santos SB, et al. A 3D bioinspired highly porous polymeric scaffolding system for: In vitro simulation of pancreatic ductal adenocarcinoma. *RSC Adv* 2018; 8: 20928–20940.
151. Gupta P, Pérez-Mancera PA, Kocher H, et al. A Novel Scaffold-Based Hybrid Multicellular Model for Pancreatic Ductal Adenocarcinoma—Toward a Better Mimicry of the in vivo Tumor Microenvironment. *Front Bioeng Biotechnol*; 8. Epub ahead of print 2020. DOI: 10.3389/fbioe.2020.00290.
152. Gupta P, Totti S, Pérez-Mancera PA, et al. Chemoradiotherapy screening in a novel biomimetic polymer based pancreatic cancer model. *RSC Adv* 2019; 9: 41649–41663.
153. García-Gareta E, Pérez MÁ, García-Aznar JM. Decellularization of tumours: A new frontier in tissue engineering. *J Tissue Eng* 2022; 13: 204173142210916.
154. García-Gareta E, Abduldaiem Y, Sawadkar P, et al. Decellularised scaffolds: just a framework? Current knowledge and future directions. *J Tissue Eng* 2020; 11: 204173142094290.
155. Al-Akkad W, Acedo P, Vilia M-G, et al. Tissue-Specific Human Extracellular Matrix Scaffolds Promote Pancreatic Tumour Progression and Chemotherapy Resistance. *Cells* 2022; 11: 3652.
156. SENSI F, D'ANGELO E, BICCARI A, et al. Establishment of a human 3D pancreatic adenocarcinoma model based on a patient-derived extracellular matrix scaffold. *Transl Res* 2022; 253: 57–67.
157. Matai I, Kaur G, Seyedsalehi A, et al. Progress in 3D bioprinting technology for tissue/organ regenerative engineering. *Biomaterials* 2020; 226: 119536.
158. Liao J, Xu B, Zhang R, et al. *Applications of decellularized materials in tissue engineering: Advantages, drawbacks and current improvements, and future perspectives*. 2020. Epub ahead of print 2020. DOI: 10.1039/d0tb01534b.
159. Puls TJ, Tan X, Husain M, et al. Development of a Novel 3D Tumor-tissue Invasion Model for High-throughput, High-content Phenotypic Drug Screening. *Sci Reports 2018 81* 2018; 8: 1–14.
160. Yang JM, Olanrele OS, Zhang X, et al. Fabrication of Hydrogel Materials for Biomedical Applications. *Adv Exp Med Biol* 2018; 1077: 197–224.
161. Sánchez-Cid P, Jiménez-Rosado M, Romero A, et al. Novel Trends in Hydrogel Development for Biomedical Applications: A Review. *Polymers (Basel)* 2022; 14: 3023.
162. Broekgaarden M, Anbil S, Bulin A-L, et al. Modulation of redox metabolism negates cancer-associated fibroblasts-induced treatment resistance in a heterotypic 3D culture platform of pancreatic cancer HHS Public Access. DOI: 10.1016/j.biomaterials.2019.119421.
163. Wong C-W, Han H-W, Tien Y-W, et al. Biomaterial substrate-derived compact cellular spheroids mimicking the behavior of pancreatic cancer and microenvironment. *Biomaterials* 2019; 213: 119202.
164. Maji S, Lee H. Engineering Hydrogels for the Development of Three-Dimensional In Vitro Models. *Int J Mol Sci 2022, Vol 23, Page 2662* 2022; 23: 2662.
165. Kesharwani P, Bisht A, Alexander A, et al. Biomedical applications of hydrogels in drug delivery system: An update. *J Drug Deliv Sci Technol* 2021; 66: 102914.
166. Zhang HJ, Sun TL, Zhang AK, et al. Tough Physical Double-Network Hydrogels Based on Amphiphilic Triblock Copolymers. *Adv Mater* 2016; 28: 4884–4890.
167. Lin C-C, Korc M. Designer hydrogels: Shedding light on the physical chemistry of the pancreatic cancer microenvironment. *Cancer Lett* 2018; 436: 22–27.
168. Liu HY, Greene T, Lin TY, et al. Enzyme-mediated stiffening hydrogels for probing activation of pancreatic stellate cells. *Acta Biomater* 2017; 48: 258–269.
169. Sapudom J, Müller CD, Nguyen K-T, et al. Matrix Remodeling and Hyaluronan Production by Myofibroblasts and Cancer-Associated Fibroblasts in 3D Collagen Matrices. *Gels* 2020; 6: 33.

170. Liu H-Y, Korc M, Lin C-C. Biomimetic and enzyme-responsive dynamic hydrogels for studying cell-matrix interactions in pancreatic ductal adenocarcinoma. *Biomaterials* 2018; 160: 24–36.
171. Rubiano A, Delitto D, Han S, et al. Viscoelastic properties of human pancreatic tumors and in vitro constructs to mimic mechanical properties. *Acta Biomater* 2018; 67: 331.
172. Puls TJ, Tan X, Whittington CF, et al. 3D collagen fibrillar microstructure guides pancreatic cancer cell phenotype and serves as a critical design parameter for phenotypic models of EMT. *PLoS One* 2017; 12: e0188870.
173. Monteiro M V., Rocha M, Gaspar VM, et al. Programmable Living Units for Emulating Pancreatic Tumor-Stroma Interplay. *Adv Healthc Mater* 2022; 2102574.
174. Antunes J, Gaspar VM, Ferreira L, et al. In-air production of 3D co-culture tumor spheroid hydrogels for expedited drug screening. *Acta Biomater* 2019; 94: 392–409.
175. Pednekar KP, Heinrich MA, van Baarlen J, et al. Novel 3d μtissues mimicking the fibrotic stroma in pancreatic cancer to study cellular interactions and stroma-modulating therapeutics. *Cancers (Basel)*; 13. Epub ahead of print 1 October 2021. DOI: 10.3390/CANCERS13195006/S1.
176. Hakobyan D, Médina C, Dusserre N, et al. Laser-assisted 3D bioprinting of exocrine pancreas spheroid models for cancer initiation study. *Biofabrication*; 12. Epub ahead of print 1 July 2020. DOI: 10.1088/1758-5090/ab7cb8.
177. Yue K, Trujillo-de Santiago G, Alvarez MM, et al. Synthesis, properties, and biomedical applications of gelatin methacryloyl (GelMA) hydrogels. *Biomaterials* 2015; 73: 254–271.
178. Blanco-Fernandez B, Gaspar VM, Engel E, et al. Proteinaceous Hydrogels for Bioengineering Advanced 3D Tumor Models. *Adv Sci* 2021; 8: 2003129.
179. Langer EM, Allen-Petersen BL, King SM, et al. Modeling Tumor Phenotypes In Vitro with Three-Dimensional Bioprinting. *Cell Rep* 2019; 26: 608-623.e6.
180. Ma X, Yu C, Wang P, et al. Rapid 3D bioprinting of decellularized extracellular matrix with regionally varied mechanical properties and biomimetic microarchitecture. *Biomaterials* 2018; 185: 310–321.
181. Jain P, Kathuria H, Dubey N. Advances in 3D bioprinting of tissues/organs for regenerative medicine and in-vitro models. *Biomaterials* 2022; 287: 121639.
182. Ke D, Niu C, Yang X. Evolution of 3D bioprinting-from the perspectives of bioprinting companies. *Bioprinting* 2022; 25: e00193.
183. Wishart G, Gupta P, Schettino G, et al. 3d tissue models as tools for radiotherapy screening for pancreatic cancer 1,2. *Radiol* 2021; 94: 20201397.
184. Tomás-Bort E, Kieler M, Sharma S, et al. 3D approaches to model the tumor microenvironment of pancreatic cancer. *Issue 11 Theranostics* 2020; 10: 5074–5089.
185. Gündel B, Liu X, Löhr M, et al. Pancreatic Ductal Adenocarcinoma: Preclinical in vitro and ex vivo Models. *Front Cell Dev Biol* 2021; 9: 1–12.
186. Uzunparmak B, Sahin IH. Pancreatic cancer microenvironment: a current dilemma. *Clin Transl Med 2019 81* 2019; 8: 1–8.
187. Hingorani SR. Epithelial and stromal co-evolution and complicity in pancreatic cancer. *Nat Rev Cancer* 2023; 23: 57–77.
188. Eichholz KF, Hoey DA. Mediating human stem cell behaviour via defined fibrous architectures by melt electrospinning writing. *Acta Biomater* 2018; 75: 140–151.
189. Bernal PN, Bouwmeester M, Madrid-Wolff J, et al. Volumetric Bioprinting of Organoids and Optically Tuned Hydrogels to Build Liver-Like Metabolic Biofactories. *Adv Mater* 2022; 34: 2110054.
190. Madrid-Wolff J, Boniface A, Loterie D, et al. Controlling Light in Scattering Materials for Volumetric Additive Manufacturing. *Adv Sci* 2022; 9: 2105144.
191. Gehlen J, Qiu W, Müller R, et al. Volumetric Tomographic 3D Bioprinting of Heterocellular Bone- like Tissues in Seconds. 2021; 1–24.
192. Rizzo R, Ruetsche D, Liu H, et al. Optimized Photoclick (Bio)Resins for Fast Volumetric Bioprinting. *Adv Mater*; 33. Epub ahead of print 2021. DOI: 10.1002/adma.202102900.
193. Ning L, Shim J, Tomov ML, et al. A 3D Bioprinted in vitro Model of Neuroblastoma Recapitulates Dynamic Tumor-Endothelial Cell Interactions Contributing to Solid Tumor Aggressive Behavior. *Adv Sci* 2022; 9: 2200244.
194. Kinstlinger IS, Saxton SH, Calderon GA, et al. Generation of model tissues with dendritic

vascular networks via sacrificial laser-sintered carbohydrate templates. *Nat Biomed Eng* 2020; 4: 916–932.

Chapter II

2D and 2.5D models

Abstract

Pancreatic ductal adenocarcinoma (PDAC) mainly develops in the head of the pancreas, within the acino-ductal unit composed by acinar and ductal cells surrounded by pancreatic stellate cells (PSCs). PSCs strongly influence the tumor microenvironment by triggering an intense stromal deposition which plays a key role in tumor progression and limits the drugs perfusion. This chapter aims at describing the development process of 2D and 2.5D models used to evaluate the PDAC-stromal cells relationship. Specifically, the cell crosstalk was firstly analyzed under co-culture conditions on 24-well inserts including a biomimetic nanofibrous PCl/Gel membrane. This simplified model, recreating the multicellular composition of the exocrine parncreas, interestly shows that the human fibroblasts change their morphology and secrete higher amount of IL-6 cytokines in presence of tumor cells confirming the activation of stromal cells under co-culture. The same electrospun membrane was also used to establish the 2.5D model, consisting in a multilayer PDAC-on-chip device that was designed to culture the PDAC cells and the PSCs embedded in a type I collagen gel in the top and bottom layers, respectively. The presence of the biomimetic nanofibrous substrate in the middle of the chip permits to control the interactions between the two cell lines and to easily analyze the effect of the crosstalk on cell behavior. Moreover, this high-throughput downscaled engineered system allows to culture cells at a miniaturized length scale and provides physiological hydrodynamic cues to cells. The PDAC-on-chip system was validated by demonstrating that human fibroblasts seeded in a collagen matrix in the bottom microchannel also change to a myofibroblasts-like shape with increased expression of α-SMA and secrete higher amount of IL-6 cytokines. Moreover, this microfluidic system resulted suitable for the evaluation of drugs efficacy and represents a powerful tool to replicate the initial steps of PDAC evolution towards the establishment of an efficient *in vitro* platform for innovative therapies validation. The here reported work has been published in Biomaterials Science journal (Sgarminato *et al*., PDAC-on-chip for *in vitro* modeling of stromal and pancreatic cancer cell crosstalk. Biomater Sci., 2023,11, 208-224).

2.1 Introduction

Current research is focusing on the development of PDAC *in vitro* models for a deeper understanding of the complex mechanisms involved in pancreatic cancer evolution, the identification of new biomarkers and the establishment of screening tests, in order to enable an earlier detection of the pathology and to improve the prognosis[1–6]. However, one of the major limitations of PDAC *in vitro* models is the lack in replicating the tumor microenvironment surrounding the gland and the PDAC-stroma crosstalk, which constitutes an important feature as it significantly affects the tumor's evolution and the drugs resistance[6–10]. Among the existing *in vitro* models, organ-on-chip microfluidic systems represent a powerful tool to reproduce the cancer cells-stroma interactions in a controllable environment and under real-time monitoring[3,11–13]. In addition, these devices make drug tests and cell analysis accessible and immediate due to the presence of typical micrometer-sized channels that allow a controlled patterning of stromal and cancer cells[14]. As shown in the previous chapter, recent studies have demonstrated the possibility to include the stromal components on microfluidic platforms to better replicate the PDAC microenvironment[4,15–18]. However, further improvements are needed in the design of microfluidic systems to establish valuable high-throughput platforms, helpful for drug screening and for the achievement of the complete understanding of pancreatic cancer.

This chapter describes the steps followed to develop a transwell-based 2D model and a novel biomimetic PDAC-on-chip (2.5D model) (Fig. 2.1).

The 2D model was employed to preliminary test the activity of different cell types (stromal and epithelial) that were allowed to grow in mono- or co-culture on the two sides of a nanofibrous membrane.

In detail, commercial 24-well inserts were modified by replacing the polyethylene terephthalate (PET) membrane with a polycaprolactone/gelatin (PCL/Gel) nanofibrous mat, which represents a biomimetic substrate since the ECM-like architecture typical of the electrospun matrices is able to enhance cell adhesion, spreading and functions[19–22]. The blend of a synthetic thermoplastic polymer (PCL) and a natural polymer (Gel) has been widely adopted in the fabrication of nanofibrous scaffolds as it allows to achieve a combination of suitable mechanical and physicochemical properties with an improved biocompatibility[23–26]. This 2D model was then used to investigate the behavior of human fibroblasts and human ductal cells (wild type or KRAS-mutated) seeded in mono- or co-culture (Fig. 2.1a). The PDAC-on-chip, on the other hand, was designed to model the pancreatic cancer and its interaction with the surrounding environment. Indeed, PSCs were embedded in a type I collagen gel and cultured in bottom microchambers of the multilayered device, designed to both confine the gel (the central microchannel) and to guarantee the nutrients transport in automated and dynamic conditions (the two lateral microchannels). The ductal cancer cells, on the other hand, were seeded in the top layer of the platform, on the top of the biomimetic nanofibrous PCL/Gel membrane (Fig. 2.1b). The introduction of the electrospun matrix in the middle of the chip represents an innovative bioengineering strategy to make the microfluidic system more biomimetic. In addition, it permits to control the interactions between the two cell lines and to easily analyze the effect of the crosstalk on cell behavior.

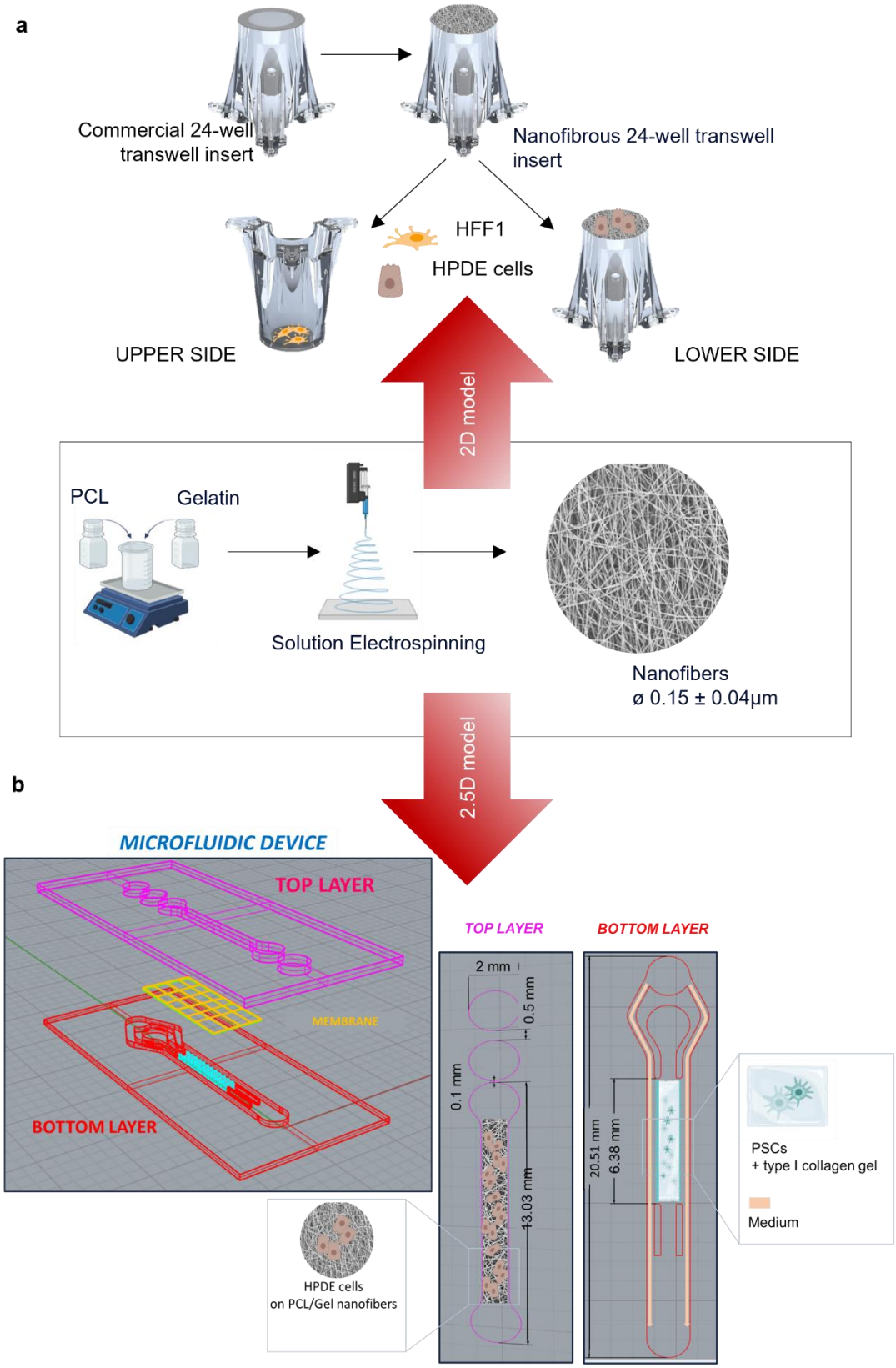

Fig. 2.1 2D and 2.5D PDAC *in vitro* models. (a) A transwell-based 2D model and (b) a novel biomimetic PDAC-on-chip (2.5D model) were developed to evaluate the PDAC-stromal cells relationship. A biomimetic electrospun nanofibrous membrane was used both in the microfluidic device and in the 2D model to control the interactions between the two cell lines and to easily analyze the effect of the crosstalk on cell behavior.

2.2 Transwell-based model

2.2.1 Experimental Section

2.2.1.1 Cell culture

Human pancreatic ductal epithelial cells (HPDE) stably expressing activated KRAS (HPDE-KRAS) and wild-type HPDE (HPDE-wt) were kindly provided by Prof. F. Bussolino and cultured in RPMI-1640 medium (Gibco) supplemented with 1% Penicillin-Streptomycin (Gibco), 1% L-glutamine (Gibco) and 10% fetal bovine serum (FBS) (Gibco). Human foreskin fibroblasts (HFF1) were obtained from ATCC® and cultured in Dulbecco's Modified Eagle's Medium (DMEM) supplemented with 1% Penicillin-Streptomycin (Gibco), 2% L-glutamine (Gibco) and 15% FBS (Gibco). Cell lines were maintained in a humidified CO_2 incubator at 37 °C and 5% CO_2.

2.2.1.2 Preparation of modified transwell inserts using the PCL/Gel electrospun membrane

The PCL/Gel membrane was produced via solution electrospinning, in accordance with previously optimized protocols[19]. In brief, PCL/Gel solution at 15% w/v was prepared mixing the PCL and Gel polymers (respectively in the ratio of 80:20 w/w) in a mixture of acetic acid and formic acid in the ratio of 1:1 v/v. GPTMS (3-glycidoxypropyltrimethoxysilane) was added as gelatin crosslinker to the final solution in a concentration of 3.68% v/v[22,27]. The electrospinning process was performed by employing the NovaSpider v5 instrument (CIC nanoGUNE) and the parameters were set, in accordance with earlier tests, at 12 kV voltage, 0.5 ml/h flow rate and 12 cm distance.

PCL/Gel nanofibers were integrated on the commercial 24-well inserts. Specifically, each insert was modified by removing the polyethylene terephthalate (PET) membrane and leaving only the polystyrene support. The electrospun membranes were then cut in small square pieces and applied on the plastic inserts by employing poly-dimethylsiloxane (PDMS; Sylgard 184) to favor the adhesion. In order to avoid an excessive impregnation of membranes with PDMS, a thin layer of PDMS was brushed on the insert's outer walls and a first pre-crosslinking was performed by maintaining the supports at 90 °C for about 5 min. After the positioning of the PCL/Gel fibers on the polystyrene supports, an additional layer of PDMS was applied on the edges of the membranes and they were then kept at 70 °C for about 2 min to complete the curing of PDMS.

2.2.1.3 Cell seeding in 2D model

The transwell inserts modified with PCL/Gel electrospun membranes were sterilized via UV light for 1 hour before cell seeding. Cells were cultured both on the PCL/Gel electrospun membrane modified supports (TW_PCL/Gel) and on the commercial 24-well PET inserts (TW_PET) with 8.0 µm pore size, 0.1×10^6 per cm^2 pore density and 0.3 cm^2 growth area. HFF1, HPDE-wt and HPDE-KRAS cells were seeded in mono- and co-culture. The co-culture medium was prepared in accordance with preliminary tests performed to individuate the appropriate concentration of supplements. In particular, HFF1 were cultured in DMEM (HFF1_DMEM) and in DMEM/F-12 supplemented with 10% FBS (HFF1_F12 10%) or 15% FBS (HFF1_F12 15%) while HPDE-KRAS cells were cultured in RPMI (HPDE-KRAS_RPMI) and in DMEM/F-12 supplemented with 10% FBS (HPDE-KRAS_F12 10%) or 15% FBS (HPDE-KRAS_F12 15%). The 1:3 ratio of HPDE-wt and HPDE-KRAS to HFF1 cells was adopted

for the co-culture conditions. The human fibroblasts and the ductal cells were seeded at densities of 3 x 10^4 cells/transwell and 1 x 10^4 cells/transwell, respectively. In particular, 35 µl of medium containing HFF1 and 20 µl of medium containing HPDE-KRAS or HPDE-wt were respectively pipetted on the upper and lower side of the membrane. After seeding the cells were allowed to adhere for approximately 1 hour at 37 °C and 5% CO_2 before adding the medium both in the inner and the outer compartments of the modified inserts. The medium was refreshed every 2 days during the culture.

2.2.1.4 Interleukin-6 (IL-6) cytokines release

Cytokines' concentration was determined in cell supernatants that were collected from the upper side of the TW_PET and TW_PCL/Gel membranes after 24h, 48h, 72h and 7d of culture using the IL-6 Human ELISA Kit (Invitrogen, BMS213-2). The concentrations were calculated using the standard curve generated by plotting the absorbance values of each standard sample on the ordinate and the human IL-6 standard concentrations on the abscissa. This assay has allowed to quantify the IL-6 cytokines released by cells seeded both on TW_PET and TW_PCL/Gel in mono- and co-culture.

2.2.1.5 Morphological analysis of HFF1 seeded on TW_PET inserts

Fluorescence imaging was carried out to analyze the changes in cell morphology of human fibroblasts seeded in co-culture with HPDE-KRAS on the commercial PET transwell inserts (TW_PET). The inserts were washed once with 1x phosphate-buffered saline (PBS; Gibco) and fixed with 4% paraformaldehyde (PFA; Sigma Aldrich) for 30 min at room temperature, after 24h, 48h and 72h of culture. They were then washed twice with 1x PBS, permeabilized in 0.5% Triton X-100 (Sigma Aldrich) in 1x PBS for 10 min and incubated with 1% bovine serum albumin (BSA; Invitrogen) for 30 min to improve the staining. The cytoskeletons of HPDE-KRAS and HFF1 were stained with Alexa Fluor™ 488 Phalloidin (Invitrogen, A12379) at 1:60 concentration in 1x PBS with 1% BSA solution while nuclei were visualized with DAPI reagent (4',6-Diamidino-2-Phenylindole, Dihydrochloride; Invitrogen, D1306) at 1:1000 concentration in 1x PBS solution. All samples were then imaged by confocal microscopy (Eclipse Ti2, Nikon). The aspect ratios of HFF1 cells both in mono- and co-culture were also measured using ImageJ software.

2.2.1.6 Statistical Analysis

All bar graph data are presented as the mean ± standard deviation (SD) for three independent experiments per condition or time point. Significance was measured as indicated for each experiment, with two-way or one-way ANOVA followed by pairwise comparison with Tukey's multiple comparisons test using GraphPad Prism 9.3.1; *$p < 0.05$, **$p < 0.01$, ***$p < 0.001$, ****$p < 0.0001$.

2.2.2 Results

2.2.2.1 Optimization of medium supplements concentration for co-culture conditions

The optimal medium composition for co-culture experiments was identified by performing a viability assay (CellTiter-Blue, Promega, G8080) on HFF1 and HPDE-KRAS cells seeded in monoculture within plastic wells and cultured for 7 days with different compositions of media (Fig. 2.2). Cells cultured in

DMEM/F-12 supplemented with 15% FBS showed the most similar fluorescence intensities compared to the respective controls (HFF1_DMEM and HPDE-KRAS_RPMI).

2.2.2.2 Increased IL-6 cytokines release by human fibroblasts under co-culture conditions

In order to evaluate the effect of the interaction between the human fibroblasts and the ductal cells, the concentration of IL-6 cytokines was measured through the ELISA test (Fig. 2.3) by analyzing the supernatants of HFF1, HPDE-KRAS and HPDE-wt seeded in mono- and co-culture on TW_PCL/Gel and TW_PET inserts. The highest amount of IL-6 released by cells under monoculture (Fig. 2.3a) have been quantified at 24h after seeding on the TW_PET membranes by HFF1 cells. After 24h, 48h and 72h from seeding, the IL-6 concentration analyzed in the monoculture HFF1 medium on the TW_PCL/Gel membranes resulted significantly lower compared to the TW_PET. This behavior could be ascribed to the more biomimetic architecture (Fig. 2.4) and composition of electrospun nanofibers compared to PET, which reduces the fibroblasts activation after cell culturing. The amount of IL-6 determined in the media of HPDE-KRAS and HPDE-wt in monoculture resulted minimal (Fig. 2.3a)

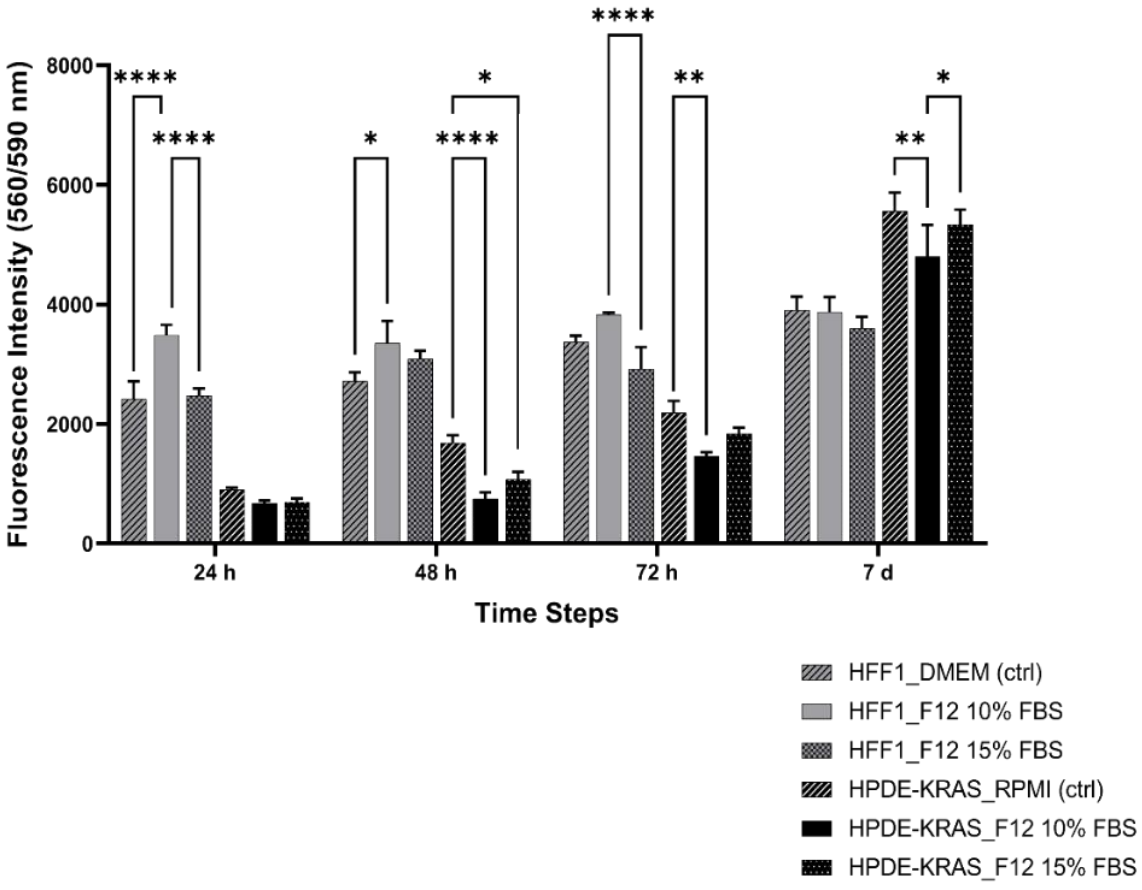

Fig. 2.2 Viability assay to identify the appropriate FBS concentration in the co-culture medium. The bar graph shows the fluorescence intensity measured for HFF1 cultured in DMEM (HFF1_DMEM) and in DMEM/F-12 supplemented with 10% FBS (HFF1_F12 10%) or 15% FBS (HFF1_F12 15%) and for HPDE-KRAS cultured in RPMI (HPDE-KRAS_RPMI) and in DMEM/F-12 supplemented with 10% FBS (HPDE-KRAS_F12 10%) or 15% FBS (HPDE-KRAS_F12 15%). The viability assay (CellTiter-Blue, Promega, G8080) was performed on cell seeded in a plastic multiwell plate (n=3). Tukey's multiple comparisons test: *$p < 0.05$, **$p < 0.01$, ***$p < 0.001$, ****$p < 0.0001$.

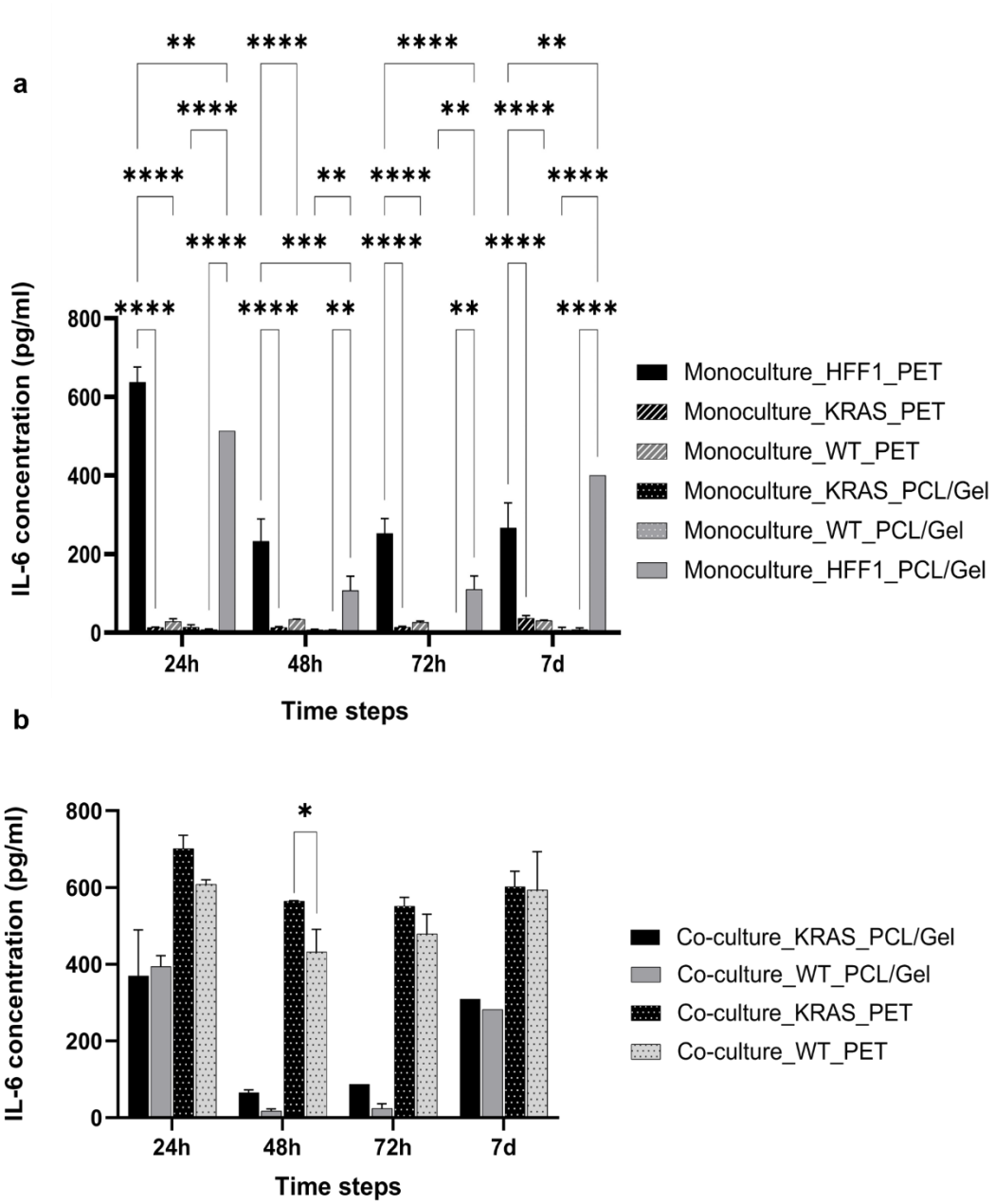

Fig. 2.3 IL-6 cytokines concentration in supernatants collected from mono- and co-cultures in the transwell inserts. Bar plots of the data obtained from ELISA test IL-6 analysis for each culture condition on TW_PET (a) and TW_PCL/Gel (b) grouped per time step (n=3). Each condition has been assayed in duplicate following the manufacturer's instructions. Tukey's multiple comparisons test: *p < 0.05, **p < 0.01, ***p < 0.001, ****p < 0.0001.

for all the tested conditions. In general, the most consistent release of cytokines has been quantified in the supernatant of HFF1 in co-culture with the HPDE-KRAS cells (Fig. 2.3b).
The same trend has been observed on the TW_PCL/Gel membranes, although the concentrations are lower than those measured on the TW_PET membranes.

2.2.2.3 Morphological changes of human fibroblasts co-cultured with HPDE cells

Confocal imaging at different magnifications was performed to analyze the effect of tumor-stroma crosstalk on fibroblasts morphology.

As expected, HFF1 seeded on the TW_PET inserts have showed changes in cytoskeletal organization when cultured with the HPDE-KRAS cells. Indeed, the human fibroblasts assumed a more spindle-shaped conformation from 24h to 72h after seeding and in comparison with the monocultures, as confirmed by the aspect ratio measurements (Fig. 2.5). Representative images of cell morphology changes are reported in Fig. 2.6.

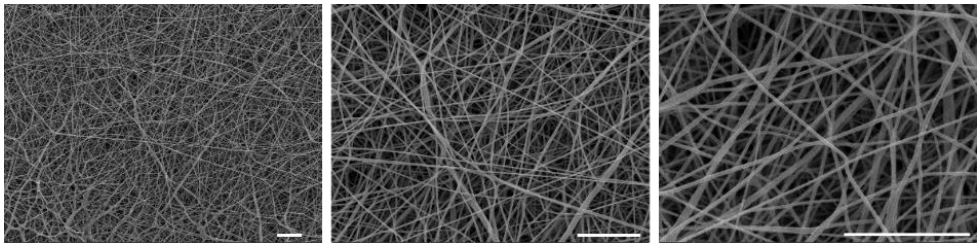

Fig. 2.4 Biometic nanofibrous membrane produced *via* electrospinning. Images from Scanning Electron Microscopy (SEM) analyses at different magnifications showing the PCL/Gel nanofibrous membrane architecture. Scale bars 5 µm.

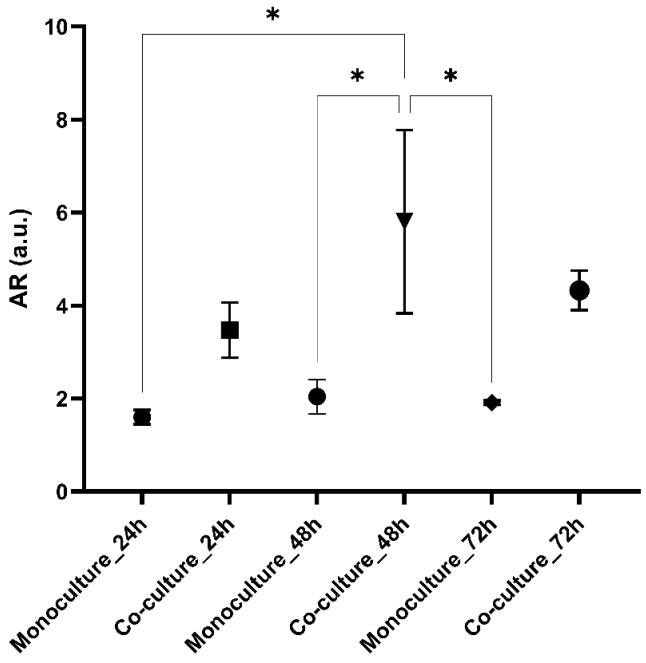

Fig. 2.5 Change in HFF1 aspect ratio under co-culture with HPDE-KRAS cells. Elongated fibroblasts show a mean aspect ratio above 3.9 while the round shape of HFF1 is reflected by an aspect ratio ~ 2. Tukey's multiple comparisons test: *p < 0.05, **p < 0.01, ***p < 0.001, ****p < 0.0001. 60 cells in three images per condition (n=3) were analyzed.

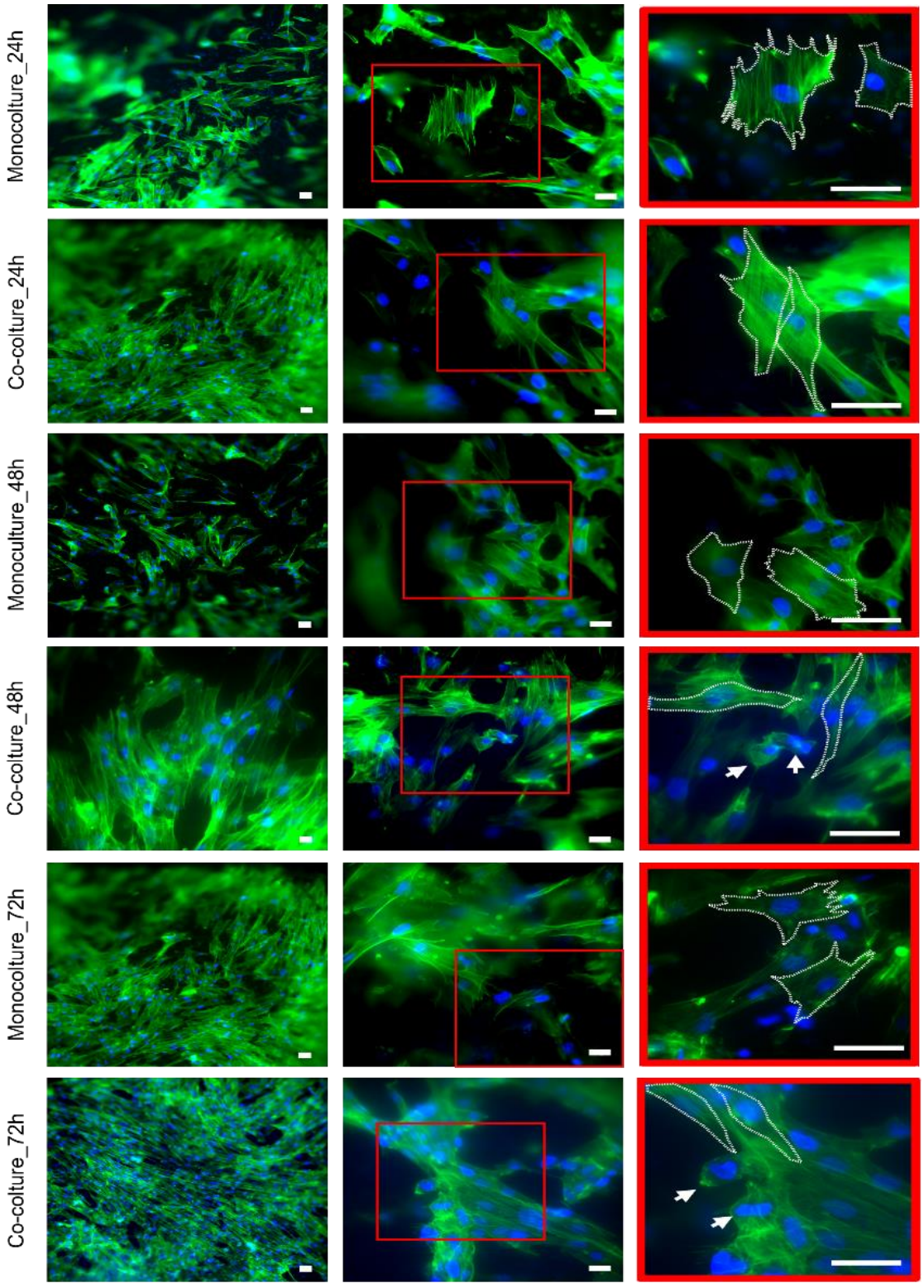

Fig. 2.6 Effect of tumor-stroma crosstalk on human fibroblasts morphology. Representative confocal images at different magnifications (20X, 60X and 100X) obtained upon the HFF1 and HPDE-KRAS staining of nuclei (DAPI) and F-actin (Alexa Fluor™ 488 Phalloidin) in monocultures (HFF1) and co-cultures (HFF1+HPDE-KRAS) after 24h, 48h and 72h from seeding (n=3). The white arrows in the images at 100X indicate the HPDE-KRAS cells in co-culture with the human fibroblasts. Scale bars 50 µm.

2.2.3 Discussion

The effects of the PDAC-stromal cells crosstalk on cellular behavior were firstly analyzed in terms of fibroblasts activation, that typically occurs during the inflammatory response characterizing the tumor development[28–31]. HFF1 cell line was used to perform these preliminary tests since the differences with PSCs are minimal[32], with the advantage of major resistance and stability of functions over extended *in vitro* passages. Indeed, despite the genetic differences between PSCs and HFF1[33], the use of fibroblasts from non-pancreatic origins has been helpful for understanding the relationship between stromal and cancer cells, as many studies have demonstrated[18,34–37]. The results proved the influence of the co-culture conditions on fibroblasts behavior, corresponding to an increment of IL-6 cytokines release (Fig. 2.3) and a change in cytoskeletal morphology (Fig. 2.5, Fig. 2.6). In particular, a higher IL-6 concentration in the supernatant of HFF1 in co-culture with the HPDE-KRAS cells was quantified, compared to the co-culture with healthy ductal cells (HPDE-wt). These outcomes are in line with the data reported by other studies in literature showing that the expression of the oncogenic KRAS correlates with the signaling pathways involved in the inflammatory cascade and in the activation of stromal cells in pancreatic cancer[38–41]. Moreover, the IL-6 cytokines play an important role in pancreatic tumor progression and are produced in abundance by components of stroma including PSCs and fibroblasts[41–43]. As shown in Fig. 2.3, an increment of IL-6 produced by HFF1 in co-culture with HPDE-KRAS was noticed, with a significant increase at 48h.

These data were also confirmed by the morphological analyses performed on the HFF1 seeded in mono- and co-culture with the HPDE KRAS cells on the TW_PET inserts and stained after 24h, 48h and 72h (Fig. 2.6). Indeed, the human fibroblasts exhibited a more detectable spindle-shaped conformation after 72h in co-culture.

Therefore, this 2D transwell-based model resulted suitable to preliminary assess the reciprocal influence of different cell types involved in pancreatic cancer evolution, as confirmed by recent studies reporting the use of these systems for PDAC analyses[44,45]. Moreover, the here developed transwell set-up including an electrospun biomimetic membrane represents a novelty among the existing 2D models of exocrine pancreas tissue[46]. However, this platform is a simplified system able to poorly mimic the multiple PDAC hallmarks. Therefore, the proposed 2D model has been integrated with advance engineering tools towards increasing model biologically relevancy.

2.3 PDAC-on-chip

2.3.1 Experimental section

2.3.1.1 Cell culture

Human pancreatic ductal epithelial cells (HPDE) stably expressing activated KRAS (HPDE-KRAS) and wild-type HPDE (HPDE-wt) were kindly provided by Prof. F. Bussolino and cultured in RPMI-1640 medium (Gibco) supplemented with 1% Penicillin-Streptomycin (Gibco), 1% L-glutamine (Gibco) and 10% fetal bovine serum (FBS) (Gibco).
Human foreskin fibroblasts (HFF1) cells were obtained from ATCC® and cultured in Dulbecco's Modified Eagle's Medium (DMEM) supplemented with 1% Penicillin-Streptomycin (Gibco), 2% L-glutamine (Gibco) and 15% FBS (Gibco). PSCs were purchased from iXCells Biotechnologies and cultured in Stellate Cell Growth Medium kit (iXCells Biotechnologies) composed by Stellate Cell Basal Medium supplemented with 0.2% Stellate Cell Growth Supplement, 1% Penicillin-Streptomycin-Amphotericin B Solution 100x and 10% FBS. Cell lines were maintained in a humidified CO_2 incubator at 37 °C and 5% CO_2.

2.3.1.2 Design and fabrication of the multilayer microfluidic device

The microfluidic device, composed by a bottom layer and a top layer connected by an electrospun membrane, was firstly designed by Rhinoceros® CAD software (Robert McNeel & Associates) and then fabricated by replica molding. Briefly, poly-dimethylsiloxane (PDMS; Sylgard 184) base and crosslinking agent were mixed thoroughly at a ratio of 10:1 w/w and poured onto the master mold and cured for 3h at 60 °C.
An additional layer was successively introduced to allocate the medium reservoirs, whose mold was fabricated through a laser cutter (Microla slider) on a polymethylmethacrylate (PMMA) substrate.

Bottom Layer. The mold of the bottom layer was obtained by SU-8 photolithography. Briefly, an SU-8 patterned master was custom-made using photolithography and then conventional soft lithography was applied to produce several PDMS replicas.
The bottom layer has three channels: a central compartment (6.38 mm length, 1 mm width and 250 µm height) delimited by micropillars, with 100 µm diameter and 250 µm height and two lateral channels (20.51 mm length, 500 µm width and 250 µm height).

Top Layer. The top layer was obtained by laser machining in a laser cutter (Microla slider) on a 3 mm thick PMMA substrate.

Electrospun membrane. The PCL/Gel membrane was produced via solution electrospinning, as previously described (see 2.2 Two-dimensional model; 2.2.1 Experimental section).

The chip has been assembled through a plasma oxygen treatment of the PDMS surfaces to decrease the hydrophobicity and therefore facilitate the bond between the different layers.
The electrospun PCL/Gel membrane was inserted between the top and bottom layers to create an ECM-like substrate for epithelial cell growth.

2.3.1.3 Fluidic characterization of the bottom layer

Liquid insertion and diffusivity tests were performed to evaluate the influence of the distance between the pillars on the retention of a collagen gel within the middle microchannel and the diffusivity of the medium from the lateral to the central channels, respectively. In particular, gaps of 50 µm and 75 µm between the pillars were analyzed.

Insertion test. A solution of deionized water and blue food dye was loaded into the inlet of the central channel in the bottom layer through a manual micropipette and under an optical microscope (Leica M205 A, Leica Microsystems) to monitor confinement of the liquid inside the microchannel. This test was repeated by loading the colored acellularized collagen gel within the middle channel.

Diffusivity test. The collagen gel solution (10 mg/ml) was prepared by mixing sterile collagen type I from bovine hides (FibriCol®, Advanced Biomatrix) with 10x phosphate-buffered saline (PBS; Gibco) and sterile distilled water. The pH was adjusted to 7.4 using 0.1 M NaOH. The gel was then loaded into the central channel while a fluorescent solution was prepared by adding a blue emitting dye to deionized water. Successively, 10 µl of fluorescent solution was inserted in the lateral channels and the chip was observed with an inverted confocal microscope (Eclipse Ti2, Nikon). Images were acquired every 30 seconds for 30 minutes and the fluorescence intensities at different time points were calculated as mean value of pixels measured in six regions of interest (ROIs), that cover 60% of the effective area in the central channel.

2.3.1.4 Embedding stromal cells into the collagen gel

The collagen gel solution (10 mg/ml) was prepared as previously described. Briefly, collagen type I from bovine hides (FibriCol®, Advanced Biomatrix) was mixed with 10x phosphate-buffered saline (PBS; Gibco) and sterile distilled water. The pH was then adjusted to 7.4 using 0.1 M NaOH. Cells were embedded into the collagen gel at densities of 1 x 10^6 cells/ml (D1), 3 x 10^6 cells/ml (D2) and 5 x 10^6 cells/ml (D3). To compare the viability of human fibroblasts seeded at D1, D2 and D3 inside the collagen gel, the CellTiter-Glo 3D Cell Viability Assay (Promega, G9681) was performed according to the manufacturers' protocols. In addition, the LIVE/DEAD™ Assay (Invitrogen, L3224) was carried out on the cells loaded within the collagen gel at the density which resulted optimal, in order to further confirm the quantitative test (metabolic activity assay) results. Images were acquired with a fluorescent cell imager (ZOE™; Bio-Rad) and analyzed using ImageJ software. The HFF1 cells were harvested and embedded in the type I collagen solution at a final density of 3×10^6 cells/ml. The same procedure was adopted to embed the PSCs in the collagen gel.

2.3.1.5 Cell seeding in the microfluidic device

The platform was treated with UV light for 1 hour as sterilization process before cell culture.

Stromal cells. PSCs were loaded into the central channel of the bottom layer by injecting 3 µl of cell-hydrogel mixture at a density of 10×10^3 cells/channel. After polymerization at 37 °C and 5% CO_2 for about 40 min, the lateral microchannels in the bottom layer and the reservoirs were filled with culture medium and returned to the incubator for culture. Sterile PBS was added into the wells to avoid dehydration of the hydrogel. Medium was changed every day.

Ductal cells. HPDE-KRAS cells were seeded in the top layer on the PCL/Gel electrospun membrane at a density of 35×10^3 cells/channel by pipetting 5 µl of medium with cells inside the chamber. The chips were then placed in incubator for about 30 min to enhance attachment of cells to the nanofibers.
Successively, the reservoirs were filled with culture medium and returned to the incubator. Medium was changed every day during the culture period.

Co-culture. Stromal cells (HFF1 and PSCs respectively) and cancer ductal cells (HPDE-KRAS) were co-cultured in the assembled multilayer chip. A 1:3 ratio of cancer cells to stromal cells was used since it has been reported as a commonly adopted value due to the relevancy that ratios of 1:1 to 1:3 have *in vivo* [47–49]. Particularly, densities of 3.5×10^3 cells/channel and 10×10^3 cells/channel were used for cancer and stromal cells respectively. Cells were co-cultured and maintained in DMEM/F-12 supplemented with 15% FBS (Gibco), 1% Penicillin-Streptomycin (Gibco) and 2% L-glutamine (Gibco) since previous tests demonstrated the efficacy of this culture medium composition in promoting the cell viability (Fig. 2.2).
Stromal cells were embedded in the type I collagen gel as previously described and loaded in the central chamber of the bottom layer by using the inlet on the top layer corresponding to the central channel in the bottom layer. HPDE-KRAS cells were seeded by injecting 5 µl of medium with cells inside the inlet corresponding to the chamber in the top layer. Reservoirs were filled with culture medium and medium was changed every day during the culture period.

Viability of cells inside the platform was analyzed by LIVE/DEAD assay at different time points. Preliminary assessments were performed on single layers (top layer including the nanofibrous membrane and bottom layer sealed on a glass coverslip). Then, the co-culture was implemented inside the assembled chip as described above.

In particular, cells seeded within the microfluidic platforms and on the common polystyrene multiwell cell culture plate (controls) were incubated with LIVE/DEAD™ reagents (Invitrogen, L3224) according to the manufacturer's protocol. The PSCs embedded in the type I collagen gel and seeded in a plastic multiwell plate were also stained and used as control.
Subsequently, the cultures were imaged by employing ZOE™ fluorescent cell imager. Fluorescence staining and imaging were also performed to evaluate the morphology and the spatial distribution of HPDE-KRAS and PSCs seeded in the microfluidic platforms, both in mono- and co-culture, at different time steps.
Each compartment of the device was washed once with 1x PBS (Gibco) and fixed with 4% PFA (Sigma Aldrich) for 30 min at room temperature. After washing twice with 1x PBS, the chambers were filled with 0.5% solution of Triton X-100 (Sigma Aldrich) in 1x PBS and maintained for 10 min at room temperature to allow cell membrane permeabilization. Then, samples were incubated with 1% BSA (Invitrogen) for 30 min to improve the staining.
The cytoskeletons of cells in monoculture were visualized using the green-fluorescent Alexa Fluor™ 488 Phalloidin (Invitrogen, A12379) while the actin filaments of cells seeded in co-culture were stained with Rhodamine Phalloidin (Invitrogen, R415) at 1:60 and 1:400 concentrations in solutions of 1x PBS with 1% BSA, respectively. Nuclei were observed with DAPI reagent (Invitrogen, D1306) as previously described. Images were acquired by confocal microscopy (Eclipse Ti2, Nikon) and analyzed using ImageJ software.

2.3.1.6 Administration of tumor supernatant to human fibroblasts seeded in the bottom layer

HFF1 embedded in type I collagen gel and seeded in the bottom layer of the microfluidic device were treated with supernatant collected from the previously developed 2D model, specifically the TW_PCL/Gel seeded with HPDE-KRAS in monoculture after 72h. Indeed, the tumor supernatant was administered to HFF1 after 48h of culture in the bottom layer. The same procedure was applied to HFF1 embedded in the type I collagen gel and seeded in a plastic multiwell plate, as control. The expression of alpha-smooth muscle actin (α-SMA) was determined by immunofluorescence staining. Briefly, cultures in microchannels and in the controls were fixed after 48h of incubation with HPDE-KRAS supernatant using 4% PFA for 30 min and further treated with 0.5% Triton X-100 for 10 min. After blocking non-specific binding with 1% BSA, the primary antibody against α-SMA (1:100, Sigma Aldrich, A7607) was applied for overnight incubation at 4 °C. After incubation with Goat anti-Mouse IgG1 Secondary Antibody (1:1000, Invitrogen, SA5-10264), Alexa Fluor™ 488 Phalloidin (Invitrogen, A12379) and DAPI (1:1000, Invitrogen, D1306), samples were analyzed by confocal microscopy (Eclipse Ti2, Nikon). The images were then analyzed and the fluorescence intensity (mean gray values) distribution was plotted using the ImageJ software. In addition, the concentration of IL-6 cytokines released by HFF1 seeded in the bottom layer of the microfluidic chip was quantified using the IL-6 Human ELISA Kit (Invitrogen, BMS213-2) after 48h of incubation with the HPDE-KRAS supernatant.

2.3.1.7 Testing the drug efficacy to induce HPDE-KRAS cell death using PDAC-on-chip

HPDE-KRAS were cultured in the top layer as previously described. To test the effect of anti-cancer agents on the cell viability, 100 nM bortezomib (SelleckChem) and 1 µM gemcitabine (SelleckChem) in the HPDE growth medium were injected in the inlet corresponding to the microchamber of the top layer. HPDE-KRAS grown for 48h were treated with drug for 24h and 96h and they were successively stained using LIVE/DEAD™ reagents (Invitrogen, L3224) in accordance with the manufacturer's instructions.

2.3.1.8 Statistical Analysis

All bar graph data are presented as the mean ± standard deviation (SD) for three independent experiments per condition or time point. Significance was measured as indicated for each experiment, with two-way or one-way ANOVA followed by pairwise comparison with Tukey's multiple comparisons test using GraphPad Prism 9.3.1; *$p < 0.05$, **$p < 0.01$, ***$p < 0.001$, ****$p < 0.0001$.

2.3.2 Results

2.3.2.1 Development of a functional multilayer device

The fabrication of the PDMS microfluidic system was carried out as previously illustrated. The platform consists of a top and a bottom layer divided by an electrospun PCL/Gel membrane (Fig. 2.7).

Top Layer. The final dimensions of the microchannel resulted 12 mm length, 400 µm width and 500 µm height. Inlets and outlet allocated at this level have 2.2 mm diameters (Fig. 2.7a).

Bottom Layer. The bottom layer has three channels: a central compartment (6.38 mm length, 1 mm width and 250 µm height) delimited by micropillars, with 100 µm diameter and 250 µm height, which aim to confine a collagen gel loaded with the PSCs and two lateral channels (20.51 mm length, 500 µm width and 250 µm height) to control the nutrients passage (Fig. 2.7b). The Field Emission Scanning Electron Microscopy (FESEM) images (Fig. 2.7$b_{i\text{-}iii}$) allowed to evaluate the repeatability of the SU8-photolithograhy process which has permitted to achieve high resolutions in terms of micropillars dimensions and geometrical accuracy. In addition, digital microscopy confirmed the support given by the two rows of pillars in maintaining the PCL/Gel membrane flat in the assembled chip configuration (Fig. 2.7c). The bottom layer was also characterized to determine the influence of the distance between the pillars on the retention of the gel within the middle microchannel and the diffusivity of the medium from the lateral to the central channels. As reported in Fig. 2.8, both water-based liquids and collagen hydrogel resulted confined into the central microchamber, for the two pillars gaps tested (50 µm and 75 µm). On the other hand, the diffusivity test allowed to establish the optimal distance between the micropillars, by analyzing the diffusion of a fluorescent solution from the lateral channels to the middle chamber containing the type I collagen gel (Fig. 2.8b-f). Fig. 2.8b-c show the measurements of the fluorescence intensity at different time intervals for the two layouts (50 µm and 75 µm pillars gaps). The average fluorescence intensity of the analyzed ROIs was indicated as I_0 at time $t_0 = 0$ s, while for $t > 0$ s it was generically indicated as I. The first peaks of intensity are due to the initial addition of the fluorescent dye. The trend is linear for both layouts, indicating a uniform diffusion within the collagen gel for both 75 µm and 50 µm inter-micropillars distances. In addition, the angular coefficient of the interpolation line describing the diffusivity coefficient in the collagen gel is the same for both layouts. However, the model with a gap of 75 µm between pillars (Fig. 2.8b) has proved to be the most promising model as the diffusion is faster and the central channel is completely fluorescent in less than 30 minutes, thus suggesting a good compromise for the nutrients transport to the cells embedded in the gel.

2.3.2.2 Viability of stromal cells embedded in type I collagen gel

CellTiter-Glo 3D Assay and LIVE/DEAD Assay were performed to evaluate the viability of fibroblasts loaded within the type I collagen gel and cultured for one week (Fig. 2.9). Luminescence values of the three different cell densities were compared at each time point. The increase of viability during time indicates a higher number of live cells, which is associated with a higher proliferation.
Fig. 2.9a shows that cells seeded at a density of 3×10^6 cells/ml (D2) resulted more viable and active compared to those seeded at a lower density of 1×10^6 cells/ml (D1). In addition, the D2 density resulted better than a higher density D3 (5×10^6 cells/ml) as the cell viability increased with time resulting in optimal fibroblasts survival and proliferation within the gel. LIVE/DEAD images were acquired at 3×10^6 cells/ml (Fig. 2.9b-d) showing an increment in cell number during the culture period, confirming the optimal proliferative capability of fibroblasts embedded in the collagen gel at a density of 3×10^6 cells/ml (Fig. 2.9b-d). In particular, accordingly with the viability assay (Fig. 2.9a), cells were able to grow throughout the culture period, creating fibrillar and compact structures within the tridimensional (3D) framework (Fig. 2.9d).

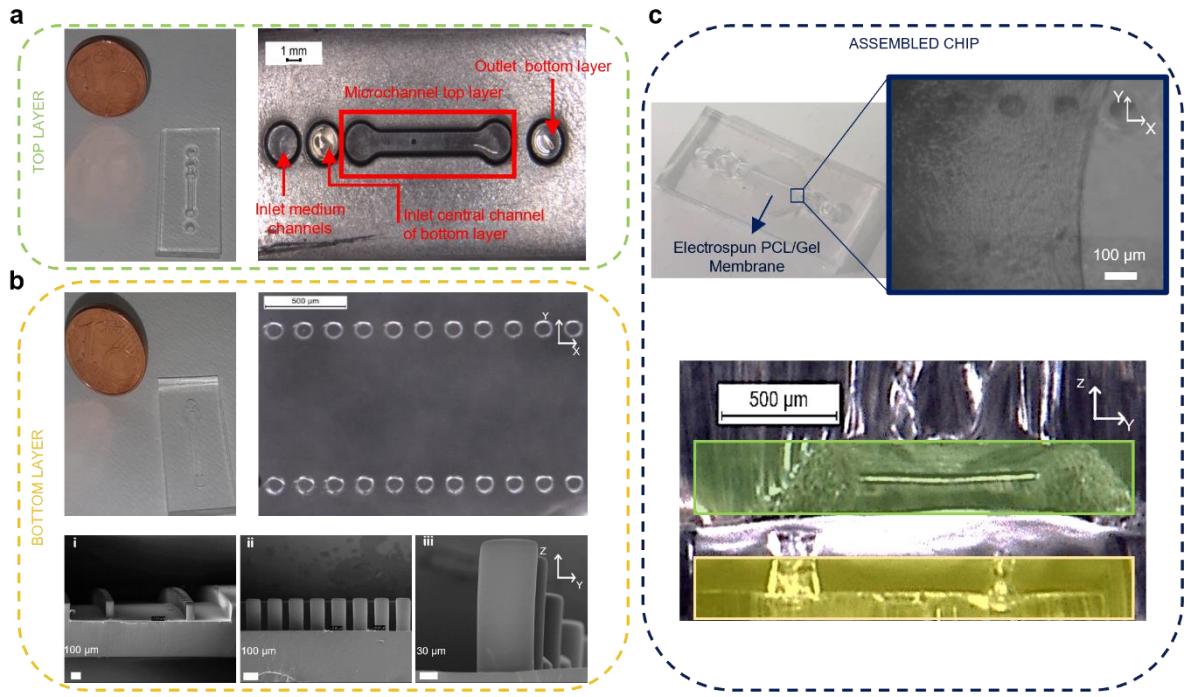

Fig. 2.7 PDAC-on-chip: multilayer microfluidic device. (a) Top layer with the inlets, the outlet and the microchannel. (b) Bottom layer with the central microchannel delimited by two rows of micropillars (i,ii,iii) and two lateral microchannels. (c) Assembled chip configuration showing the electrospun PCL/Gel membrane inside the device. In the cross view the nanofibrous matrix can be observed between the top layer (green) and the bottom layer (yellow).

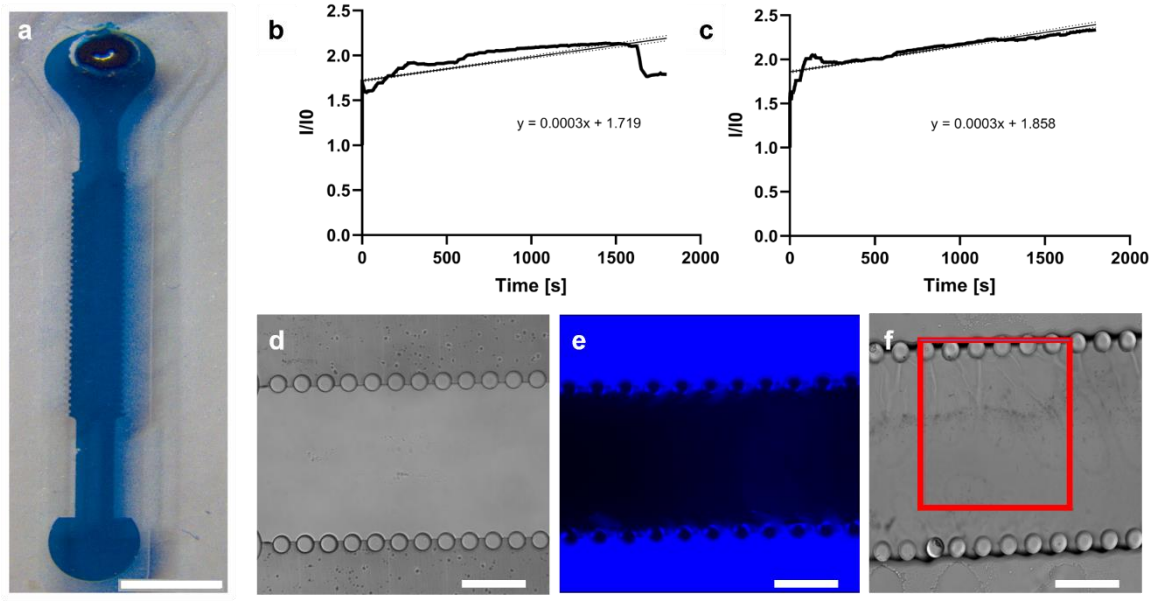

Fig. 2.8 Fluidic characterization of the bottom layer. (a) Insertion test. Monitoring of the blue colored solution confinement inside the central microchannel. Scale bar 2 mm. (b-f) Diffusivity test. The fluorescence intensity of a stained solution was measured at different time intervals, for two pillars gaps, 75 µm (b) and 50 µm (c). The central chamber was filled with type I collagen gel (d) and the fluorescent solution was injected in the lateral microchannels (E) at t_0 = 0 s. The average intensity was calculated considering the values registered in different ROIs (f). Scale bars 200 µm.

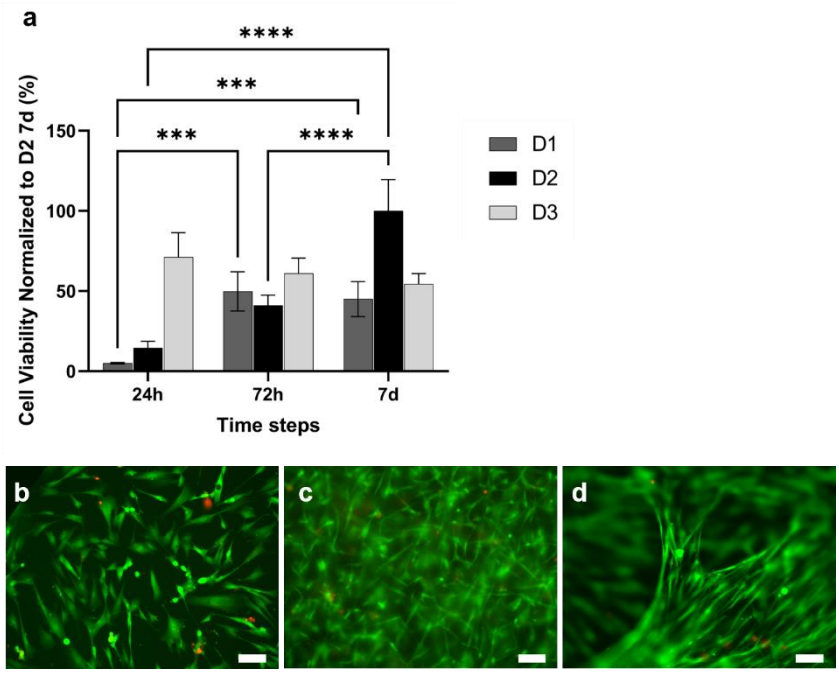

Fig. 2.9 Human fibroblasts viability in type I collagen gel. (a) Comparison between the viability of HFF1 seeded at D1 (1 x 10^6 cells/ml), D2 (3 x 10^6 cells/ml) and D3 (5 x 10^6 cells/ml) densities (n=3). Tukey's multiple comparisons test: ***p < 0.001, ****p < 0.0001. (b-d) LIVE/DEAD images of HFF1 (3 x 10^6 cells/ml) embedded in the gel at 24h (b), 72h (c) and 7d (d) after seeding. Cells were stained using calcein-AM for live cells and ethidium homodimer-1 for dead cells. Images are representative of at least six individual regions of the gels (n=3). Scale bars 100 μm.

2.3.2.3 Cell culture in the microfluidic device

The response of PSCs and HPDE-KRAS cells, seeded in the bottom and in the top layers respectively, was evaluated in terms of cell viability and cell morphology. Precisely, the PSCs embedded in the type I collagen gel and seeded in the central microchannel of the bottom layer (Fig. 2.10a) were able to colonize the chamber by modelling the hydrogel and forming a dense tissue throughout the duration of the experiment. The LIVE/DEAD images (Fig. 2.10b) reveal that the stromal cells remained viable and active despite a few dead cells in the initial phase of seeding. This is probably related to the embedding procedure which could be aggressive to the cells, causing a high number of dead cells which is remarkable from 24h to 48h and greatly decrease from 48h to 72h, after seeding. The morphological analyses have demonstrated a uniform spatial distribution of PSCs that exhibit a high degree of cell spreading, developing interconnected multicellular networks (Fig. 2.10c). Furthermore, the fluorescence images show the migratory ability of stromal cells which cross over the central channel after 4 days from seeding. The ductal cells stably expressing activated KRAS (HPDE-KRAS) were seeded in the top layer of the microfluidic device (Fig. 2.11a) to firstly evaluate their biological response in monoculture conditions. In particular, the PCL/Gel electrospun membrane and the overhead PDMS layer were bonded to a glass coverslip in order to better monitor the cell behavior. The LIVE/DEAD assay revealed a good cell viability on PCL/gelatin nanofibers thus confirming the cytocompatibility of membrane which represents an optimal culture substrate for cell adhesion and proliferation (Fig. 2.11b). In addition, the cytoskeletal organization of the ductal cells was evaluated by fluorescence microscopy which allowed to observe the formation of the characteristic cobblestone morphology proving that cells were functionally active[50,51] (Fig. 2.11c).

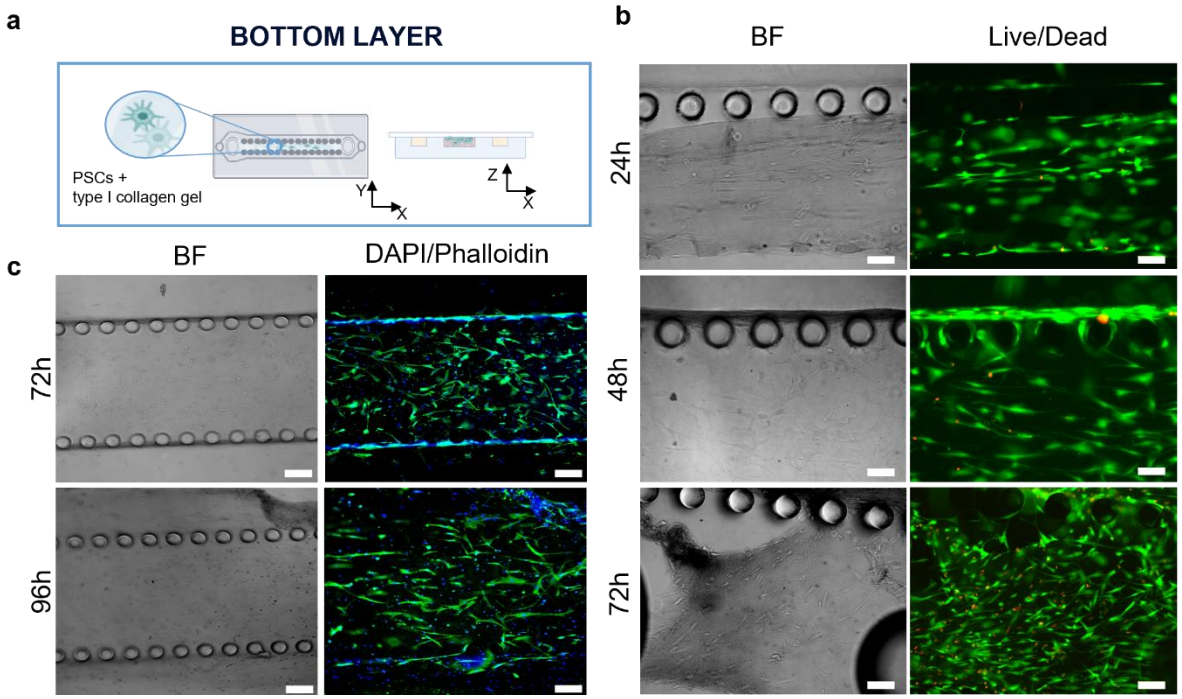

Fig. 2.10 Seeding of human pancreatic stellate cells (PSCs) within the type I collagen gel in the bottom layer. (a) Schematic illustration of the bottom layer with the central microchannel containing the PSCs embedded in the collagen gel. (b) LIVE/DEAD images showing the viability of stromal cells at 24h, 48h and 72h after seeding (n=3). (c) Representative confocal images of PSCs in brightfield and upon staining with DAPI (nuclei) and Alexa Fluor™ 488 Phalloidin (cytoskeletons) at 72h and 96h after seeding. Scale bars 100 µm.

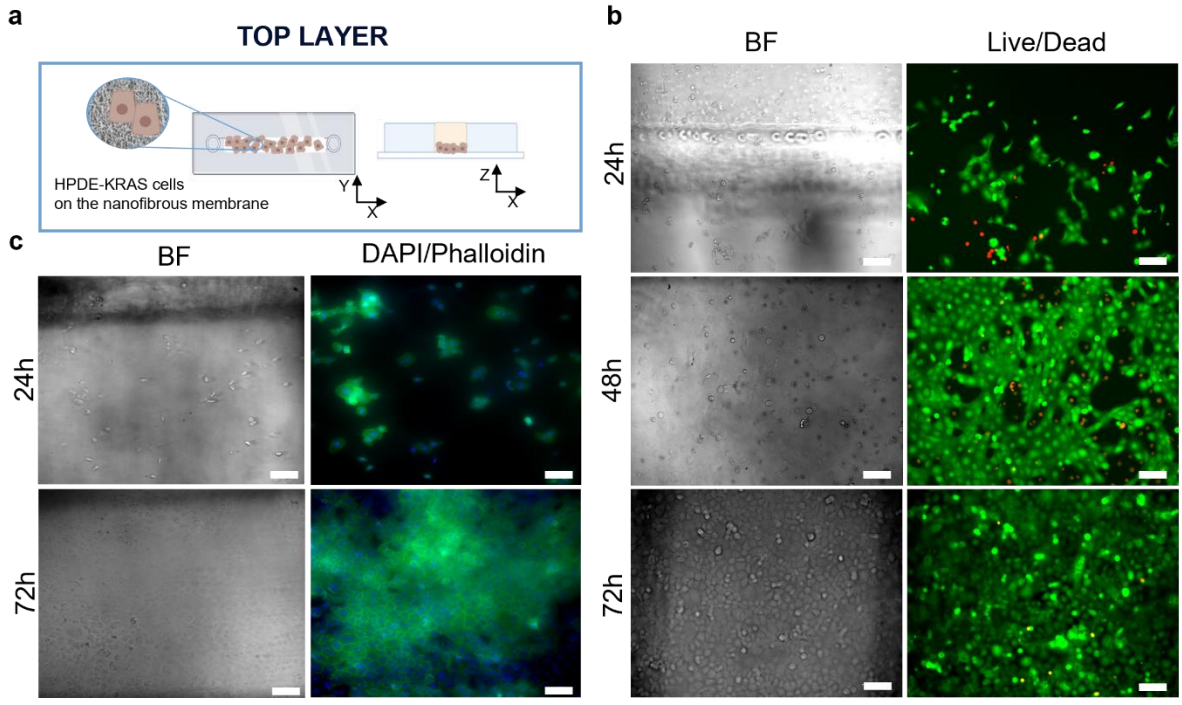

Fig. 2.11 Seeding of PDAC cells in the top layer. (a) Schematic illustration of the top layer with the HPDE-KRAS cells seeded in the microchannel on the electrospun membrane. (b) LIVE/DEAD images showing the viability of HPDE-KRAS on the nanofibrous matrix in the chip at 24h, 48h and 72h after seeding (n=3). (c) Representative confocal images of HPDE-KRAS grown on the electrospun membrane inside the device upon staining with DAPI (nuclei) and Alexa Fluor™ 488 Phalloidin (cytoskeletons) at 24h and 72h after seeding. Scale bars 100 µm.

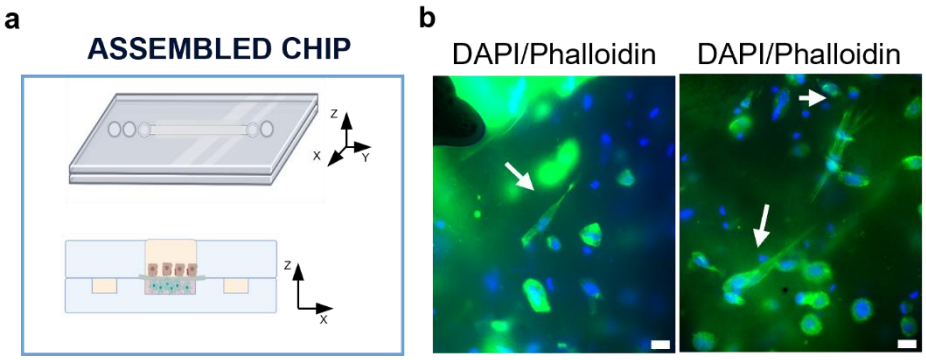

Fig. 2.12 Seeding of PSCs and HPDE-KRAS in the assembled chip under co-culture conditions. (a) Schematic illustration of the assembled chip with the HPDE-KRAS cells seeded in the top and the PSCs in the bottom layers, respectively. (b) Representative confocal images at high magnifications showing the PSCs with elongated spindle shapes, indicated by the white arrows. Scale bars 20 µm.

The co-culture condition was implemented in the assembled chip, where the different layers were joined together through a plasma oxygen treatment of the PDMS surfaces (Fig. 2.12a). Fig. 2.12b shows fluorescence images at higher magnifications where the PSCs (white arrows) display an elongated spindle shape suggesting their possible activation. However, the PSCs are hardly visible and the quality of images reported in Fig. 2.12b is considerably inferior to those of monocultures. Indeed, the hydrogel tend to impregnate the nanofibrous membrane causing autofluorescence and noising effects in confocal images limiting the detection of cell distribution.

2.3.2.4 Activation of human fibroblasts cultured with HPDE-KRAS supernatant

As shown in Fig. 2.13 and Fig. 2.14, HFF1 assumed an elongated spindle shape indicating their activation when cultured with the HPDE-KRAS supernatant for 48h and upon staining of F-actin. The change in cell morphology can be observed in Fig. 2.14a and Fig. 2.14b reporting the cytoskeletons of HFF1 in the microchamber of the bottom layers, cultured with (Fig. 2.14a) and without (Fig. 2.14b) the HPDE-KRAS supernatant. This evidence was further confirmed by the increment in α-SMA expression in fibroblasts embedded within the collagen gel and seeded both in the bottom layer and in the 24-wells used as controls (Fig. 2.14d, f). Indeed, the α -SMA amount is considerably higher in samples incubated with the tumor-derived supernatant (Fig. 2.14e-f), compared to the "untreated" samples (Fig. 2.14c-d) confirming the activation of fibroblasts towards a myofibroblast phenotype. In addition, the graphs plotting the gray value measured on fluorescence images show a more homogeneous distribution of the intensity values for the untreated conditions (Fig. 2.15$a_{i\text{-}iii}$, $b_{i\text{-}iii}$) in comparison to the distributions of the treated samples (Fig. 2.15$_{aiv\text{-}vi}$, $b_{iv\text{-}vi}$). The peaks visible in Fig. 2.15a_{vi} and Fig. 2.15b_{vi} correlate with an evident difference in the fluorescence intensity emitted by cells and background respectively, indicating a higher expression of α-SMA. Moreover, a higher level of IL-6 cytokines was measured in the medium of HFF1 seeded in PDAC-on-chip after the incubation with the pancreatic cancer cells supernatant. Indeed, a 25% increment in IL-6 cytokines amount was detected through ELISA kit when HFF1 were treated with HPDE-KRAS supernatants compared to HPDE ones (Fig. 2.17).

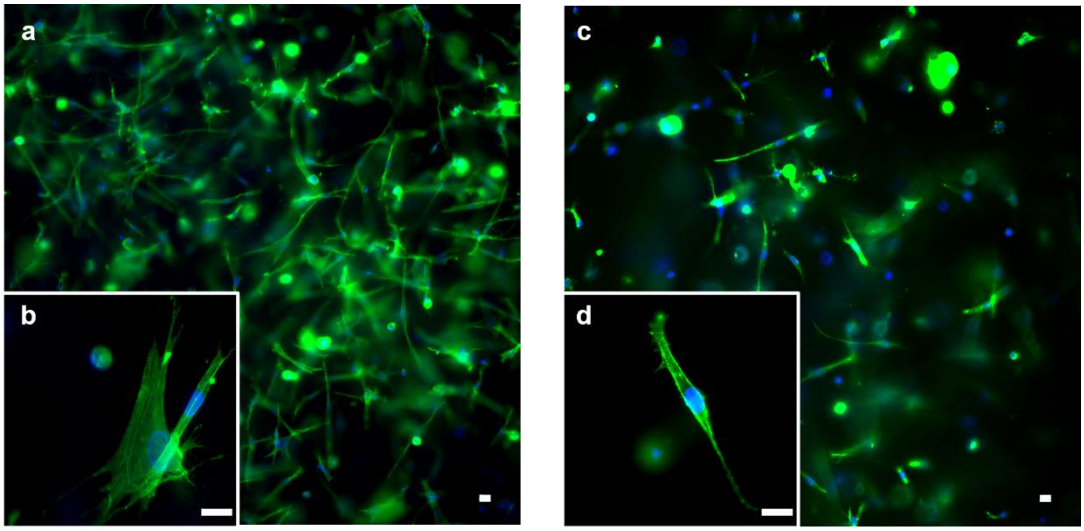

Fig. 2.13 Activation of human fibroblasts upon culture with HPDE-KRAS supernatant. (a-d) Fluorescent images of HFF1 embedded in type I collagen hydrogel and stained with Alexa Fluor™ 488 Phalloidin (F-actin) and DAPI (nuclei) to highlight the differences between the fibroblasts' cytoskeletons before (a-b) and after (c-d) the incubation with tumor supernatant. Cells were grown for 48h before the staining. Scale bars 20 µm.

2.3.2.5 Drug sensitivity of HPDE-KRAS cultured in the microfluidic device

The HPDE-KRAS response to anti-cancer chemotherapeutic agents was analyzed and the validity of the PDAC-on-chip device in evaluating the drugs efficacy was demonstrated. Indeed, the LIVE/DEAD images (Fig. 2.17) showed significant changes in viability of cells exposed to bortezomib (Fig. 2.17a) and gemcitabine (Fig. 2.17b) after a treatment period of 24h and 96h.
The evident decrease in cell number after the drugs treatment was due to cell detachment following the cell apoptosis of pancreatic cancer cells induced by the chemotherapeutic treatment

2.3.3 Discussion

The results proved the effectiveness of the 2.5D model here described, consisting of a multilayer microfluidic chip, in reproducing the PDAC microenvironment at a miniaturized scale. In particular, the bottom layer was fabricated to insert the cellularized hydrogel within the central microchamber, which is delimited by two rows of micropillars (100 µm diameter and 250 µm height) aiming at both gel confinement and nutrients passage (Fig. 2.7b). The fluidic properties of the bottom layer in granting the medium diffusion within the hydrogel was investigated, identifying 75 µm as the optimal distance between the micropillars, although larger gaps are used in literature[4,47]. Indeed, a liquid medium was able to completely diffuse from the lateral microchannels into the central chamber in 30 minutes, thus ensuring the transport of nutrients to the cells in a short time (Fig. 2.8). To replicate the composition of the pancreatic TME, the stromal cells were embedded in a type I collagen gel which represents the main constituent of the PDAC stroma[52]. The viability of HFF1 loaded within the gel was tested, demonstrating that the type I collagen hydrogel exhibits good biological properties in terms of cells viability and growth (Fig. 2.9). This result is supported by other studies showing enhanced adhesion and proliferation of human fibroblasts embedded within the 3D collagen gels[53,54]. The capability of stromal cells in remodeling the gel resulting in the formation of tridimensional and compact cellularized hydrogel structures was also observed. (Fig. 2.9d).

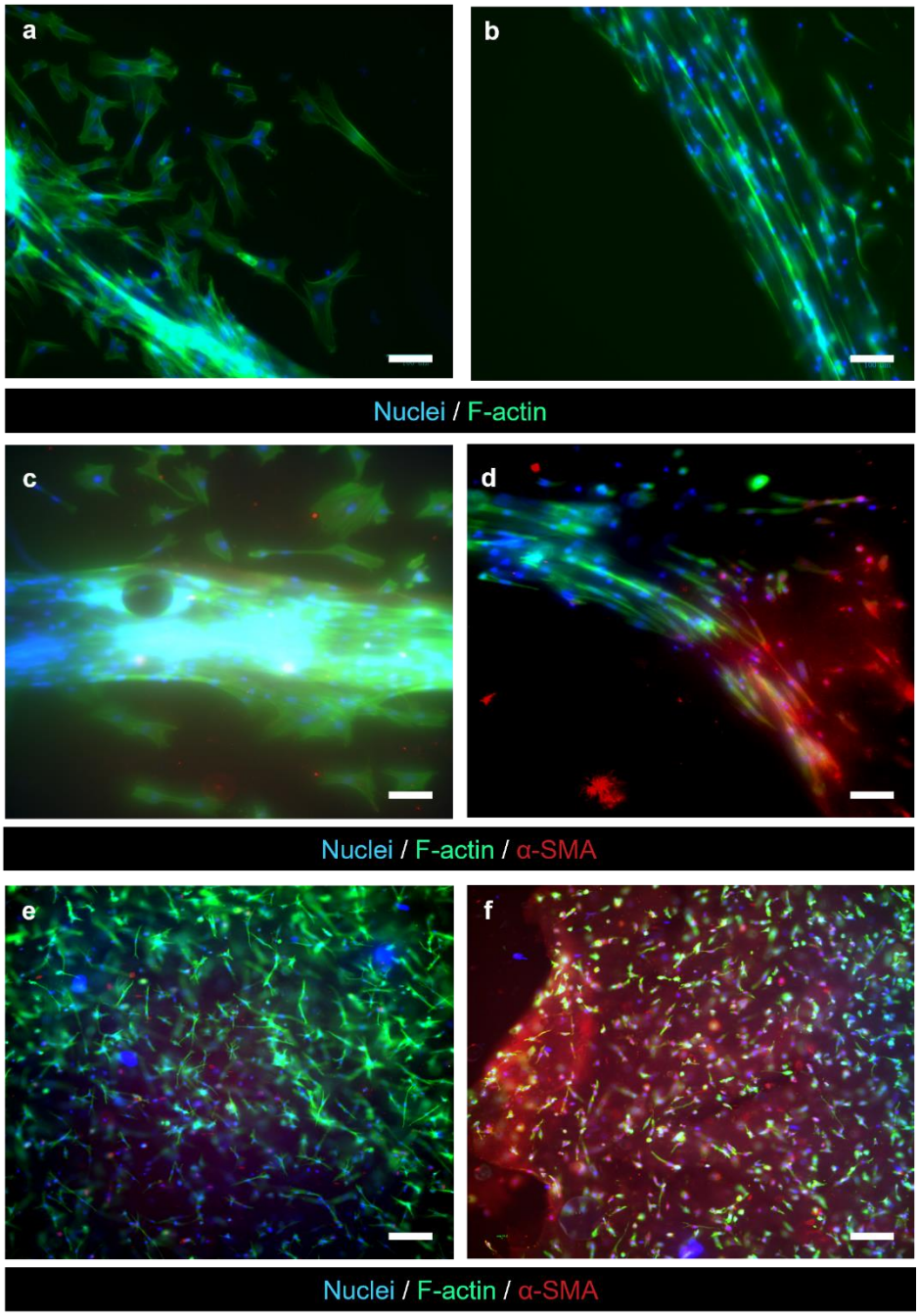

Fig. 2.14 Activation of human fibroblasts upon culture with HPDE-KRAS supernatant. (a-b) Fluorescent images of HFF1 seeded in the bottom layer of PDAC-on-chip and stained with Alexa Fluor™ 488 Phalloidin (F-actin) and DAPI (nuclei) to highlight the differences between the fibroblasts morphology before (a) and after (b) the incubation with tumor supernatant. (c-f) Representative confocal images showing the changes in α-SMA expression of HFF1 before (c,e) and after (d,f) the treatment with HPDE-KRAS supernatant. (c,d) HFF1 embedded in collagen hydrogel and seeded in the bottom layer of the microfluidic device. Scale bars 50 µm. (e,f) HFF1 grown within the type I collagen gel in the 24-wells and used as controls. Cells were grown for 48h before the staining. Images are representative of at least three images per individual experiment (n=3). Scale bars 100 µm.

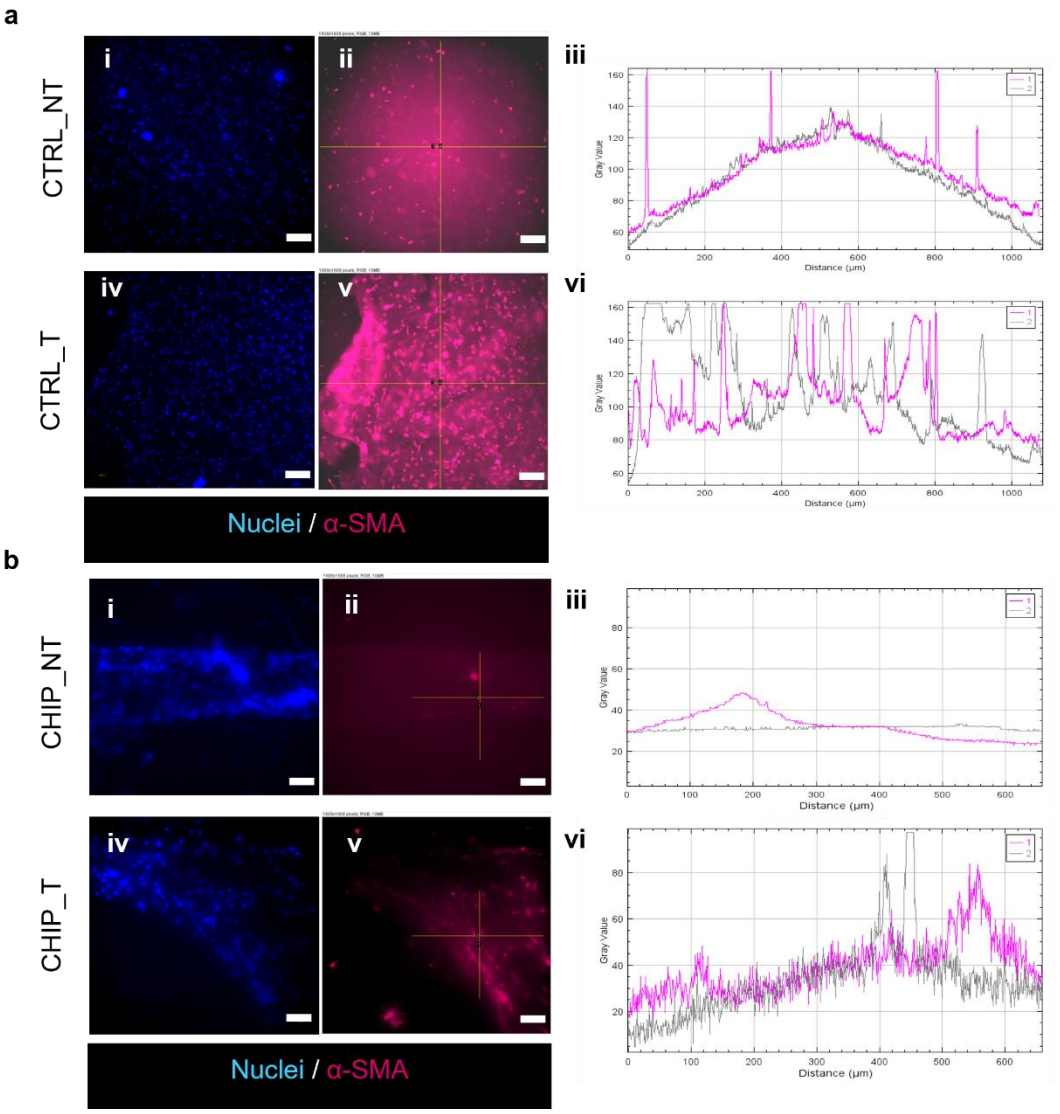

Fig. 2.15 Expression of α-SMA by stromal cells upon culture with HPDE-KRAS supernatant. (a-b) Confocal images showing the expression of α-SMA by HFF1 embedded in type I collagen hydrogel (a) and seeded in the bottom layer of the microfluidic device (b) before (i-iii) and after (iv-vi) the treatment with HPDE-KRAS supernatant. The plots ($a_{iii,vi}$-$b_{iii,vi}$) report the intensity values along the two lines drawn in the images $a_{ii,v}$ and $b_{ii,v}$ (vertical line=1; horizontal line=2). Scale bars 100 µm. (c) IL-6 cytokines concentration in supernatants collected from the bottom chamber of the microfluidic device where the fibroblasts were cultured for 48h with (Treated) and without (Untreated) the HPDE_KRAS-derived supernatant. Bar plots of the data obtained from ELISA test IL-6 analysis for each culture condition (n=2). Tukey's multiple comparisons test: *p < 0.05, **p < 0.01, ***p < 0.001, ****p < 0.0001.

The collagen gel was then employed to incorporate the PSCs seeded within the here designed multilayer microfluidic device. The use of a collagen matrix to encapsulate the PSCs seeded in dedicated microchannels was also illustrated in the experimental work of Lee and collaborators[17]. However, in our pancreatic cancer chip model a biomimetic nanofibrous membrane was employed, for the first time, to control the interaction between tumor cells (HPDE-KRAS cells) and PSCs (Fig. 2.7c).

The microfluidic device designed in this work guarantees a good cell survival and it allows to easily monitor the cell response within the chip, key features for a clinically relevant experimental *in vitro* model of healthy and pathological tissues. Indeed, the response of PSCs and HPDE-KRAS cells seeded

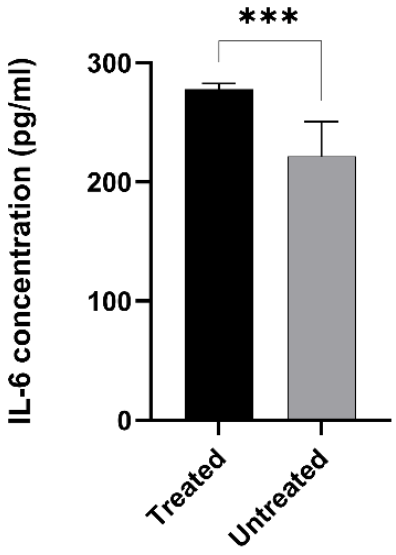

Fig. 2.16 Activation of HFF1 seeded in PDAC-on-chip device. IL-6 concentration in supernatants collected from the bottom chamber of the microfluidic device where the fibroblasts were cultured for 48h with (Treated) and without (Untreated) the HPDE_KRAS-derived supernatant. Bar plots of the data obtained from ELISA test IL-6 analysis for each culture condition (n=2). Tukey's multiple comparisons test: *p < 0.05, **p < 0.01, ***p < 0.001, ****p < 0.0001.

inside the chip was analyzed in terms of cell viability, proliferative capability and cell morphology. In particular, the PSCs resulted able to colonize the chamber by growing throughout the duration of the experiment (Fig. 2.10). However, the tests revealed a few dead cells in the initial phase of seeding which could be associated with the embedding procedure in the gel. Thus, the thermal shock given by the temperature of the collagen solution (4 °C) could be the cause of the cell apoptosis occurring during the first hours after seeding[55]. Nonetheless, the stellate cells seemed to recover from the stress and continued to proliferate, showing a high degree of cell spreading inside the collagen network (Fig. 2.10b-c). The confocal microscopy analysis allowed to observe the PSCs flat morphology indicating their viability[56] and the typical stellate shape suggesting their quiescent state in monoculture[41,57]. Focusing on the cell behavior of HPDE-KRAS seeded in the top layer (Fig. 2.11), PDAC cells remained viable and active as confirmed by the confocal images showing the typical acinar organization of the ductal cells *in vivo*[58] (Fig. 2.11c). These results underline the importance of a biomimetic substrate like the electrospun PCL/Gel nanofibrous matrix in promoting the epithelial cell viability and functionality, as widely discussed in literature[59–63]. The co-culture conditions implemented in our model have allowed to preliminary evaluate the reciprocal influence that the HPDE-KRAS cells and the PSCs have on each other. Specifically, confocal images showed the morphological change of stellate cells that appear in a spindle shape indicating their activation, as highlighted in the study of Lee and coworkers[17] (Fig. 2.12). This aspect has been further analyzed by culturing the HFF1 embedded in the type I collagen gel with the HPDE-KRAS supernatant, to correlate the fibroblasts behavior in the PDAC-on-chip device with the one observed in the 2D model. HFF1 in the collagen matrix changed from a relatively short and flat shape to a myofibroblasts-like shape with stress fiber formation and increased expression of α-SMA (Fig. 2.13 – Fig. 2.15). In addition, a higher level of IL-6 cytokines released by HFF1 seeded in PDAC-on-chip was measured. This result is in line with the previous outcomes that were obtained in the 2D model, suggesting that fibroblasts cultured inside the bottom layer experienced the same stimuli as the HFF1 seeded on TW inserts (Fig. 2.16).

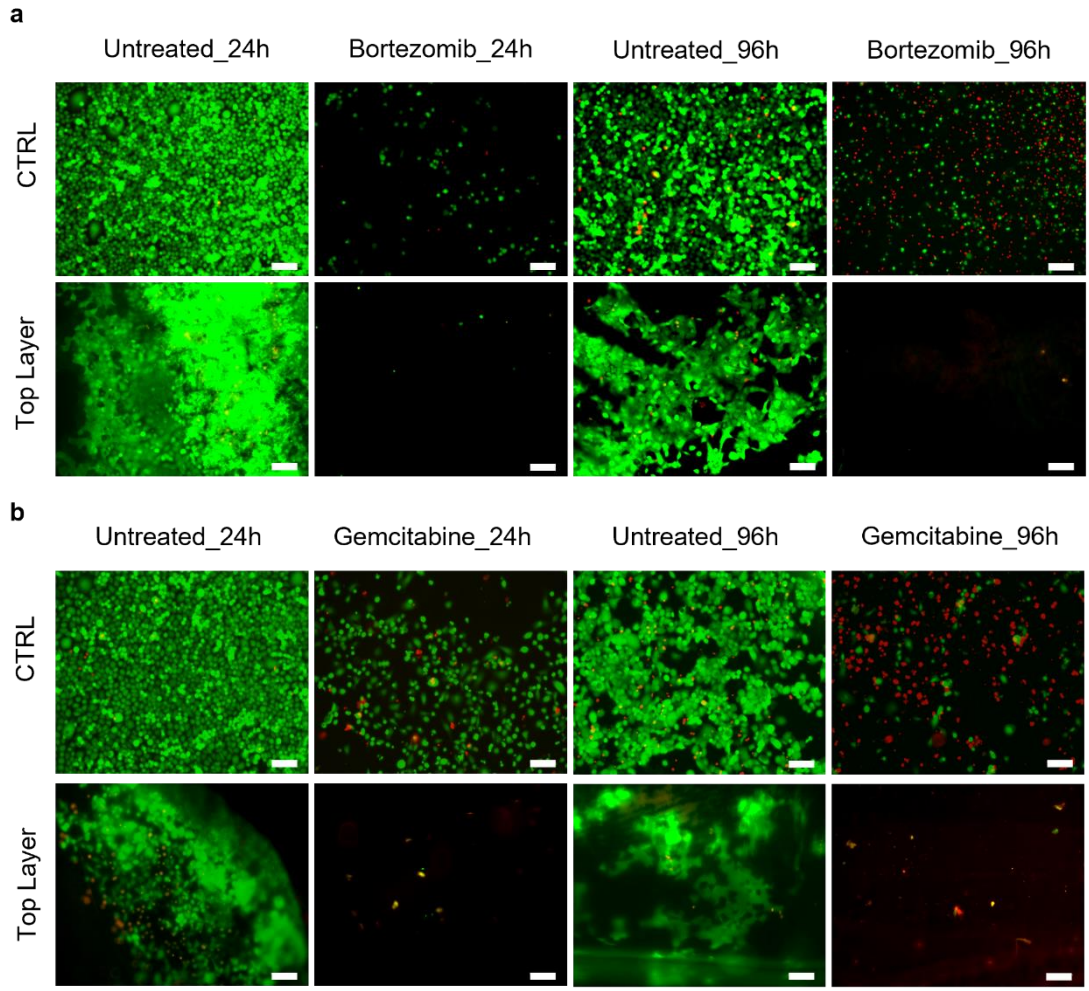

Fig. 2.17 Sensitivity of HPDE-KRAS cells to anti-cancer drugs. (a-b) Cell viability analyses of HPDE-KRAS grown for 48h and stained with calcein-AM (live cells) and ethidium homodimer-1 (dead cells) after 24h and 96h exposure to gemcitabine (a) and bortezonib (b). Images are representative of at least three images per individual experiment (n=3). Scale bars 100 μm.

The drug sensitivity of HPDE-KRAS cells cultured in the microfluidic platform was characterized through the exposure to different chemotherapeutic agents. Precisely, bortezomib and gemcitabine, that are proteosome and DNA synthesis inhibitors respectively[64], were used. Thus, the validity of the PDAC-on-chip system which can be used to test the efficacy of drugs on pancreatic cancer cells was preliminary assessed (Fig. 2.17). Indeed, our chip allows the administration of single or multiple drugs both in contact to epithelial, as well as stellate cells, and a continuous monitoring of the effect of the therapeutic treatment on both cell populations can be easily performed thanks to the presence of the electrospun membrane which confined cells in a specific chip compartment.

Finally, in the current tumor-stroma interplay on-a-chip scenario[37], the device developed in this work accurately recapitulates the key aspects of the relationship between the tumor and its microenvironment through a scalable and high-throughput approach. Moreover, the use of a nanofibrous and biomimetic membrane to compartmentalize the microfluidic device and thus separate the cancer component from the stromal tissue allows to study the effect of the inflammation stimuli on the stromal cells in a controlled and specific way.

2.4 Conclusion

A 2D transwell-based model and a multilayer PDAC-on-chip were here designed and developed to reproduce *in vitro* the tumor-stromal cells crosstalk occurring during pancreatic cancer progression. These simplified models allowed to rapidly recapitulate the interactions between stromal cells (human fibroblasts and pancreatic stellate cells) and human pancreatic ductal epithelial cells (normal or KRAS-mutated). Specifically, the nanofibrous electrospun PCL/Gel membrane was used, both in 2D and 2.5D models, as ECM mimicry to favor the adhesion and growth of epithelial cells and to control the cell interplay in a specific and accessible way. Increased level of cytokines, changes in morphology and higher expression of α-SMA were observed when human fibroblasts were cultured with HPDE-KRAS cells or HPDE-KRAS supernatant. This work thus underlines the biological relevancy that the PDAC-stromal cells interactions have in determining the tumor microenvironment remodeling during the pancreatic cancer insurgence. However, the 2D model represents an extreme simplification of the pancreatic TME, since the stromal components are only partially included and cells grow in a two-dimensional environment.

On the other hand, the 2.5D *in vitro* model allows to better study the tumor-stroma reciprocal influence as the introduction of the collagen gel is fundamental to replicate the dense and fibrotic tissue typical of pancreatic stroma. In addition, this microfluidic platform permits to easily perform drug screening towards the identification of effective personalized and high-throughput therapeutical strategies for individual patients. However, PDAC-on-chip lacks to mimic the 3D complex gland morphology proper of the functional unit of exocrine pancreas.

References

1. Cave DD, Rizzo R, Sainz B, et al. The revolutionary roads to study cell–cell interactions in 3d in vitro pancreatic cancer models. Cancers (Basel) 2021; 13: 1–19.
2. Osuna de la Peña D, Trabulo SMD, Collin E, et al. Bioengineered 3D models of human pancreatic cancer recapitulate in vivo tumour biology. Nat Commun 2021 121 2021; 12: 1–15.
3. Haque MR, Rempert TH, Al-Hilal TA, et al. Organ-Chip Models: Opportunities for Precision Medicine in Pancreatic Cancer. Cancers (Basel) 2021; 13: 4487.
4. Mollica H, Teo YJ, Tan ASM, et al. A 3D pancreatic tumor model to study T cell infiltration. Biomater Sci 2021; 9: 7420–7431.
5. Schuster B, Junkin M, Kashaf SS, et al. Automated microfluidic platform for dynamic and combinatorial drug screening of tumor organoids. Nat Commun 2020; 11: 1–12.
6. Nguyen DHT, Lee E, Alimperti S, et al. A biomimetic pancreatic cancer on-chip reveals endothelial ablation via ALK7 signaling. Sci Adv 2019; 5: 1–10.
7. Xu H, Lyu X, Yi M, et al. Organoid technology and applications in cancer research. J Hematol Oncol 2018; 11: 116.
8. Boj SF, Hwang C Il, Baker LA, et al. Organoid models of human and mouse ductal pancreatic cancer. Cell 2015; 160: 324–338.
9. Beer M, Kuppalu N, Stefanini M, et al. A novel microfluidic 3D platform for culturing pancreatic ductal adenocarcinoma cells: Comparison with in vitro cultures and in vivo xenografts. Sci Rep 2017; 7: 1–12.

10. Kramer B, De Haan L, Vermeer M, et al. Interstitial flow recapitulates gemcitabine chemoresistance in a 3D microfluidic pancreatic ductal adenocarcinoma model by induction of multidrug resistance proteins. Int J Mol Sci; 20. Epub ahead of print 2019. DOI: 10.3390/ijms20184647.
11. Swayden M, Soubeyran P, Iovanna J. Upcoming Revolutionary Paths in Preclinical Modeling of Pancreatic Adenocarcinoma. Front Oncol 2020; 9: 1443.
12. Tomás-Bort E, Kieler M, Sharma S, et al. 3D approaches to model the tumor microenvironment of pancreatic cancer. Theranostics 2020; 10: 5074–5089.
13. Low LA, Mummery C, Berridge BR, et al. Organs-on-chips: into the next decade. Nature Reviews Drug Discovery 2021; 20: 345–361.
14. Bhatia SN, Ingber DE. Microfluidic organs-on-chips. Nat Biotechnol 2014 328 2014; 32: 760–772.
15. Gioeli D, Snow CJ, Simmers MB, et al. Development of a multicellular pancreatic tumor microenvironment system using patient-derived tumor cells. Lab Chip 2019; 19: 1193–1204.
16. Bradney MJ, Venis SM, Yang Y, et al. A Biomimetic Tumor Model of Heterogeneous Invasion in Pancreatic Ductal Adenocarcinoma. Small 2020; 1905500: 1–10.
17. Lee JH, Kim SK, Khawar IA, et al. Microfluidic co-culture of pancreatic tumor spheroids with stellate cells as a novel 3D model for investigation of stroma-mediated cell motility and drug resistance. J Exp Clin Cancer Res 2018; 37: 1–12.
18. Lai BFL, Lu RXZ, Hu Y, et al. Recapitulating Pancreatic Tumor Microenvironment through Synergistic Use of Patient Organoids and Organ-on-a-Chip Vasculature. Adv Funct Mater 2020; 2000545.
19. Giuntoli G, Muzio G, Actis C, et al. In-vitro Characterization of a Hernia Mesh Featuring a Nanostructured Coating. Front Bioeng Biotechnol; 8. Epub ahead of print 20 January 2021. DOI: 10.3389/FBIOE.2020.589223/FULL.
20. Licciardello M, Ciardelli G, Tonda-Turo C. Biocompatible Electrospun Polycaprolactone-Polyaniline Scaffold Treated with Atmospheric Plasma to Improve Hydrophilicity. Bioengineering 2021; 8: 1–18.
21. Licciardello M, Tonda-Turo C, Gallina A, et al. Fabrication of extracellular matrix-like membranes for loading piezoelectric nanoparticles. J Phys Mater 2020; 3: 034004.
22. Tonda-Turo C, Cipriani E, Gnavi S, et al. Crosslinked gelatin nanofibres: Preparation, characterisation and in vitro studies using glial-like cells. Mater Sci Eng C 2013; 33: 2723–2735.
23. Gautam S, Dinda AK, Mishra NC. Fabrication and characterization of PCL/gelatin composite nanofibrous scaffold for tissue engineering applications by electrospinning method. Mater Sci Eng C 2013; 33: 1228–1235.
24. Denis P, Dulnik J, Sajkiewicz P. Electrospinning and Structure of Bicomponent Polycaprolactone/Gelatin Nanofibers Obtained Using Alternative Solvent System. http://dx.doi.org/101080/009140372014945208 2014; 64: 354–364.
25. Binulal NS, Natarajan A, Menon D, et al. PCL–gelatin composite nanofibers electrospun using diluted acetic acid–ethyl acetate solvent system for stem cell-based bone tissue engineering. http://dx.doi.org/101080/092050632013859872 2014; 25: 325–340.
26. Gil-Castell O, Badia JD, Strömberg E, et al. Effect of the dissolution time into an acid hydrolytic solvent to tailor electrospun nanofibrous polycaprolactone scaffolds. Eur Polym J 2017; 87: 174–187.

27. Mahony O, Tsigkou O, Ionescu C, et al. Hybrid Materials: Silica-Gelatin Hybrids with Tailorable Degradation and Mechanical Properties for Tissue Regeneration (Adv. Funct. Mater. 22/2010). Adv Funct Mater 2010; 20: 3808–3808.
28. Li K, Liu T, Chen J, et al. Survivin in breast cancer-derived exosomes activates fibroblasts by up-regulating SOD1, whose feedback promotes cancer proliferation and metastasis. J Biol Chem 2020; 295: 13737–13752.
29. Guo X, Oshima H, Kitmura T, et al. Stromal fibroblasts activated by tumor cells promote angiogenesis in mouse gastric cancer. J Biol Chem 2008; 283: 19864–19871.
30. Cheng C, Yan K-K, Hwang W, et al. Construction and Analysis of an Integrated Regulatory Network Derived from High-Throughput Sequencing Data. PLOS Comput Biol 2011; 7: e1002190.
31. Cai J, Tang H, Xu L, et al. Fibroblasts in omentum activated by tumor cells promote ovarian cancer growth, adhesion and invasiveness. Carcinogenesis 2012; 33: 20–29.
32. Omary MB, Lugea A, Lowe AW, et al. The pancreatic stellate cell: A star on the rise in pancreatic diseases. Journal of Clinical Investigation 2007; 117: 50–59.
33. Buchholz Hans Kestler Karlheinz Holzmann Volker Ellenrieder Wilhelm Schneiderhan Marco Siech Guido Adler Max G Bachem Thomas M Gress MA. Transcriptome analysis of human hepatic and pancreatic stellate cells: organ-specific variations of a common transcriptional phenotype. J Mol Med 2005; 83: 795–805.
34. Ohuchida K, Mizumoto K, Murakami M, et al. Radiation to Stromal Fibroblasts Increases Invasiveness of Pancreatic Cancer Cells through Tumor-Stromal Interactions. Cancer Res 2004; 64: 3215–3222.
35. Damhofer H, Medema JP, Veenstra VL, et al. Assessment of the stromal contribution to Sonic Hedgehog-dependent pancreatic adenocarcinoma mRNA-Seq. Epub ahead of print 2013. DOI: 10.1016/j.molonc.2013.08.004.
36. Majety M, Pradel LP, Gies M, et al. Fibroblasts Influence Survival and Therapeutic Response in a 3D Co-Culture Model. Epub ahead of print 2015. DOI: 10.1371/journal.pone.0127948.
37. Monteiro M V, Ferreira LP, Rocha M, et al. Journal Pre-proof Advances in bioengineering pancreatic tumor-stroma physiomimetic Biomodels. Biomaterials. Epub ahead of print 2022. DOI: 10.1016/j.biomaterials.2022.121653.
38. Ji Z, Mei FC, Xie J, et al. Oncogenic KRAS activates hedgehog signaling pathway in pancreatic cancer cells. J Biol Chem 2007; 282: 14048–14055.
39. Brentnall TA, Lai LA, Coleman J, et al. Arousal of Cancer-Associated Stroma: Overexpression of Palladin Activates Fibroblasts to Promote Tumor Invasion. PLoS One; 7. Epub ahead of print 23 January 2012. DOI: 10.1371/JOURNAL.PONE.0030219.
40. Zhou H, Qin Y, Ji S, et al. SOX9 activity is induced by oncogenic Kras to affect MDC1 and MCMs expression in pancreatic cancer. Oncogene 2018 377 2017; 37: 912–923.
41. Apte M V., Wilson JS, Lugea A, et al. A starring role for stellate cells in the pancreatic cancer microenvironment. Gastroenterology 2013; 144: 1210–1219.
42. Pandiri AR. Overview of exocrine pancreatic pathobiology. Toxicol Pathol 2014; 42: 207–216.
43. Fu Y, Liu S, Zeng S, et al. The critical roles of activated stellate cells-mediated paracrine signaling, metabolism and onco-immunology in pancreatic ductal adenocarcinoma. Molecular Cancer; 17. Epub ahead of print 19 February 2018. DOI: 10.1186/s12943-018-0815-z.
44. Yan Z, Ohuchida K, Fei S, et al. Inhibition of ERK1 / 2 in cancer-associated pancreatic stellate cells suppresses cancer – stromal interaction and metastasis. 2019; 8: 1–16.

45. Chen ST, Kuo TC, Liao YY, et al. Silencing of MUC20 suppresses the malignant character of pancreatic ductal adenocarcinoma cells through inhibition of the HGF/MET pathway. Oncogene 2018; 37: 6041–6053.
46. Heinrich MA, Mostafa AMRH, Morton JP, et al. Translating complexity and heterogeneity of pancreatic tumor: 3D in vitro to in vivo models. Advanced Drug Delivery Reviews 2021; 174: 265–293.
47. Lee JH, Kim SK, Khawar IA, et al. Microfluidic co-culture of pancreatic tumor spheroids with stellate cells as a novel 3D model for investigation of stroma-mediated cell motility and drug resistance. J Exp Clin Cancer Res 2018; 37: 1–12.
48. Jeong SY, Lee JH, Shin Y, et al. Co-culture of tumor spheroids and fibroblasts in a collagen matrix-incorporated microfluidic chip mimics reciprocal activation in solid tumor microenvironment. PLoS One 2016; 11: e0159013.
49. Fujiwara M, Kanayama K, Hirokawa YS, et al. ASF-4-1 fibroblast-rich culture increases chemoresistance and mTOR expression of pancreatic cancer BxPC-3 cells at the invasive front in vitro, and promotes tumor growth and invasion in vivo. Oncol Lett 2016; 11: 2773.
50. Wang P, Zhu Z. Prognostic and Clinicopathological Significance of E-Cadherin in Pancreatic Cancer Patients: A Meta-Analysis. Front Oncol 2021; 11: 938.
51. Golan T, Atias D, Barshack I, et al. Ascites-derived pancreatic ductal adenocarcinoma primary cell cultures as a platform for personalised medicine. Br J Cancer 2014 1109 2014; 110: 2269–2276.
52. Shields MA, Dangi-Garimella S, Krantz SB, et al. Pancreatic Cancer Cells Respond to Type I Collagen by Inducing Snail Expression to Promote Membrane Type 1 Matrix Metalloproteinase-dependent Collagen Invasion. J Biol Chem 2011; 286: 10495.
53. Bott K, Upton Z, Schrobback K, et al. The effect of matrix characteristics on fibroblast proliferation in 3D gels. Biomaterials 2010; 31: 8454–8464.
54. Tabatabaei F, Moharamzadeh K, Tayebi L. Fibroblast encapsulation in gelatin methacryloyl (GelMA) versus collagen hydrogel as substrates for oral mucosa tissue engineering. J Oral Biol Craniofacial Res 2020; 10: 573–577.
55. Baena JM, Jiménez G, López-Ruiz E, et al. Volume-by-volume bioprinting of chondrocytes-alginate bioinks in high temperature thermoplastic scaffolds for cartilage regeneration. Exp Biol Med 2019; 244: 13–21.
56. Hwang HJ, Oh MS, Lee DW, et al. Multiplex quantitative analysis of stroma-mediated cancer cell invasion, matrix remodeling, and drug response in a 3D co-culture model of pancreatic tumor spheroids and stellate cells. J Exp Clin Cancer Res; 38. Epub ahead of print 14 June 2019. DOI: 10.1186/S13046-019-1225-9.
57. Li J, Chen B, Fellows GF, et al. Activation of Pancreatic Stellate Cells Is Beneficial for Exocrine but Not Endocrine Cell Differentiation in the Developing Human Pancreas. Front Cell Dev Biol 2021; 9: 1769.
58. Paoli C, Carrer A. Organotypic Culture of Acinar Cells for the Study of Pancreatic Cancer Initiation. Cancers (Basel) 2020; 12: 1–22.
59. Cantara SI, Soscia DA, Sequeira SJ, et al. Selective functionalization of nanofiber scaffolds to regulate salivary gland epithelial cell proliferation and polarity. Biomaterials 2012; 33: 8372–8382.
60. Buscemi S, Damiano G, Fazzotta S, et al. Electrospun Polyhydroxyethyl-Aspartamide–Polylactic Acid Scaffold for Biliary Duct Repair: A Preliminary In Vivo Evaluation. Transplant Proc 2017; 49: 711–715.

61. Nelson MT, Short A, Cole SL, et al. Preferential, enhanced breast cancer cell migration on biomimetic electrospun nanofiber 'cell highways'. BMC Cancer 2014; 14: 1–16.
62. Leong MF, Chian KS, Mhaisalkar PS, et al. Effect of electrospun poly(D,L-lactide) fibrous scaffold with nanoporous surface on attachment of porcine esophageal epithelial cells and protein adsorption. J Biomed Mater Res Part A 2009; 89A: 1040–1048.
63. Burton TP, Corcoran A, Callanan A. The effect of electrospun polycaprolactone scaffold morphology on human kidney epithelial cells. Biomed Mater 2017; 13: 015006.
64. Mendle JH, Kelly J, Voci S, et al. Bortezomib and gemcitabine in relapsed or refractory Hodgkin's lymphoma. Ann Oncol 2008; 19: 1759.

Chapter III

3D models

Abstract

Pancreatic ductal adenocarcinoma (PDAC) is the most frequent type of pancreatic cancer, one of the leading causes of cancer-related deaths worldwide. PDAC is marked by a dense, fibrous tumor microenvironment, in which stromal fibroblasts surround the cancerous ductal epithelial cells. The crosstalk between pancreatic epithelial cells and the surrounding fibroblasts leads to inflammation and stiffening of the surrounding tissue, which is believed to hinder anti-cancer drugs' uptake and effectiveness. *In vitro*, fully human models of the pancreatic cancer microenvironment are needed to foster the development of new, more effective therapies; but it is still challenging to make these models anatomically and functionally relevant. This chapter describes the exploitation of two different technical approaches (*i.e.*, layer-by-layer techniques and tomographic volumetric bioprinting) to reproduce the typical gland morphology of the functional unit of exocrine pancreas. In particular, fused deposition modeling (FDM) and melt electrowriting (MEW) have been employed to model *in vitro* the half structure of the pancreatic acino-ductal unit, while the volumetric bioprinting (VBP) was used to fabricate cell-laden viable constructs with complete anatomically relevant geometry. Human fibroblasts (HFF1) were seeded inside the layer-by-layer scaffolds, produced by processing polycaprolactone (PCL) through FDM and MEW, to obtain 3D stromal models at different length scales. In VBP model, HFF1 were embedded in a gelatin methacrylate (GelMA) hydrogel. Then, human pancreatic ductal epithelial (HPDE) cells, wild type or cancerous, were seeded into MEW and VBP constructs to build fully human models mimicking the PDAC-stromal cells relationship. The feasibility of reproducing the glandular structure by using an extrusion-based technique and the VBP was assessed. The viability of fibroblasts seeded into the different 3D structures was confirmed. Finally, the effect of the interplay between fibroblasts and pancreatic ductal cells on fibroblasts behavior was investigated in the MEW and VBP models by immunostaining and biochemical assays.
The results described in this chapter suggest that these models could potentially be used in drug development or to shed light on the early progression of the disease.

3.1 Introduction

For many years cancer research has been based on the use of two-dimensional cell cultures that poorly recapitulate the biological complexity of the disease. Recently, more representative preclinical *in vitro* models have been investigated, leading to the development of three-dimensional (3D) culture systems, which better mimic tumor *in vivo* conditions and allow a deeper understanding of PDAC physiopathology. However, only a few novel studies in literature focus on the development of biomimetic platforms reproducing the microanatomy (in terms of 3D architecture and cellular composition) of the exocrine pancreas and lack to resemble the native compartmentalized architecture of tumor microenvironment that is widely recognized to affect cell functionality and cancer-cell response to therapeutics[1–3]. In particular, the glandular complex geometry has been reproduced in simplified ways by employing different techniques[4–7], that have disadvantages such as the low reproducibility, throughput and shape fidelity.
This chapter focuses on the engineering strategies adopted to develop three different 3D *in vitro* models that resemble the functional unit of exocrine pancreas. The additive manufacturing techniques used in this work can be grouped into layer-by-layer approaches and tomographic volumetric bioprinting.

Specifically, fused deposition modeling (FDM) and melt electrowriting (MEW) have been employed to model *in vitro* the half structure of the pancreatic acino-ductal unit (Fig. 3.1). In detail, FDM and MEW are bottom up and rapid prototyping techniques consisting in the precise and controlled layer-by-layer deposition of a thermoplastic polymer which is melt and extruded through a nozzle[8,9]. While in FDM process the distance between nozzle and collector is minimal (*i.e.*, a few hundreds of microns), melt electrowriting can be defined as a contactless 3D printing technique due to the higher distance between needle and print bed. Indeed, this technology combines principles of conventional electrospinning (solution electrospinning) with melt extrusion-based methods. Like solution electrospinning, a high voltage (HV) is applied between the nozzle and the collector to exert an electrostatic attraction on the molten material, and a so-called Taylor cone forms at the nozzle tip. The electrical field forces the formation of a microscale polymer filament from the Taylor cone, which is deposited into a micrometer fiber on the collector[10,11]. Due to the distance between nozzle and platform and the fiber stretching induced by the electric field, the size of the extruded filament in MEW is about ten times lower than the filament diameter in FDM[12], resulting in a better resolution of the printed structures. Thus, macro- and microscale polycaprolactone (PCL) scaffolds mimicking the half structure of the exocrine pancreatic functional unit were respectively obtained by FDM and MEW (Fig. 3.1a-c). In particular, the FDM and MEW scaffolds were seeded with stromal cells (human fibroblasts) to obtain 3D stromal models (Fig. 3.1d_i). FDM scaffolds were treated by an atmospheric plasma before cell seeding to favor the fibroblasts adhesion and penetration within the PCL scaffold (Fig. 3.1b). Indeed, plasma induces the formation of surface radicals as a result of the breakage of covalent bonds contained in the polymer chains. The free radicals react with the ions contained in the gas plasma, giving rise to polar groups on the polymer surfaces, that increase their wettability[13,14].

Because of the better resolution of MEW structures and the easiest seeding protocol which does not require a pre-treatment of the scaffold surface through plasma, the implementation of co-culture conditions by seeding human pancreatic ductal epithelial cells (HPDE) was carried out only in MEW scaffolds, as they allow to achieve a good resolution and biomimicry in terms of both morphological and biological features (Fig. 3.1d_{ii}). The idea is to obtain the complete acino-ductal model (close structure) by assembling the two halves into the final 3D hollow structure under microscope guidance to guarantee the right cell-cell interaction at the interface (Fig. 3.1e). However, this further step is technically difficult and requires precise manual procedures. Therefore, achieving the final assembled model could reveal time-consuming and poorly repeatable.

These limitations can be overcome by the use of volumetric bioprinting (VBP) which represents an emerging light-based technology capable of fabricating 3D constructs with high-resolution and complex geometries rapidly[15–18]. Indeed, this technique permits to print hollow structures without the need for support and in a very short building time (down to a few tens of seconds compared to tens of minutes for layer-by-layer approaches)[16]. Furthermore, one of the main advantages of VBP is the cell-friendly procedure lying in the one-step manufacturing process which reduces the stress experienced by cells as compared to other multistep techniques such as the common solvent-casting method[19]. More specifically, VBP consists of illuminating a photosensitive cell-laden hydrogel with visible light from multiple angles, using a sequence of tomographic back projections of the desired object[20–22], leading to the photopolymerization of the material.

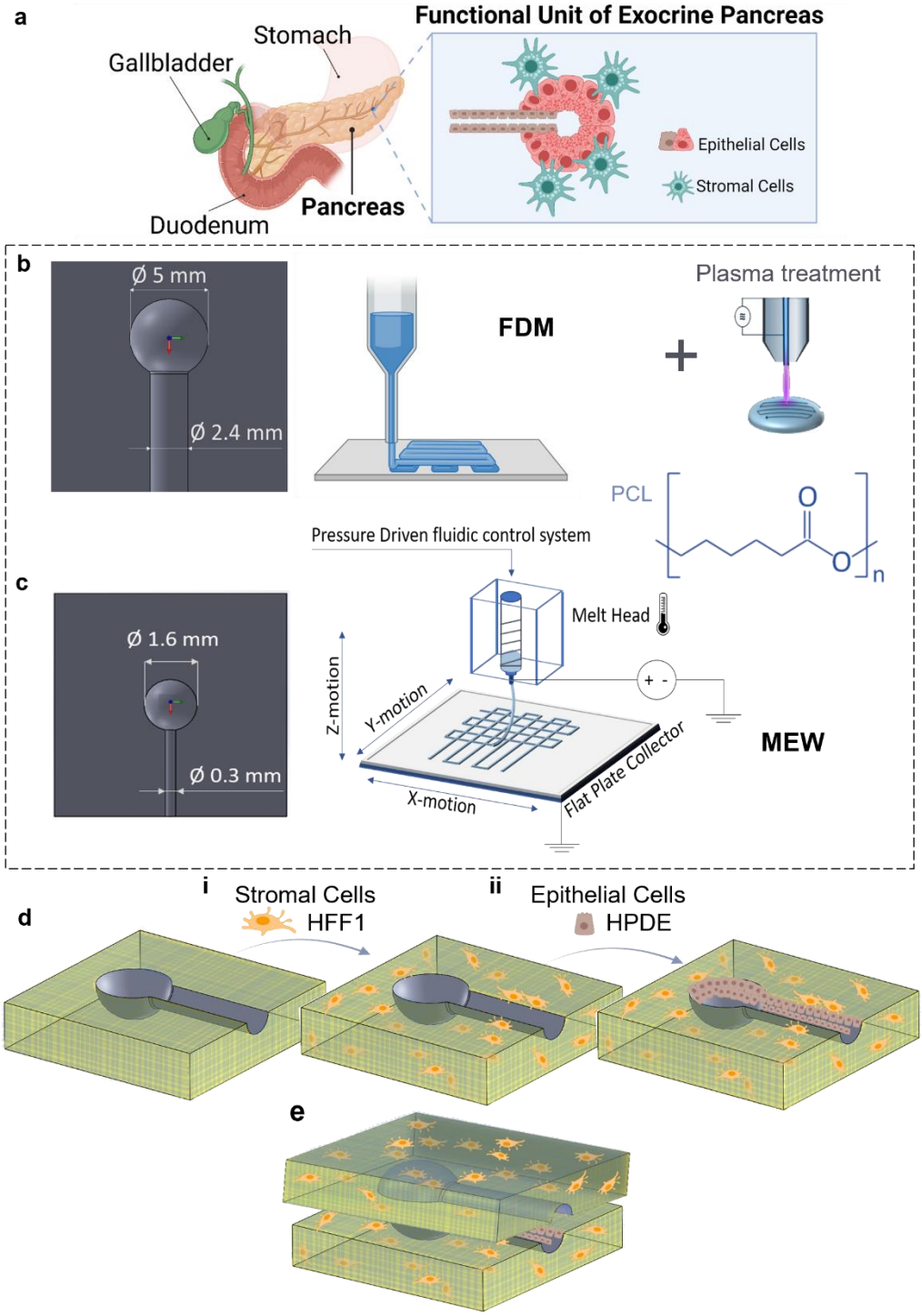

Fig. 3.1 3D layer-by-layer models. (a) Illustration of the functional unit of exocrine pancreas, composed by epithelial cells surrounded by stromal cells. (b-c) The FDM (b) and MEW (c) approaches were employed by starting from CAD drawings and processing polycaprolactone (PCL) to finally obtain macro- and microscale *in vitro* models, respectively. A surface plasma treatment was applied to FDM scaffolds in order to enhance cell penetration. (d) The FDM and MEW scaffolds were then cellularized by seeding human fibroblasts and epithelial cells. (e) Two halves assembling to obtain the complete model (close structure).

In this doctoral thesis project, VBP was adopted to develop a fully human 3D *in vitro* model resembling the physiological acinar- and ductal-like structure of the pancreatic gland (Fig. 3.2). In particular, a gelatin methacrylate hydrogel (GelMA) has been *ad hoc* prepared and loaded with human fibroblasts to mimic the stromal compartment. Numerous fibroblast-laden structures were fabricated by VBP (Fig. 3.2a). Then, healthy HPDE cells (HPDE-wt) or stably expressing the KRAS oncogene (HPDE-KRAS) were introduced inside the construct's cavity and co-culture was monitored overtime (Fig. 3.2b). The tumor-stroma crosstalk effect was analyzed measuring the appearance of a myofibroblast-like phenotype by quantifying expression of alpha-smooth muscle actin (α-SMA) proteins in fibroblasts (Fig. 3.2c).

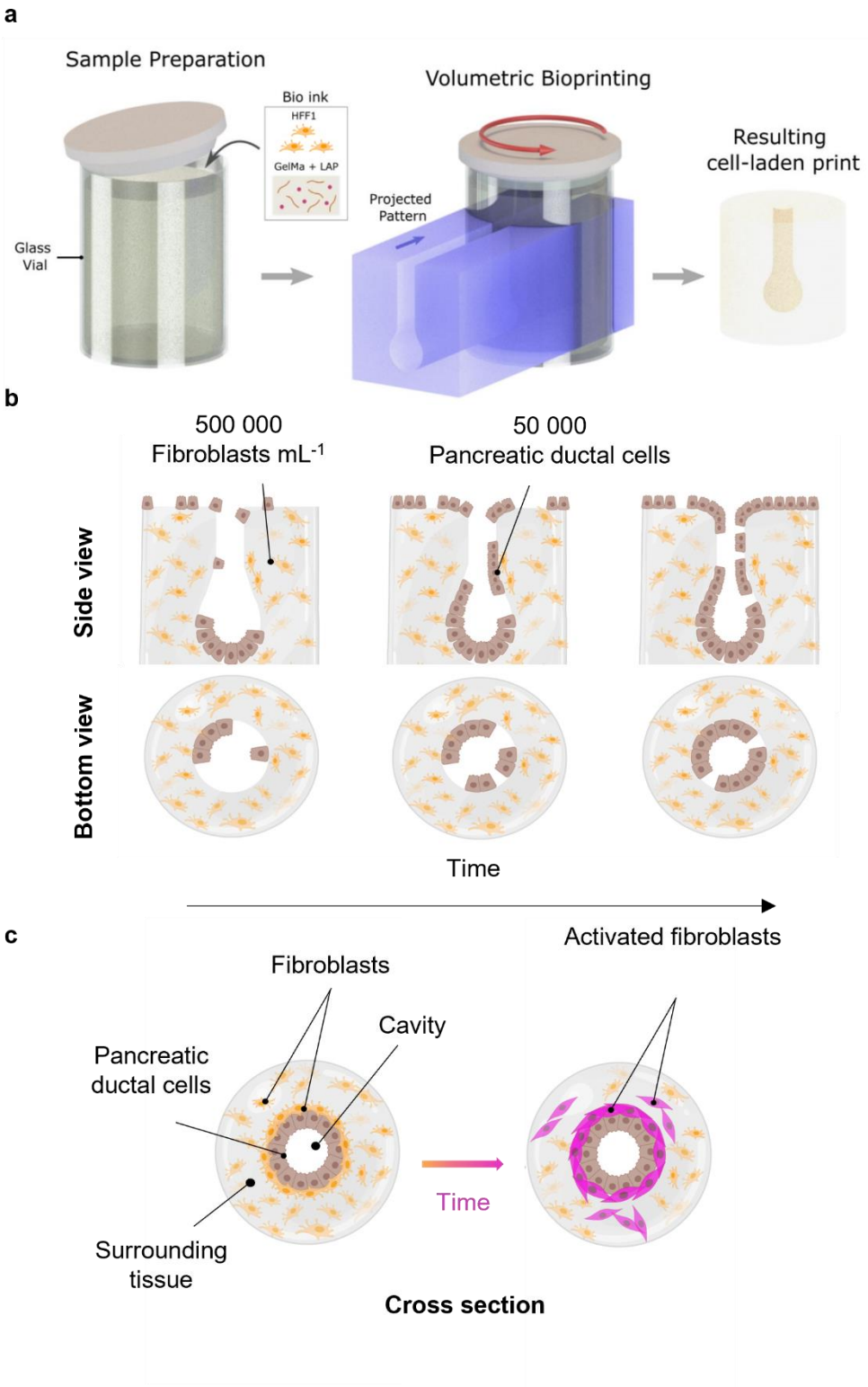

Fig. 3.2. Experimental pipeline for VBP models. (a) Schematic representation of volumetric bioprinting process. (b) Human pancreatic ductal epithelial cells were injected into fibroblast-laden bioprinted constructs, where they attached and coated the inner surface of the duct with time. (c) To recapitulate fibroblast-associated activation, the interaction between HPDE-KRAS and the surrounding fibroblasts was monitored by measuring the expression of α-SMA versus actin in the cytoskeletons of the latter. (Figure drawn using Biorender.com).

3.2 Layer-by-layer approaches

3.2.1 Experimental Section

3.2.1.1 Cell culture

Human pancreatic ductal epithelial cells (HPDE) stably expressing activated KRAS (HPDE-KRAS) and wild-type HPDE (HPDE-wt) were kindly provided by Prof. F. Bussolino and cultured in RPMI-1640 medium (Gibco) supplemented with 1% Penicillin-Streptomycin (Gibco), 1% L-glutamine (Gibco) and 10% fetal bovine serum (FBS) (Gibco). Human foreskin fibroblasts (HFF1) cells were obtained from ATCC® and cultured in Dulbecco's Modified Eagle's Medium (DMEM) supplemented with 1% Penicillin-Streptomycin (Gibco), 2% L-glutamine (Gibco) and 15% FBS (Gibco). Cell lines were maintained in a humidified CO_2 incubator at 37 °C and 5% CO_2.

3.2.1.2 Scaffold design and fabrication by fused deposition modeling (FDM)

The 3D FDM model was firstly designed by SolidWorks® CAD software (Dassault Systèmes) to reproduce the physiological glandular structure typical of the functional unit of exocrine pancreas (Fig. 3.1a). With this aim, a 15 x 15 x 5.2 mm^3 cuboid was drawn, with a central section constituted by a hollow hemisphere having 5 mm diameter connected to a hollow duct with a diameter of 2.40 mm (Fig. 3.1b).
Polycaprolactone (PCL, Mw ~ 43000 Da) pellets (Polysciences Inc, 19561-500) were processed by fused deposition modeling (FDM) to fabricate the scaffold. Specifically, ROKIT INVIVO 3D bioprinter (ROKIT InVivo, Rokit Healthcare) was employed for PCL scaffolds fabrication, using a 0.2 mm diameter nozzle and a petri dish as print support. In particular, the 3D CAD model was transformed to an .stl file, which was then sliced through the NewCreatorK software (Rokit Healthcare) to obtain a G-code. The G-code was also modified to introduce a pause after the deposition of each layer, an essential condition for allowing the polymer solidification and preventing the flattening of the printed filament. In addition, Repetier-Host software (Hot-World GmbH & Co) was used to visualize the layer-by-layer print preview and the XY moves of the platform. The fabrication process was optimized to achieve high pore interconnectivity, accuracy in geometry and precise control of pore size. Particularly, the control of printing parameters such as processing temperature, applied voltage, collector distance, printing speed, fill density and applied pressure, played a key role in the development of the complex exocrine glandular structure. Table 3.1 lists the parameters tested in the FDM process.

Table 3.1 – Process parameters used to fabricate the FDM scaffolds.

Nozzle size [mm]	0.2
Layer height [mm]	[0.1, 0.2]
Fill density [%]	[35, 45]
Infill rotate angle	[30°, 45°, 90°]
Printing Speed [mm/s]	[10, 15, 20]
Retraction Speed [mm/s]	[20, 25, 30]
Printing Temperature [°C]	[120, 130]
Pressure [kPa]	[450 ± 10, 530 ± 10, 560 ± 10]
Platform Temperature [°C]	[15, 20, 25]

3.2.1.3 Plasma surface modification of FDM scaffold

The surface modification of PCL scaffolds, fabricated by FDM, was performed using an atmospheric plasma jet device (Stylus Plasma Noble, Nadir). The use of argon as process gas determines the formation of oxygen-containing functional groups on the PCL surface. The process parameters were optimized to avoid the degradation and morphological alterations of the samples. Specifically, plasma was maintained for 30 seconds on the top surface of each scaffold with an argon flow at 2 bar and a cooling nitrogen flow at 2 bar. The following parameters have been set: 11 kV peak-to-peak voltage (Vpp), flow rate between 7 and 8 l/min, and 10 W radio frequency power.

3.2.1.4. Optical microscopy and SEM analyses of FDM structures

The morphological investigation of FDM scaffolds was carried out to examine the architecture of the 3D printed constructs, in terms of geometry, pore interconnectivity and pore size. The analysis was performed by using a stereo microscope (Leica, M205 A) and a scanning electron microscope (SEM, Tescan Vega). Before analysis, all the samples were coated with a thin platinum layer. Some of the samples were frozen and then cut with a blade to enable the image acquisition from the cross-sectional view. Images were visualized using ImageJ[23] software.

3.2.1.5. Water contact angle analysis on FDM constructs

The wettability of PCL structures was quantified by performing the static water contact angle (WCA) analysis on the surface of the printed models. Particularly, the effectiveness of the plasma exposure has been verified by comparing the contact angle values and the absorption rate of the water droplets deposited on treated and untreated samples. The analysis was conducted by using the Drop Shape Analyzer apparatus equipped with Advance software (Krüss Gmbh) for data acquisition. Measurements were performed by depositing a 2 µl water drop on the sample surface and the WCA measurements were recorded using the ellipse fitting method of the data acquisition software. Considering the size of the scaffold, the measures have been repeated for three different regions of the same sample. Three individual experiments were carried out per condition (plasma treated and untreated). All the obtained data were then exported and elaborated using GraphPad Prism 9.3.1.

3.2.1.6 Scaffold design and fabrication by melt electrowriting (MEW)

The 3D MEW models were designed through SolidWorks® CAD software. The CAD models consist of a square-based 3D structure with a central cavity (Fig. 3.1c). The cuboid final dimensions were set at 10 mm length, 10 mm width and 2.5 mm thickness. Different cavity geometries were also tested focusing on the acinus shape. Specifically hemispherical and cylindrical hollow structures on the top of the cuboid were examined. In detail, cavity diameters ranging from 1 mm to 3 mm were tested for both the hemisphere and the cylinder, and depths from 1 mm to 2 mm were analyzed for the cylinder. CAD models were discretized into triangles and .stl files were thus generated. Then, the G-codes were obtained using the Ultimaker Cura 4.8.0 software by setting the parameters needed to perform the slicing and later optimized using the Repetier-Host and NC Viewer v1.1.3 software. Specifically, the automated g-codes, generated by the .stl files slicing, were further edited to (i) prevent the needle from passing over the scaffold between one layer and the next, depositing undesired fibers and (ii) to

implement an additional extrusion step at the initial phase of the printing process, in order to stabilize the jet.

NovaSpider v5 instrument (CIC nanoGUNE) was employed to fabricate PCL (Polysciences Inc, 19561-500, Mw ~ 43000 Da) scaffolds by melt electrowriting. To achieve a printed structure with proper filament diameter, pore size, and shape fidelity, several process parameters were tested, by varying their values in the ranges shown in Table 3.2. Ambient parameters (*i.e.*, chamber temperature and humidity) were set at 27.5°C ± 3 and 44% ± 2, respectively. In detail, the humidity was monitored and controlled by an external humidifier (miniClima Humidity Control) connected to the NovaSpider apparatus.

3.2.1.7 Dimensional analyses of MEW scaffolds

The effect of parameters tuning on printed scaffold resolution was evaluated by scanning electron microscopy (Tescan Vega) of MEW scaffolds.

Table 3.2 – Process parameters used to fabricate the MEW scaffolds.

Nozzle size [mm]	[0.3, 0.5]
Flow [%]	[20 - 40]
Infill line distance [µm]	[80 - 111]
Infill rotate angle	[45°, 90°]
Speed [mm/s]	[40 - 90]
Distance [mm]	[6 - 12]
Printing Temperature [°C]	[90 - 130]
Voltage [kV]	[5 - 7]

Before analysis, all the samples were coated with a thin platinum layer. SEM images were then analyzed using ImageJ[23], quantifying the fibers average size. In detail, two scaffolds per condition were examined, measuring 40 values for each scaffold.

3.2.1.8 Seeding of stromal cells in FDM and MEW constructs

The layer-by-layer models (*i.e.*, FDM and MEW constructs) were firstly incubated in a 70% ethanol with 30% water solution overnight and then irradiated with UV light for 1 hour (30 min each side) as sterilization process before cell seeding.

The FDM scaffolds were functionalized by plasma surface modification after the incubation in ethanol solution to avoid possible interactions between alcohol groups and the oxygen-containing polar groups[24]. HFF1 were seeded in the FDM structures (15 x 15 x 5.2 mm^3) at a density of 750 × 10^3 cells/ml by pipetting 300 µl of medium with cells on the top of the scaffolds, in the space around the cavity. The cellularized scaffolds, placed in a 12-well plate, were then kept in incubator for about 1 hour to enhance attachment of cells to the PCL fibers. Successively, each well was filled with 1 ml culture medium and returned to the incubator.

Human fibroblasts were seeded in sterile MEW scaffolds placed in a 48-well plate. In particular, 1.6 x 10^6 cells/ml were seeded on MEW constructs by pipetting 40 µl of medium with HFF1 on the top of the

scaffolds. The cell number seeded on MEW structures was selected by considering the differences with FDM scaffolds, in terms of constructs size.
The constructs were maintained at 37 °C and 5% CO_2 for 1 hour before adding 600 µl of medium in each well.

3.2.1.9 Viability of stromal cells in FDM and MEW models

The viability of human fibroblasts (HFF1) cultured in the FDM and MEW constructs was analyzed by monitoring the metabolic activity through the fluorimetric resazurin reduction method (CellTiter-Blue, Promega, G8080) 3, 7, 14, and 21 days after seeding. A further time point at 28 days after seeding was considered for the MEW constructs, where culture has been carried out for 4 weeks. The test was performed according to the manufacturers' protocols. Briefly, culture medium was carefully removed and constructs were washed with 1x phosphate-buffered saline (PBS; Gibco). A solution of 16% CellTiter-Blue in complete cell culture medium was prepared and added to the constructs, followed by 3-4 h incubation at 37 °C. At the end of the incubation period, 100 µl of the medium was pipetted into different wells of a 96-well plate, and fluorescence was measured from the bottom of the plate using a plate reader (Synergy HTX Multi-Mode Reader, BioTek) at 530 nm excitation and 590 nm emission. All the obtained data were then exported and elaborated using GraphPad Prism 9.3.1.

3.2.1.10 Stromal cells distribution within the FDM and MEW scaffolds: confocal microscopy and SEM analyses

Fluorescence imaging was carried out to analyze the distribution of human fibroblasts seeded within the 3D layer-by-layer constructs at the initial stage of culture period. The cellularized scaffolds were washed once with 1x PBS and fixed with 4% paraformaldehyde (PFA; Sigma Aldrich) for 30 min at room temperature (RT), after 72h in culture. They were then washed twice with 1x PBS, permeabilized in 0.5% Triton X-100 (Sigma Aldrich) in 1x PBS for 10 min and incubated with 1% bovine serum albumin (BSA; Invitrogen) for 30 min to improve the staining. The cytoskeletons of HFF1 seeded in FDM and MEW scaffolds were stained with Rhodamine Phalloidin (Invitrogen, R415) at 1:400 concentration in solution of 1x PBS with 1% BSA and Alexa Fluor™ 488 Phalloidin (Invitrogen, A12379) at 1:60 concentration in solution of 1x PBS with 1% BSA, respectively. Nuclei were visualized with DAPI reagent (4',6-Diamidino-2-Phenylindole, Dihydrochloride; Invitrogen, D1306) at 1:1000 concentration in 1x PBS solution. All samples were then imaged by confocal microscopy (Eclipse Ti2, Nikon). The resulting images were post-processed with ImageJ software.

The SEM analyses were performed upon dehydration of fixed fibroblasts within the scaffolds. Samples were dehydrated by soaking them into ethanol/water solutions starting from 30/70 up to 100/0. Before analysis, all the samples were coated with a thin platinum layer. Because of the centimeter-scale dimensions, the FDM scaffolds were sliced both orthogonally and in parallel to the z axis to facilitate the SEM analysis at different magnifications.

3.2.1.11 Epithelization of the cavity in MEW model

HPDE-KRAS and HPDE-wt cells were detached from the culture flask, counted and resuspended to a 10 µl volume. Then, cells were manually injected with micropipette into the cavity of the cellularized

MEW scaffold, where HFF1 were allowed to grow for 2 weeks. The co-cultured constructs were placed in a 48-well plate.
The cell ratio between HPDE cells and HFF1 was fixed at 1:3, in accordance with studies reporting the relevancy that ratios of 1:1 to 1:3 have *in vivo*[25–27]. Co-cultures were maintained in DMEM/F-12 supplemented with 15% FBS (Gibco), 1% Penicillin-Streptomycin (Gibco) and 2% L-glutamine (Gibco) since previous tests demonstrated the efficacy of this culture medium composition in promoting the cell viability (see 2.2 Two-dimensional model; 2.2.2 Results). One hour later, 600 µl medium was added to the wells, covering the full constructs. The cellularized structures were maintained in a humidified CO_2 incubator at 37 °C and 5% CO_2.

3.2.1.12 Immunocytochemistry and confocal microscopy

The co-cultured MEW constructs were fixed with 4% paraformaldehyde (PFA; Sigma Aldrich) for 30 min at room temperature, after 3d, 7d, 10d and 14d of co-culture. They were then rinsed with PBS twice and kept at 4°C. Each sample was then permeabilized with 0.2% Triton X-100 in PBS for 10 minutes at RT and successively washed 3 times for 5 minutes with PBS + 0.1% Tween 20 (PBST) at RT.
Then, samples were blocked with 2% bovine serum albumin (BSA) in PBST for 60 minutes and rinsed three times with PBST. Primary antibodies, Alpha-Smooth Muscle Actin Recombinant Rabbit Monoclonal Antibody (Invitrogen, 701457 100 µg, 1:200), and E-cadherin Monoclonal Antibody (HECD-1) (Invitrogen, 13-1700, 1:2000) in PBST + 1% BSA were incubated for 24h at 4°C. Samples were then rinsed 3 times with PBST at RT for 5 minutes. The secondary antibodies, Cyanine5 conjugated goat anti-mouse secondary antibody (Invitrogen, A10524) and Alexa Fluor™ 555 conjugated goat anti-rabbit secondary antibody (Invitrogen, A27017), were respectively incubated at a concentration of 1:200 and 1:500 in PBST + 1% BSA for 2h at RT. Samples were rinsed with PBST for 5 minutes at RT 3 times. The cytoskeletons of HFF1 and HPDE cells seeded in MEW scaffolds were then stained with Alexa Fluor™ 488 Phalloidin (Invitrogen, A12379) at 1:60 concentration in solution of 1x PBS with 1% BSA. Samples were rinsed with PBS for 5 minutes at RT 3 times, before the staining with DAPI (Invitrogen, D1306) in PBS (1:1000) for 5 minutes at RT.
They were then washed once with PBS, and finally mounted on glass coverslips using Fluoromount™ Aqueous Mounting Medium (Invitrogen, 00-4958-02) for imaging. All samples were then imaged by confocal microscopy (Eclipse Ti2, Nikon). The resulting images were post-processed and analyzed with ImageJ software. In particular, the fluorescence intensity (mean gray values along z-axis) corresponding to the E-cadherin signal was analyzed in z-stack acquisitions and plotted to compare the epithelial cells distributions at different time points of culture period.
The fluorescence intensity values were normalized to the minimum value measured by the software for each sample.

3.2.1.13 Interleukin-6 (IL-6) cytokines release in MEW model

Cytokines' concentration was determined in cell supernatants that were collected, after 48h, 72h, 10d and 14d from HPDE cells seeding, from the wells containing the MEW scaffolds co-cultured with HFF1, HFF1+HPDE-WT and HFF1+HPDE-KRAS cells. IL-6 cytokines were quantified with the IL-6 Human ELISA Kit (Invitrogen, BMS213-2). The concentrations were calculated using the standard curve generated by plotting the absorbance values of each standard sample on the ordinate and the human IL-6 standard concentrations on the abscissa.

3.2.1.14 Statistical Analysis

All bar graph data are presented as the mean ± standard deviation (SD) for at least three independent experiments per condition or time point. Significance was measured as indicated for each experiment, with two-way or one-way ANOVA followed by pairwise comparison with Tukey's multiple comparisons test using GraphPad Prism 9.3.1; *p < 0.05, **p < 0.01, ***p < 0.001, ****p < 0.0001.

3.2.2 Results

3.2.2.1 Fabrication of acino-ductal structures by FDM

PCL scaffolds were fabricated by fused deposition modeling (FDM), tuning the process parameters to obtain a valuable and repeatable printing protocol. In particular, the manufacturing was optimized to obtain structures with high pore interconnectivity, suitable pore size and enhanced geometrical accuracy (Fig. 3.3).
Indeed, these features represent key requirements to achieve a good cell growth and tissue formation within the scaffold. The morphology of the 3D FDM constructs was analyzed by optical microscopy and SEM to investigate the correlation between pore interconnectivity and infill deposition angle. Fig. 3.3a shows that pore interconnectivity significantly improves by varying the infill deposition angle from 90° (Fig.3.3$a_{i\text{-}iii}$) to 30° (Fig.3.3$a_{iv\text{-}vi}$) and 45° (Fig.3.3$a_{vii\text{-}ix}$). The structure obtained with an infill deposition angle of 45° was found to be the optimal in terms of pore interconnectivity and regularity of pore size and shape, as confirmed by the optical microscope images (Fig. 3.3$a_{i,iv,vii}$). Moreover, two different fill densities have been considered during the fabrication step (Fig. 3.3b). As expected, pore size is significantly lower in the case of major fill density (177 µm *vs.* 253 µm), while the filament size is uniform (≈ 185 µm) and comparable with the nozzle diameter (0.2 mm). Images reported in Fig. 3.2c demonstrate the effectiveness of the optimization process which led to the formation of a continuous filament, defect-free structures and accurate acino-ductal geometry.

3.2.2.2 Effect of plasma surface modification on FDM constructs hydrophilicity

The surface wettability of PCL scaffolds produced by FDM was evaluated through the contact angle analysis on plasma-treated and untreated constructs. The use of plasma treatment reduced the contact angle of drops deposited on PCL scaffolds approximately from 86° ± 2°, to 52° ± 1° (Fig. 3.4). These results suggest that the presence of oxygen-containing polar groups on the surface of the treated scaffolds led to a greater wettability compared to the untreated ones. The drops of water deposited on untreated PCL structures maintained a convex shape for about 1 minute, while the absorption time of the drop deposited on treated PCL scaffolds corresponded to a few seconds.

3.2.2.3 Fabrication of acinar structures by MEW

The effect of the process parameters on the resulted MEW scaffolds was evaluated qualitatively by observing the print shape fidelity with respect to the CAD design at the macroscopic scale, and more quantitatively by measuring the fibers diameter (Fig. 3.5). The SEM images in Fig. 3.5a show the differences in terms of precision in filament deposition, pore interconnectivity and fibers size in MEW scaffolds produced by varying the process parameters in the ranges reported in Table 3.2.

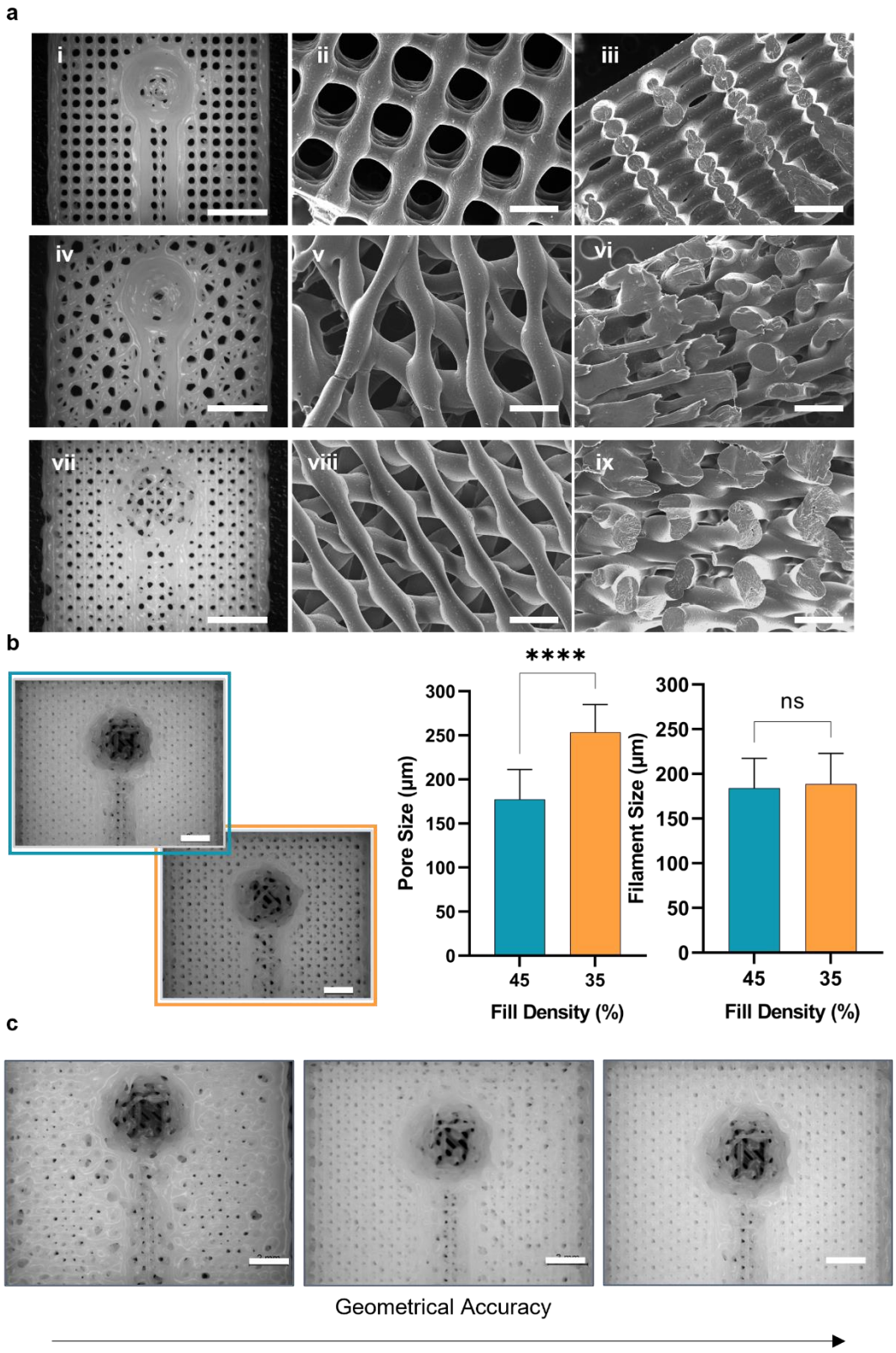

Fig. 3.3 Fabrication of acino-ductal structures by FDM. (a) Images from optical microscopy (i, iv, vii) and SEM analyses (ii, iii, v, vi, viii, ix). Structures obtained with infill angle of 90° (i-iii) 30° (iv-vi) and 45° (vii-ix). Scale bars 1 mm (i, iv, vii) and 500 µm (ii, iii, v, vi, viii, ix). (b) Optical microscope images and bar plots reporting the dimensional analyses (filament and pore size) on scaffolds with 45% (blu) and 35% (orange) fill density. (n = 2; 40 images per scaffold). Tukey's multiple comparisons test: *p < 0.05, **p < 0.01, ***p < 0.001, ****p < 0.0001. Scale bars 2 mm. (c) Photographs of the printed structures showing the geometrical accuracy dependency on process parameters optimization.

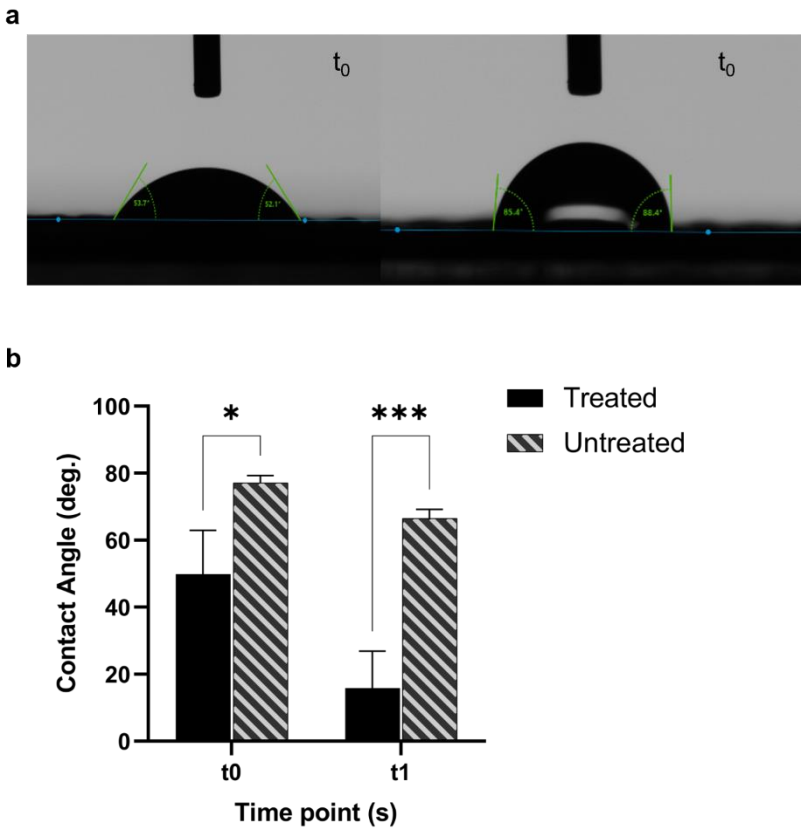

Fig. 3.4 Improvement of FDM constructs' hydrophilicity upon the plasma treatment. (a) Water droplets on PCL plasma- treated (left) and untreated (right) scaffolds at t0 (t = 0s). (b) Bar plots reporting the contact angle measurements at t0 and t1 (t = 10s) on treated and untreated PCL scaffolds. Tukey's multiple comparisons test: *p < 0.05, **p < 0.01, ***p < 0.001, ****p < 0.0001.

In general, the constructs obtained with the highest printing temperature (130 °C) are characterized by randomly deposited fibers (Fig. 3.5a_i) while the pores of scaffolds produced with an infill deposition angle of 45° resulted poorly interconnected (Fig. 3.5a_{ii}). Decreasing the flow and the nozzle diameter and increasing the distance between needle and platform improves the accuracy of filament deposition and the structure resolution as the filament size also decreases (Fig. 3.5a_{iii-iv} and Fig. 3.5b). Due to the difficulties in obtaining structures with well-defined acino-ductal geometry, the original CAD model has been simplified by including a single cylindrical cavity in the middle of the cuboid (Fig. 3.5c). Indeed, shape fidelity was found to be affected by ambient parameters besides by the process parameters as shown in Fig. 3.5d, indeed the acino-ductal geometry suffered a poor shape-fidelity while the reproducibility of a single cylindrical cavity was maintained. Specifically, by decreasing the humidity from 54% to 44% the geometry accuracy of printed constructs visibly improves.

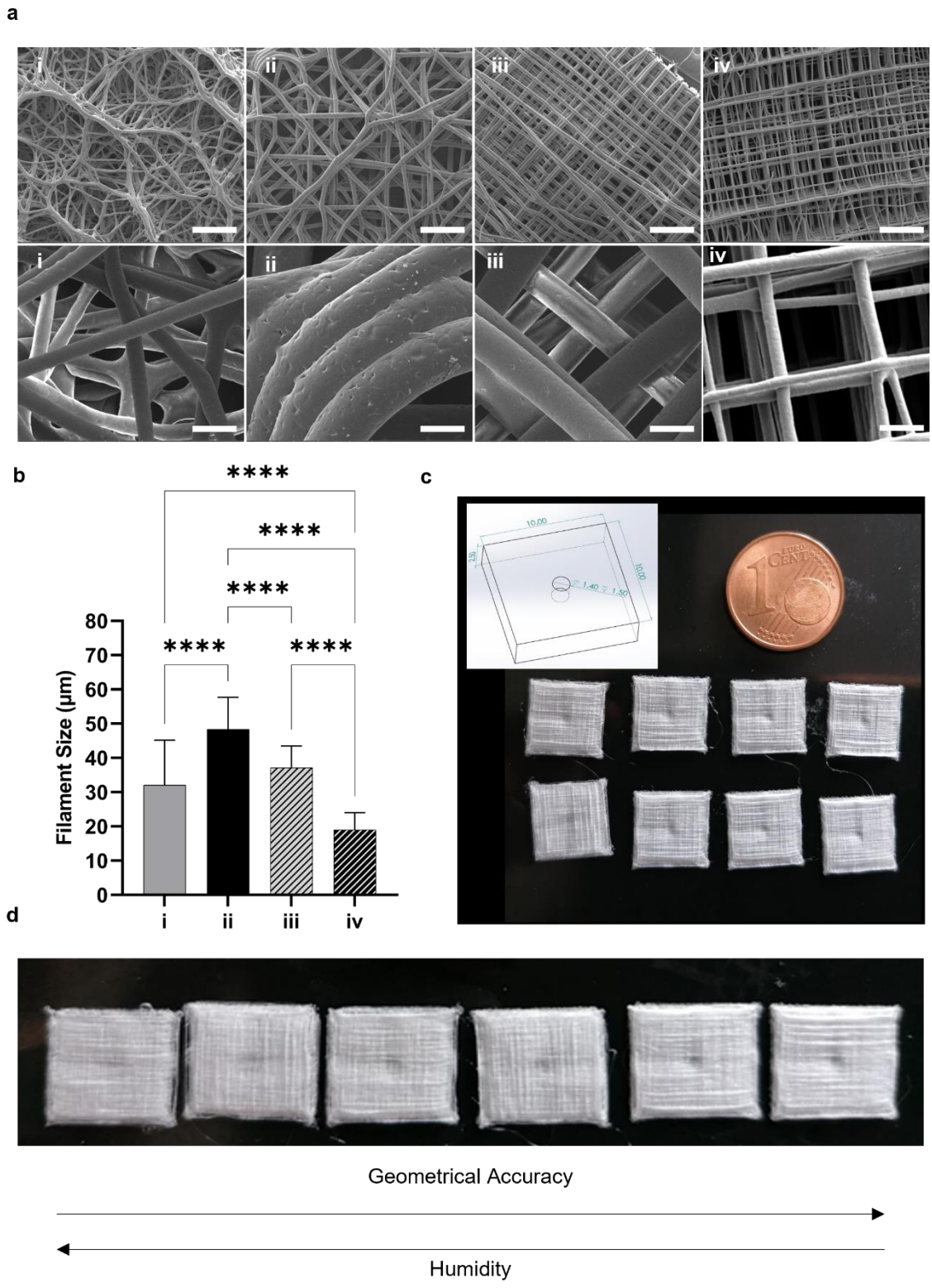

Fig. 3.5 Fabrication of acinar structures by MEW. (a) SEM images of scaffolds obtained by setting different process parameters. Scale bars 500 (first row) and 100 (second row) µm. (b) Bar plots reporting the dimensional analysis (filament size) on scaffolds fabricated with different process parameters (n = 2; 40 images per scaffold). Tukey's multiple comparisons test: *p < 0.05, **p < 0.01, ***p < 0.001, ****p < 0.0001. (c) Starting CAD drawing and photographs of the printed structures. (d) Photographs showing the relationship between geometrical accuracy and humidity.

3.2.2.4 Viability of stromal cells within the FDM and MEW scaffolds

The viability of stromal cells within the layer-by-layer models was assessed by monitoring the metabolic activity of fibroblasts overtime (Fig. 3.5). Fig. 3.6a,c shows fluorometric measurements of the CellTiter-Blue cell-viability assay, in which resazurin is reduced by metabolic reactions in the cells to resorufin, a fluorescent molecule. Higher fluorescence intensity indicates higher cell viability. Cells seeded on 2D plastic substrates were used as control. The results demonstrate the ability of FDM and MEW constructs in supporting the growth of human fibroblasts for 21 and 28 days, respectively (Fig. 3.6b,d). In particular, a significant ($p < 0.0001$), marked increase in metabolic activity was observed from 3d and 7d to 21d after HFF1 seeding on FDM scaffolds, while the cell viability remined almost constant from 14d to 21d (Fig. 3.6a). As concern the metabolic activity of stromal cells seeded on MEW constructs, a statistically significant increment in cell the increment from 21d to 28d resulted minimal (Fig. 3.6c). The proliferation rate of cells cultured on FDM and MEW scaffolds has been compared (Fig. 3.6d). Specifically, the fluorescence values measured at each time point were normalized to the fluorescence value at 3d, which was found to be the same for both FDM and MEW scaffolds. As shown in Fig. 3.6d the difference between the slopes of the regression lines is significant, suggesting a two-fold higher proliferation rate for cells cultured on MEW constructs.

3.2.2.5 Distribution of stromal cells within the FDM and MEW scaffolds

The distribution of cells inside the 3D layer-by-layer scaffolds was evaluated by fluorescence microscopy and SEM analyses on the cellularized structures. Representative confocal images of HFF1 at 72h after seeding on FDM scaffolds are reported in Fig. 3.7. Cells appear elongated and spread, while cell interconnections across fibers are not visible at this initial stage of culture period. Indeed, cells started to form bridges through the pores from 7 days after seeding as confirmed by SEM analyses (Fig. 3.8). In particular, the human fibroblasts seeded on the FDM scaffolds colonized the entire three-dimensional structure and created a stromal matrix after 3 weeks in culture (Fig. 3.8a). The cross-sections obtained by cutting the FDM constructs in parallel to the z axis allowed to verify the presence of stromal cells within the 3D scaffolds, despite their centimeter-scale dimension (Fig. 3.8b). Indeed, cells were able to grow in the 3D volume, by migrating and interacting through the highly interconnected pores. Confocal and SEM images of MEW scaffolds seeded with HFF1 are reported in Figure 3.9. An increment in stromal cells proliferation within the 3D MEW structures can be qualitatively observed from 14d to 21d and 28d (Fig. 3.9b). Indeed, starting from 3 weeks of culture, the formation of a stromal matrix occurred and the developed new tissue covered much of the scaffold surface after 28 days in culture. The fibers dimension comparable to the cells size allowed an optimal colonization by fibroblasts that were able to adhere to different fibers, creating bridges across the pores, and to grow supported by the polymeric grid, in a very biomimetic way. Moreover, the presence of granular corpuscles on the fibers at 21d and 28d after seeding, could be ascribe to the extracellular matrix deposition by HFF1.

3.2.2.6 Distribution of epithelial and stromal cells co-cultured in MEW model

The ability of the developed MEW model in reproducing the natural compartmentalization typical of the exocrine pancreatic microenvironment was analyzed. The confocal images reported in Fig. 3.10 and Fig. 3.11 show the presence of HPDE-KRAS cells predominantly inside the cavity of the MEW scaffolds, thus confirming the success of the seeding procedure.

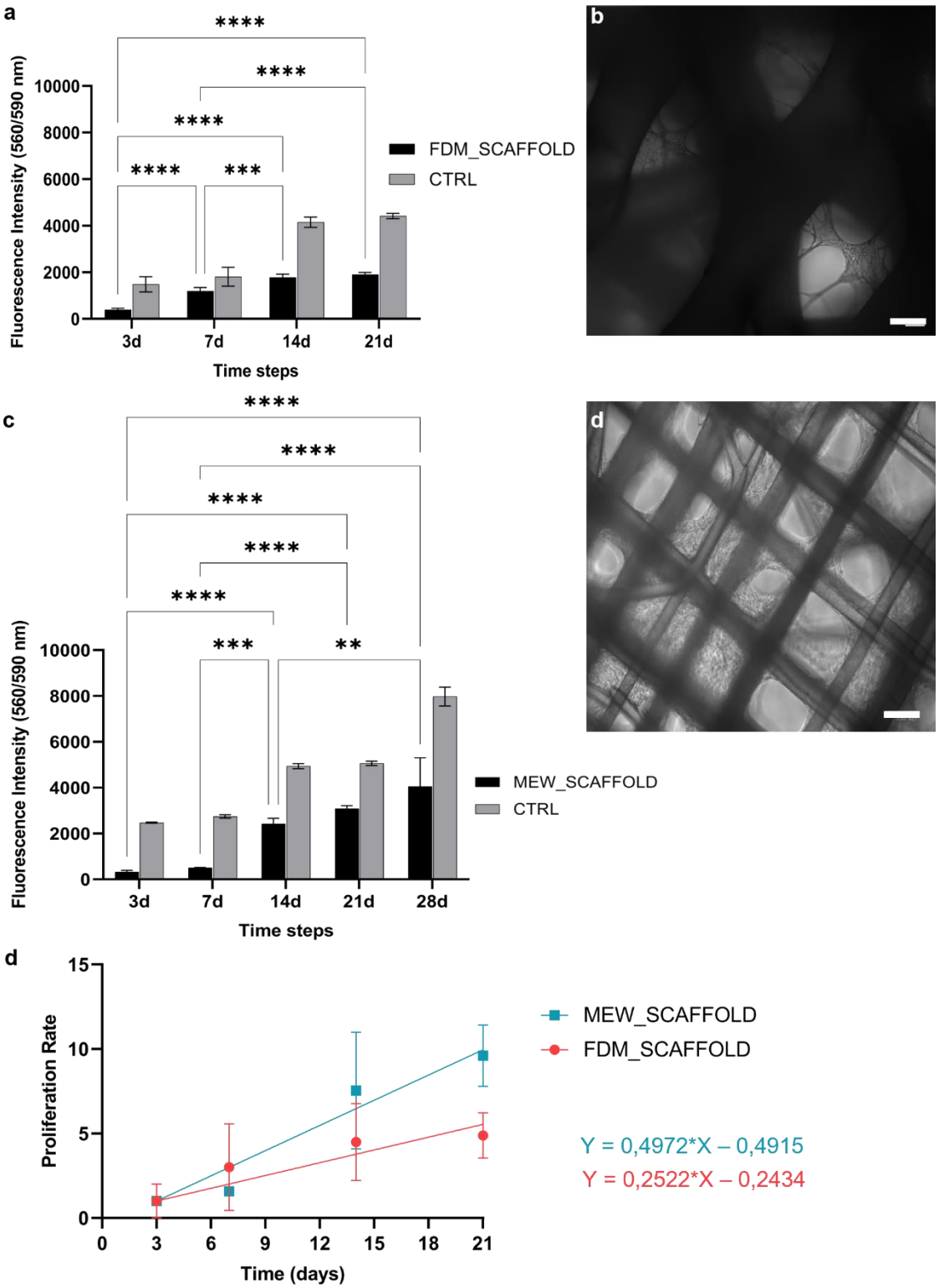

Fig. 3.6 Viability of stromal cells within the 3D layer-by-layer scaffolds. (a,c) Metabolic activity of fibroblasts seeded on FDM (a) and MEW (b) scaffolds (black) and on 2D plastic substrates (gray) as a function of time, measured from the reduction of resazurin (nFDM_scaffold = 5, nFDM_scaffold = 3). Tukey's multiple comparisons test: *p < 0.05, **p < 0.01, ***p < 0.001, ****p < 0.0001. (b,d) Bright-field images from optical microscopy of cellularized FDM (b) and MEW (d) scaffolds at 21d after seeding. Scale bars 100 µm. (e) Comparison between the proliferation rates of cells cultured on FDM and MEW constructs. Simple regression analysis on fluorescent values normalized to the values at 3d (nFDM_scaffold = 5, nFDM_scaffold = 3).

The epithelial cells remained collimated in the biomimetic cavity for 10 days, while they were also visible in the portion around the cavity 14 days after seeding. Indeed, the migration of HPDE-KRAS cells from the cavity toward the upper part of the scaffold occurring 2 weeks after seeding was confirmed by the analyses on fluorescence intensity of E-cadherin signal in z-stack acquisitions (Fig. 3.12). The plots relative to E-cadherin signal from epithelial cells at 7 and 10 days after seeding are characterized by a peak of fluorescence intensity in correspondence to the cavity's bottom ($z \approx 700$ µm), while the fluorescence intensity of epithelial cells co-cultured for 14 days with HFF1 resulted highest for the focal planes proximal to the upper surface of the model ($z = 0$ µm). fluorescence intensity in correspondence to the cavity's bottom ($z \approx 700$ µm), while the fluorescence intensity of epithelial cells co-cultured for 14 days with HFF1 resulted highest for the focal planes proximal to the upper surface of the model ($z = 0$ µm). Moreover, the intensity values measured in models after 10 days from HPDE-KRAS cells seeding are two-fold higher than those quantified after 7 days. Therefore, a culture period of 10 days seems to be optimal to guarantee the collimation of epithelial cells inside the cavity while maintaining a good level of proliferation.

The interactions between stromal and HPDE-KRAS cells within the cavity have been also qualitatively analyzed in confocal images at higher magnifications (Fig. 3.13). Interestingly, the images relative to 3 and 7 days of co-culture allow to observe the tendence of epithelial cells in forming 3D clusters between fibroblasts interconnections, reassembling the cell organization similar to the physiological exocrine pancreatic unit (epithelial cells surrounded by stromal cells). After 7, 10 and 14 days in culture, HPDE-KRAS cells visibly proliferated within the MEW model, growing on fibers and on the stromal tissue and colonizing most of the cavity's bottom.

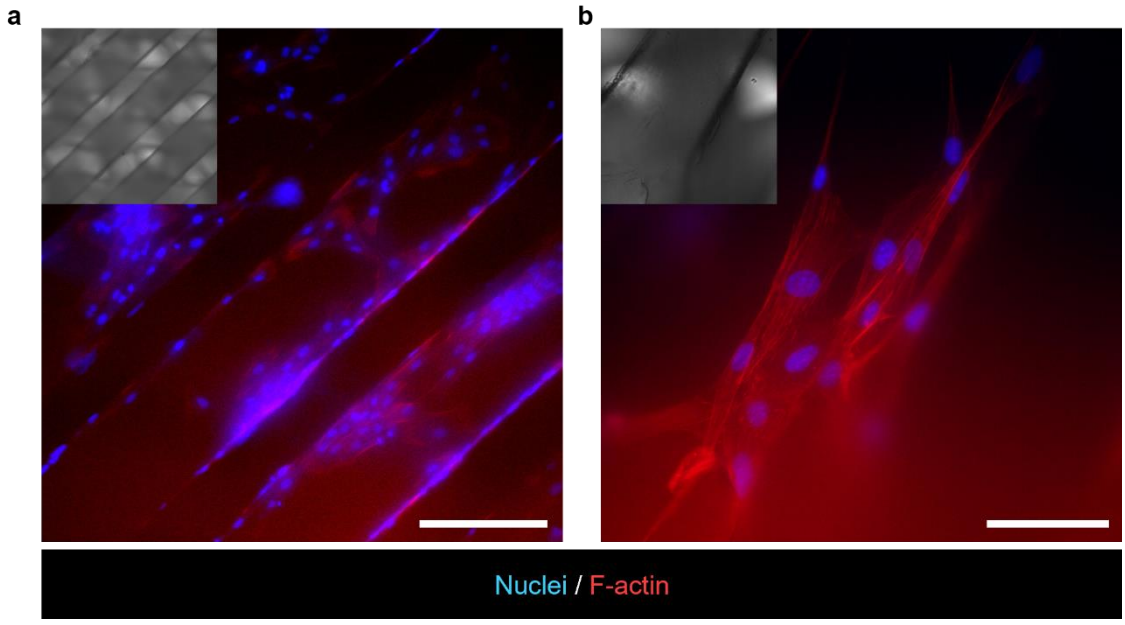

Fig. 3.7 Distribution of stromal cells in 3D FDM scaffolds. Representative confocal images at 20x (a) and 60x (b) magnifications showing the HFF1 spread and elongated along the PCL fibers. Scale bars 200 (a) and 20 (b) µm.

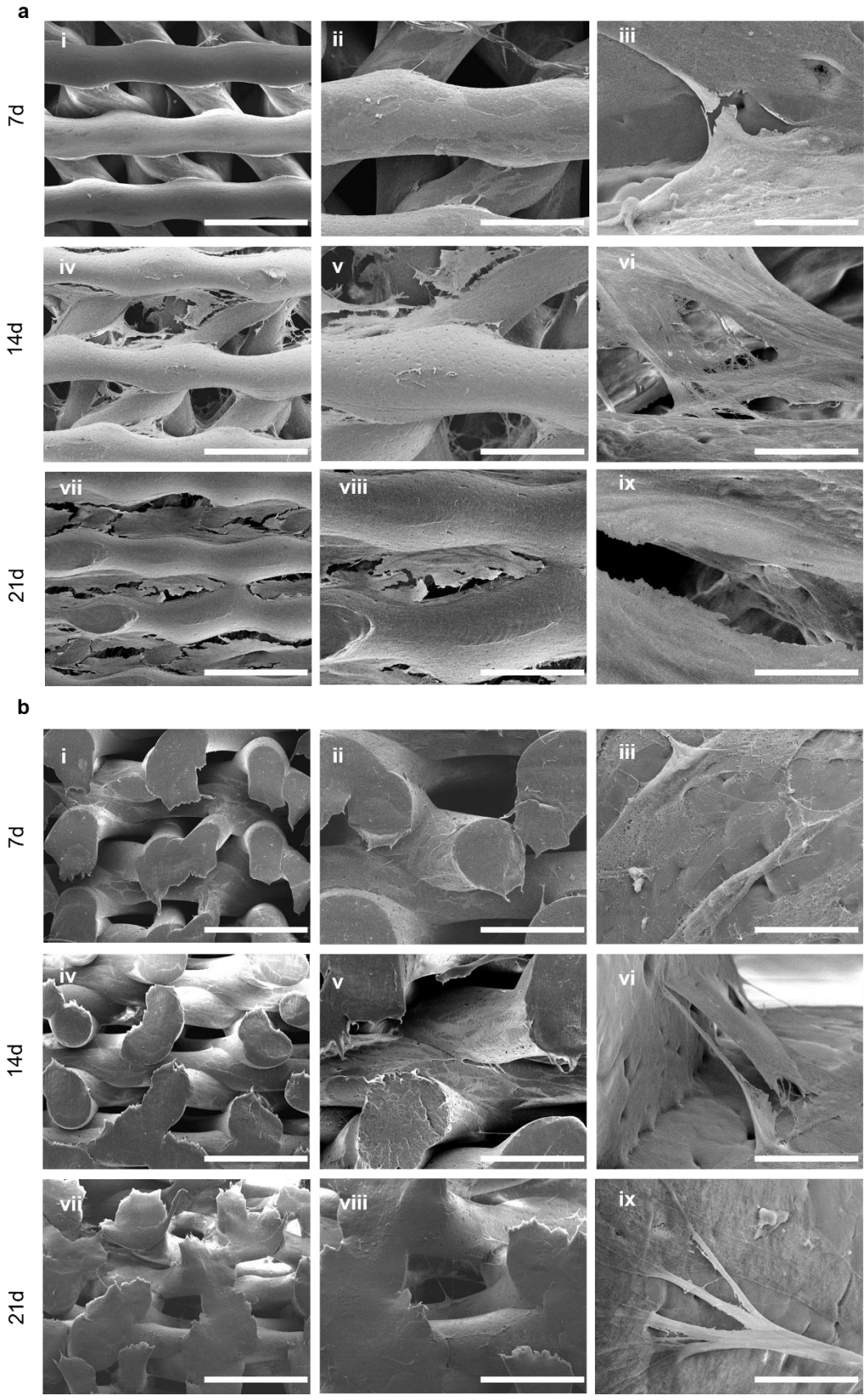

Fig. 3.8 Distribution of stromal cells in 3D FDM scaffolds. Representative SEM images at different magnifications showing the HFF1 colonization within the FDM constructs. (a) Sections obtained by sliced the scaffolds orthogonally to the z axis. (b) Sections obtained by cutting the scaffolds in parallel to the z axis. Scale bars 500 (i, iv, vii), 250 (ii, v, viii) and 20 (iii, vi, ix) µm.

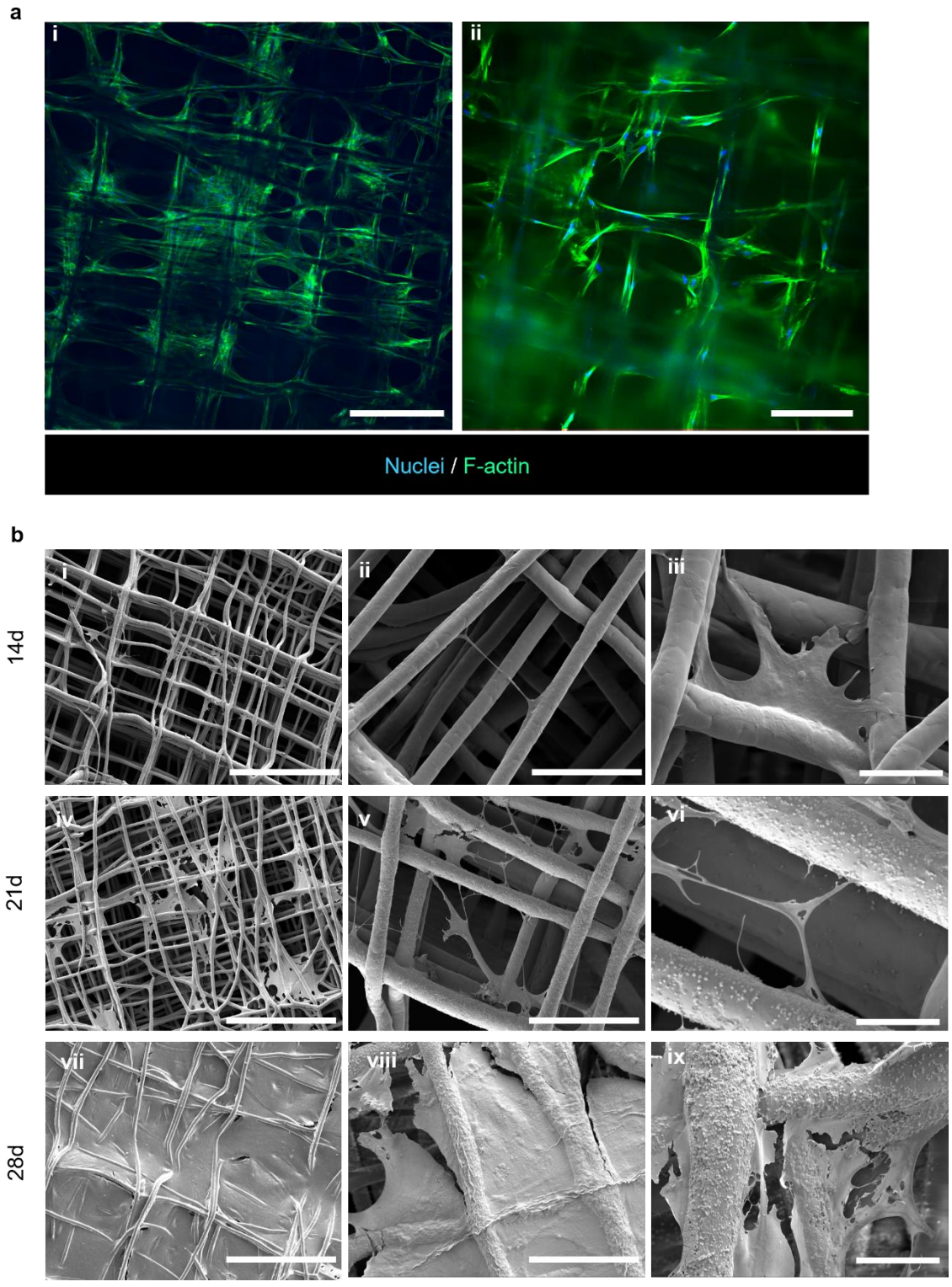

Fig. 3.9 Distribution of stromal cells in 3D MEW scaffolds. (a) Representative confocal images at 10x (i) and 20x (ii) magnifications of HFF1 14 days after seeding. Scale bars 100 (i) and 50 (ii) µm. (b) SEM images at different magnifications showing the HFF1 colonization within the MEW constructs. Scale bars 500 (i, iv, vii), 100 (ii, v, viii) and 20 (iii, vi, ix) µm.

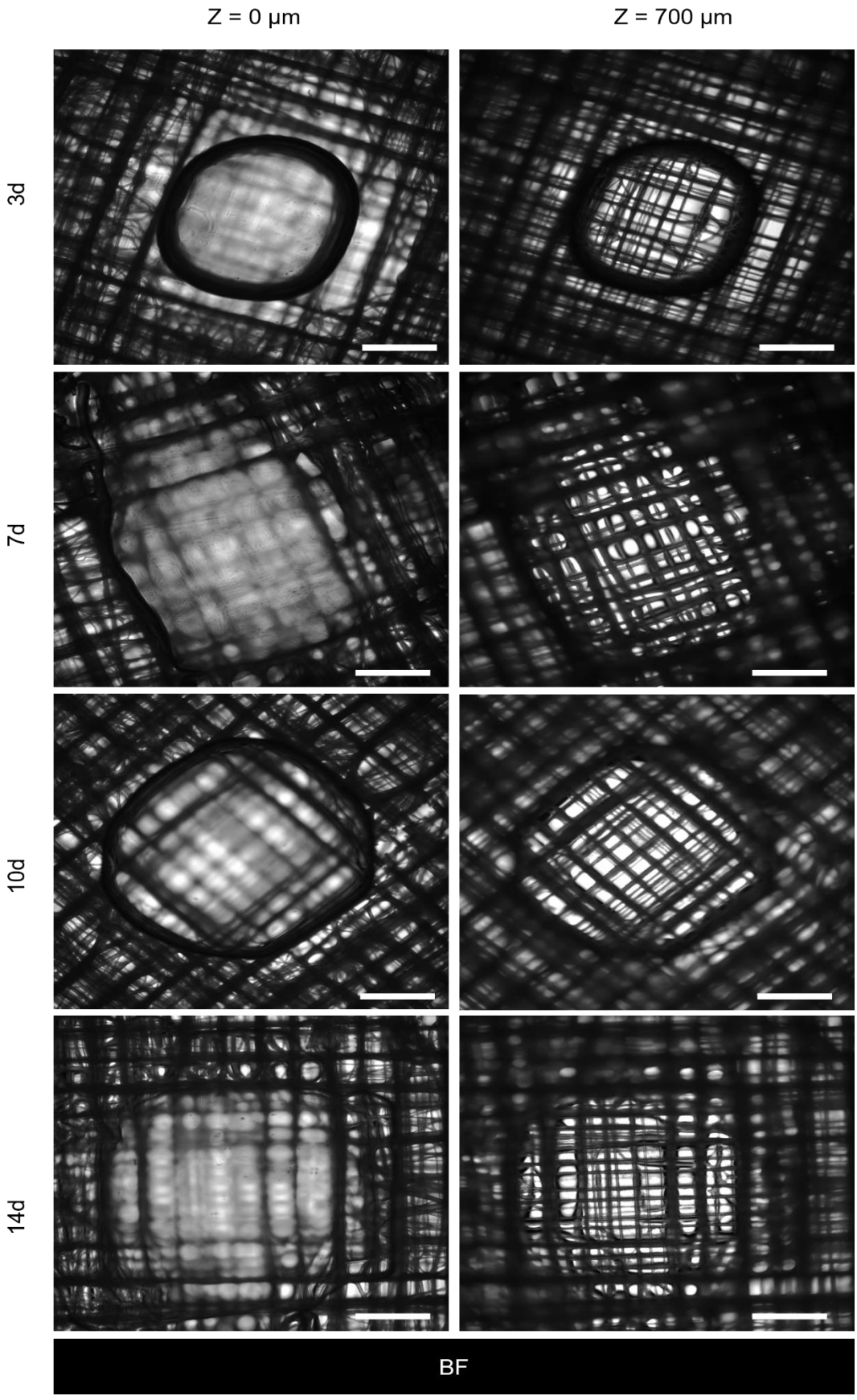

Fig. 3.10 Distribution of epithelial cells co-cultured with fibroblasts in 3D MEW scaffolds. Representative brightfield (BF) images at 4x magnification showing constructs slices at different depths, after 3d, 7d, 10d and 14d from HPDE-KRAS cells seeding. Scale bars 500 µm.

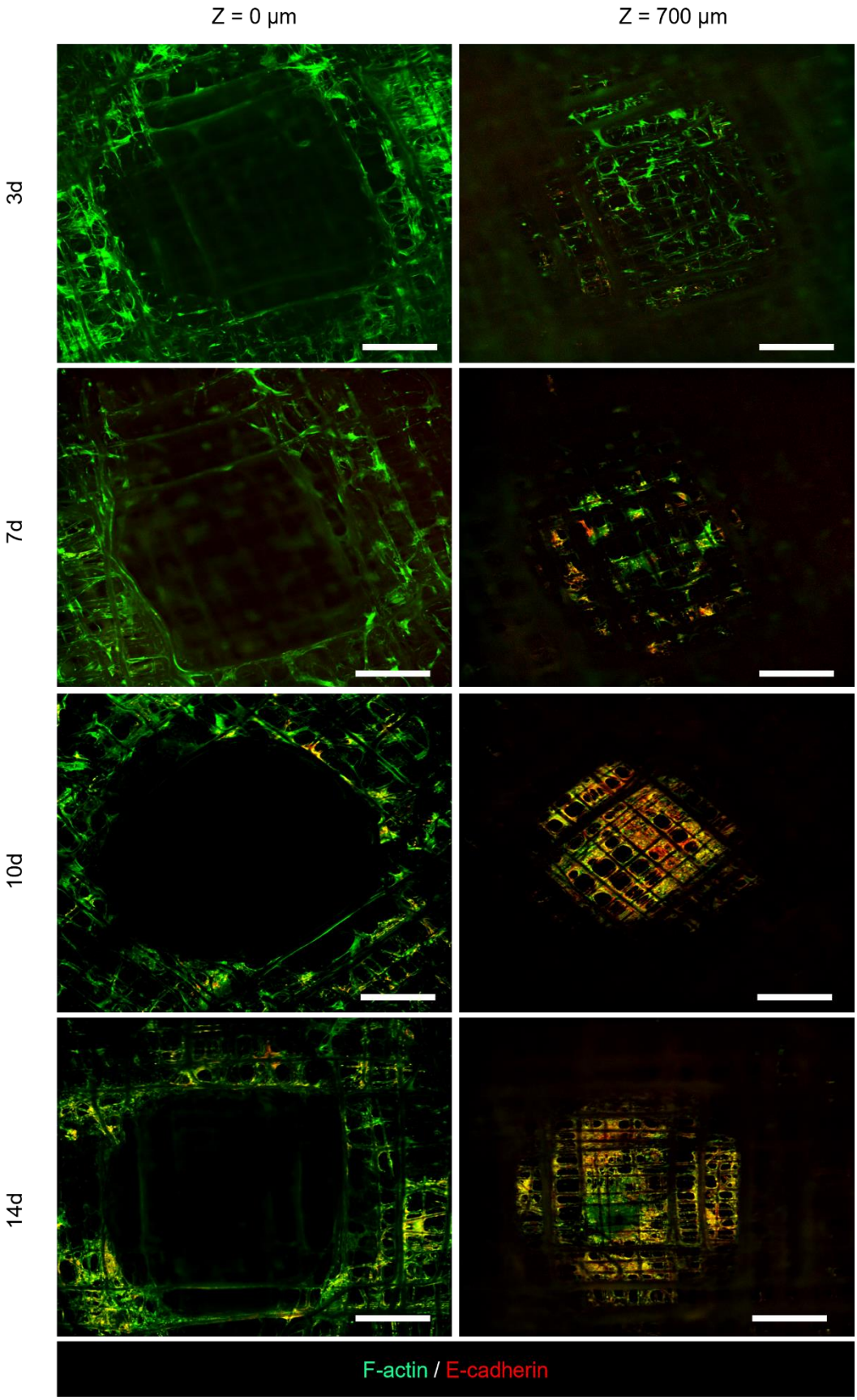

Fig. 3.11 Distribution of epithelial cells co-cultured with fibroblasts in 3D MEW scaffolds. Representative confocal images at 4x magnification showing constructs slices at different depths, after 3d, 7d, 10d and 14d from HPDE-KRAS cells seeding. Scale bars 500 µm.

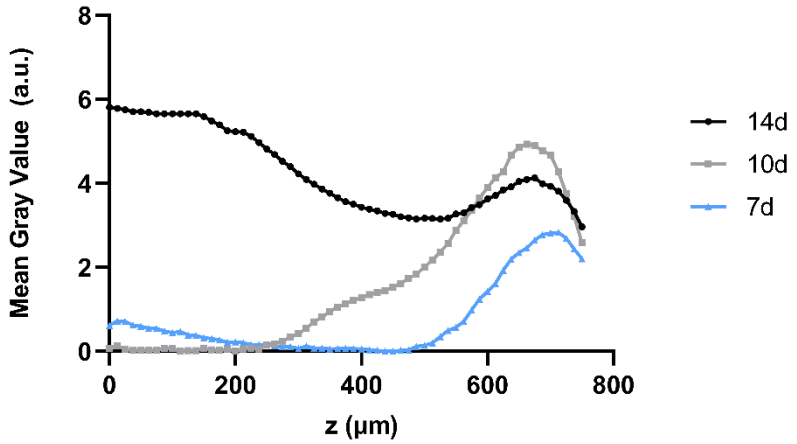

Fig. 3.12 Distribution of epithelial cells co-cultured with fibroblasts in 3D MEW scaffolds. Plots reporting the intensity values of E-cadherin signal along z-axis in constructs co-cultured with HFF1 and HPDE-KRAS cells for 7, 10 and 14 days.

Indeed, the migration of HPDE-KRAS cells from the cavity toward the upper part of the scaffold occurring 2 weeks after seeding was confirmed by the analyses on fluorescence intensity of E-cadherin signal in z-stack acquisitions (Fig. 3.12). The plots relative to E-cadherin signal from epithelial cells at 7 and 10 days after seeding are characterized by a peak of fluorescence intensity in correspondence to the cavity's bottom ($z \approx 700$ µm), while the fluorescence intensity of epithelial cells co-cultured for 14 days with HFF1 resulted highest for the focal planes proximal to the upper surface of the model ($z = 0$ µm). fluorescence intensity in correspondence to the cavity's bottom ($z \approx 700$ µm), while the fluorescence intensity of epithelial cells co-cultured for 14 days with HFF1 resulted highest for the focal planes proximal to the upper surface of the model ($z = 0$ µm). Moreover, the intensity values measured in models after 10 days from HPDE-KRAS cells seeding are two-fold higher than those quantified after 7 days. Therefore, a culture period of 10 days seems to be optimal to guarantee the collimation of epithelial cells inside the cavity while maintaining a good level of proliferation.

The interactions between stromal and HPDE-KRAS cells within the cavity have been also qualitatively analyzed in confocal images at higher magnifications (Fig. 3.13). Interestingly, the images relative to 3 and 7 days of co-culture allow to observe the tendence of epithelial cells in forming 3D clusters between fibroblasts interconnections, reassembling the cell organization similar to the physiological exocrine pancreatic unit (epithelial cells surrounded by stromal cells). After 7, 10 and 14 days in culture, HPDE-KRAS cells visibly proliferated within the MEW model, growing on fibers and on the stromal tissue and colonizing most of the cavity's bottom.

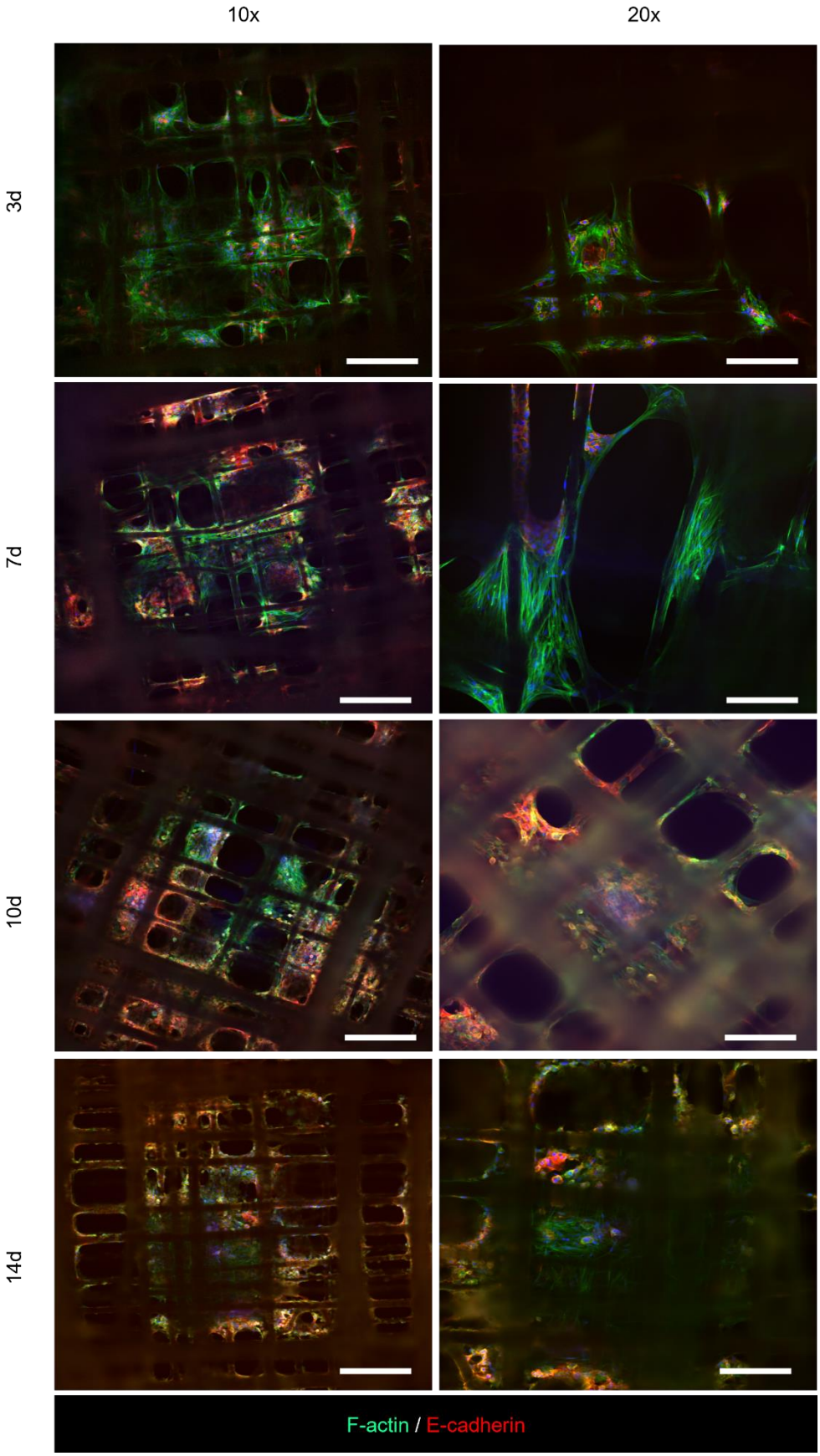

Fig. 3.13 Interactions between stromal and HPDE-KRAS cells within the cavity of MEW model. Representative confocal images at 10x and 20x magnifications showing HFF1 and HPDE-KRAS cells co-cultured within the cavity, after 3d, 7d, 10d and 14d from HPDE-KRAS cells seeding. Scale bars 200 µm (left column) and 100 µm (right column).

3.2.2.7 Effect of stromal-epithelial cells crosstalk on IL-6 cytokines release

The interplay between HPDE cells and HFF1 was analyzed in terms of fibroblasts inflammation by measuring the interleukin-6 (IL-6) release in serum collected by MEW models seeded with HFF1 (monoculture), HFF1+HPDE-KRAS cells or HFF1+HPDE-WT cells at different time points of the culture period. As shown in Fig.3.14, the level of IL-6 cytokines resulted higher for fibroblasts co-cultured with HPDE-KRAS cells for 48h and 72h, compared to the other conditions (HFF1 and HFF1+HPDE-WT). This proves the increased inflammation caused by the presence of HPDE-KRAS cells in co-culture with stromal cells. However, at later time points (10d and 14d) the IL-6 release decreased, suggesting the inflammation mediated by pro-inflammatory cytokines such as IL-6 mainly occurred in the initial phase of tumor-stroma crosstalk.

3.2.3 Discussion

Although the 2D models represent valuable low-cost systems to easily perform experiments *in vitro*[28], they fail in truly recapitulating the biological and biophysical complexity of human tumor microenvironment[29]. Indeed, several studies have largely proved that pancreatic cancer and stromal cells grown in a 3D bioengineered environment respond to drugs differently than cells in 2D models and show features more similar to the ones typical of PDAC components (*e.g.*, chemoresistance, biochemical gradients, tumor-stroma cytoarchitecture)[30–34]. For this reason, pancreatic cancer research has been oriented in recent years towards the development of three-dimensional models to better mimic the tumor microenvironment[35,36]. So far, only a few studies focused on replicating the 3D gland geometry of the functional unit of exocrine pancreas[3–5,37,38], and they still fail in fully reproducing the acino-ductal morphology[4,37] or in incorporating the stromal components[5,39]. In this work, two different

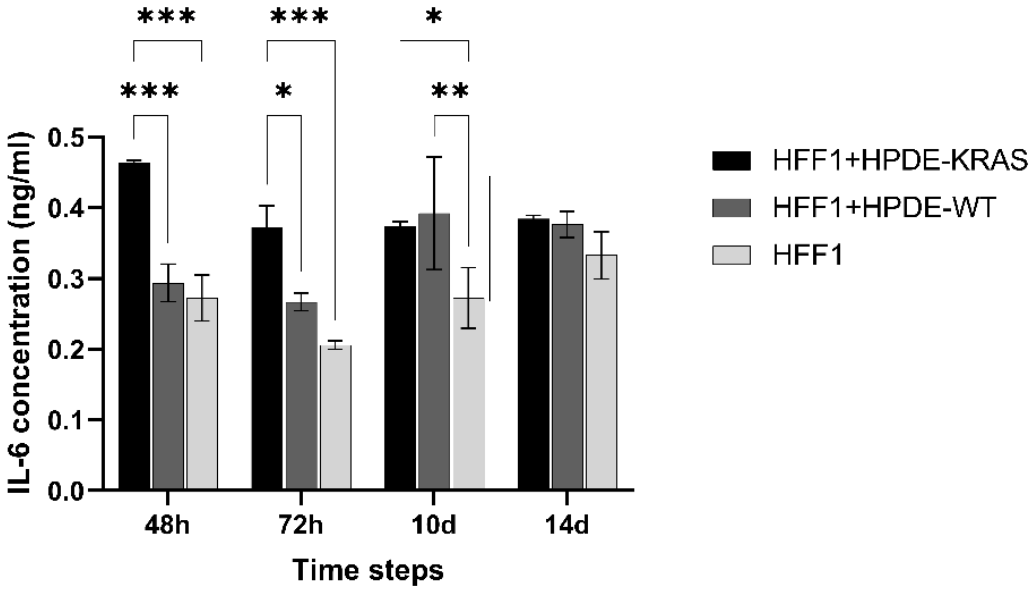

Fig. 3.14 IL-6 cytokines concentration in supernatants collected from mono- and co-cultures in MEW models. Bar plots of the data obtained from ELISA test IL-6 analysis for each culture condition (HFF1, HFF1+HPDE-WT and HFF1+HPDE-KRAS) grouped per time step (n=3). Each condition has been assayed in duplicate following the manufacturer's instructions. Tukey's multiple comparisons test: *p < 0.05, **p < 0.01, ***p < 0.001, ****p < 0.0001.

3D models, based on layer-by-layer PCL scaffolds, were designed and fabricated to resemble the morphology and composition of the exocrine pancreatic functional unit. In particular, distinct additive manufacturing approaches (*i.e.*, fused deposition modeling and melt electrowriting) were used to obtain macro- and microscale models, respectively. FDM resulted an effective technique to produce scaffolds that accurately replicate the gland structure and, at the same time, have strictly controlled pore size and pore interconnectivity (Fig. 3.3). Due to the hydrophobicity of polycaprolactone and the thickness of FDM scaffolds (5.2 mm), a plasma surface treatment was performed to increase the construct hydrophilicity (Fig. 3.4) and consequently enhance the cell adhesion and penetration within the 3D PCL network[24,40]. Melt electrowriting, on the other hand, permits to achieve better resolutions of the printed structures, that have dimensions about four times smaller than those of FDM constructs (considering the acinus diameter). Therefore, compared to FDM model, MEW model is more biomimetic in terms of dimensional scale, which is only seven times bigger than the physiological size of the pancreatic acinus (diameter of acinar portion ≈ 200 μm). In addition, cells growing in MEW scaffolds experience physiological stimuli, since the MEW fibers are similar in size to natural ECM fibers. For instance, collagen fibers have diameters ranging from 1 to 20 μm[41] and an average fibers size of 17 μm was achieved in MEW structures, compared to 185 μm in FDM scaffolds (Fig. 3.3b and Fig. 3.5a,b).
However, the accuracy in obtaining 3D complex geometries is higher in FDM than MEW, where the polymer extrusion is continuous and the ambient parameters (*e.g.*, humidity and ambient temperature) significantly affect the jet stability and the filament deposition (Fig. 3.5d). Therefore, the geometry of MEW scaffolds has been simplified by introducing a single cylindrical cavity in the middle of the cuboid (Fig. 3.5c). Nevertheless, the work described in this section goes beyond the state-of-the-art in MEW field[42,43] and can be considered as a pioneered study since such gland complex geometry at a millimeter-scale is obtained without the need of any supports and/or cylindrical rotary mandrels[44–49]. Thus, our approach allows to bypass the technical difficulties in separating the printed scaffolds from the supports and permits to fabricate morphologies independently from the mandrels shape and dimensions. Complex tubular structures were also recently obtained by incorporating the method of layer shifting in the programmed toolpath, using planar collectors[50,51]. However, these scaffolds resulted poorly interconnected as fibers tend to adhere to each other.
The printing of relevant object shape for biological studies was obtained, as well as a suitable environment for the adhesion and proliferation of stromal cells (HFF1) that remained viable and active for at least 3 weeks in FDM models and 4 weeks in MEW constructs (Fig. 3.6). These results are supported by other studies in literature, showing the culture of cells on PCL scaffolds, obtained by FDM[52] or MEW[45,53], for several weeks. Therefore, the results have demonstrated the ability of PCL scaffolds in promoting the cell growth and tissue formation, both in FDM and MEW structures. This is in line with the numerous studies reporting the large use of this material in additive manufacturing approaches for biomedical applications[54–57].
Although a uniform and good distribution of stromal cells was obtained inside the FDM structures with an almost total coverage of the pores by HFF1 (Fig. 3.7 and Fig. 3.8), the proliferation rate of human fibroblasts cultured on MEW scaffolds resulted significantly higher than the one of cells in FDM constructs (Fig. 3.6d). This can be ascribed to the structural differences (*i.e.*, filament dimension and pore size) between FDM and MEW scaffolds that make the MEW model more biomimetic and suitable for long term culture of human fibroblasts, that were able to cover almost completely the surface of MEW scaffolds forming a stromal matrix after 28 days in culture (Fig. 3.9). Moreover, the presence of granular corpuscles on fibers of cellularized MEW models was observed 21 and 28 days after HFF1 seeding (Fig. 3.9b). Evidence in literature seem to confirm our hypothesis which associates the presence

of such corpuscles with the deposition of ECM by fibroblasts[58,59]. However further analyses are needed to deeply investigate this phenomenon.

These results led us to proceed with the implementation of co-culture conditions only in MEW scaffolds, by seeding human pancreatic ductal epithelial cells (HPDE) in the cavity of the structures, where HFF1 were allowed to grow for 2 weeks. The two cell types were co-cultured for 2 weeks, monitoring their interactions by immunofluorescence imaging (Fig. 3.10, Fig. 3,11, Fig. 3.12 and Fig.3.13). In particular, the ability of the human MEW model in reproducing the natural compartmentalization typical of the exocrine pancreatic microenvironment was demonstrated, observing the epithelial cells that were localized within the cavity while fibroblasts colonized the 3D structure. Indeed, HPDE-KRAS cells grew within the acino-like structure and remained collimated in the cavity up to 10 days of co-culture period and then started to migrate within the scaffold and on the scaffold upper surface (Fig. 3.12).

Therefore, the optimal protocol for co-culture implementation within the MEW structure was set: 14 days of fibroblasts culture alone plus 10 days of fibroblasts and epithelial cells co-culture. Indeed these time points permitted to create a cellularized MEW model mimicking the native compartmentalized 3D tumor architecture which is widely recognized to significantly influence cancer cells behavior[1,60,61].

The epithelial-stromal cells crosstalk occurring in the MEW model was also studied in terms of pro-inflammatory cues produced by fibroblasts (fig. 3.14). Indeed, the release of IL-6 by inflamed tumor-associated fibroblasts plays a key role in PDAC-stroma interplay and regulates a wide range of mechanisms involved in pancreatic cancer, such as angiogenesis, epithelial-to-mesenchymal transition and immunosuppression[62–64]. Our results indicated a higher IL-6 release by fibroblasts in co-culture with HPDE-KRAS cells for 48 and 72 hours, in comparison with HFF1 alone or HFF1 under co-culture with healthy HPDE cells (HPDE-wt). This is in line with studies in literature reporting the role of the KRAS oncogene as driver for the IL-6 production by stromal cells[65,66].

Therefore, the here developed MEW model recapitulates the *in vivo* pathological situation, involving the IL-6 secretion by fibroblasts when inflammatory stimuli are triggered by cancer cells[67]. The ability of this model in reproducing the inflammatory cascade occurring in pancreatic cancer is furtherly confirmed by numerous studies showing notable differences of IL-6 serum levels in PDAC patients compared with healthy patients[68–74].

However, the differences in IL-6 concentrations of fibroblasts co-cultured with KRAS or healthy epithelial cells resulted statistically significant only at early stages of experiment period, suggesting that the IL-6 mediated inflammation occurred mainly during the first hours (up to 72 hours). At later phases of the experiment the inflammation might be mediated by the released of other cues[75].

Therefore, this human MEW model can be applied to study the interactions between PDAC and stromal cells occurring at different stages of pancreatic cancer progression in a very controlled and biomimetic way.

3.3 VBP model

3.3.1 Experimental section

3.3.1.1 Cell culture

Human foreskin fibroblasts (HFF1) cells were purchased from ATCC® and cultured in Dulbecco's Modified Eagle's Medium (DMEM) without phenol red, supplemented with 1% Penicillin-Streptomycin (Gibco), 2% L-glutamine (Gibco) and 15% FBS (Gibco). Human pancreatic ductal epithelial cells (HPDE) stably expressing activated KRAS (HPDE-KRAS) and wild-type HPDE (HPDE-wt) were cultured in RPMI-1640 medium (Gibco) supplemented with 1% Penicillin-Streptomycin (Gibco), 1% L-glutamine (Gibco) and 10% fetal bovine serum (FBS) (Gibco). Cells were maintained in a humidified CO_2 incubator at 37 °C and 5% CO_2.

3.3.1.2 GelMA Hydrogels

GelMA was produced from porcine gelatin (Sigma) following the protocol by Van De Bulcke *et al.*[76]. Briefly, type A porcine gelatin powder (Sigma, G2500) was fully dissolved at 10% w/v into Phosphate Buffered Saline (PBS) 1x at 50 °C. Methacrylic anhydride (Sigma, 760-93-0) was added dropwise for gelatin modification at 50 °C for 3h. The solution was then lyophilized and stored away from light at −20 °C until use.
The 5% w/v GelMA solution was created by reconstituting lyophilized GelMA powder into sterile DMEM without phenol red (Gibco, 31053028) with Lithium phenyl-2,4,6-trimethylbenzoylphosphinate (LAP, Sigma-Aldrich, 900889) at a concentration of 0.16 mg ml^{-1} and filter-sterilized at 40°C. GelMA solutions were stored away from ambient light at 4 °C for no longer than 2 weeks.

3.3.1.3 Photorheological analyses on GelMA hydrogels

The rheological properties of GelMA hydrogels were evaluated employing a stress-controlled rheometer (AntonPaar GmbH, MCR302) equipped with 25 mm parallel plate geometry. In order to evaluate the photocrosslinking kinetics, filtered GelMA solution + LAP was poured on the rheometer plate and time sweep test was performed using a visible light source at 405 nm wavelength (Prizmatix, FC-LED-405A) at constant temperature (approximately 25 °C), applying a rotational oscillation of 1 Hz and a strain amplitude of 1% in the linear viscoelastic region (measured through strain sweep test).

3.3.1.4 Tomographic bioprinting

For printing, fibroblasts were detached, counted, and centrifuged. A small volume of cells, corresponding to a final density of 0.5 million cells ml^{-1}, was resuspended into GelMA with LAP and gently agitated using a 1000 µl pipette tip with a cut tip. 1.5 ml of the GelMA + LAP + HFF1 mix was poured into ethanol sterilized cylindrical glass vials (diameter 12 mm) with a hermetically sealing cap. All these manipulations were carried out under sterile conditions in a biosafety cabinet.
The glass flasks were dipped into water at 2°C to gelify the GelMA. They were then printed using a tomographic volumetric printer[15]. In this printer, blue light from three 405 nm laser diodes (Ushio, HL40033G) is sent through a square-core multi-mode optical fiber (CeramOptec, WF

70×70/115/200/400N), expanded, and projected on a Digital Micromirror Device (mirror size=13.7 μm, Vialux, VIS-7001), which displays the tomographic patterns. Two plano-convex lenses with focal length f_1 = 150 mm and f_2 = 250 mm project the images from the DMD onto the rotating vial. The vial is set to rotate using a high-precision stage (Zaber, X-RSW60C), and is inside a cubic glass container filled with cold water, acting as a refractive-index matching bath.

The calculations to produce the required tomographic patterns were performed using the software described in a previous work[16], and scattering corrections were applied to compensate for the diffusive effects of the cell-laden hydrogels. These calculations were performed on a GPU using PyTorch[77]. This software takes 3D models in the shape of .stl files, which were designed using AutoCAD, and calculates tomographic projections using non-negative tomographic filtered back-projections. Sets of 1000 8-bit tomographic patterns were used, each displayed for an angular interval of $\Delta\theta$ = 0.36°. The cylindrical vials were set to rotate at a constant angular speed of 12°/s during printing. Prints were completed in around 2.5 minutes.

After printing, glass vials were slowly heated to 27°C for 5 minutes by dipping them into water. Under sterile conditions in a biosafety cabinet, pre-warmed PBS at 37°C was gently pipetted into the glass vials, then they were gently manually agitated to rinse away the uncross-linked GelMA. The rinsed bioprinted fibroblast-laden constructs were carefully transferred to 24-well plates filled with cell medium and kept in the humidified CO_2 incubator at 37°C.

3.3.1.5 Stromal cells viability in bioprinted constructs

The viability of human fibroblasts embedded in the bioprinted gel constructs was analyzed by monitoring the metabolic activity through the fluorimetric resazurin reduction method (CellTiter-Blue, Promega, G8080) at 1, 2, 3, 4 and 9 days after the tomographic bioprinting process. The test was performed according to the manufacturers' protocols as described in the previous section. Briefly, culture medium was carefully removed and constructs were washed with PBS (500 μl). A solution of 16% CellTiter-Blue in complete cell culture medium was prepared and added to the constructs, followed by 5-6 h incubation at 37 °C. At the end of the incubation period, 200 μl of the medium was pipetted into different wells of a 96-well plate, and fluorescence was measured from the bottom of the plate using a plate reader (BioTek) at 530 nm excitation and 590 nm emission. Fluorescence of CellTiter-Blue solutions in contact with GelMA hydrogels without cells were subtracted to avoid overestimations. Plates were covered with an adhesive film to prevent evaporation during the measurements.

Moreover, Live/Dead Assay was carried out to furtherly evaluate the HFF1 viability over the culture period, at pre-determined time points (1, 3, 7 and 14 days). Specifically, the Live/Dead solution was prepared by adding ethidium homodimer-1 (Adipogen, CDX-E0512-M001, 2mM in DMSO) and calcein-AM (Merck, 206700-1MG, resuspended to 4mM in DMSO) to PBS in concentrations of 4 μM and 2 μM respectively. The solution, prepared afresh every time it was used, was vortex-agitated for some seconds and kept at room temperature protected from light. The cellularized constructs were rinsed once with pre-warmed PBS at 37°C and transferred to a 24-well plate with wells filled with 800 μl of Live/Dead solution. Constructs were incubated in the dark for 1h, with gentle manual agitation every 15 minutes. Samples were rinsed twice with PBS and placed in optical-grade multiwell microscope slides for imaging. Imaging was conducted immediately after staining and performed in a fluorescence confocal inverted microscope (Leica, SP8) with 5x NA 0.15 (Leica, HC PL Fluotar, WD 13.7 mm), 10x NA 0.30 (Leica, HC PL Fluotar, WD 11.0 mm), and 20x NA 0.75 (Leica, HC PL APO, WD 0.62 mm) objectives. In the microscope, calcein-AM was excited at 488 nm and its emission collected from 498 to 542 nm. Ethidium homodimer was excited at 552 nm.

To avoid crosstalk with the emission spectrum of calcein-AM, the emission of Ethidium was collected from 620 nm to 650 nm.

3.3.1.6 Epithelization of the cavity

To epithelize the constructs, HPDE cells were detached from the culture flask, counted and resuspended to a 10 µl volume. Then, they were gently manually injected with micropipette into the duct of the fibroblast-laden hydrogel.
Specifically, before the epithelization, the rinsed bioprinted fibroblast-laden constructs were cultured for 96h.
The cell ratio between HPDE cells and HFF1 was fixed at 1:3, In accordance with studies reporting the relevancy that ratios of 1:1 to 1:3 have *in vivo*[25–27]. After injection, the constructs were placed in 24-well plates, with enough cell medium to keep them hydrated, but not enough to cover the entry of the lumen, to prevent HPDE cells from floating into the media. C
o-cultures were maintained in DMEM/F-12 supplemented with 15% FBS (Gibco), 1% Penicillin-Streptomycin (Gibco) and 2% L-glutamine (Gibco) since previous tests demonstrated the efficacy of this culture medium composition in promoting the cell viability (see 2.2 Two-dimensional model; 2.2.2 Results). Two hours later, more medium was added to the wells, this time covering the full constructs. The constructs were maintained in a humidified CO_2 incubator at 37 °C and 5% CO_2.

3.3.1.7 Immunocytochemistry

Bioprinted constructs were fixed in formaldehyde 4% v/v in PBS for 5 minutes, then rinsed with PBS twice and kept at 4°C. The fixed constructs were embedded in low-melting point agarose 4% w/v in pre-warmed PBS and sliced to a thickness of 300 µm with a vibratome (Leica Biosystems, VT1000S) filled with PBS 1x. Samples were sliced orthogonally to the axis of the duct, in order to obtain circular cross-sections. After slicing, the surrounding agarose was detached gently with a brush.
Slices were put onto microscope slides with adhesive imaging spacers making wells (Merck, GBL654004-100EA), covered with PBS and with a coverslip and kept at 4°C in a dark wet chamber until they were stained for imaging.
Samples were then permeabilized with 0.1% Triton X-100 in PBS for 10 minutes at RT and successively washed 3 times for 5 minutes with PBS + 0.1% Triton X-100 (PBST) at RT. Then, samples were blocked with 2% bovine serum albumin (BSA) in PBST for 60 minutes and rinsed once with PBS. Primary antibodies, rabbit polyclonal to alpha-smooth muscle actin (Abcam, ab5694-100ug, 1:50), and mouse monoclonal fibroblasts antibody TE-7 (Novus Biologicals, NBP2-50082, 1:80) in PBST + 1% BSA were incubated for 36h at 4°C.
Samples were then rinsed 3 times with PBST at RT for 5 minutes. The secondary antibodies, donkey anti-rabbit IgG + Alexa 647 (Invitrogen, A31573) and donkey anti-Mouse IgG + Alexa 568 (Invitrogen, A10037), were incubated at a concentration of 1:200 in PBST + 1% BSA for 2h at RT.
Samples were rinsed with PBST for 5 minutes at RT 3 times. ((R)-4-Hydroxy-4-methyl-Orn(FITC)^{7})-Phalloidin (1:60, 0.16 nmol ml^{-1} was incubated in PBST + 1% BSA for 30 minutes at RT. Slices were rinsed with PBS for 5 minutes at RT 3 times, before the staining with DAPI (Invitrogen, D1306) in PBS (1:1000) for 5 minutes at RT.
They were then washed once with PBS, and finally covered with coverslips for imaging. Samples were kept in wet chambers and protected from intense light during all the immunostaining protocol.

3.3.1.8 Quantification of human fibroblasts activation

The constructs were imaged with a motorized inverted confocal microscope (Leica SP8) using a 10x NA 0.30 air objective (WD = 11.0 mm, HC PL Fluorotar, Leica). Fluorescence excitation was performed with solid-state lasers at 405, 488, 552, and 638 nm, and its emission was collected with two twin Hybrid Detectors. An additional photomultiplier tube collected transmitted light from the excitation laser. To acquire images of the full cross-sections of the bioprinted constructs, the automatic motorized stage was used to take sequential images along grids that were later stitched together. Two sequential two-channel acquisitions were performed for each sample; one collecting the fluorescence from DAPI (440-480 nm) and TE-7-bound secondary antibody (568-620 nm), and another collecting the fluorescence from Phalloidin-FITC (498-542 nm) and α-SMA-bound secondary antibody (648-720 nm). Both acquisitions used the same grid coordinates of the motorized stage and included a bright field image acquisition. Lasers intensities, detector gain, and optical path were kept unchanged across image acquisitions to guarantee intensities were comparable. Microscopy images were automatically acquired using LAS X software (Leica). Images were acquired for almost 100 slices of 14 independent biological samples. Due to the large area of the acquired microscopy images (> 250 mm^2 in some cases) and to the soft and elastic nature of hydrogels, there was displacement between the DAPI-TE-7 and the Phalloidin-α-SMA images for some samples (note however, that because Phalloidin and α-SMA were always acquired in parallel and not sequentially, there was never displacement between these two channels).
Displacement between the DAPI-Te-7 and Phalloidin- α-SMA images was corrected with a custom-made Python code. The code compared the bright-field channels of corresponding DAPI-Te-7-BF and Phalloidin- α-SMA-BF tiles, calculated the necessary homography ($n_{features}$ = 5000) that needed to be applied to the DAPI-Te-7-BF image so that it matched the Phalloidin- α-SMA- BF image[78]. The code would then apply such homography and save a transformed copy of DAPI-Te-7-BF image.
Images were batch-stitched together using the Grid/Collection stitching plugin[79] on ImageJ[23] using the Phalloidin channel as reference. Multichannel microscopy images (DAPI, Phalloidin, Te-7, α-SMA, BF) depicting multiple slices of the same bioprinted construct were then manually cropped to fit only one slice per image. Inflammation was quantified from microscopy images by measuring the ratio between the intensity of α-SMA vs. actin. This calculation was done with a custom-made Python code. The code first segments cell nuclei from the DAPI channel.
Then, the code segments all regions of at least 13.4 μm^2 with a non-zero actin or α-SMA intensity in size and which are adjacent to a cell nucleus. An average intensity is calculated for these masked regions for the actin and α-SMA channels, and a ratio is reported. Actin and α-SMA intensities were additionally normalized to excitation light intensities, to make the ratio comparable across multiple acquisitions.
The ratio of actin to α-SMA intensities was also computed for segmented single cells. Hand-made digital annotations of the outline of the inner channel of the bioprinted pancreatic constructs (based on the bright field and fluorescence channels of the microscopy images) were used to measure the distance of the individual cells to the channel.
Multi-channel microscopy images were visualized using ImageJ and the Look-Up Tables from Christophe Leterrier for the Live/Dead experiments and from the BioImaging and Optics Platform at EPFL for the co-culture inflammation experiments. Brightness and contrast were set the same for each channel of all images that were compared (particularly actin and α-SMA). Sketches of cell-laden constructs were created with BioRender.com. Plots were produced using matplotlib.org[80] and seaborn.pydata.org[81].

3.3.1.9 Statistical analysis

Data were arranged and analyzed using Pandas[82]. The graph data are presented as the mean ± standard deviation (SD) for at least three independent experiments ($n \geq 3$). Significance was measured with one-way ANOVA followed by pairwise comparison with Tukey's multiple comparisons test, using GraphPad Prism 9.3.1 for metabolic activity experiment (*$p < 0.05$, **$p < 0.01$, ***$p < 0.001$, ****$p < 0.0001$) and using SciPy's statsmodels for inflammation quantification.

3.3.2 Results

3.3.2.1 Fabrication of exocrine pancreatic units through VBP

The fabricated constructs followed a ductal geometry, with an acinus of larger diameter at the end. In VBP, a set of tomographic light patterns was projected into cell-laden GelMA (5% w/v in DMEM w/o phenol
red + 0.5 million fibroblasts ml^{-1}) in which the photoinitiator was added at a low concentration (0.16 mg ml^{-1}) (Fig.3.15a). The selected concentration of the photoinitiator allows the crosslinking of GelMA upon visible light irradiation at 405 nm wavelength (Fig. 3.15a-c) and it is low enough to reduce cytotoxicity and light absorption. The photorheological test proved the sol-gel transition of GelMA as a result of light irradiation (Fig. 3.15b,c). The increment of storage modulus (G') until reaching a stable plateau at 0.4 KPa indicates the elastic response of the material, whose viscoelastic properties are comparable to those of pancreatic tissue[83] (Fig. 3.15b). The light-scattering effect caused by the presence of cells within the gel causes a loss of resolution in the constructed object, such as a resulting obstructed duct or an incomplete acinus. However, by performing a numerical correction of the light dose that uses quantitative information on the light scattering[16], an improvement in shape fidelity and resolution of the printed structures was obtained (Fig. 3.16). Features of the final geometry, such as the wall thickness and the duct diameter, were optimized to guarantee printability and maximize anatomical relevance. This is because there is a trade-off between structural integrity and cell viability, as metabolic activity in cells within hydrogels is known to decrease with distance from the outer borders of the hydrogel[84].

3.3.2.2 Viability of exocrine pancreatic units

The viability of cells within the bioprinted pancreatic ductal models was firstly assessed by monitoring the state of the fibroblasts. Fig. 3.17a shows fluorescence microscopy images of constructs 24 hours, 72 hours, 7 days, and 14 days after printing. Live cells, shown in blue, had been stained with calcein-AM, a membrane-permeant dye that is converted into a fluorescent calcein by intracellular esterases. Dead cells, shown in orange, had been stained with ethidium homodimer-1, which is a membrane-impermeant high-affinity nucleic acid stain that is weakly fluorescent until bound to DNA. The micrographs show the region around the duct, 300 μm deep inside the constructs, with fibroblasts assuming an elongated shape and fully colonizing the inner walls of the duct over time. Micrographs also demonstrate that most cells survived after the printing process and that they were homogenously distributed within the hydrogels at 24h. Then, cell proliferation and maturation occurred over two weeks as confirmed by the metabolic activity of fibroblasts which increased with time. Indeed, Fig. 3.17b shows fluorometric measurements of the CellTiter-Blue cell-viability assay ($n_{GelMA + cells} = 7$, $n_{GelMa} = 7$), in which resazurin is reduced by metabolic reactions in the cells to resorufin, a fluorescent molecule.

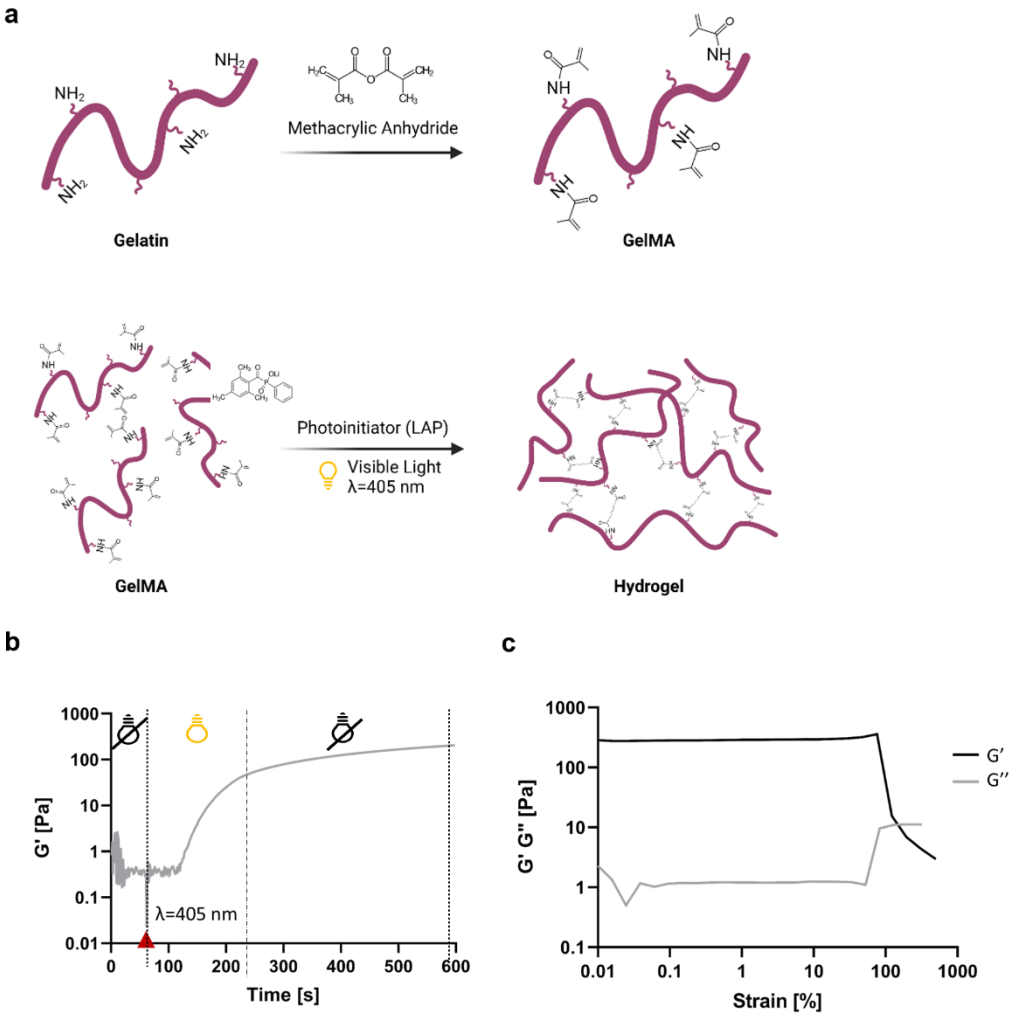

Fig. 3.15 Fabrication of GelMA constructs. (a) Synthesis and photocrosslinking of GelMA inspired from Yoon *et al.*[107]. Gelatin was reacted with methacrylic anhydride (MA) to introduce a methacryloyl substitution group on the reactive amine and hydroxyl groups of the amino acid residues. The GelMA photocrosslinking occurs after exposure to visible light (405 nm wavelength). The free radicals generated by the photoinitiator initiate the chain polymerization with methacryloyl substitution resulting in the hydrogel formation. (b) Photorheology test to evaluate the photocrosslinking kinetic by monitoring the storage modulus (G') overtime. The crosslinking reaction started after 60 s following the emission of visible light (405 nm wavelength). (c) Strain sweep test: G' (black) and G" (gray) versus strain amplitude. Filtered solution of 5% GelMA with LAP at a concentration of 0.16 mg ml-1 was used for the tests.

Higher fluorescence intensity indicates higher cell viability. A significant ($p < 0.0001$), marked increase in metabolic activity 72 to 96 hours after printing was observed, which is sustained at least until 9 days after printing. This significant increment in cell viability at 96h is probably associated to the cell recovery from stress that the biofabrication process may cause. GelMA hydrogels have residual free radicals left after gelation, which can themselves account for the reduction of rezasurin[85]. This effect was evaluated by measuring the fluorescence intensity also in bioprinted GelMA hydrogels without cells. A reduction 2 orders of magnitude lower than the one in cell-laden hydrogels was observed (Fig. 3.17b).

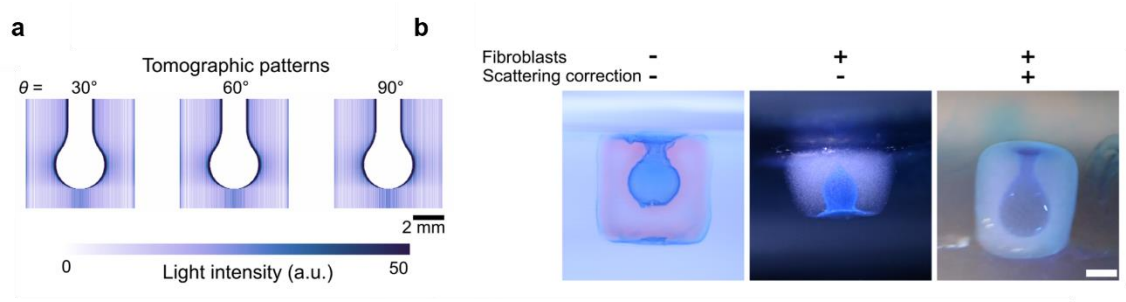

Fig. 3.16 Fabrication of viable 3D pancreatic acino-ductal models. (a) Some tomographic patterns used to fabricate the scattering-corrected constructs. In total, 1000 different tomographic patterns are displayed along each turn of the cylindrical vial during printing. (b) Photographs of 3D printed GelMA constructs, immersed in water and with the duct filled with a glycerol-based blue dye for illustrative purposes. Including cells in the gel affects print fidelity, but it can be compensated by correcting for scattering effects.

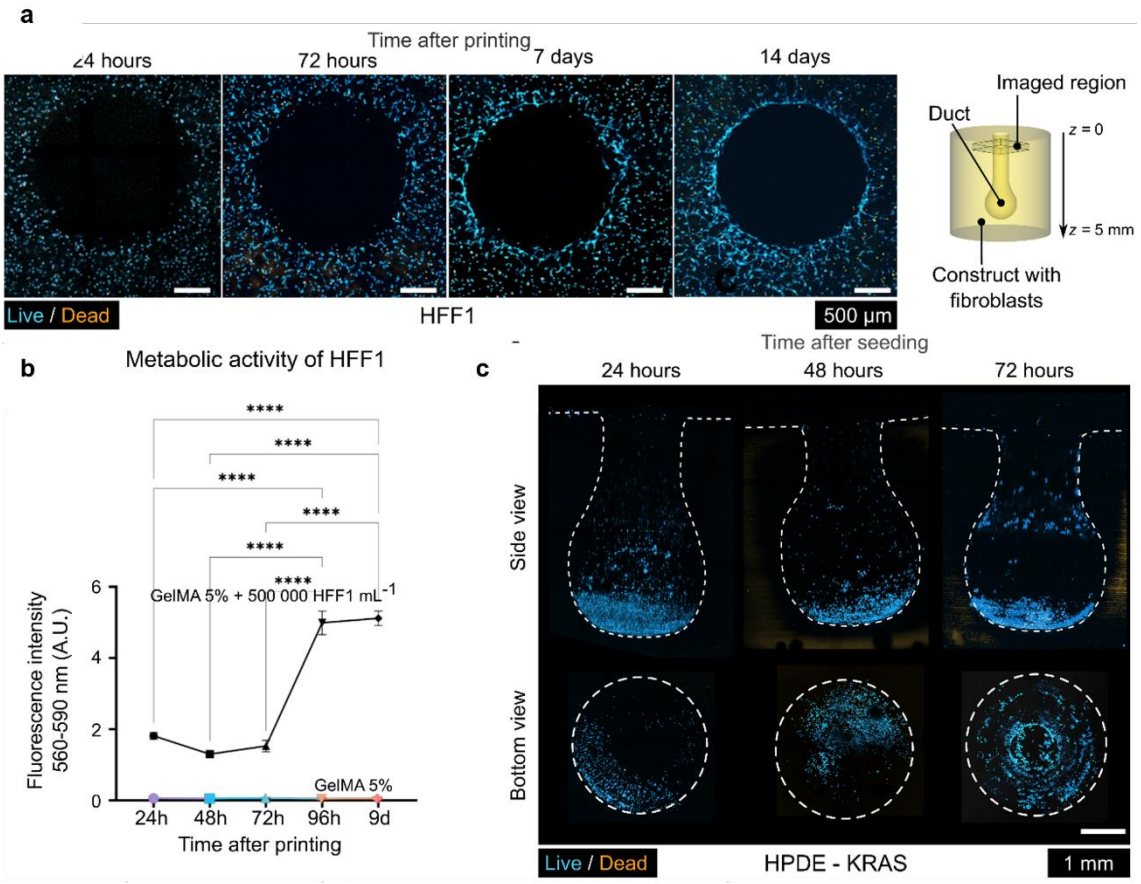

Fig. 3.17 Viability of pancreatic ductal models. (a) Live/Dead assay of fibroblasts performed on different samples 1, 3, 7 and 14 days after volumetric bioprinting. A schematic shows the region where these microscopy images were acquired. Scale bars 500 µm. (b) Metabolic activity of fibroblasts (black) as a function of time, measured from the reduction of resazurin. Cell-free printed hydrogels (color) are used as a control (nGelMA + cells = 7, nGelMa = 7). Tukey's multiple comparisons test: *p < 0.05, **p < 0.01, ***p < 0.001, ****p < 0.0001. (c) Injected HPDE cells progress over time to line the inner face of the 3D bioprinted pancreatic model duct. Scale bar 1 mm.

In the meantime, the capacity of HPDE cells to epithelize the walls of the cavity (duct and acinus) of the bioprinted constructs was analyzed. For this, HPDE cells were injected into the GelMA bioprinted structures without fibroblasts. Fig. 3.17c shows microscopy images from a Live/Dead assay (calcein-AM and ethidium homodimer-1) of HPDE cells 24, 48, and 72 hours after seeding into the cavity of the constructs. Dashed lines indicate the contour of the cavity. The images, which correspond to the intensity sum over planes along 500 μm of the microscope's optical axis, show that HPDE cells covered larger extents of the duct walls with time and produced a lining of > 1 mm^2 72 hours after seeding. When co-cultured with fibroblasts, HPDE cells form large linings and invade the bulk, as shown with arrows in Fig. 3.18a. In Fig. 3.18b multi-channel fluorescence microscopy images of the duct wall of a fibroblast-laden construct co-cultured with HPDE-KRAS cells are reported.

3.3.2.3 Evaluation of cell-cell crosstalk within the VBP model

The effect of crosstalk between HPDE cells and HFF1 was studied by evaluating changes in the cytoskeleton composition of the latter. In particular, healthy HPDE (HPDE-wt) and HPDE overexpressing the KRAS mutation (HPDE-KRAS) were seeded in the fibroblast-laden hydrogels 4 days after the bioprinting process. The HFF1 recovery occurring during the first 96h, when the viability significantly increased, was exploited to implement the co-culture conditions. Immunofluorescence microscopy was performed on 300 μm thick transversal slices of HFF1-laden constructs containing HPDE-wt cells, HPDE-KRAS, and without HPDE cells as a control (n = 4 replicas for HPDE-wt 72 hours; n = 3 for all other treatments) at 5 and 7 days after printing (24 and 72 hours after HPDE seeding), as seen in Fig. 3.19. Thin slices of the gel obtained with a vibratome were used to guarantee that antibodies would penetrate evenly throughout the constructs and that all cells in co-culture could be imaged. Anti- α-SMA antibody, phalloidin-FITC (an actin marker), and DAPI (a DNA marker) were used to identify cells morphology and to evaluate the appearance of a myofibroblast phenotype associated with an increased expression of α-SMA. Qualitatively, fibroblasts in constructs seeded with HPDE-KRAS cells exhibited stronger expression of α-SMA, which increased with time (Fig. 3.19). An algorithm to automatically and blindly quantify the expression of α-SMA with respect to actin over hundreds of cells in several complete slices of the constructs was developed and the slices were imaged under a confocal microscope following a standardized protocol. The automated analysis used the DAPI signal to detect cells, from which it would then compute the ratio of the intensities of α-SMA vs. actin, a proxy of fibroblast activation, as shown in Fig. 3.20. This analysis showed that the mean fibroblast activation increased after exposure to HPDE-KRAS, but not so after exposure to the non-cancerous HPDE-wt. The level of fibroblast activation is also significantly higher after being in co-culture with HPDE-KRAS for 72 hours compared to 24 hours ($p = 0.018$) (Fig. 3.20b).

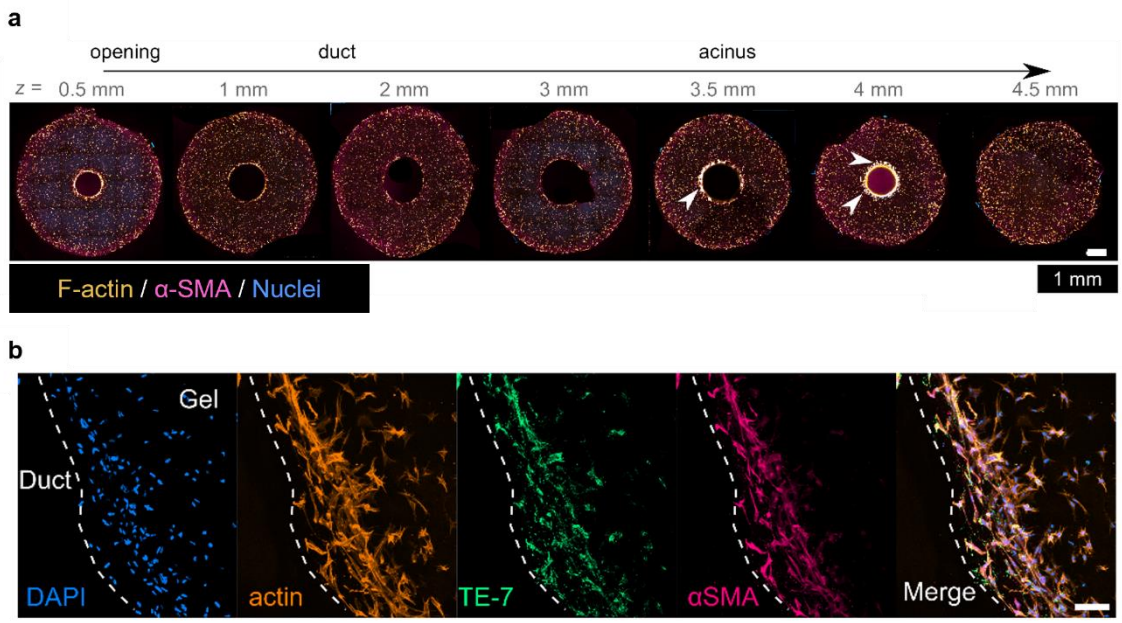

Fig. 3.18 Co-culture of stromal and epithelial cells inside the 3D bioprinted model. (a) Immunofluorescence micrographs of seven 300 µm thick slices of a VBP model taken 72 hours after HPDE-KRAS cells seeding and 5 days after bioprinting process. White arrows highlight migration of HPDE-KRAS cells inside the fibroblast-laden hydrogel. Scale bar 1 mm. (b) High-magnification multi-channel fluorescence microscopy images of the duct wall of a fibroblast-laden construct co-cultured with HPDE-KRAS cells. Scale bar 100 µm.

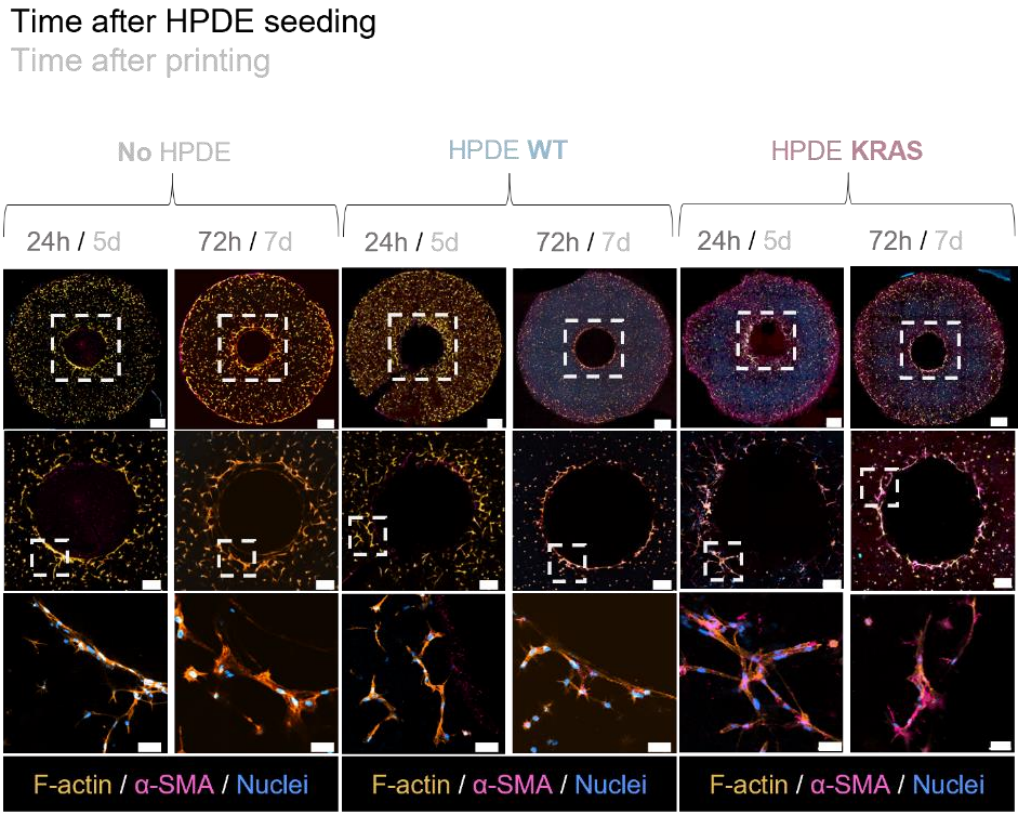

Fig. 3.19 Qualitative analysis of cancer-associated fibroblasts activation within the VBP model. Fluorescence microscopy images of full slices of constructs without HPDE cells and seeded with HPDE-wt or HPDE-KRAS cells 24 hours (5 days) and 72 hours (7 days) after bioprinting. Lower rows correspond to close-ups of the dashed regions. Scale bars 500 µm (top row), 200 µm (mid row) and 50 µm (bottom row).

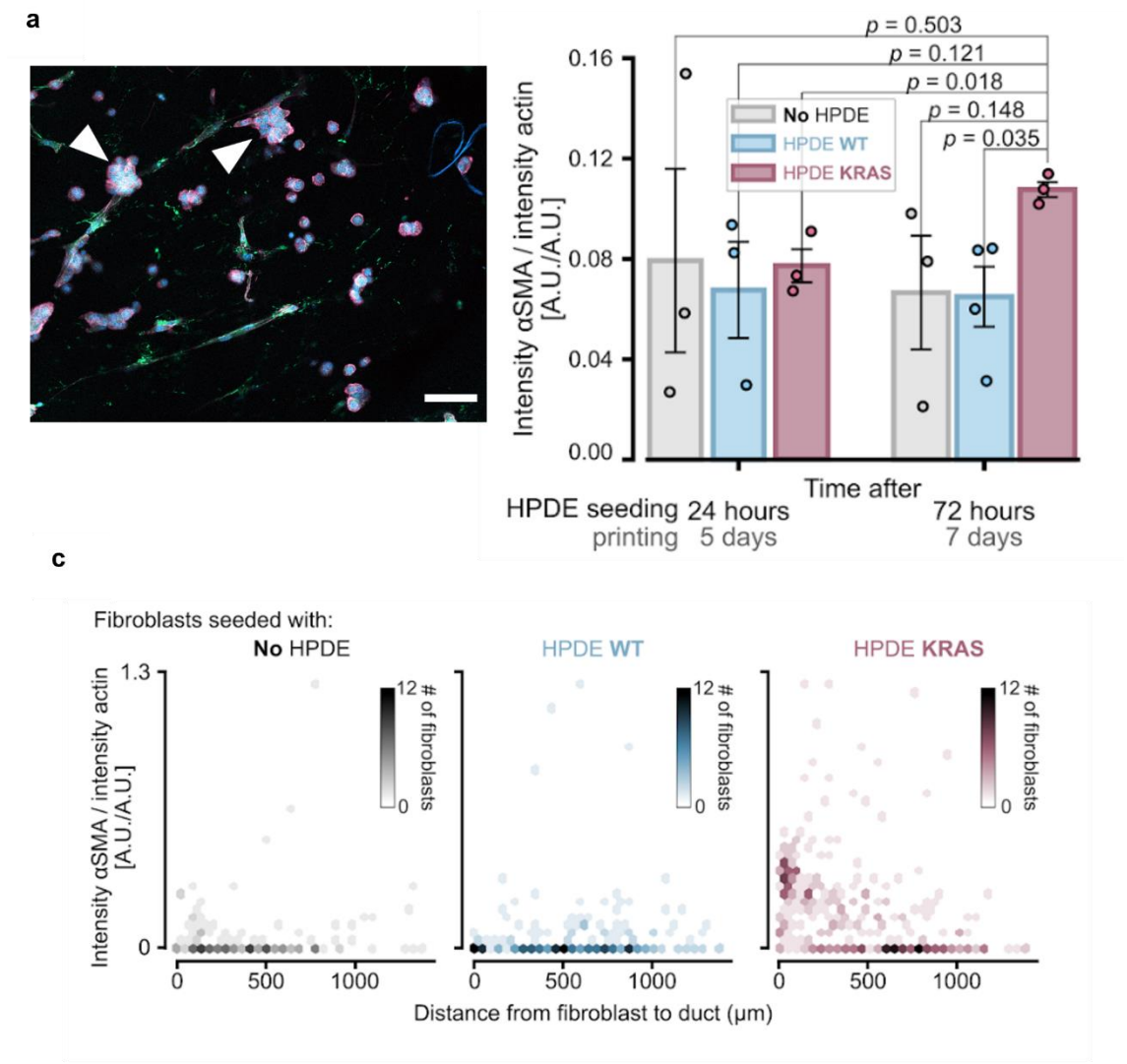

Fig. 3.20. Quantitative analysis of cancer-associated fibroblasts activation within the VBP model. (a) Fibroblasts (green) co-cultured with HPDE cells (pink), that form grape-like clusters of smaller round cells (white arrows). Scale bar 100 μm. (b) Ratio of fluorescence intensity of α-SMA vs. actin. (n = 4 for HPDE-wt 72 hours after seeding, n = 3 for all other treatments). Error bars indicate standard error of the mean. p-values come from one-way ANOVA tests. (c) Density maps of the ratio of α-SMA intensity over actin intensity in individual fibroblasts vs. distance from the cell to the edge of the duct. Data come from samples 7 days after printing (72 hours after seeding). Number of fibroblasts: nNo HPDE = 143, nHPDE wt = 231, nHPDE KRAS = 350.

The dependence of fibroblast activation with the distance to the duct was also studied at the single cell level. Fig. 3.20c shows these measurements, suggesting an increased activation for fibroblasts closer to the duct, where HPDE-KRAS cells laid. In contrast, fibroblasts co-cultured with HPDE-wt cells or with no HPDE cells did not exhibit a decaying degree of activation with distance to the duct. These results indicate that the activation of fibroblasts occurred predominantly when they are co-cultured with HPDE-KRAS cells and that the dependence of α-SMA expression on the distance from the duct is evident only in this condition.

3.3.3 Discussion

Despite several efforts focused on the investigation of pancreatic cancer progression over the past decades, pancreatic ductal adenocarcinoma (PDAC) remains one of the most lethal tumors, with the highest 1-year, 5-year and 10-year mortalities of any cancer type. Modeling the dynamic phenomena involved in tumor-stroma interplay is essential not only to increase the knowledge of the disease but also experiment with new and more effective treatments to cure it. Indeed, the stromal tissue surrounding the PDAC site represents a histopathological hallmark of pancreatic cancer[86–91] and plays a fundamental role in tumor progression[92,93].

In this study a 3D *in vitro* model of the exocrine pancreas which mimics the compartmentalized architecture of the native tissue and allows to recapitulate the stromal and pancreatic cancer cells crosstalk on the same miniaturized construct was developed. Human fibroblasts modeling the stromal component were co-cultured with human pancreatic epithelial cells, healthy or expressing the KRAS oncogene, reproducing the exocrine pancreatic tissue, respectively normal or pathological (Fig. 3.2).

To microfabricate the acinar- and ductal-like geometry, typical of the functional unit of the exocrine pancreas, tomographic volumetric bioprinting was adopted. This one-step, cell-friendly and scalable approach guaranteed high shape fidelity allowing to obtain in a few minutes a 3D cell-laden hydrogel incorporating a cavity, which is constituted of a duct converging to an enlarged lumen (acinus) (Fig. 3.15 and Fig. 3.16). The printing of relevant object shape for biological studies was obtained, as well as a suitable environment for the growth of stromal cells (HFF1) that remained viable and active for at least 2 weeks after the manufacturing process (Fig. 3.17a,b). This is in line with other works, which have cultured tomographically printed constructs that stayed viable for several weeks[15,20,94]. Therefore, the results proved the beneficial effects given by GelMA as bioink, matching with previous reports on the extensive use of this material in biomedical applications[95–99]. Moreover, by exploiting VBP features, the complex hollow structure of the exocrine pancreas can be fabricated without the use of a mold and without the need for sacrificial or support materials as opposed to more conventional (bio)printing and additive manufacturing methods that typically build 3D objects in a layer-by-layer fashion[100]. This innovative biofabrication approach also avoids the technical difficulties and time-consuming procedures associated with the assembling of different cellularized compartments into a unique 3D structure[4]. The cavity within the printed construct constitutes a biomimetic niche which can be easily epithelized by seeding the human pancreatic ductal epithelial cells, suspended in a proper volume of cell medium. The proliferation of HPDE cells was monitored over time and their ability to cover the inner walls of the lumen by growing as an epithelial monolayer was assessed, as already reported by other studies in literature[5,101]. However, the total coverage of the cavity has not been achieved during the experiment period (3 days) (Fig. 3.17c), which was found to be insufficient to reach confluence condition of epithelial cells on GelMA substrates[102]. Under co-culture conditions (Fig. 3.18) the activation of stromal cells was monitored by quantifying, through a custom-made Python code, the signal intensity coming from the expression of α-SMA proteins (Fig. 3.19 and Fig. 3.20). The results, showing a higher α-SMA expression in fibroblasts co-cultured with HPDE-KRAS rather than in contact with HPDE-wt cells, allow to validate this *in vitro* model as it can efficiently replicate the physiological inflammation cascade occurring in activated stromal cells[103–105]. Moreover, the developed model is the first to recapitulate the tumor-stroma interplay occurring in pancreatic cancer while also accurately reproducing the anatomical structure of the exocrine gland. The geometrical and morphological features of a tissue can affect the cell functionality and therefore represent another crucial aspect to consider in the design of a biomimetic model[3,106]. Although different engineering strategies have been adopted to obtain tubular lumen structures[3–5,38,101], they lack in fully creating the 3D acinar- and ductal-like

geometry[4,101] or in incorporating the stromal component[5,39]. However, this VBP model currently replicates the glandular structure with rescaled dimensions as compared to the physiological human gland (diameter of acinar portion 200 µm, of duct portion 50 µm). The resolution achieved in this work is comparable or better than that of other models replicating the morphology of the pancreatic gland, including a hollow duct[4,5]. Additional work should be performed to enhance the resolution of the printed cavity, to make it more anatomically relevant[39]. In this context, the methodology applied to produce the *in vitro* model allows for a highly versatile approach, therefore, this model could be further improved by incorporating other cells involved in pathology development. For instance, tissue-resident immune cells could be included inside the construct to assess the role of immune system in the early stages of pancreatic cancer progression.
Finally, this model recapitulating the tumor-associated fibroblasts activation could open new avenues to understand the role of tumor microenvironment in pancreatic cancer progression and offers a new and relevant platform to establish effective therapeutical strategies. The approach described in this work permits to overcome the limitations of the existing *in vitro* models that do not properly mimic the morphology, the cell composition and the cell-stroma interplay of the exocrine pancreas environment. In addition, it represents a valid alternative to the costly and low-throughput animal models which are ethically questionable and limited in emulating the stromal components of PDAC[33,34]. Indeed, the rapid fabrication process allows to obtain several scalable human models that can be tested and validated according to a high-throughput screening approach.

3.4 Conclusion

In this chapter, the development of different 3D *in vitro* models mimicking the complex three-dimensional microanatomy of the exocrine pancreas was described. Specifically, layer-by-layer approaches were used to obtain for the first time a macroscale FDM model and a microscale MEW model that accurately reproduce the half-structure of the complex gland morphology. In particular, the FDM model was used to preliminary assess the feasibility of reproducing the glandular structure by employing a layer-by-layer approach and to monitor the fibroblasts viability on PCL printed structures over several weeks. The ability of both PCL scaffolds (FDM and MEW scaffolds) in supporting the growth of stromal cells was demonstrated, as well as the achievement of a uniform and optimal distribution of human fibroblasts inside the 3D constructs. However, the MEW model revealed to be better in terms of biomimetic fibers size, and consequently biological stimuli to reach a better cell adhesion and growth rate. Therefore, it was used to study the interactions between human pancreatic ductal epithelial cells, seeded in the cavity of the MEW structure, and the surrounding stromal cells. The fully human MEW model resulted optimal in reproducing the natural compartmentalization typical of the exocrine pancreatic microenvironment and optimized co-culturing conditions were set within this work. Moreover, the ability of this model in recapitulating the IL-6 mediated inflammatory process occurring *in vivo* was demonstrated. Despite the layer-by-layer techniques used in this work allowed to fabricate scaffolds with controlled porosity and pore size, that are key features to affect the cell fate and favor the formation of new tissue, obtaining the complete acino-ductal model (close structure) could reveal time-consuming and poorly repeatable. The volumetric bioprinting, a recently developed and powerful printing technique, was used to fabricate acinar- and ductal-like structures in a single step. This biofabrication approach allowed the series production of several human models with shape-fidelity, high resolution and geometrical accuracy. The GelMA-based environment resulted optimal in

promoting the proliferation of stromal cells which remained viable and active for several weeks within the gel structure thus permitting a long follow-up.

The co-culture of human pancreatic ductal epithelial cells, healthy or overexpressing the KRAS oncogene, and stromal cells in this biofabricated *in vitro* model can recapitulate the pancreatic TME as confirmed by the stromal cells' activation through the tumor-stroma crosstalk. In particular, the ability of this model in reproducing the stromal cells activation in a very short period (3 days under co-culture and 7 days after biofabrication) was demonstrated.

Moreover, the construct can be monitored over time in an accessible and non-destructive way by microscopy to quantitively interrogate the model and easily get the information. These results validate our approach that is scalable and therefore potentially applicable in a personalized medicine workflow, in which the patients' own cells are used to build many models of the exocrine pancreas' microanatomy in a short period of time to rapidly adjust the therapy to the patient. This could enhance treatment outcomes and reduce healthcare costs. Thus, the demonstration of these fully human 3D models represents a powerful tool for the understanding of mechanisms implicated in pancreatic cancer insurgence and for testing new diagnostic and therapeutical approaches.

References

1. Kota J, Hancock J, Kwon J, et al. Pancreatic cancer: Stroma and its current and emerging targeted therapies. Cancer Lett 2017; 391: 38–49.
2. Pothula SP, Pirola RC, Wilson JS, et al. Pancreatic stellate cells: Aiding and abetting pancreatic cancer progression. Pancreatology 2020; 20: 409–418.
3. Hajiabbas M, D'Agostino C, Simińska-Stanny J, et al. Bioengineering in salivary gland regeneration. J Biomed Sci 2022 291 2022; 29: 1–24.
4. Gupta P, Pérez-Mancera PA, Kocher H, et al. A Novel Scaffold-Based Hybrid Multicellular Model for Pancreatic Ductal Adenocarcinoma—Toward a Better Mimicry of the in vivo Tumor Microenvironment. Front Bioeng Biotechnol; 8. Epub ahead of print 2020. DOI: 10.3389/fbioe.2020.00290.
5. Venis SM, Moon HR, Yang Y, et al. Engineering of a functional pancreatic acinus with reprogrammed cancer cells by induced: PTF1a expression. Lab Chip 2021; 21: 3675–3685.
6. Charbonneau AM, Kinsella JM, Tran SD. 3D cultures of salivary gland cells in native or gelled egg yolk plasma, combined with egg white and 3D-printing of gelled egg yolk plasma. Materials (Basel) 2019; 12: 1–16.
7. Jain P, Kathuria H, Dubey N. Advances in 3D bioprinting of tissues/organs for regenerative medicine and in-vitro models. Biomaterials 2022; 287: 121639.
8. Rajan K, Samykano M, Kadirgama K, et al. Fused deposition modeling: process, materials, parameters, properties, and applications. Int J Adv Manuf Technol 2022; 120: 1531–1570.
9. Bachs-Herrera A, Yousefzade O, Del Valle LJ, et al. Melt electrospinning of polymers: Blends, nanocomposites, additives and applications. Appl Sci 2021; 11: 1–39.
10. Loewner S, Heene S, Baroth T, et al. Recent advances in melt electro writing for tissue engineering for 3D printing of microporous scaffolds for tissue engineering. Front Bioeng Biotechnol; 10. Epub ahead of print 17 August 2022. DOI: 10.3389/fbioe.2022.896719.
11. Hutmacher DW, Dalton PD. Melt electrospinning. Chem - An Asian J 2011; 6: 44–56.
12. Kade JC, Dalton PD. Polymers for Melt Electrowriting. Adv Healthc Mater 2021; 10: 2001232.

13. Sivan M, Madheswaran D, Asadian M, et al. Plasma treatment effects on bulk properties of polycaprolactone nanofibrous mats fabricated by uncommon AC electrospinning: A comparative study. Surf Coatings Technol; 399. Epub ahead of print 2020. DOI: 10.1016/j.surfcoat.2020.126203.
14. Patelli A, Verga E, Nodari L, et al. A customised atmospheric pressure plasma jet for conservation requirements. IOP Conf Ser Mater Sci Eng; 364. Epub ahead of print 2018. DOI: 10.1088/1757-899X/364/1/012079.
15. Bernal PN, Bouwmeester M, Madrid-Wolff J, et al. Volumetric Bioprinting of Organoids and Optically Tuned Hydrogels to Build Liver-Like Metabolic Biofactories. Adv Mater 2022; 34: 2110054.
16. Madrid-Wolff J, Boniface A, Loterie D, et al. Controlling Light in Scattering Materials for Volumetric Additive Manufacturing. Adv Sci 2022; 9: 2105144.
17. Gehlen J, Qiu W, Müller R, et al. Volumetric Tomographic 3D Bioprinting of Heterocellular Bone- like Tissues in Seconds. 2021; 1–24.
18. Rizzo R, Ruetsche D, Liu H, et al. Optimized Photoclick (Bio)Resins for Fast Volumetric Bioprinting. Adv Mater; 33. Epub ahead of print 2021. DOI: 10.1002/adma.202102900.
19. Sola A, Bertacchini J, D'Avella D, et al. Development of solvent-casting particulate leaching (SCPL) polymer scaffolds as improved three-dimensional supports to mimic the bone marrow niche. Mater Sci Eng C 2019; 96: 153–165.
20. Bernal PN, Delrot P, Loterie D, et al. Volumetric Bioprinting of Complex Living-Tissue Constructs within Seconds. Adv Mater 2019; 31: 1904209.
21. Loterie D, Delrot P, Moser C. High-resolution tomographic volumetric additive manufacturing. Nat Commun 2020; 11: 1–6.
22. Kelly BE, Bhattacharya I, Heidari H, et al. Volumetric additive manufacturing via tomographic reconstruction. Science (80-) 2019; 363: 1075–1079.
23. Abràmoff MD, Magalhães PJ, Ram SJ. Image Processing with ImageJ. Biophotonics Int 2004; 11: 36–42.
24. Booth JP, Mozetič M, Nikiforov A, et al. Foundations of plasma surface functionalization of polymers for industrial and biological applications. Plasma Sources Sci Technol; 31. Epub ahead of print 2022. DOI: 10.1088/1361-6595/ac70f9.
25. Lee JH, Kim SK, Khawar IA, et al. Microfluidic co-culture of pancreatic tumor spheroids with stellate cells as a novel 3D model for investigation of stroma-mediated cell motility and drug resistance. J Exp Clin Cancer Res 2018; 37: 1–12.
26. Jeong SY, Lee JH, Shin Y, et al. Co-culture of tumor spheroids and fibroblasts in a collagen matrix-incorporated microfluidic chip mimics reciprocal activation in solid tumor microenvironment. PLoS One 2016; 11: e0159013.
27. Fujiwara M, Kanayama K, Hirokawa YS, et al. ASF-4-1 fibroblast-rich culture increases chemoresistance and mTOR expression of pancreatic cancer BxPC-3 cells at the invasive front in vitro, and promotes tumor growth and invasion in vivo. Oncol Lett 2016; 11: 2773.
28. Weeber F, Ooft SN, Dijkstra KK, et al. Tumor Organoids as a Pre-clinical Cancer Model for Drug Discovery. Cell Chem Biol 2017; 24: 1092–1100.
29. Kapałczyńska M, Kolenda T, Przybyła W, et al. 2D and 3D cell cultures - a comparison of different types of cancer cell cultures. Arch Med Sci 2018; 14: 910–919.
30. Desoize B. Multicellular resistance: a paradigm for clinical resistance? Crit Rev Oncol Hematol 2000; 36: 193–207.

31. Brancato V, Oliveira JM, Correlo VM, et al. Could 3D models of cancer enhance drug screening? Biomaterials; 232. Epub ahead of print 2020. DOI: 10.1016/j.biomaterials.2019.119744.
32. Shichi Y, Sasaki N, Michishita M, et al. Enhanced morphological and functional differences of pancreatic cancer with epithelial or mesenchymal characteristics in 3D culture. Sci Rep 2019; 9: 10871.
33. Fang Y, Eglen RM. Three-Dimensional Cell Cultures in Drug Discovery and Development. SLAS Discov 2017; 22: 456–472.
34. Laschke MW, Menger MD. Life is 3D: Boosting Spheroid Function for Tissue Engineering. Trends Biotechnol 2017; 35: 133–144.
35. Tomás-Bort E, Kieler M, Sharma S, et al. 3D approaches to model the tumor microenvironment of pancreatic cancer. Theranostics 2020; 10: 5074–5089.
36. Monteiro M V., Ferreira LP, Rocha M, et al. Advances in bioengineering pancreatic tumor-stroma physiomimetic Biomodels. Biomaterials 2022; 287: 121653.
37. Bradney MJ, Venis SM, Yang Y, et al. A Biomimetic Tumor Model of Heterogeneous Invasion in Pancreatic Ductal Adenocarcinoma. Small 2020; 1905500: 1–10.
38. Sung JH, Shuler ML. Microtechnology for mimicking in vivo tissue environment. Ann Biomed Eng 2012; 40: 1289–1300.
39. Randriamanantsoa S, Papargyriou A, Maurer HC, et al. Spatiotemporal dynamics of self-organized branching in pancreas-derived organoids. Nat Commun 2022; 13: 1–15.
40. Suntornnond R, An J, Chua CK. Effect of gas plasma on polycaprolactone (PCL) membrane wettability and collagen type i immobilized for enhancing cell proliferation. Mater Lett 2016; 171: 293–296.
41. Ushiki T. Collagen fibers, reticular fibers and elastic fibers. A comprehensive understanding from a morphological viewpoint. Archives of Histology and Cytology 2002; 65: 109–126.
42. Cao K, Zhang F, Zaeri A, et al. Advances in design and quality of melt electrowritten scaffolds. Mater Des; 226. Epub ahead of print 1 February 2023. DOI: 10.1016/J.MATDES.2023.111618.
43. Loewner S, Heene S, Baroth T, et al. Recent advances in melt electro writing for tissue engineering for 3D printing of microporous scaffolds for tissue engineering. Front Bioeng Biotechnol 2022; 10: 1481.
44. Saidy NT, Shabab T, Bas O, et al. Melt Electrowriting of Complex 3D Anatomically Relevant Scaffolds. Front Bioeng Biotechnol 2020; 8: 793.
45. Peiffer QC, de Ruijter M, van Duijn J, et al. Melt electrowriting onto anatomically relevant biodegradable substrates: Resurfacing a diarthrodial joint. Mater Des 2020; 195: 109025.
46. Brooks-Richards TL, Paxton NC, Allenby MC, et al. Dissolvable 3D printed PVA moulds for melt electrowriting tubular scaffolds with patient-specific geometry. Mater Des 2022; 215: 110466.
47. Saha U, Nairn R, Keenan O, et al. A Deeper Insight into the Influence of the Electric Field Strength When Melt-Electrowriting on Non-Planar Surfaces. Macromol Mater Eng 2021; 306: 2100496.
48. Constante G, Apsite I, Alkhamis H, et al. 4D Biofabrication Using a Combination of 3D Printing and Melt-Electrowriting of Shape-Morphing Polymers. ACS Appl Mater Interfaces 2021; 13: 12767–12776.
49. van Genderen AM, Jansen K, Kristen M, et al. Topographic Guidance in Melt-Electrowritten Tubular Scaffolds Enhances Engineered Kidney Tubule Performance. Front Bioeng Biotechnol; 8. Epub ahead of print 18 January 2021. DOI: 10.3389/fbioe.2020.617364.

50. Liashenko I, Hrynevich A, Dalton PD. Designing Outside the Box: Unlocking the Geometric Freedom of Melt Electrowriting using Microscale Layer Shifting. Adv Mater 2020; 32: 2001874.
51. Bakirci E, Schaefer N, Dahri O, et al. Melt Electrowritten In Vitro Radial Device to Study Cell Growth and Migration. Adv Biosyst 2020; 4: 2000077.
52. Arif ZU, Khalid MY, Noroozi R, et al. Recent advances in 3D-printed polylactide and polycaprolactone-based biomaterials for tissue engineering applications. International Journal of Biological Macromolecules 2022; 218: 930–968.
53. Korpershoek J V., Ruijter M de, Terhaard BF, et al. Potential of Melt Electrowritten Scaffolds Seeded with Meniscus Cells and Mesenchymal Stromal Cells. Int J Mol Sci 2021; 22: 11200.
54. Backes EH, Harb SV, Beatrice CAG, et al. Polycaprolactone usage in additive manufacturing strategies for tissue engineering applications: A review. J Biomed Mater Res Part B Appl Biomater 2022; 110: 1479–1503.
55. Großhaus C, Bakirci E, Berthel M, et al. Melt Electrospinning of Nanofibers from Medical-Grade Poly(ε-Caprolactone) with a Modified Nozzle. Small 2020; 16: 2003471.
56. Kumar N, Joisher H, Ganguly A. Polymeric scaffolds for pancreatic tissue engineering: A review. Rev Diabet Stud 2017; 14: 334–353.
57. Yang X, Wang Y, Zhou Y, et al. The Application of Polycaprolactone in Three-Dimensional Printing Scaffolds for Bone Tissue Engineering. Polymers (Basel) 2021; 13: 2754.
58. Neves SC, Moreira Teixeira LS, Moroni L, et al. Chitosan/Poly(ε-caprolactone) blend scaffolds for cartilage repair. Biomaterials 2011; 32: 1068–1079.
59. Malakpour Permlid A, Roci P, Fredlund E, et al. Unique animal friendly 3D culturing of human cancer and normal cells. Toxicol Vitr 2019; 60: 51–60.
60. Pothula SP, Pirola RC, Wilson JS, et al. Pancreatic stellate cells: Aiding and abetting pancreatic cancer progression. Pancreatology 2020; 20: 409–418.
61. Koikawa K, Ohuchida K, Ando Y, et al. Basement membrane destruction by pancreatic stellate cells leads to local invasion in pancreatic ductal adenocarcinoma. Cancer Lett 2018; 425: 65–77.
62. Kuen J, Darowski D, Kluge T, et al. Pancreatic cancer cell/fibroblast co-culture induces M2 like macrophages that influence therapeutic response in a 3D model. PLoS One 2017; 12: e0182039.
63. van Duijneveldt G, Griffin MDW, Putoczki TL. Emerging roles for the IL-6 family of cytokines in pancreatic cancer. Clin Sci 2020; 134: 2091–2115.
64. Öhlund D, Handly-Santana A, Biffi G, et al. Distinct populations of inflammatory fibroblasts and myofibroblasts in pancreatic cancer. J Exp Med 2017; 214: 579–596.
65. Feurino LW, Zhang Y, Bharadwaj U, et al. IL-6 stimulates Th2 type cytokine secretion and upregulates VEGF and NRP-1 expression in pancreatic cancer cells. Cancer Biol Ther 2007; 6: 1096–1100.
66. Ancrile B, Lim K-H, Counter CM. Oncogenic Ras-induced secretion of IL6 is required for tumorigenesis. Genes Dev 2007; 21: 1714–1719.
67. Nagasaki T, Hara M, Nakanishi H, et al. Interleukin-6 released by colon cancer-associated fibroblasts is critical for tumour angiogenesis: anti-interleukin-6 receptor antibody suppressed angiogenesis and inhibited tumour–stroma interaction. Br J Cancer 2014; 110: 469–478.
68. Ebrahimi B, Tucker SL, Li D, et al. Cytokines in pancreatic carcinoma. Cancer 2004; 101: 2727–2736.
69. Wigmore S, Fearon K, Sangster K, et al. Cytokine regulation of constitutive production of interleukin-8 and -6 by human pancreatic cancer cell lines and serum cytokine concentrations in patients with pancreatic cancer. Int J Oncol. Epub ahead of print 1 October 2002. DOI: 10.3892/ijo.21.4.881.

70. Talar-Wojnarowska R, Gasiorowska A, Smolarz B, et al. Clinical Significance of Interleukin-6 (Il-6) Gene Polymorphism and Il-6 Serum Level in Pancreatic Adenocarcinoma and Chronic Pancreatitis. Dig Dis Sci 2009; 54: 683–689.
71. Barber MD, Fearon KCH, Ross JA. Relationship of serum levels of interleukin-6, soluble interleukin-6 receptor and tumour necrosis factor receptors to the acute-phase protein response in advanced pancreatic cancer. Clin Sci 1999; 96: 83–87.
72. Okada S, Okusaka T, Ishii H, et al. Elevated Serum Interleukin-6 Levels in Patients with Pancreatic Cancer. Jpn J Clin Oncol 1998; 28: 12–15.
73. Błogowski W, Deskur A, Budkowska M, et al. Selected Cytokines in Patients with Pancreatic Cancer: A Preliminary Report. PLoS One 2014; 9: e97613.
74. Mroczko B, Groblewska M, Gryko M, et al. Diagnostic usefulness of serum interleukin 6 (IL-6) and C-reactive protein (CRP) in the differentiation between pancreatic cancer and chronic pancreatitis. J Clin Lab Anal 2010; 24: 256–261.
75. Chen K, Wang Q, Li M, et al. Single-cell RNA-seq reveals dynamic change in tumor microenvironment during pancreatic ductal adenocarcinoma malignant progression. EBioMedicine 2021; 66: 103315.
76. Van AI, Bulcke D, Bogdanov B, et al. Structural and Rheological Properties of Methacrylamide Modified Gelatin Hydrogels. Epub ahead of print 2000. DOI: 10.1021/bm990017d.
77. Paszke A, Gross S, Massa F, et al. PyTorch: An Imperative Style, High-Performance Deep Learning Library. Neural Inf Process Syst 2019; 32.
78. Van Der Weken D, Nachtegael M, Kerre EE. Using similarity measures and homogeneity for the comparison of images. Image Vis Comput 2004; 22: 695–702.
79. Preibisch S, Saalfeld S, Tomancak P. Globally optimal stitching of tiled 3D microscopic image acquisitions. Bioinformatics 2009; 25: 1463.
80. Hunter JD. Matplotlib: A 2D graphics environment. Comput Sci Eng 2007; 9: 90–95.
81. Waskom ML. seaborn: statistical data visualization. J Open Source Softw 2021; 6: 3021.
82. McKinney W. Data Structures for Statistical Computing in Python. In: Proceedings of the 9th Python in Science Conference. SciPy, 2010, pp. 56–61.
83. Wex C, Fröhlich M, Brandstädter K, et al. Experimental analysis of the mechanical behavior of the viscoelastic porcine pancreas and preliminary case study on the human pancreas. J Mech Behav Biomed Mater 2015; 41: 199–207.
84. Kinstlinger IS, Saxton SH, Calderon GA, et al. Generation of model tissues with dendritic vascular networks via sacrificial laser-sintered carbohydrate templates. DOI: 10.1038/s41551-020-0566-1.
85. Lee GM, Kim S jeong, Kim EM, et al. Free radical-scavenging composite gelatin methacryloyl hydrogels for cell encapsulation. Acta Biomater 2022; 149: 96–110.
86. Procacci P, Moscheni C, Sartori P, et al. Tumor–Stroma Cross-Talk in Human Pancreatic Ductal Adenocarcinoma: A Focus on the Effect of the Extracellular Matrix on Tumor Cell Phenotype and Invasive Potential. Cells 2018, Vol 7, Page 158 2018; 7: 158.
87. Matsuzawa A, Cortesi M, Zanoni M, et al. Pancreatic Cancer and Cellular Senescence: Tumor Microenvironment under the Spotlight. Int J Mol Sci 2022, Vol 23, Page 254 2021; 23: 254.
88. Thomas D, Radhakrishnan P. Tumor-stromal crosstalk in pancreatic cancer and tissue fibrosis. Mol Cancer; 18. Epub ahead of print 21 January 2019. DOI: 10.1186/S12943-018-0927-5.
89. Hadden M, Mittal A, Samra J, et al. Mechanically stressed cancer microenvironment: Role in pancreatic cancer progression. Biochim Biophys Acta - Rev Cancer 2020; 1874: 188418.

90. Gardian K, Janczewska S, Olszewski WL, et al. Analysis of Pancreatic Cancer Microenvironment: Role of Macrophage Infiltrates and Growth Factors Expression. J Cancer 2012; 3: 285.
91. Farrow B, Albo D, Berger DH. The Role of the Tumor Microenvironment in the Progression of Pancreatic Cancer. J Surg Res 2008; 149: 319–328.
92. Ho WJ, Jaffee EM, Zheng L. The tumour microenvironment in pancreatic cancer — clinical challenges and opportunities. Nature Reviews Clinical Oncology 2020; 17: 527–540.
93. Sperb N, Tsesmelis M, Wirth T. Crosstalk between tumor and stromal cells in pancreatic ductal adenocarcinoma. International Journal of Molecular Sciences 2020; 21: 1–23.
94. Ning L, Shim J, Tomov ML, et al. A 3D Bioprinted in vitro Model of Neuroblastoma Recapitulates Dynamic Tumor-Endothelial Cell Interactions Contributing to Solid Tumor Aggressive Behavior. Adv Sci 2022; 9: 2200244.
95. Colosi C, Shin SR, Manoharan V, et al. Microfluidic Bioprinting of Heterogeneous 3D Tissue Constructs Using Low-Viscosity Bioink. Adv Mater 2016; 28: 677-684a.
96. Kilic Bektas C, Hasirci V. Cell loaded 3D bioprinted GelMA hydrogels for corneal stroma engineering. Biomater Sci 2020; 8: 438–449.
97. Billiet T, Gevaert E, De Schryver T, et al. The 3D printing of gelatin methacrylamide cell-laden tissue-engineered constructs with high cell viability. Biomaterials 2014; 35: 49–62.
98. Klotz BJ, Gawlitta D, Rosenberg AJWP, et al. Gelatin-Methacryloyl Hydrogels: Towards Biofabrication-Based Tissue Repair. Trends Biotechnol 2016; 34: 394–407.
99. Alexa RL, Iovu H, Ghitman J, et al. 3D-printed gelatin methacryloyl-based scaffolds with potential application in tissue engineering. Polymers (Basel) 2021; 13: 1–17.
100. Moroni L, Boland T, Burdick JA, et al. Biofabrication: A Guide to Technology and Terminology. Trends Biotechnol 2018; 36: 384–402.
101. Moon HR, Ozcelikkale A, Yang Y, et al. An engineered pancreatic cancer model with intra-tumoral heterogeneity of driver mutations. Lab Chip 2020; 20: 3720–3732.
102. Pamplona R, González-Lana S, Romero P, et al. Tuning of Mechanical Properties in Photopolymerizable Gelatin-Based Hydrogels for In Vitro Cell Culture Systems. ACS Appl Polym Mater 2023; 5: 1487–1498.
103. Lai BFL, Lu RXZ, Hu Y, et al. Recapitulating Pancreatic Tumor Microenvironment through Synergistic Use of Patient Organoids and Organ-on-a-Chip Vasculature. Adv Funct Mater 2020; 2000545: 1–16.
104. Lazzari G, Nicolas V, Matsusaki M, et al. Multicellular spheroid based on a triple co-culture: A novel 3D model to mimic pancreatic tumor complexity. Acta Biomater 2018; 78: 296–307.
105. Monteiro M V., Rocha M, Gaspar VM, et al. Programmable Living Units for Emulating Pancreatic Tumor-Stroma Interplay. Adv Healthc Mater 2022; 2102574.
106. Downing TL, Soto J, Morez C, et al. Biophysical regulation of epigenetic state and cell reprogramming. Nat Mater 2013; 12: 1154–1162.
107. Yoon HJ, Shin SR, Cha JM, et al. Cold Water Fish Gelatin Methacryloyl Hydrogel for Tissue Engineering Application. PLoS One 2016; 11: e0163902.

Chapter IV
Conclusive remarks

4.1 General discussion

Pancreatic ductal adenocarcinoma (PDAC), commonly known as pancreatic cancer, is the most frequent type of exocrine pancreas tumors and one of the leading causes of cancer-related death worldwide with a five-year survival rate of below 9%[1,2]. The main reason that leads to consider PDAC a notably aggressive disease concerns the rapid cancer's evolution without clear symptoms in the early stages, resulting in a late diagnosis and poor clinical prognosis.

In addition, the unique bioarchitecture of the pancreatic tumor microenvironment (TME) weakens the effectiveness of the current treatments that, despite the advances in the discovery of new therapeutic strategies, result insufficient to treat this particularly aggressive pathology[3,4].

In particular, the PDAC microenvironment is mainly composed by a desmoplastic stroma which strongly affects the tumor's evolution and represents a barrier against chemotherapy and radiotherapy[5–8]. The stroma is generated by the excessive extracellular matrix (ECM) deposition principally from the pancreatic stellate cells (PSCs) that trigger an intense desmoplastic reaction within the tissue surrounding the cancer cells[8,9]. More specifically, PSCs are normally located in the periacinar space around the acinar and ductal cells constituting the fundamental unit of the exocrine pancreas and the region where the pancreatic intraepithelial neoplasia (PanIN) occurs[3,10]. During tumorigenesis, the PSCs that are in a quiescent state become active and change their morphology in a spindle-shaped, exhibiting a myofibroblasts-like phenotype. Their primary activation is the result of an inflammatory stimulus which causes the production of cytokines such as the interleukin-6 (IL-6) by PSCs, which induce the mutation of oncogenes (mainly KRAS oncogene) triggering the progression from PanIN to PDAC[5,11].

Even though important risk factors can contribute to the evolution of pancreatic cancer (like smoking, obesity, type 2 diabetes, chronic pancreatitis, and alcoholism[6]) and although the mechanisms of maturation from the neoplasia are well documented[12,13], the alterations that give rise to the early lesions (PanIN) remain still unclear[14].

For these reasons, current research is focusing on the development of PDAC *in vitro* models for a deeper understanding of this pathology, the identification of new biomarkers and the establishment of screening tests, in order to enable an earlier detection of pancreatic cancer thus improving the prognosis[15–20]. Indeed, *in vitro* models represent an important alternative for animal experiments and powerful tools for biomedical research, drug discovery, diagnostics, and regenerative medicine. 2D models, cancer-on-a-chip platforms, multicellular spheroids, organoids and 3D biofabricated constructs (scaffolds or hydrogel-based models) are the currently available bioengineered models mimicking the pancreatic tumor-stroma interplay[21].

However, although recent studies have shown the possibility of modeling the PDAC microenvironment *in vitro*[15,16,18,22–27], the tumor-stroma crosstalk remains extremely challenging to be reproduced and monitored in functionally effective models[28–30].

The main purpose of this PhD project is to reproduce the functional unit of the exocrine pancreas, constituted by epithelial and stromal cells. Specifically, this work aims at developing human *in vitro* models that allow to analyze the PDAC-stroma interplay and the mechanisms implicated during the initial stage of tumor progression. In detail, different approaches were explored to fabricate devices that can be classified as two-dimensional (2D), two-and-a-half-dimensional (2.5D) and three-dimensional (3D) models. The latter were obtained by layer-by-layer approaches (FDM and MEW models) and tomographic volumetric bioprinting (VBP model), respectively.

Each model, although showing advantages and limitations, represented an important step in the process toward the development of a valuable and effective *in vitro* platform for the study of pancreatic cancer.

Moreover, all the here designed and fabricated models constitute, for different reasons, innovative engineering strategies that go beyond the state-of-the-art in cancer research.

Specifically, the 2D transwell-based model and the PDAC-on-chip can be defined, for the presence of the electrospun biomimetic membrane, a novelty among the existing 2D and microfluidic systems modeling the exocrine pancreatic tissue. The 2D model, although representing a simplified replica of the PDAC microenvironment, revealed useful to get important information on co-culturing conditions and cells interactions that were then used to implement advance engineering tools towards increasing model biologically relevancy. For instance, the transwell-based system allowed to preliminary assess the reciprocal influence of different cell types (*i.e.*, HFF1 and HPDE cells). Indeed, by using the 2D platform, the behavior of human fibroblasts in co-culture with healthy and KRAS-mutated epithelial cells was studied, as well as the ability of HFF1 cell line in reproducing the stromal component. In particular, the increased Il-6 release and the changes in cell morphology of fibroblasts co-cultured with HPDE-KRAS cells led us to consider HFF1 as representative of the stromal cells. Therefore, HFF1 cell line was also used in the following developed models since the differences with PSCs are minimal[31], with the advantage of major resistance and stability of functions over extended *in vitro* passages. Indeed, despite the genetic differences between PSCs and HFF1[32], the use of fibroblasts from non-pancreatic origins has been helpful for understanding the relationship between stromal and cancer cells, as many studies have demonstrated[21,33–36]. Moreover, this simplified model was employed to optimize the co-culture conditions, such as epithelial-stromal cells ratio and the co-culture medium composition.

The PDAC-on-chip, consisting of a multilayer microfluidic device, represented an effective tool in reproducing the PDAC microenvironment at a miniaturized scale. Indeed, the presence of collagen gel inside the chip allowed to replicate the composition of the pancreatic TME, as PDAC stroma is mainly constituted by type I collagen[37]. The here developed PDAC-on-chip was employed to analyze the state of PSCs, HFF1 and HPDE-KRAS in terms of cell viability, proliferative capability and cell morphology. In fact, this 2.5D model permitted to perform tests and analyses in a fast and accessible manner, while also representing (mainly because of the presence of the collagen gel) a more biomimetic model compared to the transwell-based model. Findings showed that HFF1 in the collagen matrix changed from a relatively short and flat shape to a myofibroblasts-like shape with stress fiber formation and increased expression of α-SMA associated with higher IL-6 release when co-cultured with HPDE-KRAS supernatant.

Furthermore, results proved that this system can be used to test the efficacy of drugs on pancreatic cancer cells, allowing the administration of single or multiple drugs both in contact to epithelial, as well as stromal cells, and a continuous monitoring of the effect of the therapeutic treatment on both cell populations can be easily performed thanks to the presence of the electrospun membrane which confines cells in a specific compartment of the chip.

However, PDAC-on-chip fails to mimic the 3D complex gland morphology proper of the functional unit of exocrine pancreas. So far, only a few novel studies in literature focus on the development of biomimetic platforms reproducing the microanatomy (in terms of 3D architecture and cellular composition) of the exocrine pancreas and lack to resemble the native compartmentalized architecture of tumor microenvironment that is widely recognized to affect cell functionality and cancer-cell response to therapeutics[38–40]. In particular, the glandular complex geometry has been reproduced in simplified ways by employing different techniques, that have disadvantages such as the low reproducibility, throughput and shape fidelity. In particular, they still fail in fully replicating the acino-ductal morphology[41,42] or in incorporating the stromal components[43,44]. The layer-by-layer techniques used in this thesis project allowed to obtain macro- and microscale models replicating the half-structure of the complex gland morphology.

The FDM model, despite useful to preliminary assess the feasibility of reproducing the glandular structure by employing a layer-by-layer approach and to monitor the fibroblasts viability on PCL printed structures over several weeks, resulted inadequately biomimetic as compared to the MEW model. Indeed, MEW permitted to achieve better resolutions of the printed structures, that have dimensions about four times smaller than those of FDM constructs. In particular, cells growing in MEW scaffolds experience physiological stimuli, since the fibers have similar diameter to natural ECM fibers (ranging from 1 to 20 μm[45]). An average fibers size of 17 μm was achieved in MEW structures, compared to 185 μm in FDM scaffolds. These features make the MEW model suitable for long term culture of human fibroblasts, as confirmed by the results showing the ability of MEW constructs in supporting the growth of HFF1 and the formation of a stromal tissue after 4 weeks in culture. These studies led us to proceed with the implementation of co-culture conditions only in MEW scaffolds, by seeding HPDE cells in the cavity of the structures, where HFF1 were allowed to grow for 2 weeks. The biomimicry of this model was analyzed in terms of (i) compartmentalization of PDAC microenvironment and (ii) fibroblasts inflammation. HPDE-KRAS cells remained collimated in the cavity up to 10 days of co-culture period (14 days) and then started to migrate within the scaffold and on the scaffold upper surface. This experiment allowed us to set the optimal protocol for co-culture implementation within the MEW structure: 14 days of fibroblasts culture alone plus 10 days of fibroblasts and epithelial cells co-culture. The fibroblasts inflammation, on the other hand, was evaluated by monitoring the release of IL-6 in supernatants collected from monocultures (*i.e.*, HFF1) and co-cultures (*i.e.*, HFF1+HPDE-KRAS; HFF1+HPDE-wt) 2, 3, 10 and 14 days after epithelial cells seeding. Results indicated that the MEW model truly recapitulates the *in vivo* pathological situation, involving IL-6 secretion by fibroblasts when inflamed by cancer cells. Indeed, a significant increase in IL-6 release by fibroblasts in co-culture with HPDE-KRAS cells for 2 and 3 days was observed, in comparison with HFF1 alone or HFF1 under co-culture with HPDE-wt cells. Interestingly, the differences in IL-6 concentrations of fibroblasts co-cultured with KRAS-mutated or healthy epithelial cells resulted enhanced in this 3D model with respect to the 2D transwell-based model. This result confirms the thesis stating that 3D bioengineered systems represent, compared to 2D cultures, more reliable and predictive models of the complex TME typical of pancreatic cancer[46–51]. Therefore, this human MEW model can be realistically applied to study the interactions between PDAC and stromal cells in a very controlled and biomimetic way.

Focusing on the microscale model, the manufacturing procedure adopted to produce the 3D MEW model can be considered as a pioneer study, since such gland complex geometry at a millimeter-scale was obtained without the need of any supports and/or cylindrical rotary mandrels[52–57]. Thus, our approach allows to bypass the technical difficulties in separating the printed scaffolds from the supports and permits to fabricate morphologies independently from the mandrels shape and dimensions.

However, the technical difficulties in obtaining the complete acino-ductal model (close structure) by assembling the two halves into the final 3D hollow structure prompted us to shift through other one-step manufacturing approaches such as tomographic volumetric bioprinting. This innovative technique permits to print hollow structures without the need for supports and in a very short building time (a few minutes)[58–61]. In addition, VBP avoids the technical difficulties and time-consuming procedures associated with the assembling of different cellularized compartments into a unique 3D structure[42].

Furthermore, one of the main advantages of this biofabrication approach is the cell-friendly procedure lying in the one-step manufacturing process which reduces the stress experienced by cells as compared to other multistep techniques such as the common solvent-casting method[62]. Thus, VBP was employed here for the first time to obtain a 3D fully human *in vitro* model of the exocrine pancreatic unit, by using human fibroblasts embedded in a GelMA hydrogel to reproduce the stromal component and HPDE cells injected in the cavity of the bioprinted construct to resemble the epithelial tissue. The developed soft

model, having viscoelastic properties comparable to those of the pancreatic tissue[63], allowed to easily monitor the successful proliferation of HFF1 within the gel over the culture period (up to 14 days) and the growth of HPDE cells on the duct walls. Finally, this model at the microscale permitted to assess the activation of stromal cells by quantifying the signal intensity coming from the expression of α-SMA proteins, demonstrating the ability of the bioprinted *in vitro* model in replicating the physiological inflammation cascade occurring in activated stromal cells[22,26,27].
With respect to the state-of-the-art, the developed model is the first to recapitulate the tumor-stroma interplay occurring in pancreatic cancer while also accurately reproducing the microanatomy of the exocrine gland. Therefore, it represents a powerful tool to reproduce the mechanisms involved at the early stages of PDAC evolution, study the pathology, perform efficient drug screening and elaborate personalized therapies to fight pancreatic cancer.

4.2 Final conclusion and future work

The work described in this dissertation focused on the development of *in vitro* models to replicate the functional unit of exocrine pancreas, for the study of pancreatic cancer. Different approaches have been explored to obtain models with increased biomimicry, ranging from a 2D transwell-based model to 3D constructs reproducing the compartmentalized architecture of exocrine pancreatic unit. The feasibility of the biofabrication techniques in obtaining scalable human *in vitro* models that can be tested and validated according to a high-throughput screening approach was demonstrated. The effectiveness of these systems in mimicking the crosstalk between human PDAC and stromal cells was also proved, in terms of cancer-associated inflammatory cascade and stromal cells activation. Therefore, the engineering strategies here adopted represent key technological advancements which allow to develop *in vitro* models that emulate the complex microanatomy of human organs including multiple cell phenotypes with 3D complex architectures. Indeed, the devices developed in this PhD project can contribute to make a step toward personalized cancer treatment, through the series production of several human and patient-specific models (using patients own cells), by adjusting the therapy to the patient's own situation, enhancing treatment outcomes and reducing healthcare costs.
Future steps of this work will address the improvement of models' ability in recapitulating the cellular composition of pancreatic cancer microenvironment[41,57,58].
In particular, endothelial cells and immune system cells will be introduced to analyze also other mechanisms involved in PDAC-stroma interplay, such as the collapse of blood vessels[20,59] and immunosuppression[18,60,61].
Moreover, for what concerns the drug treatment and the response to chemotherapies, PDAC-on-chip will be employed to carry out additional studies in order to evaluate the influence of stromal cells seeded in the microfluidic device on drug diffusion, through the implementation of an automated perfusion system.
Finally, the geometrical complexity of the 3D human VBP model will be furtherly enhanced by fabricating multiple acini connected to a duct (Fig. 4.1), thus mirroring the physiological grape-like structures.

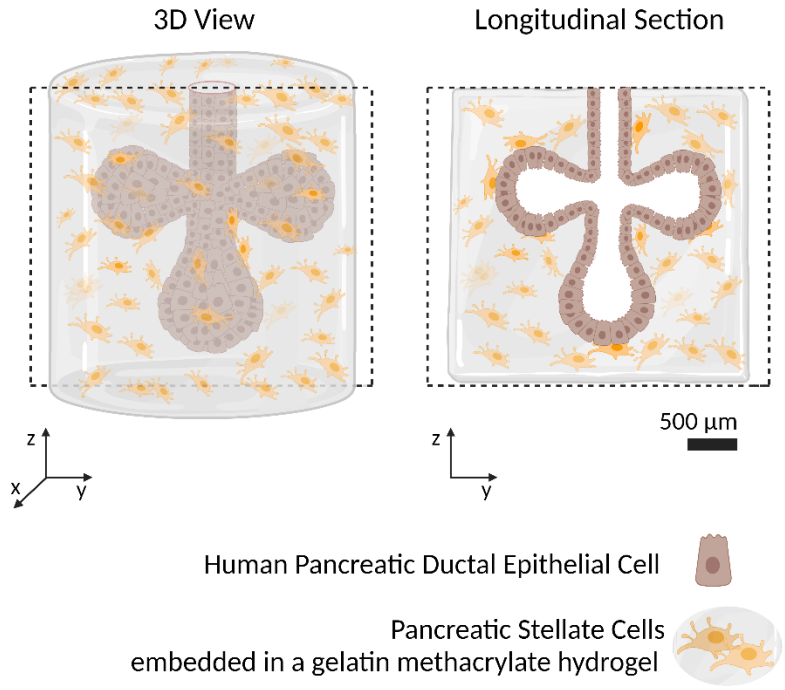

Fig. 4.1 Future work. Schematic illustration of the final geometry which will be implemented in the 3D human VBP model. (Figure drawn using Biorender.com).

In conclusion, the *in vitro* models developed in this PhD project represent attractive and powerful tools for the establishment of new diagnostic approaches and for the screening and testing of drugs. Therefore, they can be fundamental to improve the knowledge of the complex mechanisms implicated in PDAC and find innovative therapeutical strategies to fight pancreatic cancer

References

1. Khomiak A, Brunner M, Kordes M, et al. Recent Discoveries of Diagnostic, Prognostic and Predictive Biomarkers for Pancreatic Cancer. *Cancers (Basel)* 2020; 12: 3234.
2. Siegel RL, Miller KD, Jemal A. Cancer statistics, 2020. *CA Cancer J Clin* 2020; 70: 7–30.
3. Orth M, Metzger P, Gerum S, et al. Pancreatic ductal adenocarcinoma: Biological hallmarks, current status, and future perspectives of combined modality treatment approaches. *Radiation Oncology* 2019; 14: 1–20.
4. Brunet LR, Hagemann T, Andrew G, et al. Have lessons from past failures brought us closer to the success of immunotherapy in metastatic pancreatic cancer? *Oncoimmunology*; 5. Epub ahead of print 2 April 2016. DOI: 10.1080/2162402X.2015.1112942.
5. Apte M V., Wilson JS, Lugea A, et al. A starring role for stellate cells in the pancreatic cancer microenvironment. *Gastroenterology* 2013; 144: 1210–1219.
6. Nielsen MFB, Mortensen MB, Detlefsen S. Key players in pancreatic cancer-stroma interaction: Cancer-associated fibroblasts, endothelial and inflammatory cells. *World Journal of Gastroenterology* 2016; 22: 2678–2700.
7. Watt J, Kocher HM. The desmoplastic stroma of pancreatic cancer is a barrier to immune cell infiltration. *Oncoimmunology*; 2. Epub ahead of print 2013. DOI: 10.4161/ONCI.26788.
8. Weniger M, Honselmann KC, Liss AS. The extracellular matrix and pancreatic cancer: A

complex relationship. *Cancers*; 10. Epub ahead of print 6 September 2018. DOI: 10.3390/cancers10090316.
9. Fu Y, Liu S, Zeng S, et al. The critical roles of activated stellate cells-mediated paracrine signaling, metabolism and onco-immunology in pancreatic ductal adenocarcinoma. *Molecular Cancer*; 17. Epub ahead of print 19 February 2018. DOI: 10.1186/s12943-018-0815-z.
10. Hidalgo M, Cascinu S, Kleeff J, et al. Addressing the challenges of pancreatic cancer: Future directions for improving outcomes. *Pancreatology* 2015; 15: 8–18.
11. Bynigeri RR, Jakkampudi A, Jangala R, et al. Pancreatic stellate cell: Pandora's box for pancreatic disease biology. *World J Gastroenterol* 2017; 23: 382.
12. Hruban RH, Adsay NV, Albores-Saavedra J, et al. Pathology of genetically engineered mouse models of pancreatic exocrine cancer: Consensus report and recommendations. *Cancer Res* 2006; 66: 95–106.
13. Chari ST. Detecting Early Pancreatic Cancer: Problems and Prospects. *Semin Oncol* 2007; 34: 284–294.
14. Cui SJ, Tang TY, Zou XW, et al. Role of imaging biomarkers for prognostic prediction in patients with pancreatic ductal adenocarcinoma. *Clin Radiol*. Epub ahead of print 2020. DOI: 10.1016/j.crad.2019.12.023.
15. Cave DD, Rizzo R, Sainz B, et al. The revolutionary roads to study cell–cell interactions in 3d in vitro pancreatic cancer models. *Cancers (Basel)* 2021; 13: 1–19.
16. Osuna de la Peña D, Trabulo SMD, Collin E, et al. Bioengineered 3D models of human pancreatic cancer recapitulate in vivo tumour biology. *Nat Commun 2021 121* 2021; 12: 1–15.
17. Haque MR, Rempert TH, Al-Hilal TA, et al. Organ-Chip Models: Opportunities for Precision Medicine in Pancreatic Cancer. *Cancers (Basel)* 2021; 13: 4487.
18. Mollica H, Teo YJ, Tan ASM, et al. A 3D pancreatic tumor model to study T cell infiltration. *Biomater Sci* 2021; 9: 7420–7431.
19. Schuster B, Junkin M, Kashaf SS, et al. Automated microfluidic platform for dynamic and combinatorial drug screening of tumor organoids. *Nat Commun* 2020; 11: 1–12.
20. Nguyen DHT, Lee E, Alimperti S, et al. A biomimetic pancreatic cancer on-chip reveals endothelial ablation via ALK7 signaling. *Sci Adv* 2019; 5: 1–10.
21. Monteiro M V, Ferreira LP, Rocha M, et al. Journal Pre-proof Advances in bioengineering pancreatic tumor-stroma physiomimetic Biomodels. *Biomaterials*. Epub ahead of print 2022. DOI: 10.1016/j.biomaterials.2022.121653.
22. Monteiro M V., Rocha M, Gaspar VM, et al. Programmable Living Units for Emulating Pancreatic Tumor-Stroma Interplay. *Adv Healthc Mater* 2022; 2102574.
23. Wishart G, Gupta P, Schettino G, et al. 3d tissue models as tools for radiotherapy screening for pancreatic cancer 1,2. *Radiol* 2021; 94: 20201397.
24. Brancato V, Comunanza V, Imparato G, et al. Bioengineered tumoral microtissues recapitulate desmoplastic reaction of pancreatic cancer. *Acta Biomater* 2017; 49: 152–166.
25. Tomás-Bort E, Kieler M, Sharma S, et al. 3D approaches to model the tumor microenvironment of pancreatic cancer. *Issue 11 Theranostics* 2020; 10: 5074–5089.
26. Lazzari G, Nicolas V, Matsusaki M, et al. Multicellular spheroid based on a triple co-culture: A novel 3D model to mimic pancreatic tumor complexity. *Acta Biomater* 2018; 78: 296–307.
27. Lai BFL, Lu RXZ, Hu Y, et al. Recapitulating Pancreatic Tumor Microenvironment through Synergistic Use of Patient Organoids and Organ-on-a-Chip Vasculature. *Adv Funct Mater* 2020; 2000545: 1–16.
28. Yu Y, Yang G, Huang H, et al. Preclinical models of pancreatic ductal adenocarcinoma: challenges and opportunities in the era of precision medicine. *Journal of Experimental and Clinical Cancer Research* 2021; 40: 1–13.
29. Gündel B, Liu X, Löhr M, et al. Pancreatic Ductal Adenocarcinoma: Preclinical in vitro and ex vivo Models. *Front Cell Dev Biol* 2021; 9: 1–12.
30. Uzunparmak B, Sahin IH. Pancreatic cancer microenvironment: a current dilemma. *Clin Transl Med 2019 81* 2019; 8: 1–8.
31. Omary MB, Lugea A, Lowe AW, et al. The pancreatic stellate cell: A star on the rise in pancreatic diseases. *Journal of Clinical Investigation* 2007; 117: 50–59.
32. Buchholz Hans Kestler Karlheinz Holzmann Volker Ellenrieder Wilhelm Schneiderhan Marco

Siech Guido Adler Max G Bachem Thomas M Gress MA. Transcriptome analysis of human hepatic and pancreatic stellate cells: organ-specific variations of a common transcriptional phenotype. *J Mol Med* 2005; 83: 795–805.
33. Lai BFL, Lu RXZ, Hu Y, et al. Recapitulating Pancreatic Tumor Microenvironment through Synergistic Use of Patient Organoids and Organ-on-a-Chip Vasculature. *Adv Funct Mater* 2020; 2000545.
34. Ohuchida K, Mizumoto K, Murakami M, et al. Radiation to Stromal Fibroblasts Increases Invasiveness of Pancreatic Cancer Cells through Tumor-Stromal Interactions. *Cancer Res* 2004; 64: 3215–3222.
35. Damhofer H, Medema JP, Veenstra VL, et al. Assessment of the stromal contribution to Sonic Hedgehog-dependent pancreatic adenocarcinoma mRNA-Seq. Epub ahead of print 2013. DOI: 10.1016/j.molonc.2013.08.004.
36. Majety M, Pradel LP, Gies M, et al. Fibroblasts Influence Survival and Therapeutic Response in a 3D Co-Culture Model. Epub ahead of print 2015. DOI: 10.1371/journal.pone.0127948.
37. Shields MA, Dangi-Garimella S, Krantz SB, et al. Pancreatic Cancer Cells Respond to Type I Collagen by Inducing Snail Expression to Promote Membrane Type 1 Matrix Metalloproteinase-dependent Collagen Invasion. *J Biol Chem* 2011; 286: 10495.
38. Kota J, Hancock J, Kwon J, et al. Pancreatic cancer: Stroma and its current and emerging targeted therapies. *Cancer Lett* 2017; 391: 38–49.
39. Pothula SP, Pirola RC, Wilson JS, et al. Pancreatic stellate cells: Aiding and abetting pancreatic cancer progression. *Pancreatology* 2020; 20: 409–418.
40. Hajiabbas M, D'Agostino C, Simińska-Stanny J, et al. Bioengineering in salivary gland regeneration. *J Biomed Sci 2022 291* 2022; 29: 1–24.
41. Bradney MJ, Venis SM, Yang Y, et al. A Biomimetic Tumor Model of Heterogeneous Invasion in Pancreatic Ductal Adenocarcinoma. *Small* 2020; 1905500: 1–10.
42. Gupta P, Pérez-Mancera PA, Kocher H, et al. A Novel Scaffold-Based Hybrid Multicellular Model for Pancreatic Ductal Adenocarcinoma—Toward a Better Mimicry of the in vivo Tumor Microenvironment. *Front Bioeng Biotechnol*; 8. Epub ahead of print 2020. DOI: 10.3389/fbioe.2020.00290.
43. Venis SM, Moon HR, Yang Y, et al. Engineering of a functional pancreatic acinus with reprogrammed cancer cells by induced: PTF1a expression. *Lab Chip* 2021; 21: 3675–3685.
44. Randriamanantsoa S, Papargyriou A, Maurer HC, et al. Spatiotemporal dynamics of self-organized branching in pancreas-derived organoids. *Nat Commun* 2022; 13: 1–15.
45. Ushiki T. Collagen fibers, reticular fibers and elastic fibers. A comprehensive understanding from a morphological viewpoint. *Archives of Histology and Cytology* 2002; 65: 109–126.
46. Kapałczyńska M, Kolenda T, Przybyła W, et al. 2D and 3D cell cultures - a comparison of different types of cancer cell cultures. *Arch Med Sci* 2018; 14: 910–919.
47. Desoize B. Multicellular resistance: a paradigm for clinical resistance? *Crit Rev Oncol Hematol* 2000; 36: 193–207.
48. Brancato V, Oliveira JM, Correlo VM, et al. Could 3D models of cancer enhance drug screening? *Biomaterials*; 232. Epub ahead of print 2020. DOI: 10.1016/j.biomaterials.2019.119744.
49. Shichi Y, Sasaki N, Michishita M, et al. Enhanced morphological and functional differences of pancreatic cancer with epithelial or mesenchymal characteristics in 3D culture. *Sci Rep* 2019; 9: 10871.
50. Fang Y, Eglen RM. Three-Dimensional Cell Cultures in Drug Discovery and Development. *SLAS Discov* 2017; 22: 456–472.
51. Laschke MW, Menger MD. Life is 3D: Boosting Spheroid Function for Tissue Engineering. *Trends Biotechnol* 2017; 35: 133–144.
52. Saidy NT, Shabab T, Bas O, et al. Melt Electrowriting of Complex 3D Anatomically Relevant Scaffolds. *Front Bioeng Biotechnol* 2020; 8: 793.
53. Peiffer QC, de Ruijter M, van Duijn J, et al. Melt electrowriting onto anatomically relevant biodegradable substrates: Resurfacing a diarthrodial joint. *Mater Des* 2020; 195: 109025.
54. Brooks-Richards TL, Paxton NC, Allenby MC, et al. Dissolvable 3D printed PVA moulds for melt electrowriting tubular scaffolds with patient-specific geometry. *Mater Des* 2022; 215:

110466.
55. Saha U, Nairn R, Keenan O, et al. A Deeper Insight into the Influence of the Electric Field Strength When Melt-Electrowriting on Non-Planar Surfaces. *Macromol Mater Eng* 2021; 306: 2100496.
56. Constante G, Apsite I, Alkhamis H, et al. 4D Biofabrication Using a Combination of 3D Printing and Melt-Electrowriting of Shape-Morphing Polymers. *ACS Appl Mater Interfaces* 2021; 13: 12767–12776.
57. van Genderen AM, Jansen K, Kristen M, et al. Topographic Guidance in Melt-Electrowritten Tubular Scaffolds Enhances Engineered Kidney Tubule Performance. *Front Bioeng Biotechnol*; 8. Epub ahead of print 18 January 2021. DOI: 10.3389/fbioe.2020.617364.
58. Bernal PN, Bouwmeester M, Madrid-Wolff J, et al. Volumetric Bioprinting of Organoids and Optically Tuned Hydrogels to Build Liver-Like Metabolic Biofactories. *Adv Mater* 2022; 34: 2110054.
59. Madrid-Wolff J, Boniface A, Loterie D, et al. Controlling Light in Scattering Materials for Volumetric Additive Manufacturing. *Adv Sci* 2022; 9: 2105144.
60. Gehlen J, Qiu W, Müller R, et al. Volumetric Tomographic 3D Bioprinting of Heterocellular Bone- like Tissues in Seconds. 2021; 1–24.
61. Rizzo R, Ruetsche D, Liu H, et al. Optimized Photoclick (Bio)Resins for Fast Volumetric Bioprinting. *Adv Mater*; 33. Epub ahead of print 2021. DOI: 10.1002/adma.202102900.
62. Sola A, Bertacchini J, D'Avella D, et al. Development of solvent-casting particulate leaching (SCPL) polymer scaffolds as improved three-dimensional supports to mimic the bone marrow niche. *Mater Sci Eng C* 2019; 96: 153–165.
63. Wex C, Fröhlich M, Brandstädter K, et al. Experimental analysis of the mechanical behavior of the viscoelastic porcine pancreas and preliminary case study on the human pancreas. *J Mech Behav Biomed Mater* 2015; 41: 199–207.
64. Lazzari G, Nicolas V, Matsusaki M, et al. Multicellular spheroid based on a triple co-culture: A novel 3D model to mimic pancreatic tumor complexity. *Acta Biomater* 2018; 78: 296–307.
65. Chung CK, Long HP, Lai CC. Microfluidic chip using foil-assisted CO2 laser ablation for suspended particle separation. *Micro Nano Lett* 2015; 10: 500–503.
66. Nielsen MFB, Mortensen MB, Detlefsen S. Key players in pancreatic cancer-stroma interaction: Cancer-associated fibroblasts, endothelial and inflammatory cells. *World Journal of Gastroenterology* 2016; 22: 2678–2700.
67. Liu X, Xu J, Zhang B, et al. The reciprocal regulation between host tissue and immune cells in pancreatic ductal adenocarcinoma: new insights and therapeutic implications. *Mol Cancer* 2019; 18: 184.
68. Wang S, Li Y, Xing C, et al. Tumor microenvironment in chemoresistance, metastasis and immunotherapy of pancreatic cancer. *Am J Cancer Res* 2020; 10: 1937.
1. Khomiak A, Brunner M, Kordes M, et al. Recent Discoveries of Diagnostic, Prognostic and Predictive Biomarkers for Pancreatic Cancer. Cancers (Basel) 2020; 12: 3234.
2. Siegel RL, Miller KD, Jemal A. Cancer statistics, 2020. CA Cancer J Clin 2020; 70: 7–30.
3. Orth M, Metzger P, Gerum S, et al. Pancreatic ductal adenocarcinoma: Biological hallmarks, current status, and future perspectives of combined modality treatment approaches. Radiation Oncology 2019; 14: 1–20.
4. Brunet LR, Hagemann T, Andrew G, et al. Have lessons from past failures brought us closer to the success of immunotherapy in metastatic pancreatic cancer? Oncoimmunology; 5. Epub ahead of print 2 April 2016. DOI: 10.1080/2162402X.2015.1112942.
5. Apte M V., Wilson JS, Lugea A, et al. A starring role for stellate cells in the pancreatic cancer microenvironment. Gastroenterology 2013; 144: 1210–1219.
6. Nielsen MFB, Mortensen MB, Detlefsen S. Key players in pancreatic cancer-stroma interaction: Cancer-associated fibroblasts, endothelial and inflammatory cells. World Journal of Gastroenterology 2016; 22: 2678–2700.

7. Watt J, Kocher HM. The desmoplastic stroma of pancreatic cancer is a barrier to immune cell infiltration. Oncoimmunology; 2. Epub ahead of print 2013. DOI: 10.4161/ONCI.26788.
8. Weniger M, Honselmann KC, Liss AS. The extracellular matrix and pancreatic cancer: A complex relationship. Cancers; 10. Epub ahead of print 6 September 2018. DOI: 10.3390/cancers10090316.
9. Fu Y, Liu S, Zeng S, et al. The critical roles of activated stellate cells-mediated paracrine signaling, metabolism and onco-immunology in pancreatic ductal adenocarcinoma. Molecular Cancer; 17. Epub ahead of print 19 February 2018. DOI: 10.1186/s12943-018-0815-z.
10. Hidalgo M, Cascinu S, Kleeff J, et al. Addressing the challenges of pancreatic cancer: Future directions for improving outcomes. Pancreatology 2015; 15: 8–18.
11. Bynigeri RR, Jakkampudi A, Jangala R, et al. Pancreatic stellate cell: Pandora's box for pancreatic disease biology. World J Gastroenterol 2017; 23: 382.
12. Hruban RH, Adsay NV, Albores-Saavedra J, et al. Pathology of genetically engineered mouse models of pancreatic exocrine cancer: Consensus report and recommendations. Cancer Res 2006; 66: 95–106.
13. Chari ST. Detecting Early Pancreatic Cancer: Problems and Prospects. Semin Oncol 2007; 34: 284–294.
14. Cui SJ, Tang TY, Zou XW, et al. Role of imaging biomarkers for prognostic prediction in patients with pancreatic ductal adenocarcinoma. Clin Radiol. Epub ahead of print 2020. DOI: 10.1016/j.crad.2019.12.023.
15. Cave DD, Rizzo R, Sainz B, et al. The revolutionary roads to study cell–cell interactions in 3d in vitro pancreatic cancer models. Cancers (Basel) 2021; 13: 1–19.
16. Osuna de la Peña D, Trabulo SMD, Collin E, et al. Bioengineered 3D models of human pancreatic cancer recapitulate in vivo tumour biology. Nat Commun 2021 121 2021; 12: 1–15.
17. Haque MR, Rempert TH, Al-Hilal TA, et al. Organ-Chip Models: Opportunities for Precision Medicine in Pancreatic Cancer. Cancers (Basel) 2021; 13: 4487.
18. Mollica H, Teo YJ, Tan ASM, et al. A 3D pancreatic tumor model to study T cell infiltration. Biomater Sci 2021; 9: 7420–7431.
19. Schuster B, Junkin M, Kashaf SS, et al. Automated microfluidic platform for dynamic and combinatorial drug screening of tumor organoids. Nat Commun 2020; 11: 1–12.
20. Nguyen DHT, Lee E, Alimperti S, et al. A biomimetic pancreatic cancer on-chip reveals endothelial ablation via ALK7 signaling. Sci Adv 2019; 5: 1–10.
21. Monteiro M V, Ferreira LP, Rocha M, et al. Journal Pre-proof Advances in bioengineering pancreatic tumor-stroma physiomimetic Biomodels. Biomaterials. Epub ahead of print 2022. DOI: 10.1016/j.biomaterials.2022.121653.
22. Monteiro M V., Rocha M, Gaspar VM, et al. Programmable Living Units for Emulating Pancreatic Tumor-Stroma Interplay. Adv Healthc Mater 2022; 2102574.
23. Wishart G, Gupta P, Schettino G, et al. 3d tissue models as tools for radiotherapy screening for pancreatic cancer 1,2. Radiol 2021; 94: 20201397.
24. Brancato V, Comunanza V, Imparato G, et al. Bioengineered tumoral microtissues recapitulate desmoplastic reaction of pancreatic cancer. Acta Biomater 2017; 49: 152–166.
25. Tomás-Bort E, Kieler M, Sharma S, et al. 3D approaches to model the tumor microenvironment of pancreatic cancer. Issue 11 Theranostics 2020; 10: 5074–5089.
26. Lazzari G, Nicolas V, Matsusaki M, et al. Multicellular spheroid based on a triple co-culture: A novel 3D model to mimic pancreatic tumor complexity. Acta Biomater 2018; 78: 296–307.

27. Lai BFL, Lu RXZ, Hu Y, et al. Recapitulating Pancreatic Tumor Microenvironment through Synergistic Use of Patient Organoids and Organ-on-a-Chip Vasculature. Adv Funct Mater 2020; 2000545: 1–16.
28. Yu Y, Yang G, Huang H, et al. Preclinical models of pancreatic ductal adenocarcinoma: challenges and opportunities in the era of precision medicine. Journal of Experimental and Clinical Cancer Research 2021; 40: 1–13.
29. Gündel B, Liu X, Löhr M, et al. Pancreatic Ductal Adenocarcinoma: Preclinical in vitro and ex vivo Models. Front Cell Dev Biol 2021; 9: 1–12.
30. Uzunparmak B, Sahin IH. Pancreatic cancer microenvironment: a current dilemma. Clin Transl Med 2019 81 2019; 8: 1–8.
31. Omary MB, Lugea A, Lowe AW, et al. The pancreatic stellate cell: A star on the rise in pancreatic diseases. Journal of Clinical Investigation 2007; 117: 50–59.
32. Buchholz Hans Kestler Karlheinz Holzmann Volker Ellenrieder Wilhelm Schneiderhan Marco Siech Guido Adler Max G Bachem Thomas M Gress MA. Transcriptome analysis of human hepatic and pancreatic stellate cells: organ-specific variations of a common transcriptional phenotype. J Mol Med 2005; 83: 795–805.
33. Lai BFL, Lu RXZ, Hu Y, et al. Recapitulating Pancreatic Tumor Microenvironment through Synergistic Use of Patient Organoids and Organ-on-a-Chip Vasculature. Adv Funct Mater 2020; 2000545.
34. Ohuchida K, Mizumoto K, Murakami M, et al. Radiation to Stromal Fibroblasts Increases Invasiveness of Pancreatic Cancer Cells through Tumor-Stromal Interactions. Cancer Res 2004; 64: 3215–3222.
35. Damhofer H, Medema JP, Veenstra VL, et al. Assessment of the stromal contribution to Sonic Hedgehog-dependent pancreatic adenocarcinoma mRNA-Seq. Epub ahead of print 2013. DOI: 10.1016/j.molonc.2013.08.004.
36. Majety M, Pradel LP, Gies M, et al. Fibroblasts Influence Survival and Therapeutic Response in a 3D Co-Culture Model. Epub ahead of print 2015. DOI: 10.1371/journal.pone.0127948.
37. Shields MA, Dangi-Garimella S, Krantz SB, et al. Pancreatic Cancer Cells Respond to Type I Collagen by Inducing Snail Expression to Promote Membrane Type 1 Matrix Metalloproteinase-dependent Collagen Invasion. J Biol Chem 2011; 286: 10495.
38. Kota J, Hancock J, Kwon J, et al. Pancreatic cancer: Stroma and its current and emerging targeted therapies. Cancer Lett 2017; 391: 38–49.
39. Pothula SP, Pirola RC, Wilson JS, et al. Pancreatic stellate cells: Aiding and abetting pancreatic cancer progression. Pancreatology 2020; 20: 409–418.
40. Hajiabbas M, D'Agostino C, Simińska-Stanny J, et al. Bioengineering in salivary gland regeneration. J Biomed Sci 2022 291 2022; 29: 1–24.
41. Bradney MJ, Venis SM, Yang Y, et al. A Biomimetic Tumor Model of Heterogeneous Invasion in Pancreatic Ductal Adenocarcinoma. Small 2020; 1905500: 1–10.
42. Gupta P, Pérez-Mancera PA, Kocher H, et al. A Novel Scaffold-Based Hybrid Multicellular Model for Pancreatic Ductal Adenocarcinoma—Toward a Better Mimicry of the in vivo Tumor Microenvironment. Front Bioeng Biotechnol; 8. Epub ahead of print 2020. DOI: 10.3389/fbioe.2020.00290.
43. Venis SM, Moon HR, Yang Y, et al. Engineering of a functional pancreatic acinus with reprogrammed cancer cells by induced: PTF1a expression. Lab Chip 2021; 21: 3675–3685.
44. Randriamanantsoa S, Papargyriou A, Maurer HC, et al. Spatiotemporal dynamics of self-organized branching in pancreas-derived organoids. Nat Commun 2022; 13: 1–15.

45. Ushiki T. Collagen fibers, reticular fibers and elastic fibers. A comprehensive understanding from a morphological viewpoint. Archives of Histology and Cytology 2002; 65: 109–126.
46. Kapałczyńska M, Kolenda T, Przybyła W, et al. 2D and 3D cell cultures - a comparison of different types of cancer cell cultures. Arch Med Sci 2018; 14: 910–919.
47. Desoize B. Multicellular resistance: a paradigm for clinical resistance? Crit Rev Oncol Hematol 2000; 36: 193–207.
48. Brancato V, Oliveira JM, Correlo VM, et al. Could 3D models of cancer enhance drug screening? Biomaterials; 232. Epub ahead of print 2020. DOI: 10.1016/j.biomaterials.2019.119744.
49. Shichi Y, Sasaki N, Michishita M, et al. Enhanced morphological and functional differences of pancreatic cancer with epithelial or mesenchymal characteristics in 3D culture. Sci Rep 2019; 9: 10871.
50. Fang Y, Eglen RM. Three-Dimensional Cell Cultures in Drug Discovery and Development. SLAS Discov 2017; 22: 456–472.
51. Laschke MW, Menger MD. Life is 3D: Boosting Spheroid Function for Tissue Engineering. Trends Biotechnol 2017; 35: 133–144.
52. Saidy NT, Shabab T, Bas O, et al. Melt Electrowriting of Complex 3D Anatomically Relevant Scaffolds. Front Bioeng Biotechnol 2020; 8: 793.
53. Peiffer QC, de Ruijter M, van Duijn J, et al. Melt electrowriting onto anatomically relevant biodegradable substrates: Resurfacing a diarthrodial joint. Mater Des 2020; 195: 109025.
54. Brooks-Richards TL, Paxton NC, Allenby MC, et al. Dissolvable 3D printed PVA moulds for melt electrowriting tubular scaffolds with patient-specific geometry. Mater Des 2022; 215: 110466.
55. Saha U, Nairn R, Keenan O, et al. A Deeper Insight into the Influence of the Electric Field Strength When Melt-Electrowriting on Non-Planar Surfaces. Macromol Mater Eng 2021; 306: 2100496.
56. Constante G, Apsite I, Alkhamis H, et al. 4D Biofabrication Using a Combination of 3D Printing and Melt-Electrowriting of Shape-Morphing Polymers. ACS Appl Mater Interfaces 2021; 13: 12767–12776.
57. van Genderen AM, Jansen K, Kristen M, et al. Topographic Guidance in Melt-Electrowritten Tubular Scaffolds Enhances Engineered Kidney Tubule Performance. Front Bioeng Biotechnol; 8. Epub ahead of print 18 January 2021. DOI: 10.3389/fbioe.2020.617364.
58. Bernal PN, Bouwmeester M, Madrid-Wolff J, et al. Volumetric Bioprinting of Organoids and Optically Tuned Hydrogels to Build Liver-Like Metabolic Biofactories. Adv Mater 2022; 34: 2110054.
59. Madrid-Wolff J, Boniface A, Loterie D, et al. Controlling Light in Scattering Materials for Volumetric Additive Manufacturing. Adv Sci 2022; 9: 2105144.
60. Gehlen J, Qiu W, Müller R, et al. Volumetric Tomographic 3D Bioprinting of Heterocellular Bone- like Tissues in Seconds. 2021; 1–24.
61. Rizzo R, Ruetsche D, Liu H, et al. Optimized Photoclick (Bio)Resins for Fast Volumetric Bioprinting. Adv Mater; 33. Epub ahead of print 2021. DOI: 10.1002/adma.202102900.
62. Sola A, Bertacchini J, D'Avella D, et al. Development of solvent-casting particulate leaching (SCPL) polymer scaffolds as improved three-dimensional supports to mimic the bone marrow niche. Mater Sci Eng C 2019; 96: 153–165.
63. Wex C, Fröhlich M, Brandstädter K, et al. Experimental analysis of the mechanical behavior of the viscoelastic porcine pancreas and preliminary case study on the human pancreas. J Mech Behav Biomed Mater 2015; 41: 199–207.

64. Lazzari G, Nicolas V, Matsusaki M, et al. Multicellular spheroid based on a triple co-culture: A novel 3D model to mimic pancreatic tumor complexity. Acta Biomater 2018; 78: 296–307.
65. Chung CK, Long HP, Lai CC. Microfluidic chip using foil-assisted CO2 laser ablation for suspended particle separation. Micro Nano Lett 2015; 10: 500–503.
66. Nielsen MFB, Mortensen MB, Detlefsen S. Key players in pancreatic cancer-stroma interaction: Cancer-associated fibroblasts, endothelial and inflammatory cells. World Journal of Gastroenterology 2016; 22: 2678–2700.
67. Liu X, Xu J, Zhang B, et al. The reciprocal regulation between host tissue and immune cells in pancreatic ductal adenocarcinoma: new insights and therapeutic implications. Mol Cancer 2019; 18: 184.
68. Wang S, Li Y, Xing C, et al. Tumor microenvironment in chemoresistance, metastasis and immunotherapy of pancreatic cancer. Am J Cancer Res 2020; 10: 1937.